**US Army Corps
of Engineers**
Waterways Experiment
Station

Numerical Hydrodynamic Modeling in Support of Water Quality and Ship Simulation Models in Los Angeles Harbor

by   *Harry V. Wang, Alan Cialone, Panola Rivers*

DTIC
ELECTE
MAR 2 3 1995
G

Approved For Public Release; Distribution Is Unlimited

19950321 176

DTIC QUALITY INSPECTED

Prepared for   U.S. Army Engineer District, Los Angeles

The contents of this report are not to be used for advertising, publication, or promotional purposes. Citation of trade names does not constitute an official endorsement or approval of the use of such commercial products.

Numerical Hydrodynamic Modeling in Support of Water Quality and Ship Simulation Models in Los Angeles Harbor

by Harry V. Wang, Alan Cialone, Panola Rivers

U.S. Army Corps of Engineers
Waterways Experiment Station
3909 Halls Ferry Road
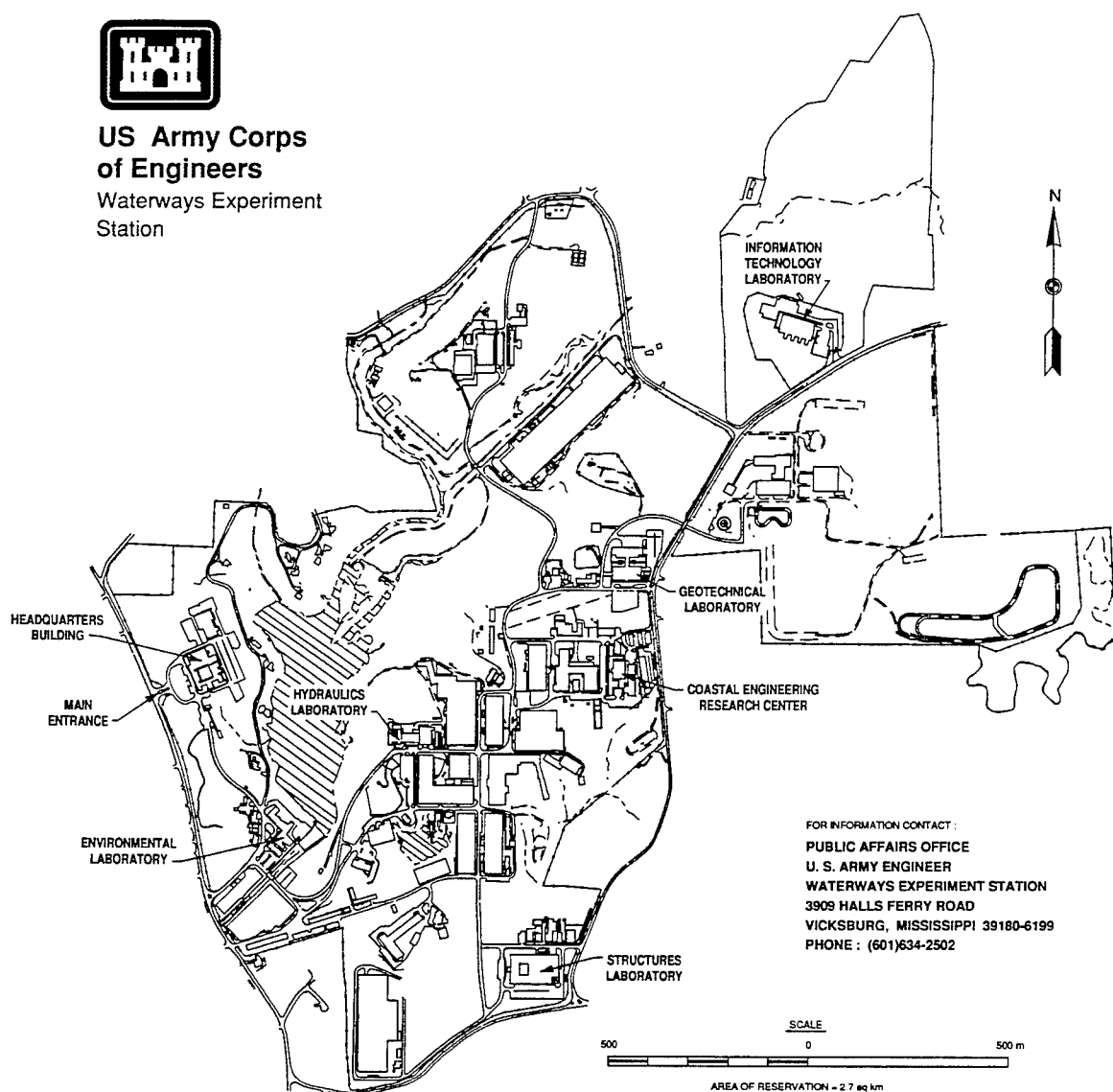Vicksburg, MS   39180-6199

Accesion For	
NTIS CRA&I	☒
DTIC TAB	☐
Unannounced	☐
Justification	
By	
Distribution /	
Availability Codes	
Dist	Avail and / or Special
A-1	

Final report

Approved for public release; distribution is unlimited

Prepared for   U.S. Army Engineer District, Los Angeles
Los Angeles, CA   90053-2325

**US Army Corps
of Engineers**
Waterways Experiment
Station

INFORMATION
TECHNOLOGY
LABORATORY

GEOTECHNICAL
LABORATORY

HEADQUARTERS
BUILDING

COASTAL ENGINEERING
RESEARCH CENTER

MAIN
ENTRANCE

HYDRAULICS
LABORATORY

ENVIRONMENTAL
LABORATORY

N

FOR INFORMATION CONTACT :
**PUBLIC AFFAIRS OFFICE
U. S. ARMY ENGINEER
WATERWAYS EXPERIMENT STATION
3909 HALLS FERRY ROAD
VICKSBURG, MISSISSIPPI 39180-6199
PHONE : (601)634-2502**

STRUCTURES
LABORATORY

SCALE

500   0   500 m

AREA OF RESERVATION = 2.7 sq km

Contents

List of Figures

List of Tables

Preface

This report describes the results of a three-dimensional numerical circulation modeling effort undertaken to investigate the hydrodynamic impact of ship channel dredging and the disposal of the dredged material at Pier 400 in Los Angeles Harbor. The report describes how the various stages of the Pier 400 expansion and channel deepening will affect circulation and current velocity in the harbor under the combined effects of tide and wind. Comparison of hydrodynamic results for both the existing and proposed conditions demonstrates the impact of the dredged channel and the proposed Pier 400 on the outer Los Angeles Harbor. The investigation was conducted during the period November 1992 through November 1993.

This study was performed as a joint endeavor between the U.S. Army Engineer Waterways Experiment Station (WES) Coastal Engineering Research Center (CERC), Environmental Laboratory (EL), and Hydraulics Laboratory (HL). CERC's responsibilities included implementing a hydrodynamic circulation model by using both coarse and fine model grids to simulate currents under normal tide, wind, and critical wind conditions. Final results of the hydrodynamic model were then transferred to EL and HL for further usage in driving water quality and ship simulation models. Separate reports will be presented by Mr. Ross Hall, EL, (water quality modeling) and Mr. J. Christopher Hewlett, HL, (ship simulation modeling).

During the course of the study, liaison was maintained between WES, the U.S. Army Engineer District, Los Angeles, and the Port of Los Angeles. Overall WES management of the study was performed by Mr. Dennis G. Markle, Chief of the Wave Processes Branch, Wave Dynamics Division. Responsible engineers at the Los Angeles District during the study were Ms. Jane Grandon, and Mr. Art Shak, Chief, Coastal Engineering Section. Mr. John Foxworthy and Mr. Dick Wittkop, followed by Dr. Kimo Walker and Mr. Russell Boudreau of Moffatt and Nichol, Engineers, were port points of contact and provided invaluable assistance.

The hydrodynamic study was performed under the general supervision of Dr. James R. Houston and Mr. Charles C. Calhoun, Jr., Director and Assistant Director, respectively, CERC. Direct supervision of this project was provided by Mr. H. Lee Butler, Chief, Research Division (RD), and Dr. Martin Miller, Chief, Coastal Oceanography Branch, RD, CERC.

Dr. Robert W. Whalin was Director of WES during the study and publication of this report. COL Leonard G. Hassell, EN, was Commander of WES during early phases of this study. At the time of publication of this report, COL Bruce K. Howard, EN, was WES Commander.

Conversion Factors, Non-SI to SI Units of Measurement

Non-SI units of measurement used in this report can be converted to SI units as follows:

Multiply	By	To obtain
acres	4,046.873	square meters
degrees (angle)	0.01745329	radians
feet	0.3048	meters
feet per second	30.48	centimeters per second
knots (international)	51.44444	centimeters per second
miles per hour (mph)	0.4470	meters per second
miles (U.S. statute)	1.609347	kilometers
square miles	2.589998	square kilometers

1 Introduction

Background Information

Los Angeles and Long Beach Harbor on the California coast (Figure 1) is one of the largest harbor systems in the world. Rising projections for harbor use necessitate the need for expansion of the port to meet the demands for larger vessels and for the port to operate more efficiently. In order for the ports of Los Angeles and Long Beach to efficiently meet their forecast cargo handling requirements for the year 2020, an extensive expansion program is proposed, including navigation improvements and creation of land for future terminals.

The port expansion is comprised of a number of components. The Recommended Federal Project at the Port of Los Angeles (POLA) was designed as a joint effort between the U.S. Army Corps of Engineers and POLA and calls for four increments of navigation channel improvements (dredging), coupled with disposal of the dredged material at Pier 400 in the Outer Los Angeles Harbor to create 582 acres[1] of new land. These four increments, Increments 2 through 5, are outlined in the Corps of Engineers Final Feasibility Report and the Environmental Impact Statement (EIS)/Environmental Impact Report (EIR) for Deep Draft Navigation Improvements at Los Angeles Harbor. (Increments 1 and 6 at the Port of Long Beach (POLB) are not being studied at this time.)

This report documents numerical hydrodynamic modeling done in support of the final designs of the project. Support includes providing long-term hydrodynamic transport information to a water quality model for assessing environmental impacts and transient current velocities to a ship simulation model for navigation studies.

---

[1] A table of factors for converting non-SI units of measurement to SI units is presented on page x.

Overviews of the Hydrodynamic Studies

An early hydrodynamic test in the Los Angeles and Long Beach Harbors used a physical model (McAnally 1975) to simulate tidal circulation in the laboratory. The experiment achieves satisfactory results for spring and neap tidal circulation. However, it was realized that the physical model could not mimic wind-driven circulation. Instead, Raney (1976a,b) and Outlaw and Raney (1979) used a vertically averaged, two-dimensional (2-D) hydrodynamic model to simulate the harbor circulation. The simulation duration was 25 hr and was applied to a proposed outer harbor oil terminal. With the numerical model, wind forcing is relatively easy to achieve. Subsequently, Seaberg and Outlaw (1984) used WIFM (WES Implicit Flooding Model) to study the 2020 plan with the additional constituent transport equation built into the model.

The 2020 plan called for dredging and landfills in various regions of the harbor complex, which resulted in greater harbor and channel depths. With the increase of depth comes the greater variation of water velocity. This is particularly true when wind forcing is present. To better evaluate the flow condition, it becomes necessary to advance to a three-dimensional (3-D) modeling system to examine variation associated with different depths in the water column.

Vemulakonda (1990) and Vemulakonda, Chou, and Hall (1991) were the first to apply a 3-D model in Los Angeles and Long Beach Harbor. The model, CH3D-WES (Curvilinear Hydrodynamics in Three Dimensions), is a time- varying, 3-D hydrodynamic model for simulating circulation affected by tide, wind, river inflow, and density currents. Vemulakonda, Chou, and Hall have reviewed the available field data and gone through various sensitivity tests to calibrate and verify CH3D-WES for the harbor.

The present effort continues the previous work with higher grid resolution in both the horizontal and vertical directions, more accurate and up-to-date geographic data, and a thoroughly coupled 3-D tidal and wind-driven circulation model. The model will be applied to various scenarios including the existing condition as well as plans proposed by POLA and the Corps. Final results will be used to drive a separate water quality model and a ship simulation model.

The organization of this report is as follows. Chapter 2 presents the numerical model formulation including the governing equations and the solution procedure. In Chapter 3, the model is calibrated and validated against field data collected during August, 1987. A numerical model/physical model comparison is also included. In Chapter 4, scenarios and results in support of the water quality study are presented. In Chapter 5, sensitivity tests of grid resolution and wind effects on harbor circulation are presented. Scenarios were then determined based on the test. Finally, results from five different harbor

proposed plans in support of ship simulation are presented. Conclusions from
the various parts of the study are summarized in Chapter 6.
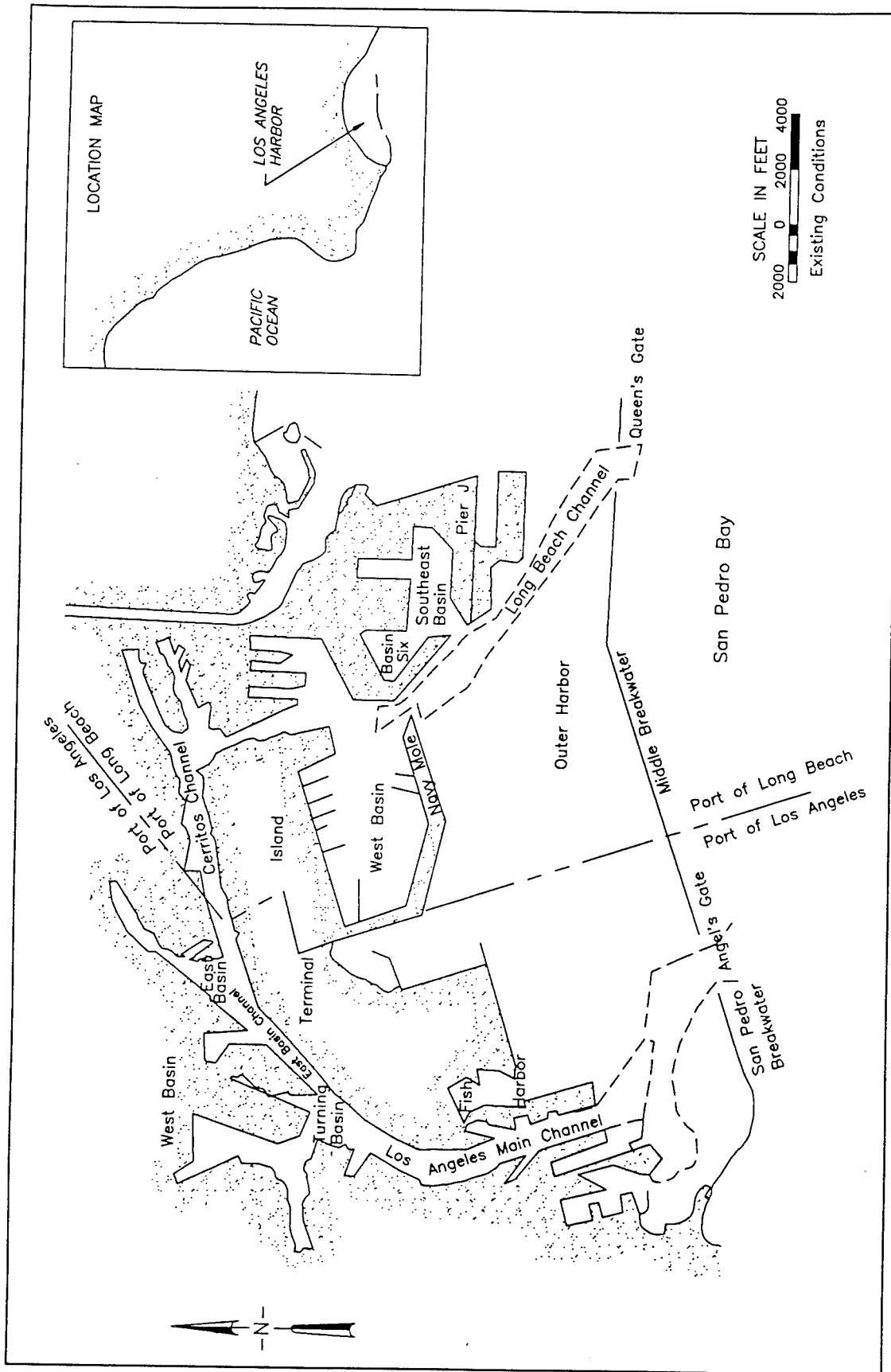
Figure 1.   Los Angeles and Long Beach Harbors layout

2 Description of the Numerical Hydrodynamic Model

The numerical hydrodynamic model CH3D-WES (Curviliner Hydrodynamics in Three Dimensions - WES) was selected to provide a hydrodynamic flow field for input to a water quality model and ship simulator. The basic model was originally developed by Sheng (1986). Subsequently, it was extensively modified by WES through algorithm re-coding and implementing numerical formulation (Johnson et al. 1991).

Governing Equations

Hydrodynamic equations used in CH3D are derived from the classical Navier-Stokes equations. The governing partial differential equations are based on the following assumptions:

a. Hydrostatic distribution adequately describes the vertical distribution of fluid pressure.

b. Boussinesq approximation is appropriate.

c. Eddy viscosity approach adequately describes turbulent mixing in the flow.

The basic equations in a right-handed Cartesian coordinate system (x,y,z) are:

$$\frac{\partial u}{\partial x} + \frac{\partial v}{\partial y} + \frac{\partial w}{\partial z} = 0 \tag{1}$$

$$\frac{\partial u}{\partial t} + \frac{\partial u^2}{\partial x} + \frac{\partial uv}{\partial y} + \frac{\partial uw}{\partial z} = fv - \frac{1}{\rho_o} \frac{\partial p}{\partial x} + \frac{\partial}{\partial x} \left(A_H \frac{\partial u}{\partial x} \right)$$

$$+ \frac{\partial}{\partial y} \left(A_H \frac{\partial u}{\partial y} \right) + \frac{\partial}{\partial z} \left(A_v \frac{\partial u}{\partial z} \right) \qquad (2)$$

$$\frac{\partial v}{\partial t} + \frac{\partial uv}{\partial x} + \frac{\partial v^2}{\partial y} + \frac{\partial vw}{\partial z} = - fu - \frac{1}{\rho_o} \frac{\partial p}{\partial y} + \frac{\partial}{\partial x} \left(A_H \frac{\partial v}{\partial x} \right)$$

$$+ \frac{\partial}{\partial y} \left(A_H \frac{\partial v}{\partial y} \right) + \frac{\partial}{\partial z} \left(A_v \frac{\partial v}{\partial z} \right) \qquad (3)$$

$$\frac{\partial p}{\partial z} = - \rho g \qquad (4)$$

$$\frac{\partial T}{\partial t} + \frac{\partial uT}{\partial x} + \frac{\partial vT}{\partial y} + \frac{\partial wT}{\partial z}$$

$$= \frac{\partial}{\partial x} \left(K_H \frac{\partial T}{\partial x} \right) + \frac{\partial}{\partial y} \left(K_H \frac{\partial T}{\partial y} \right) + \frac{\partial}{\partial z} \left(K_v \frac{\partial T}{\partial z} \right) \qquad (5)$$

$$\frac{\partial S}{\partial t} + \frac{\partial uS}{\partial x} + \frac{\partial vS}{\partial y} + \frac{\partial wS}{\partial z}$$

$$= \frac{\partial}{\partial x} \left(K_H \frac{\partial S}{\partial x} \right) + \frac{\partial}{\partial y} \left(K_H \frac{\partial S}{\partial y} \right) + \frac{\partial}{\partial z} \left(K_v \frac{\partial S}{\partial z} \right) \qquad (6)$$

$$\rho = \rho (T,S) \qquad (7)$$

where

(u,v,w) = velocities in (x,y,z) directions

t = time

f = Coriolis parameter defined as $2\Omega \sin \phi$

Ω = rotational speed of the earth

ϕ = latitude

ρ = density

p = pressure

A_H, K_H = horizontal turbulent eddy coefficients

A_v, K_v = vertical turbulent eddy coefficients

g = gravitational acceleration

T = temperature

S = salinity

Equation 4 implies that vertical accelerations are negligible and thus pressure is hydrostatic. Various forms of the equation of state can be specified for Equation 7. In the present model, the formulation given below is used:

$$\rho = P/(\alpha + 0.698P) \tag{8}$$

where

$$P = 5890 + 38T - 0.375T^2 + 3S$$

$$\alpha = 1779.5 + 11.25T - 0.0745T^2 - (3.8 + 0.01T)S$$

and T is temperature in degrees Celsius, S is salinity in parts per thousand, and ρ is density in grams per cubic centimeter.

Non-dimensionalization of Governing Equations

The dimensionless forms of the governing equations are used to facilitate relative magnitude comparisons of the various terms in the equations. The following dimensionless variables are used:

$$(u^*, v^*, w^*) = (u, v, wX_r/Z_r)/U_r$$

$$(x^*, y^*, z^*) = (x, y, zX_r/Z_r)/X_r$$

$$(\tau_x^*, \tau_y^*) = (\tau_x^w, \tau_y^w)/\rho_o fZ_r U_r$$

$$t* = tf$$

$$\zeta^* = g\zeta/fU_r X_r = \zeta/S_r$$

$$\rho^* = (\rho - \rho_o)/(\rho_r - \rho_o) \tag{9}$$

$$T^* = (T - T_o)/(T_r - T_o)$$

$$A_H^* = A_H/A_{Hr}$$

$$A_v^* = A_v / A_{vr}$$

$$K_H^* = K_H / K_{Hr}$$

$$K_v^* = K_v / K_{vr}$$

where

$\left(\tau_x^w, \tau_y^w\right)$ = wind stress in (x,y) directions

ζ = water surface elevation

These definitions yield the following dimensionless parameters in the governing equations:

Vertical Ekman Number: $E_v = A_{vr} / f Z_r^2$

Lateral Ekman Number: $E_H = A_{Hr} / f X_r^2$

Vertical Prandtl (Schmidt) Number: $Pr_v = A_{vr} / K_{vr}$

Lateral Prandtl (Schmidt) Number: $Pr_H = A_{Hr} / K_{Hr}$

Froude Number: $F_r = U_r / (g Z_r)^{1/2}$

Rossby Number: $R_o = U_r / f X_r$ 　　　　　　　　　　(10)

Densimetric Froude Number: $Fr_D = F_r / \sqrt{\varepsilon}$

where

$$\varepsilon = (\rho_r - \rho_o)/\rho_o$$

S_r, T_r, U_r, ρ_r, X_r, Z_r, A_{Hr}, A_{vr}, K_{Hr}, and K_{vr} are arbitrary reference values of the salinity, temperature, velocity, density, etc.

External-Internal Modes

The basic equations (Equations 1-4) can be integrated over the depth to yield a set of vertically integrated equations for the water surface ζ and unit flow rates U and V in the x and y directions. Using the dimensionless variables (asterisks have been dropped) and the parameters previously defined, the vertically integrated equations·constituting the external mode are:

8

$$\frac{\partial \zeta}{\partial t} + \beta \left(\frac{\partial U}{\partial x} + \frac{\partial V}{\partial y} \right) = 0 \qquad (11)$$

$$\frac{\partial U}{\partial t} = - H \frac{\partial \zeta}{\partial x} + \tau_{sx} - \tau_{bx} + V$$

$$- R_o \left[\frac{\partial}{\partial x} \left(\frac{UU}{H} \right) + \frac{\partial}{\partial y} \left(\frac{UV}{H} \right) \right] \qquad (12)$$

$$+ E_H \left[\frac{\partial}{\partial x} \left(A_H \frac{\partial U}{\partial x} \right) + \frac{\partial}{\partial y} \left(A_H \frac{\partial U}{\partial y} \right) \right]$$

$$- \frac{R_o}{Fr_D^2} \frac{H^2}{2} \frac{\partial \rho}{\partial x}$$

$$\frac{\partial V}{\partial t} = - H \frac{\partial \zeta}{\partial y} + \tau_{sy} - \tau_{by} - U$$

$$- R_o \left[\frac{\partial}{\partial x} \left(\frac{UV}{H} \right) + \frac{\partial}{\partial y} \left(\frac{VV}{H} \right) \right]$$

$$+ E_H \left[\frac{\partial}{\partial x} \left(A_H \frac{\partial V}{\partial x} \right) + \frac{\partial}{\partial y} \left(A_H \frac{\partial V}{\partial y} \right) \right] \qquad (13)$$

$$- \frac{R_o}{Fr_D^2} \frac{H^2}{2} \frac{\partial \rho}{\partial y}$$

where

$$\beta = gZr/f^2 X_r^2 \equiv (R_o/F_r)^2$$

H = total depth

As will be discussed later, the major purpose of the external mode is to provide the updated water-surface field for input to the internal mode equations.

The internal mode equations from which the 3-D velocity, salinity, and temperature fields are computed are as follows:

$$\frac{\partial hu}{\partial t} = - h \frac{\partial \zeta}{\partial x} + E_v \frac{\partial}{\partial z} \left(A_v \frac{\partial hu}{\partial z} \right) + hv$$

$$- R_o \left(\frac{\partial huu}{\partial x} + \frac{\partial huv}{\partial y} + \frac{\partial huw}{\partial z} \right)$$

$$+ E_H \left[\frac{\partial}{\partial x} \left(A_H \frac{\partial hu}{\partial x} \right) + \frac{\partial}{\partial y} \left(A_H \frac{\partial hu}{\partial y} \right) \right] \qquad (14)$$

$$- \frac{R_o}{Fr_D^2} \left(\int_z^\zeta \frac{\partial \rho}{\partial x} \, dz \right)$$

$$\frac{\partial hv}{\partial t} = - h \frac{\partial \zeta}{\partial y} + E_v \frac{\partial}{\partial z} \left(A_v \frac{\partial hv}{\partial z} \right) - hu$$

$$- R_o \left(\frac{\partial hvu}{\partial x} + \frac{\partial hvv}{\partial y} + \frac{\partial hvw}{\partial z} \right)$$

$$+ E_H \left[\frac{\partial}{\partial x} \left(A_H \frac{\partial hv}{\partial x} \right) + \frac{\partial}{\partial y} \left(A_H \frac{\partial hv}{\partial y} \right) \right] \qquad (15)$$

$$- \frac{R_o}{Fr_D^2} \left(\int_z^\zeta \frac{\partial \rho}{\partial y} \, dz \right)$$

$$W_{k+1/2} = W_{k-1/2} - \left(\frac{\partial uh}{\partial x} + \frac{\partial vh}{\partial y} \right) \qquad (16)$$

$$\frac{\partial hT}{\partial t} = \frac{E_v}{Pr_v} \frac{\partial}{\partial z} \left(K_v \frac{\partial T}{\partial z} \right) - R_o \left(\frac{\partial huT}{\partial x} + \frac{\partial hvT}{\partial y} + \frac{\partial hwT}{\partial z} \right)$$

$$+ \frac{E_H}{Pr_H} \left[\frac{\partial}{\partial x} \left(K_H \frac{\partial hT}{\partial x} \right) + \frac{\partial}{\partial y} \left(K_H \frac{\partial hT}{\partial y} \right) \right] \qquad (17)$$

$$\frac{\partial hS}{\partial t} = \frac{E_v}{Pr_v} \frac{\partial}{\partial z} \left(K_v \frac{\partial S}{\partial z} \right) - R_o \left(\frac{\partial huS}{\partial x} + \frac{\partial hvS}{\partial y} + \frac{\partial hwS}{\partial z} \right)$$

$$+ \frac{E_H}{Pr_H} \left[\frac{\partial}{\partial x} \left(K_H \frac{\partial hS}{\partial x} \right) + \frac{\partial}{\partial y} \left(K_H \frac{\partial hS}{\partial y} \right) \right] \qquad (18)$$

In these equations h is the thickness of an internal layer and $k+1/2$ and $k-1/2$ represent the top and bottom, respectively, of the kth vertical layer and W is the transcript in the z-direction.

Transformation of Governing Equations

The CH3D model utilizes a boundary-fitted or generalized curvilinear plan-form grid which can be made to conform to flow boundaries, providing a detailed resolution of the complex horizontal geometry of the flow system. This necessitates the transformation of the governing equations into boundary-fitted coordinates (ξ, η). If only the (x,y) coordinates are transformed, a system

of equations similar to those solved by Johnson (1980) for vertically averaged flow fields is obtained. However, in the CH3D model not only are the (x,y) coordinates transformed into the (ξ,η) curvilinear system but the velocity is also transformed such that its components are perpendicular to the (ξ,η) coordinate lines. This is accomplished by employing the definitions below for the components of the Cartesian velocity (u,v) in terms of contravariant components $\bar{u}$ and $\bar{v}$.

$$u = x_{\xi}\bar{u} + x_{\eta}\bar{v} \tag{19}$$

$$v = y_{\xi}\bar{u} + y_{\eta}\bar{v} \tag{20}$$

along with the following expressions for replacing Cartesian derivatives

$$f_x = \frac{1}{J}\left[(fy_{\eta})_{\xi} - (fy_{\xi})_{\eta}\right] \tag{21}$$

$$f_y = \frac{1}{J}\left[-(fx_{\eta})_{\xi} + (fx_{\xi})_{\eta}\right] \tag{22}$$

where

f is an arbitrary variable and J is the Jacobian of the coordinate transformation defined as

$$J = x_{\xi}y_{\eta} - x_{\eta}y_{\xi} \tag{23}$$

With the governing equations written in terms of the contravariant components of the velocity, boundary conditions can be prescribed on the boundary-fitted grid in the same manner as on a Cartesian grid because $\bar{u}$ and $\bar{v}$ are perpendicular to the curvilinear cell faces (e.g., at a land boundary, either $\bar{u}$ or $\bar{v}$ is set to zero).

The vertical dimension is represented through the use of what is commonly referred to as a sigma-stretched grid. Vertical depth is discretized in a fixed number of layers, each layer equal in thickness to a fixed percentage of the local depth. The sigma-stretched grid is then transformed to a fixed-space grid where the computations are easily performed.

With both the Cartesian coordinates and the Cartesian velocity transformed, the following boundary-fitted equations for $\bar{u}$, $\bar{v}$, w, S, and T to be solved in each vertical layer are obtained.

$$\frac{\partial h\overline{u}}{\partial t} = -h\left(\frac{G_{22}}{J^2}\frac{\partial \zeta}{\partial \xi} - \frac{G_{12}}{J^2}\frac{\partial \zeta}{\partial \eta}\right) + \frac{h}{J}\left(G_{12}\ \overline{u} + G_{22}\ \overline{v}\right) + \frac{R_o x_\eta}{J^2}\left[\frac{\partial}{\partial \xi}\left(Jy_\xi h\overline{u}\,\overline{u}\right.\right.$$

$$\left.\left. + Jy_\eta h\overline{u}\,\overline{v}\right) + \frac{\partial}{\partial \eta}\left(Jy_\xi h\overline{u}\,\overline{v} + Jy_\eta h\overline{v}\,\overline{v}\right)\right] - \frac{R_o y_\eta}{J^2}\left[\frac{\partial}{\partial \xi}\left(Jx_\xi h\overline{u}\,\overline{u} + Jx_\eta h\overline{u}\,\overline{v}\right)\right.$$

$$\left. + \frac{\partial}{\partial \eta}\left(Jx_\xi h\overline{u}\,\overline{v} + Jx_\eta h\overline{v}\,\overline{v}\right)\right] - R_o\left[\left(w\overline{u}\right)_{top} - \left(w\overline{u}\right)_{bot}\right] \qquad (24)$$

$$+ E_v\left[\left(A_v\frac{\partial \overline{u}}{\partial z}\right)_{top} - \left(A_v\frac{\partial \overline{u}}{\partial z}\right)_{bot}\right] - \frac{R_o h}{Fr_D^2}\left[\int_z^\zeta\left(\frac{G_{22}}{J^2}\frac{\partial \rho}{\partial \xi}\right.\right.$$

$$\left.\left. - \frac{G_{12}}{J^2}\frac{\partial \rho}{\partial \eta}\right)dz\right] + \textit{Horizontal Diffusion}$$

$$\frac{\partial h\overline{v}}{\partial t} = -h\left(-\frac{G_{21}}{J^2}\frac{\partial \zeta}{\partial \xi} + \frac{G_{11}}{J^2}\frac{\partial \zeta}{\partial \eta}\right) - \frac{h}{J}\left(G_{11}\ \overline{u} + G_{21}\ \overline{v}\right)$$

$$- \frac{R_{ox_\xi}}{J^2}\left[\frac{\partial}{\partial \xi}\left(Jy_\xi h\overline{u}\,\overline{u} + Jy_\eta h\overline{u}\,\overline{v}\right) + \frac{\partial}{\partial \eta}\left(Jy_\xi h\overline{u}\,\overline{v} + Jy_\eta h\overline{v}\,\overline{v}\right)\right]$$

$$+ \frac{R_{oy_\xi}}{J^2}\left[\frac{\partial}{\partial \xi}\left(Jx_\xi h\overline{u}\,\overline{u} + Jx_\eta h\overline{u}\,\overline{v}\right) + \frac{\partial}{\partial \eta}\left(Jx_\xi h\overline{u}\,\overline{v} + Jx_\eta h\overline{v}\,\overline{v}\right)\right] \qquad (25)$$

$$- R_o\left[\left(w\overline{v}\right)_{top} - \left(w\overline{v}\right)_{bot}\right] + \textit{Horizontal Diffusion}$$

$$w_{top} = w_{bot} - \frac{1}{J}\left(\frac{\partial J\overline{u}h}{\partial \xi} + \frac{\partial J\overline{v}h}{\partial \eta}\right) \qquad (26)$$

$$\frac{\partial hS}{\partial t} = \frac{E_v}{Pr_v}\left[\left(K_v\frac{\partial S}{\partial z}\right)_{top} - \left(K_v\frac{\partial S}{\partial z}\right)_{bot}\right] - \frac{R_o}{J}\left(\frac{\partial hJ\overline{u}S}{\partial \xi} + \frac{\partial hJ\overline{v}S}{\partial \eta}\right)$$

$$- R_o\left[\left(wS\right)_{top} - \left(wS\right)_{bot}\right] + \textit{Horizontal Diffusion} \qquad (27)$$

$$\frac{\partial hT}{\partial t} = \frac{E_v}{Pr_v}\left[\left(K_v\frac{\partial T}{\partial z}\right)_{top} - \left(K_v\frac{\partial T}{\partial z}\right)_{bot}\right] - \frac{R_o}{J}\left(\frac{\partial hJ\overline{u}T}{\partial \xi} + \frac{\partial hJ\overline{v}T}{\partial \eta}\right)$$

$$- R_o\left[\left(wT\right)_{top} - \left(wT\right)_{bot}\right] + \textit{Horizontal Diffusion} \qquad (28)$$

where

$$G_{11} = x_\xi^2 + y_\xi^2$$

$$G_{22} = x_\eta^2 + y_\eta^2$$

$$G_{12} = G_{21} = x_\xi x_\eta + y_\xi y_\eta$$

Similarly, the transformed external mode equations become:

$$\frac{\partial \zeta}{\partial t} + \beta \left(\frac{\partial \bar{U}}{\partial \xi} + \frac{\partial \bar{V}}{\partial \eta} \right) = 0 \tag{29}$$

$$\frac{\partial \bar{U}}{\partial t} = - \frac{H}{J^2} \left(G_{22} \frac{\partial \zeta}{\partial \xi} - G_{12} \frac{\partial \zeta}{\partial \eta} \right)$$

$$+ \frac{1}{J} \left(G_{12}\bar{U} + G_{22}\bar{V} \right) + \frac{R_o x_\eta}{J^2 H} \left[\frac{\partial}{\partial \xi} \left(Jy_\xi \bar{U}\bar{U} + Jy_\eta \bar{U}\bar{V} \right) + \frac{\partial}{\partial \eta} \left(Jy_\xi \bar{U}\bar{V} + Jy_\eta \bar{V}\bar{V} \right) \right]$$

$$- \frac{R_o y_\eta}{J^2 H} \left[\frac{\partial}{\partial \xi} \left(Jx_\xi \bar{U}\bar{U} + Jx_\eta \bar{U}\bar{V} \right) + \frac{\partial}{\partial \eta} \left(Jx_\xi \bar{U}\bar{V} + Jx_\eta \bar{V}\bar{V} \right) \right] \tag{30}$$

$$+ \tau_{s\xi} - \tau_{b\xi} - \frac{R_o}{Fr_D^2} \frac{H^2}{2} \left(G_{22} \frac{\partial \rho}{\partial \xi} - G_{12} \frac{\partial \rho}{\partial \eta} \right) + Horizontal\ Diffusion$$

$$\frac{\partial \bar{V}}{\partial t} = - \frac{H}{J^2} \left(- G_{21} \frac{\partial \zeta}{\partial \xi} + G_{11} \frac{\partial \zeta}{\partial \eta} \right) - \frac{1}{J} \left(G_{11} \bar{U} + G_{21}\bar{V} \right)$$

$$- \frac{R_o x_\xi}{J^2 H} \left[\frac{\partial}{\partial \xi} \left(Jy_\xi \bar{U}\bar{U} + Jy_\eta \bar{U}\bar{V} \right) + \frac{\partial}{\partial \eta} \left(Jy_\xi \bar{U}\bar{V} + Jy_\eta \bar{V}\bar{V} \right) \right]$$

$$+ \frac{R_o y_\xi}{J^2 H} \left[\frac{\partial}{\partial \xi} \left(Jx_\xi \bar{U}\bar{U} + Jx_\eta \bar{U}\bar{V} \right) + \frac{\partial}{\partial \eta} \left(Jx_\xi \bar{U}\bar{V} + Jx_\eta \bar{V}\bar{V} \right) \right] \tag{31}$$

$$+ \tau_{s\eta} - \tau_{b\eta} - \frac{R_o}{Fr_D^2} \frac{H^2}{2} \left(- G_{21} \frac{\partial \rho}{\partial \xi} + G_{11} \frac{\partial \rho}{\partial \eta} \right) + Horizontal\ Diffusion$$

Equations 29-31 are solved first to yield water-surface elevations which are then used to evaluate the water-surface slope terms in the internal mode equations. Horizontal diffusion terms are quite lengthy and thus are omitted in this report. Full documentation of the terms is presented in Johnson et al. (1991) for the internal mode equations. Similar expressions for the diffusion terms in the vertically averaged equations can be inferred from those for the internal mode.

Finite Difference Scheme

Finite differences are used to replace derivatives in the governing equations, resulting in a system of linear algebraic equations to be solved in both the external and internal modes. The external mode solution consists of the surface displacement and vertically integrated contravariant unit flows $\bar{U}$ and $\bar{V}$. All terms in the transformed vertically averaged continuity equation are treated implicitly whereas only the water-surface slope terms in the transformed vertically averaged momentum equations are treated implicitly. If the external mode is used only as a vertically averaged model, the bottom friction is also treated implicitly. Those terms treated implicitly are weighted between the new and old time-steps. The resulting finite difference equations are then factored such that an ξ-sweep followed by an η-sweep of the horizontal grid yields the solution at the new time-step.

Writing Equations 11-13 as

$$\frac{\partial \zeta}{\partial t} + \beta \left(\frac{\partial \bar{U}}{\partial \xi} + \frac{\partial \bar{V}}{\partial \eta} \right) = 0 \tag{32}$$

$$\frac{\partial \bar{U}}{\partial t} + \frac{H}{J^2} G_{22} \frac{\partial \zeta}{\partial \xi} = M \tag{33}$$

$$\frac{\partial \bar{V}}{\partial t} + \frac{H}{J^2} G_{11} \frac{\partial \zeta}{\partial \eta} = N \tag{34}$$

the ξ-sweep is

$$\xi\text{-}sweep \Rightarrow \zeta_{ij}^* + \frac{\beta\theta\Delta t}{\Delta\xi} \left(\bar{U}_{i+1,j}^* - \bar{U}_{ij}^* \right) = \zeta_{ij}^n$$

$$- (1-\theta)\frac{\Delta t}{\Delta\xi} \left(\bar{U}_{i+1,j}^n - \bar{U}_{ij}^n \right) \tag{35}$$

$$- \frac{\Delta t}{\Delta\eta} \left(\bar{V}_{i,j+1}^n - \bar{V}_{ij}^n \right)$$

$$\overline{U}_{ij}^{n+1} + \frac{\theta \Delta t H G_{22}}{\Delta \xi \, J^2} \left(\overset{*}{\zeta}_{ij} - \overset{*}{\zeta}_{i-1,j} \right) = \overline{U}_{ij}^{n}$$

$$-(1-\theta) \frac{\Delta t H G_{22}}{\Delta \xi \, J^2} \left(\zeta_{ij}^{n} - \zeta_{i-1,j}^{n} \right) + \Delta t \, M^{n} \tag{36}$$

and the η-sweep then provides the updated ζ and V at the $n+1$ time level.

$$\eta\text{-sweep} \Rightarrow \zeta_{ij}^{n+1} + \frac{\beta \theta \Delta t}{\Delta \eta} \left(\overline{V}_{i,j+1}^{n+1} - \overline{V}_{ij}^{n+1} \right) = \overset{*}{\zeta}_{i,j}$$

$$- (1-\theta) \frac{\Delta t}{\Delta \eta} \left(\overline{V}_{i,j+1}^{n} - \overline{V}_{i,j}^{n} \right) \tag{37}$$

$$+ \frac{\Delta t}{\Delta \eta} \left(\overline{V}_{i,j+1}^{n} - \overline{V}_{i,j}^{n} \right)$$

$$\overline{V}_{i,j}^{n+1} + \frac{\theta \Delta t H G_{11}}{\Delta \eta \, J^2} \left(\zeta_{i,j+1}^{n+1} - \zeta_{i,j}^{n+1} \right)$$

$$= V_{i,j}^{n} \tag{38}$$

$$-(1-\theta) \frac{\Delta t H G_{11}}{\Delta \eta \, J^2} \left(\zeta_{i,j+1}^{n} - \zeta_{i,j}^{n} \right) + \Delta t \, N^{n}$$

A typical value of θ of 0.55 yields stable and accurate solutions.

The internal mode consists of computations from Equations 24-28 for the three velocity components $\overline{u}$, $\overline{v}$, and w, salinity, and temperature. The only terms treated implicitly are the vertical diffusion terms in all equations and the bottom friction and surface slope terms in the momentum equations. Values of the water-surface elevations from the external mode are used to evaluate the surface slope terms in Equations 24 and 25. As a result, the extremely restrictive speed of a free-surface gravity wave is removed from the stability criteria. Roache's second upwind differencing scheme is used to represent the convective terms in the momentum equations, whereas a spatially third-order scheme developed by Leonard (1979) (called QUICKEST) is used to represent the advective terms in Equations 27 and 28 for salinity and temperature,

respectively. For example, if the velocity on the right face of a computational cell is positive, then with QUICKEST the value of the salinity used to compute the flux through the face is

$$S_R = \frac{1}{2}\left(S_{i,j,k} + S_{i+1,j,k}\right)$$

$$-\frac{1}{6}\left[1 - \left(\frac{\bar{U}_{i+1,j,k}\,\Delta t}{\Delta\xi}\right)^2\right]\left(S_{i+1,j,k} - 2\,S_{i,j,k} + S_{i-1,j,k}\right) \tag{39}$$

$$-\frac{1}{2}\frac{U_{i+1,j,k}\,\Delta t}{\Delta\xi}\left(S_{i+1,j,k} - S_{i,j,k}\right)$$

The more interested reader is referred to the paper by Leonard (1979).

It should be noted that once the $\bar{u}$ and $\bar{v}$ velocity components are computed, they are slightly adjusted to ensure conservation of mass. This is accomplished by forcing the sum of $\bar{u}$ over the vertical to be the vertically averaged velocity $\bar{U}/H$ and the sum of $\bar{v}$ over the vertical to equal $\bar{V}/H$, where H is the total water depth.

Turbulence Parameterization

Vertical turbulence is handled by using the concept of eddy viscosity and diffusivity to represent the velocity and density correlation terms that arise from time averaging of the governing equations. These eddy coefficients are computed from mean flow characteristics using a simplified second-order closure model originally developed by Donaldson (1973). The closure model has been further developed and applied to various types of flows by Lewellen (1977) and Sheng (1982, 1986). A discussion of the implementation of the turbulence model taken from Sheng (1990) follows. For more details, the interested reader should refer to these references and to Johnson et al. (1991).

Assuming local equilibrium of turbulence (i.e., there is no time evolution or spatial diffusion of the second-order correlations) an equation relating the turbulent kinetic energy and the macro-scale of turbulence to the mean flow shear and stratification (given by the Richardson number Ri) can be derived as

$$3A^2b^2sQ^4 + A[(bs + 3b + 7b^2s)Ri - Abs(1 - 2b)]Q^2$$
$$+ b(s + 3 + 4bs)Ri^2 + (bs - A)(1 - 2b)Ri \tag{40}$$
$$= 0$$

where

$b = 0.125$

$s = 1.8$

$A = 0.75$

and

$$Q = \frac{q}{\Lambda\sqrt{(\partial\overline{u}/\partial z)^2 + (\partial\overline{v}/\partial z)^2}} \tag{41}$$

In the above expression, q is defined as

$$q = \left(\overline{u'u'} + \overline{v'v'} + \overline{w'w'}\right)^{1/2} \tag{42}$$

and Λ is the macro-scale of turbulence. The quantities u', v', *and* w' are the turbulent velocity fluctuations and the overbar indicates time averaging.

It can also be shown that the following relations hold:

$$\overline{u'w'} = -\frac{\frac{\partial\overline{u}}{\partial z}\Lambda}{q}\frac{1 + \frac{\overline{\omega}}{A}}{1 - \omega}\overline{w'w'} \tag{43}$$

$$\overline{v'w'} = -\frac{\frac{\partial\overline{v}}{\partial z}\Lambda}{q}\frac{1 + \frac{\overline{\omega}}{A}}{1 - \omega}\overline{w'w'} \tag{44}$$

$$q^2 b = \left[\frac{(1 + \frac{\overline{\omega}}{A})}{Q^2(1 - \omega)} + \overline{\omega}\right]\overline{w'w'} \tag{45}$$

where

$$\omega = \frac{Ri}{AQ^2} \tag{46}$$

and

$$\overline{\omega} = \frac{\omega}{1 - \dfrac{\omega}{bs}} \tag{47}$$

Thus, after the velocity shear and flow stratification are determined q can be computed from Equations 40 and 41. $\overline{w'w'}$ is then determined from

$$\overline{w'w'} = \frac{\dfrac{q^2}{2} - q^2 b}{\dfrac{3}{2}(1 - 2\omega)} \tag{48}$$

Finally, after Λ is prescribed, $\overline{u'w'}$ and $\overline{v'w'}$ can be computed from Equations 43 and 44 and the vertical eddy coefficients can be determined from

$$A_v = \frac{\overline{-u'w'}}{\dfrac{\partial \overline{u}}{\partial z}} = \frac{\Lambda}{q} \frac{A + \overline{\omega}}{A(1 - \omega)} \overline{w'w'} \tag{49}$$

$$K_v = \frac{\overline{-\rho'w'}}{\dfrac{\partial \rho}{\partial z}} = \frac{\Lambda}{q} \frac{bs}{(bs - \omega)A} \overline{w'w'} \tag{50}$$

In addition to setting $\Lambda = 0.65z$ near boundaries, three basic constraints are used to compute Λ at a vertical position z

$$\left| \frac{d\Lambda}{dz} \right| \leq 0.65 \tag{51}$$

$$\Lambda \leq \frac{q}{N} = q / \left(-\frac{g}{\rho} \frac{\partial \rho}{\partial z} \right)^{0.5} \tag{52}$$

$$\Lambda \leq Q_{cut} \left(z_{q=qmax} - z_{q=qmax/2} \right) \tag{53}$$

where

N is the Brunt-Vaisala frequency. Equation 50 states that Λ is less than a fraction of the spread of turbulence as measured by the distance between the location of a maximum q^2 to where q^2 is equal to 25 percent of the maximum. The coefficient Q_{cut} is on the order of 0.15 to 0.25.

18

3 Implementation of the Numerical Model

Initial and Boundary Conditions

When initiating a run of CH3D-WES, the values of ζ, $\bar{u}$, $\bar{v}$, $\bar{w}$, $\bar{U}$ and $\bar{V}$ are set to zero. Values of salinity and temperature are read from input files. These initial data are generated from prototype measurements at a limited number of locations. Once the values in individual cells are determined by interpolating from field data, the resulting 3-D field is smoothed. Generally, the salinity and temperature fields are held constant for the first few days of a simulation.

The boundary conditions at the free surface are

$$A_v \left(\frac{\partial \bar{u}}{\partial z} , \frac{\partial \bar{v}}{\partial z} \right) = \left(\tau_{s_\xi} , \tau_{s_\eta} \right) / \rho = \left(C \, W_\xi^2 , C \, W_\eta^2 \right) \tag{54}$$

$$\frac{\partial T}{\partial z} = \frac{Pr_v}{E_v} K \, (T - T_e) \tag{55}$$

$$\frac{\partial S}{\partial z} = 0 \tag{56}$$

whereas the boundary conditions at the bottom are

$$A_v \left(\frac{\partial \bar{u}}{\partial z} , \frac{\partial \bar{v}}{\partial z} \right) = \left(\tau_{b_\xi} , \tau_{b_\eta} \right) / \rho \tag{57}$$

$$= \frac{U_r}{A_{vr}} Z_r C_d \left(\bar{u}_1^2 + \bar{v}_1^2 \right)^{1/2} \left(\bar{u}_1, \bar{v}_1 \right) \tag{58}$$

$$\frac{\partial T}{\partial z} , \frac{\partial S}{\partial z} = 0 \qquad (59)$$

where

C = surface drag coefficient

W = wind speed

K = surface heat exchange coefficient

T_e = equilibrium temperature

C_d = bottom friction coefficient

$\bar{u}_1, \bar{v}_1$ = values of the horizontal velocity components next to the bottom

C_d is given by

$$C_d = k^2 \left[\ln \left(z_1/z_o \right) \right]^{-2} \qquad (60)$$

With z_1 equal to one half the bottom layer thickness,

where

K = von Karman constant

z_o = bottom roughness height

Manning's formulation is employed for the bottom friction in the external mode equations if the model is used only to compute vertically averaged flow fields. The surface drag coefficient is computed according to Garratt (1977) as follows:

$$C = (0.75 + 0.067 \ W) \ x \ 10^{-3} \qquad (61)$$

where

W is the wind speed in meters per second

with the maximum allowable value being 0.003. The surface heat exchange coefficient K and the equilibrium temperature T_e are computed from meteorological data (wind speed, cloud cover, wet and dry bulb air temperatures, and relative humidity) as discussed by Edinger, Brady, and Geyer (1974).

At an ocean boundary, the water-surface elevation is prescribed along with time-varying vertical distributions of salinity and temperature. Specified values of salinity and temperature are employed during flood flow, whereas during ebb, interior values are advected out of the grid. Normal components of velocity, viscosity, and diffusivity are set to zero along solid boundaries.

Computational Grid

The computational grid was constructed using a rectilinear orthogonal grid system (Figure 2). The grid was aligned to coincide with the inner harbor entrance channels. This area was represented by a smoothly varying finite-difference grid with x and y axes parallel to the east-west and north-south model limits, respectively. The total grid for the Los Angeles and Long Beach Harbor included 128 cells in the x-direction and 94 cells in the y-direction (12,032 cells). Within the Los Angeles Harbor the grid measured 36 cells in the x direction and 94 cells in the y direction. The grid's finest resolution was concentrated in the outer harbor area and the inner harbor channels to provide better circulation definition for the harbor area. Cells in this area measured approximately 235 ft. The grid extended seaward of the middle breakwater approximately 4.2 miles and covered an area of 146 square miles. A vertically stretched, staggered grid scheme is used internally for computation. Figure 3 illustrates schematically the staggered grid, in which vertical velocity is shifted one half interval relative to the density, while the horizontal velocity grid is shifted by half an interval horizontally relative to density. The vertically stretched grid preserves the same order of vertical resolution for the shallow and deeper part of the water body, which leads to a smooth representation of the topography.

Calibration of the Numerical Hydrodynamic Model

Numerical modeling of hydrodynamics and transport in three dimensions is a highly complicated task. To demonstrate the capability of the model, it must undergo calibration and validation. Calibration is the procedure where certain model parameters are adjusted to maximize the agreement between model results and measured field data. The adjustable parameters in this model are friction, drag, and mixing coefficient. Once the calibration procedure is completed, the model is applied without further adjusting the parameters for validation. Obtaining good comparisons between model and measured data provides confidence that the model can simulate the hydrodynamic condition in the study area.

CH3D-WES has been extensively calibrated with the prototype measurements in Los Angeles and Long Beach Harbor (Vemulakonda, Chou, and Hall 1990). Several changes, however, have occurred since 1990 in the Los Angeles and Long Beach Harbors. Among them are: (a) the addition of Pier J in Long

Beach Harbor; (b) deepening of the channel around Pier J; and (c) change of the bottom topography around Island White near Long Beach. In addition, up-to-date topographic information is available from recent surveys. Therefore, a fine-tuning procedure around Los Angeles Harbor is necessary. Three prototype measurement stations near Los Angeles Harbor were selected (Figure 4): Stations CM2 (Los Angeles Main Channel) and CM3 (Long Beach Harbor Channel near Navy mole) for current velocity comparison, and gauge TG3 (Cerritos Channel) for water surface elevation comparison.

The calibration was conducted over a 5-day period starting at 0000 on the 7th of August, 1987, and ending at 2400 on the 11th. A time-step of 60 sec was used throughout the model runs. Measured tidal elevations (Figure 5a) were used as the open boundary condition. Semidiurnal and diurnal tides are evident in the tide record. Wind data were used to compute the wind stress on the water surface (Figures 5b,c). The average wind speeds experienced during this period of simulation were 5 mph, with wind blowing predominantly from the west and southwest. The wind direction shown is measured clockwise from true north. Also observed was diurnal variation of wind speed and direction, which indicates the influence of the sea-land breeze. The sea breeze is characterized by onshore wind during the day from the west and southwest, and a relatively quiescent condition during the night.

The model-calculated water surface elevation and the prototype measured data at Cerritos Channel are compared in Figure 6. The model accurately reproduces the surface water elevation both in phase and amplitude. The Manning n value used is equal to 0.035 for most of the area. However, in shallow areas having depths less than 20 ft but greater than 10 ft, a Manning's n equai to 0.037 was assigned, and in areas with depths less than 10 ft, a Manning's n equal to 0.040 was assigned. This refinement improves the results because velocity is sensitive to local topography. Figures 7-9 show comparisons of current speed and direction at the surface, middle, and bottom layer. Good comparisons were obtained for speed and direction in all three layers. Notable exceptions occurred during brief periods, such as hr 65-70 and 85-90, where the model underpredicts the surface current speed. It appears that during these periods, both the outer and inner harbor are experiencing steady wind from the west, which coincides with the harbor's longest fetch. In these cases, there is a strong chance for wind-generated waves to enter the harbor. These conditions can degrade the accuracy of the Endeco current meter readings.

The final set of model coefficients thus determined are: Manning's coefficient n equal to 0.035 for the global area; shallow areas having depths less than 20 ft but greater than 10 ft, a Manning's n equal to 0.037 was assigned and areas having depth less than 10 ft, n equal to 0.040 was assigned. Horizontal mixing coefficient equals 10,000 cm^2/sec and base vertical mixing coefficient equals 10 cm^2/sec. The wind drag coefficient is calculated by the formula $C = (0.75+0.67\ W) \times 10^{-3}$, where W is measured in m/sec.

22

Validation of the Numerical Hydrodynamic Model

A 5-day period in 1987, 19-23 August, was chosen for model validation. Figure 10a,b,c shows the overall tide and wind conditions, which are similar to the calibration period except that tide amplitude is somewhat reduced in magnitude. The model accurately replicated the water surface elevation to the accuracy of 0.1 cm as shown in Figure 11. At the Los Angeles Channel, the predicted current speed and direction match the prototype measurement reasonably well both at the middle and bottom layers. There was a lesser degree of accuracy at the surface layer for short periods of wind events (Figures 12-14). This discrepancy of the comparison, again, is attributed to the wind wave activity on the surface layer. Additional validation was conducted by comparison between the numerical model and a physical model. The physical hydraulic model was used by the U.S. Army Corps of Engineers for a tidal circulation study in Los Angeles and Long Beach Harbors (McAnally 1975). It was constructed based on Froude number scaling criteria with a vertical scale of 1:100 and horizontal scale of 1:400. Local current speed was measured by a float with a miniature pole, vane drogues, and ring assembly. Tidal elevation was measured with a portable point gauge graduated in 0.001-ft increments. Surface current patterns for the entire harbor area were recorded by taking time exposure photographs of confetti floater on the water surface. The physical model was verified with 1972 field data and reproduces tidal currents and astronomical tide elevation. The merit of the numerical versus physical model comparison is that it provides additional, independent information to better validate the numerical model.

With all model parameters kept the same as determined by the calibration procedure, the numerical model was run for three spring tide cycles under calm wind conditions. Figure 15 shows the computed numerical model current speed versus measured physical model speed at station CM2 near Los Angeles Channel. Since the current direction in the physical model was measured from compass quadrant, the accuracy is less certain. Therefore the velocity has been plotted by flood (plus) or ebb (minus). The agreement appears to be fairly good. The spatial distribution of surface circulation was also obtained from physical model measurements. Comparison of circulation patterns between the numerical and physical models at maximum ebb current is presented in Figure 16. The two results are in close agreement. One may observe in the numerical simulation the existence of an eddy slightly west of the Los Angeles-Long Beach Harbor city boundary, which was also reported in the physical model. Both models show a relatively strong current jet, formed by the combined flows east and west of the gate and flowing out of the harbor through Angel's Gate. At the Long Beach Harbor Channel near the Navy mole, both models show a strong southward current. Figure 17 shows the current pattern 1 hr before high tide. Again, similarities between the two models are noted. This proves that the calibrated numerical model not only reproduces the temporal variation but also mimics the spatial distribution of the flow field.
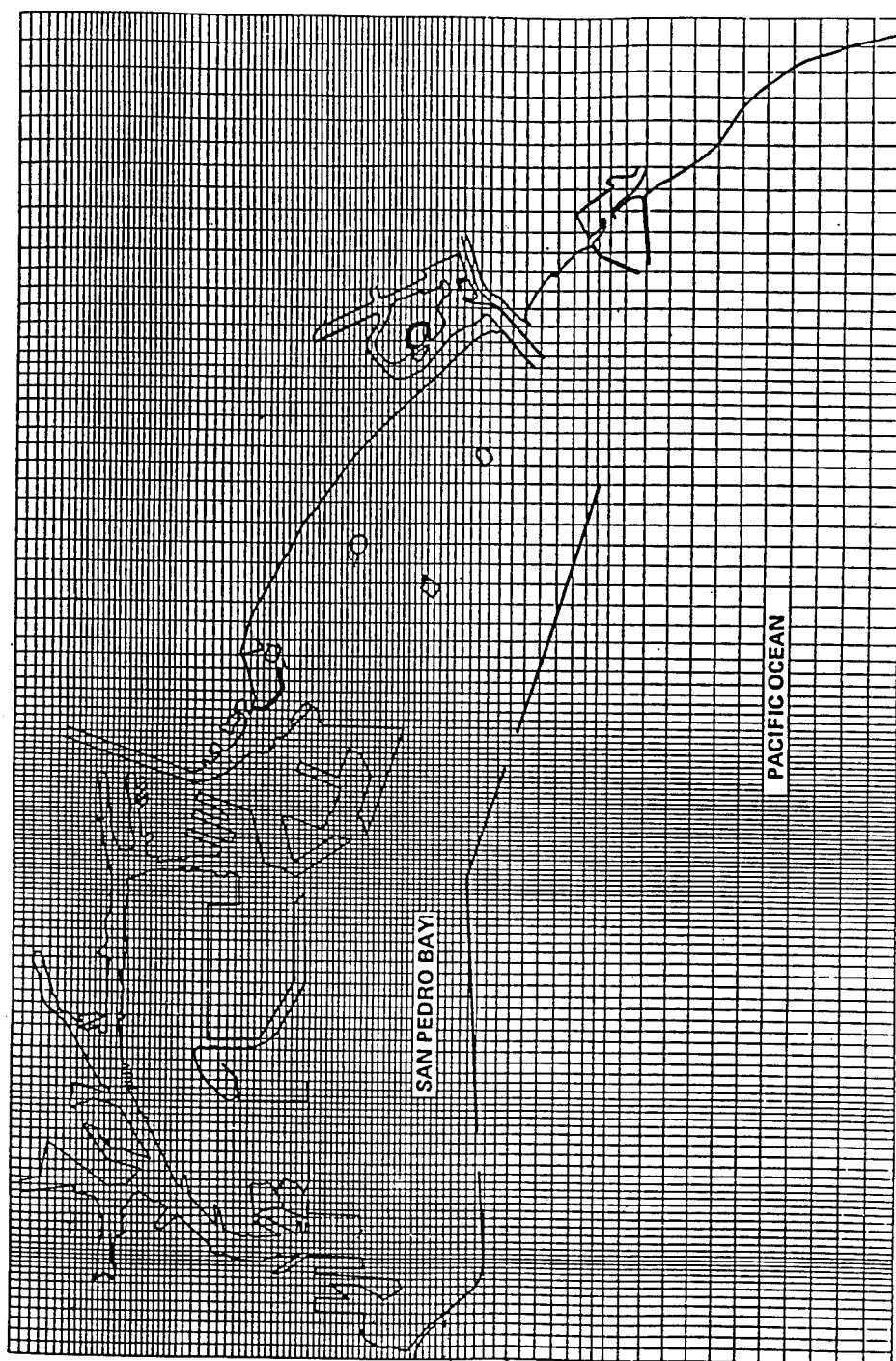
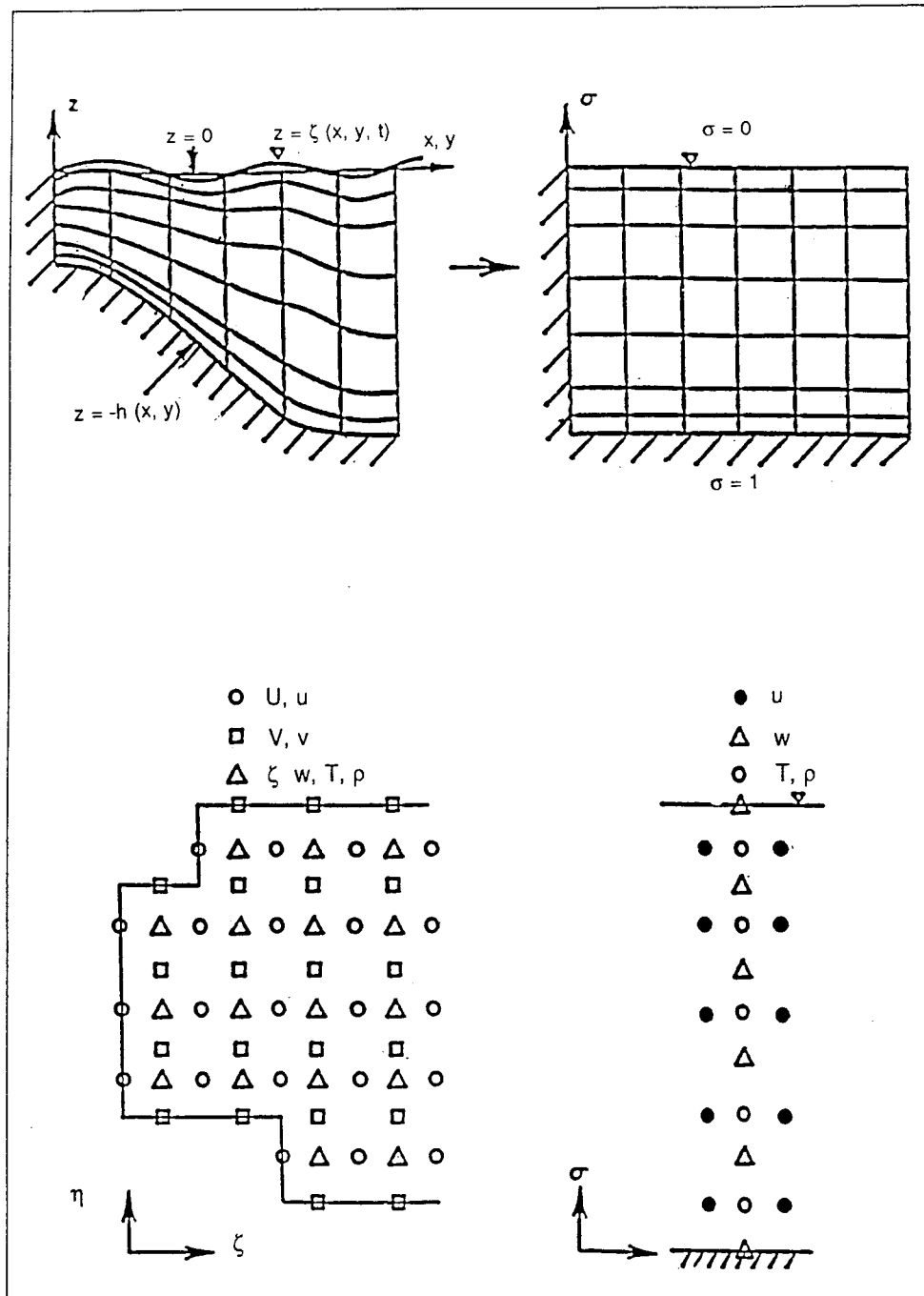Figure 2. Grid layout over the Los Angeles and Long Beach Harbor

PACIFIC OCEAN

SAN PEDRO BAY

Figure 3. Vertically stretched (top), staggered (bottom) numerical grid
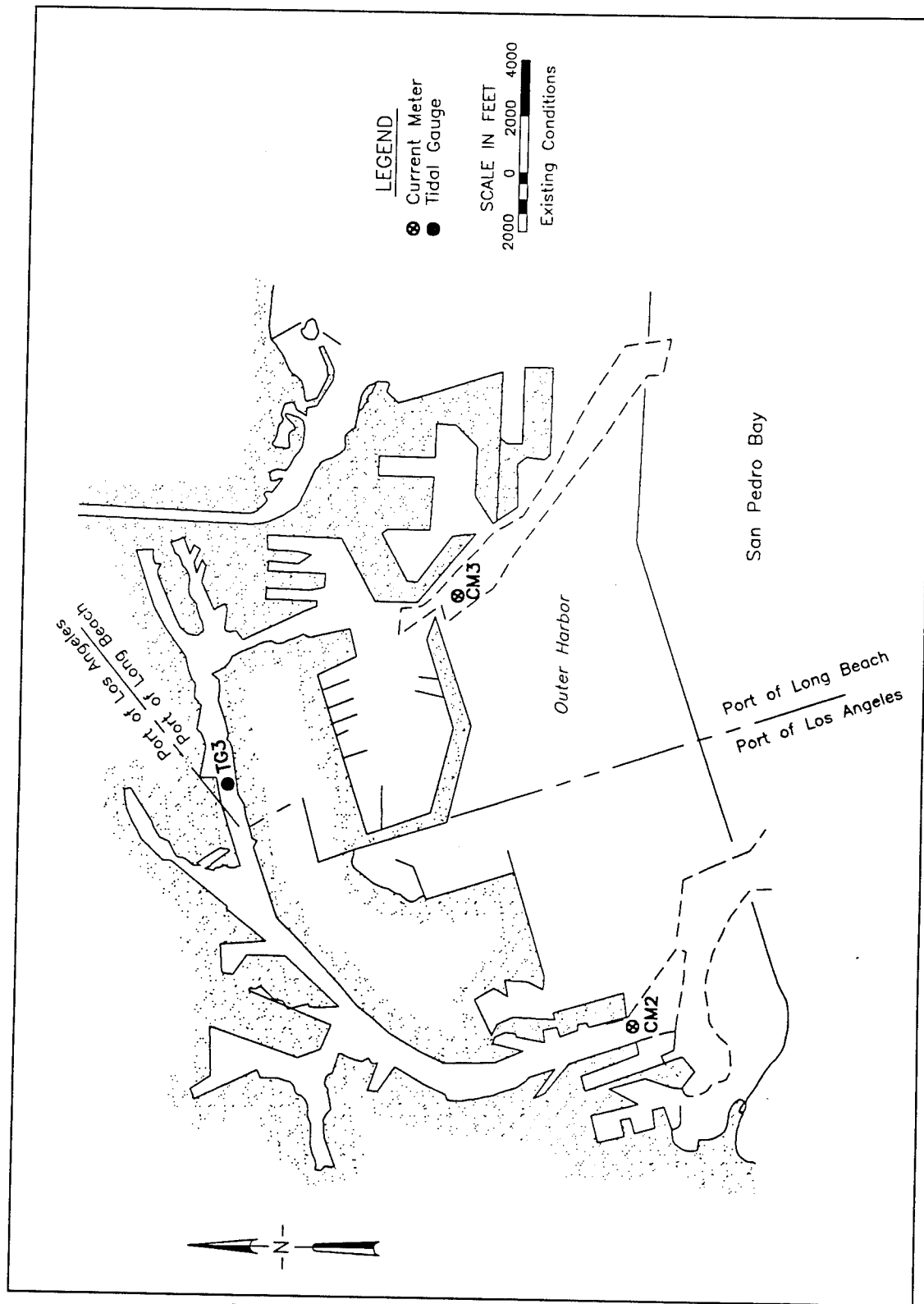
Figure 4. Current meter and tidal gauge stations

a. Ocean tide for calibration period
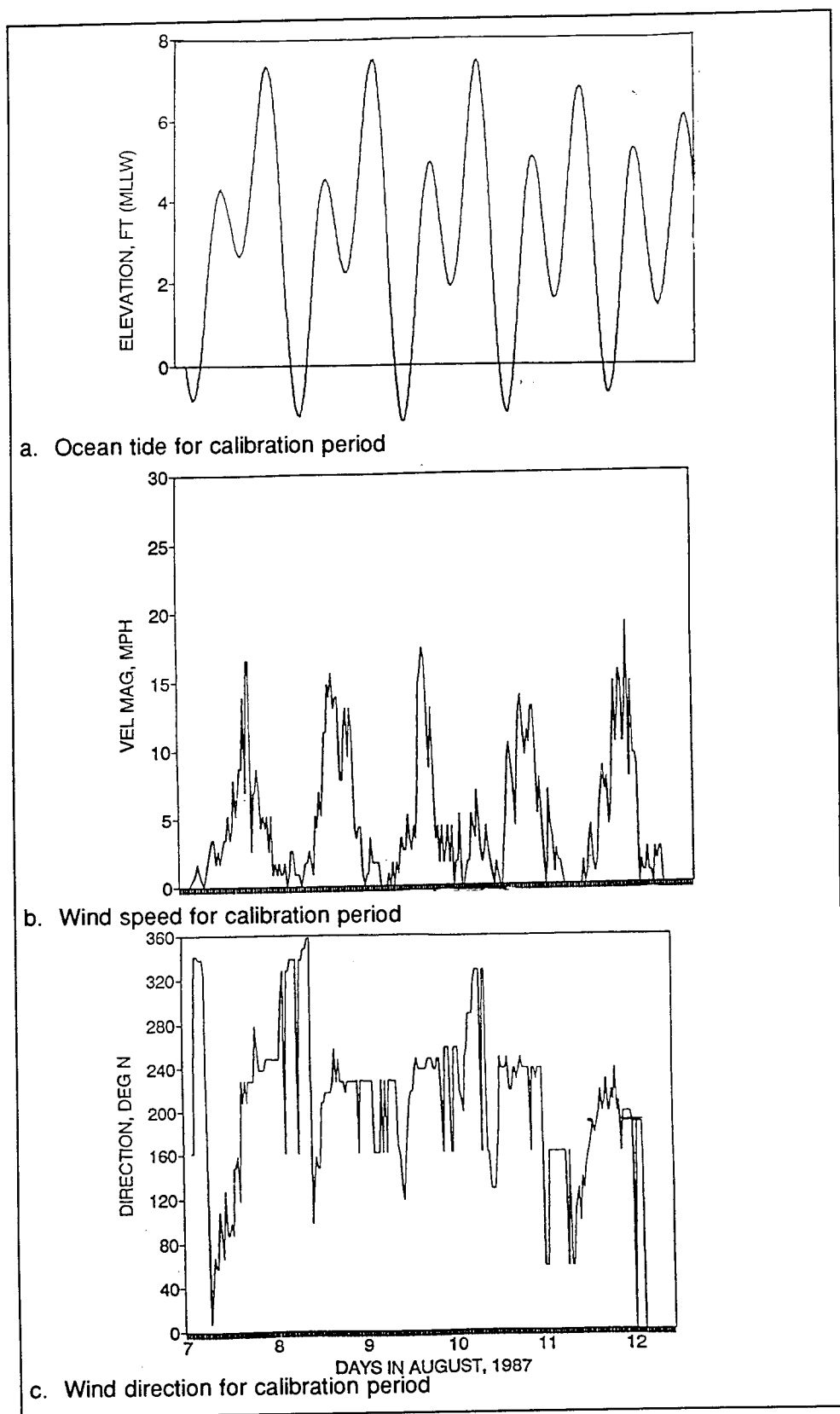
b. Wind speed for calibration period

c. Wind direction for calibration period

DAYS IN AUGUST, 1987

Figure 5. Tidal elevations, wind velocity, and wind direction, August 1987
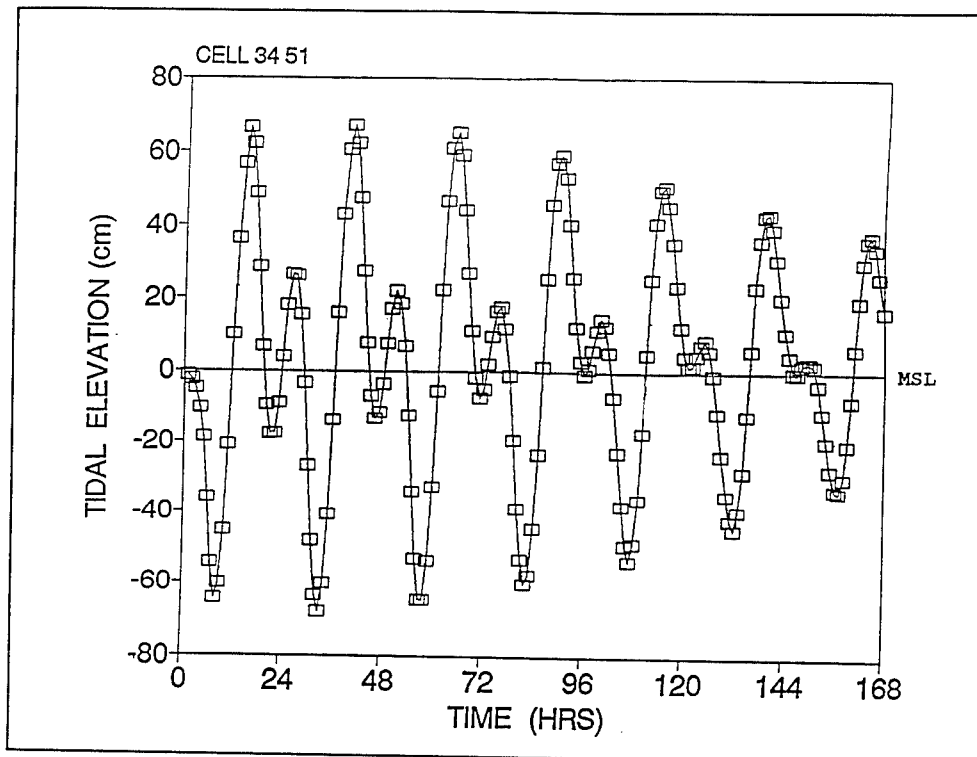
Figure 6. Computed versus measured surface water elevation (□ = measured values, solid line is computed values)
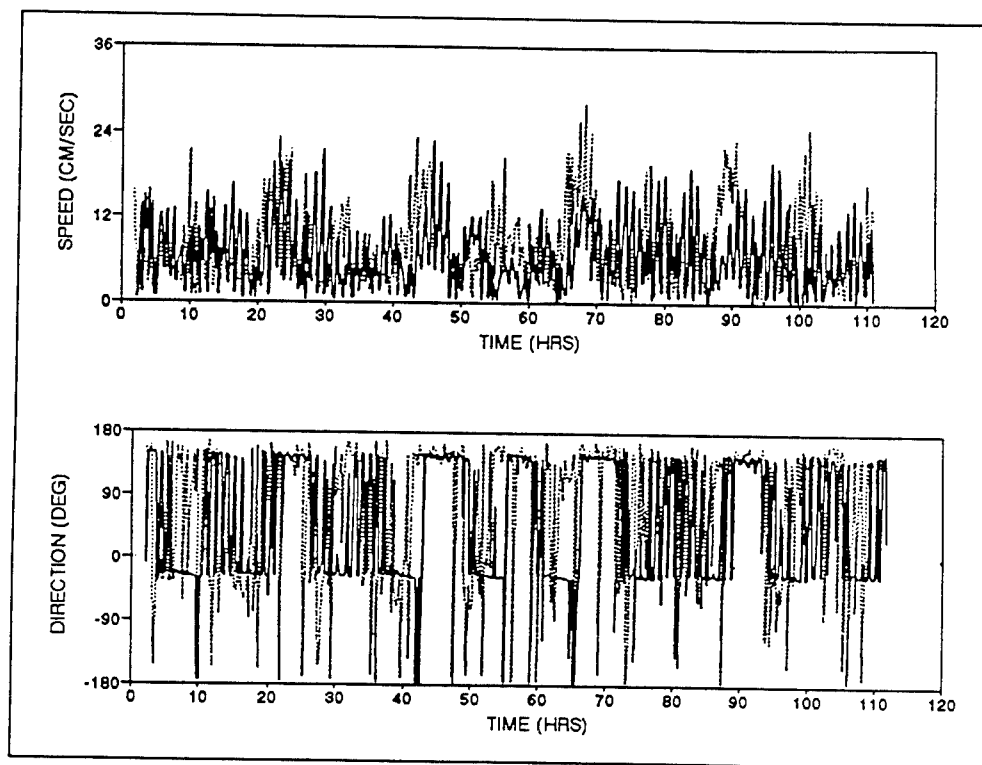
Figure 7. Computed versus measured current velocity (surface layer). Broken line represents observed values, solid line is computed values
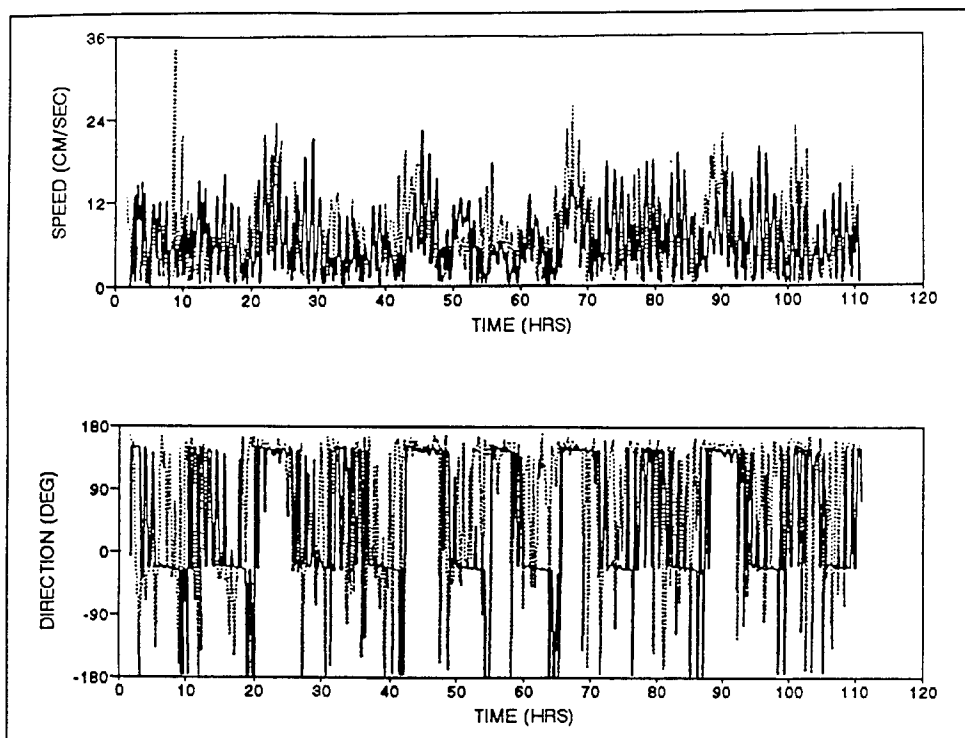
Figure 8. Computed versus measured current velocity (middle layer). Broken line represents observed values, solid line is computed values
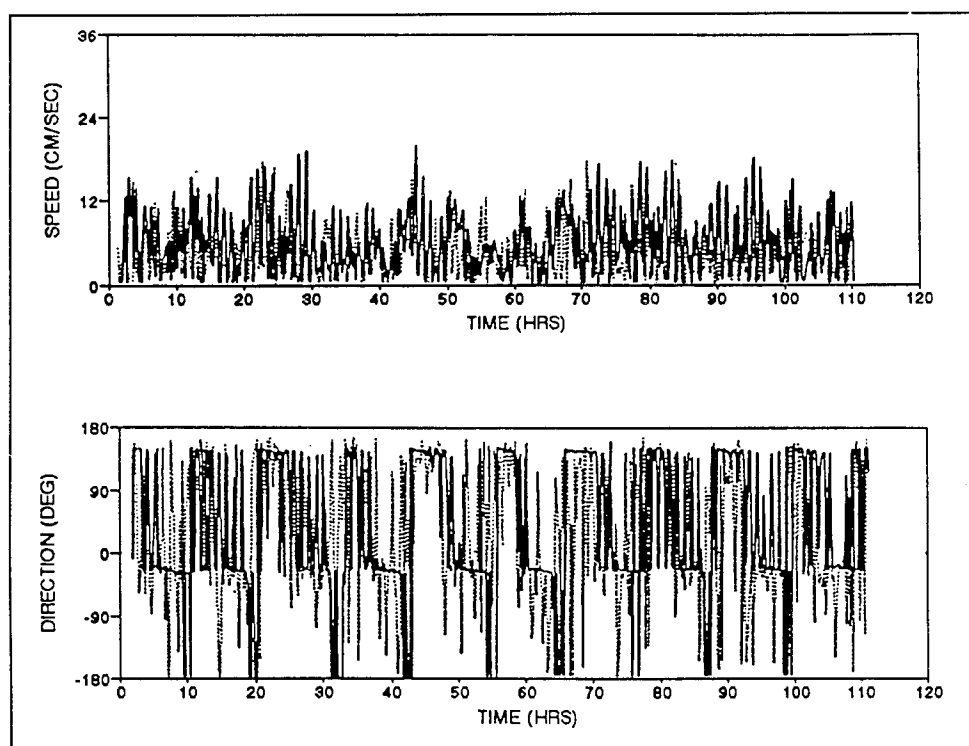
Figure 9. Computed versus measured current velocity (bottom layer). Broken line represents observed values, solid line is computed values

a. Ocean tide for validation period

b. Wind speed for calibration period

DAYS IN AUGUST, 1987

c. Wind direction for calibration period
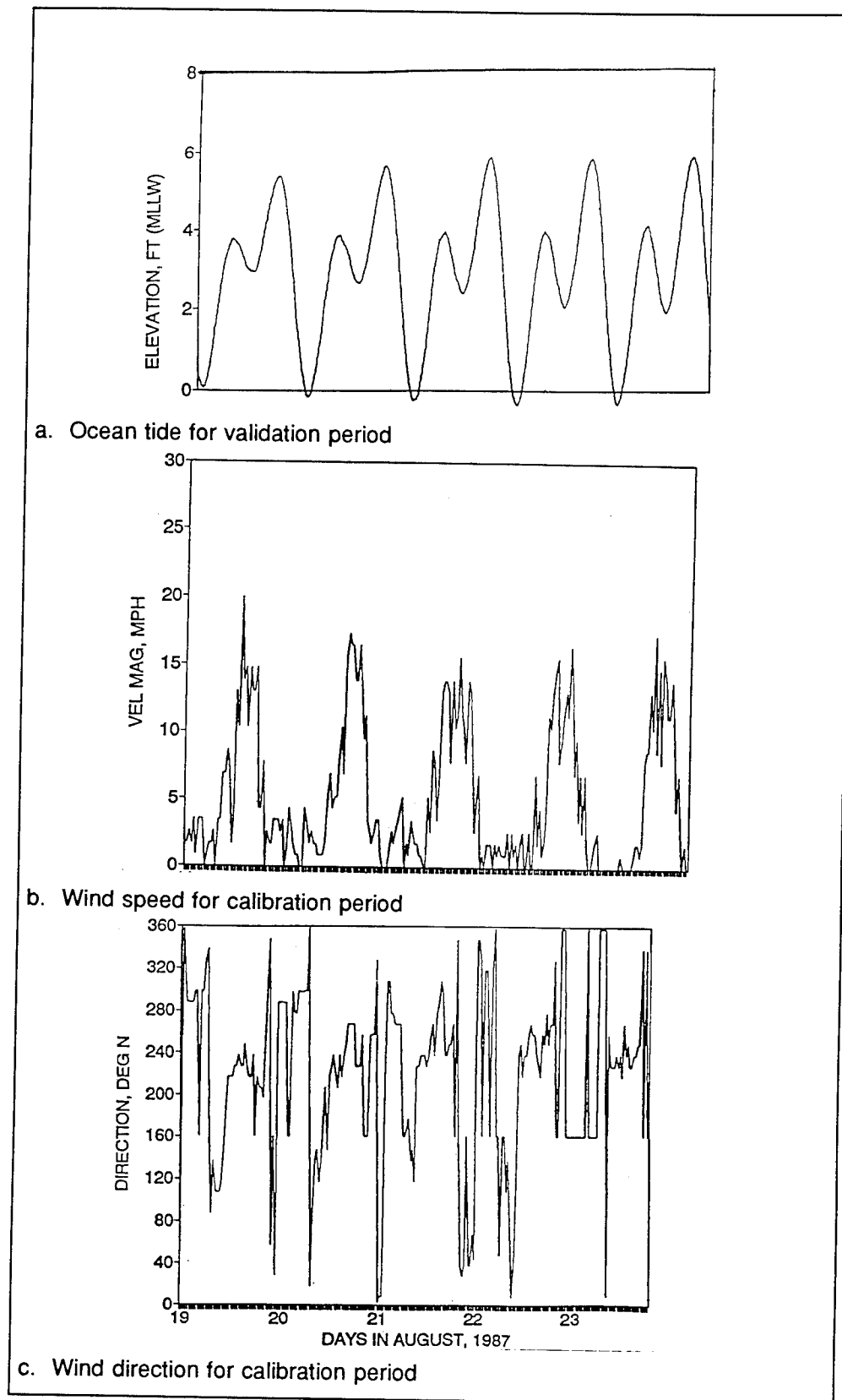
Figure 10. Overall tide and wind conditions
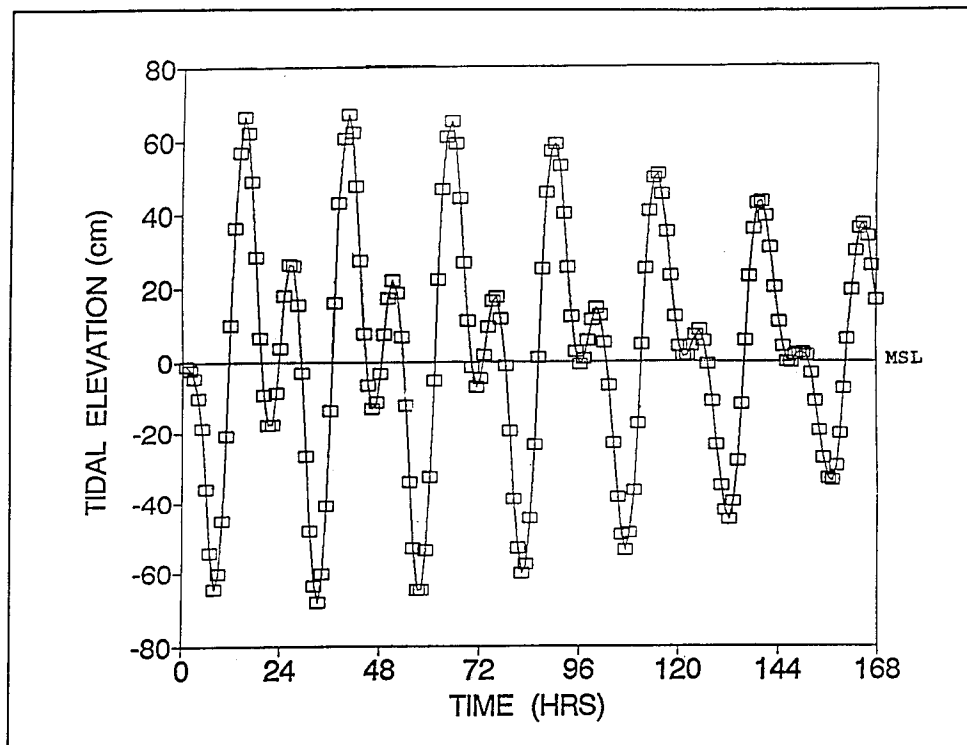
Figure 11. Computed versus measured surface water elevation (□ = observed values, solid line is computed values)
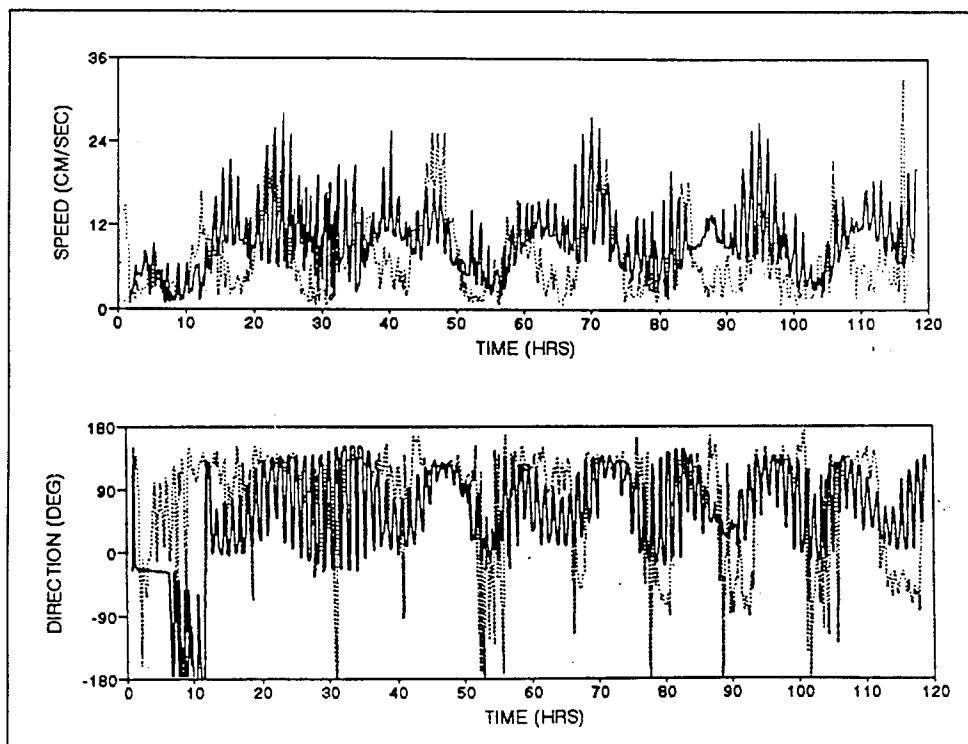
Figure 12. Computed versus measured current velocity (surface layer). Broken line represents observed values, solid line is computed values
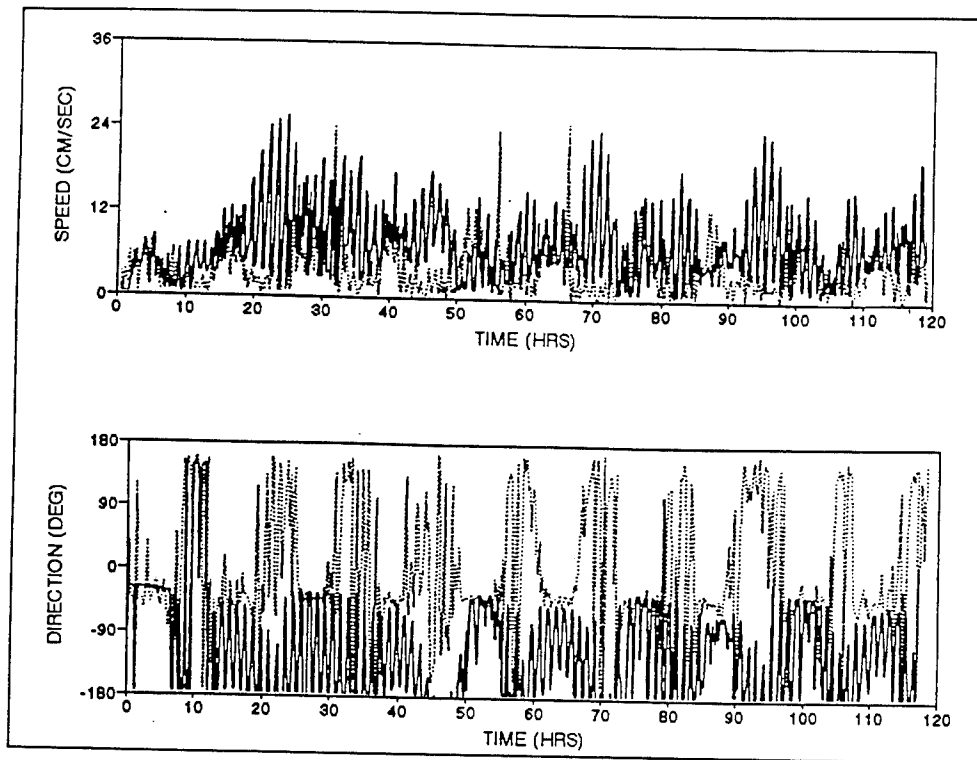
Figure 13. Computed versus measured current velocity (middle layer). Broken line represents observed values, solid line is computed values
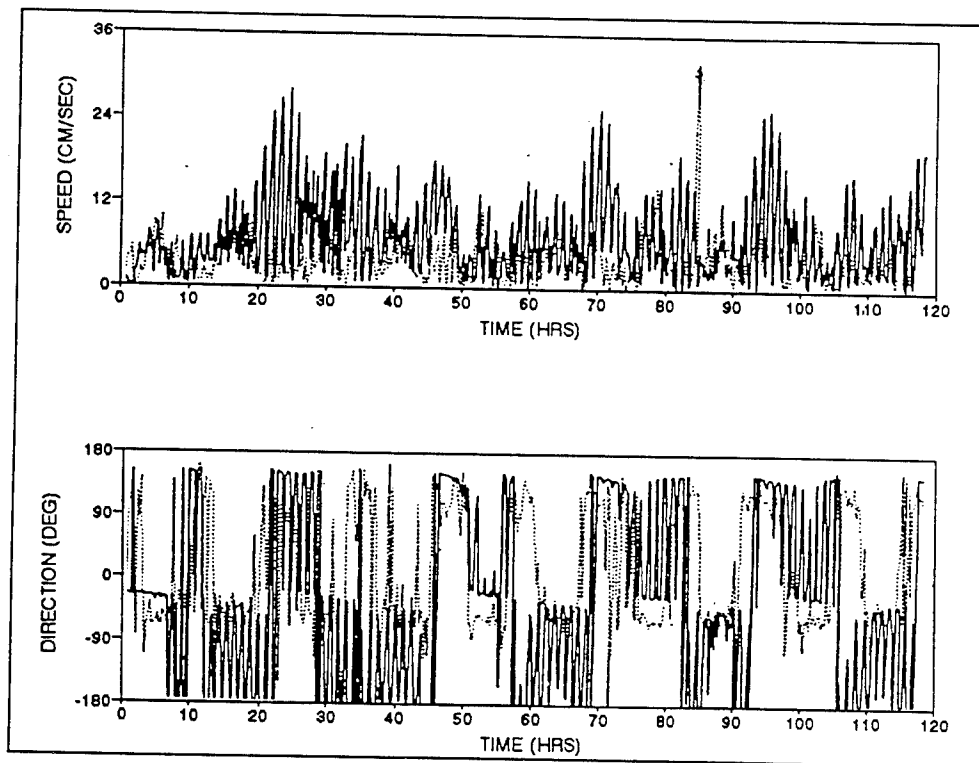
Figure 14. Computed versus measured current velocity (bottom layer). Broken line represents observed values, solid line is computed values

32
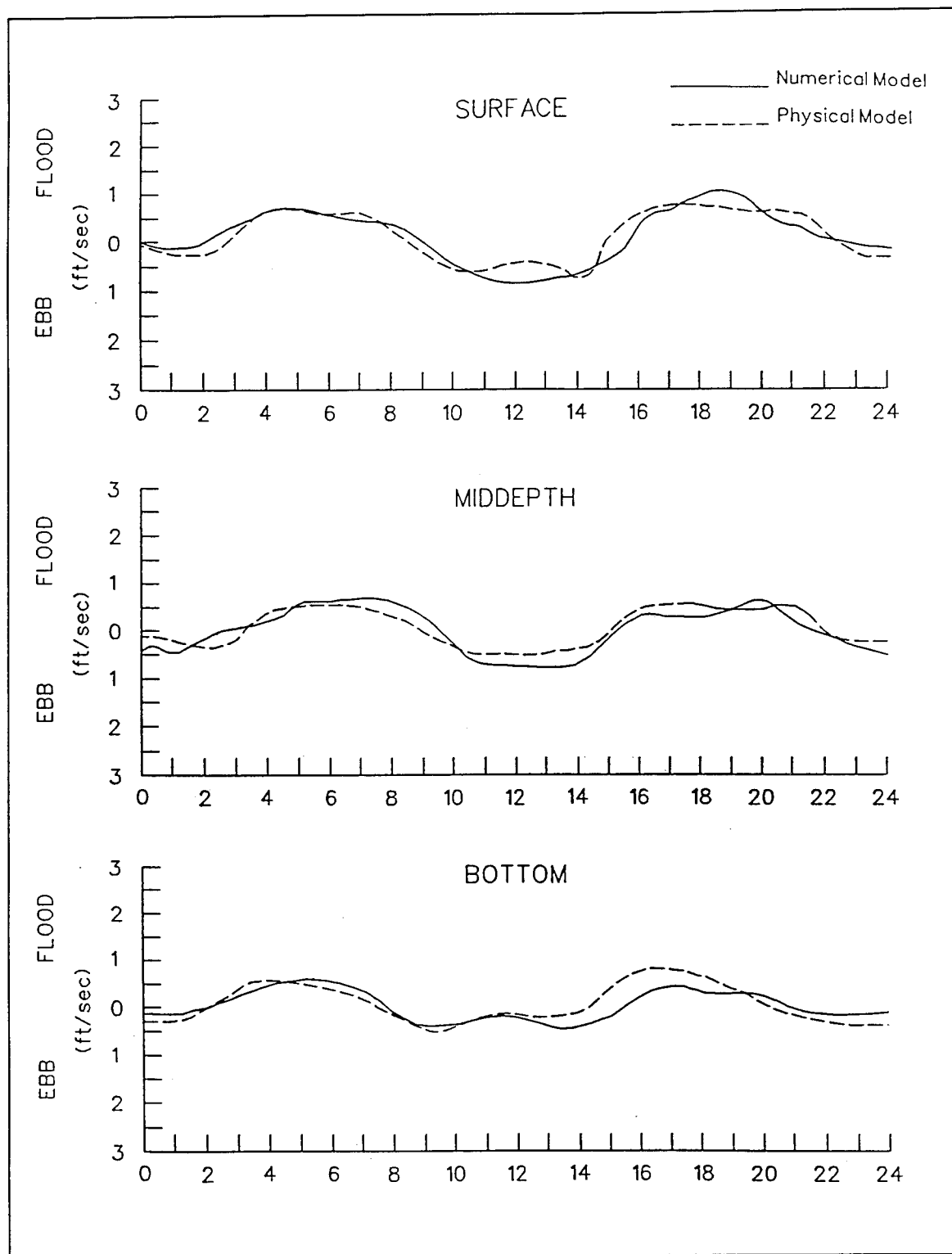
Figure 15. Numerical and physical model comparison
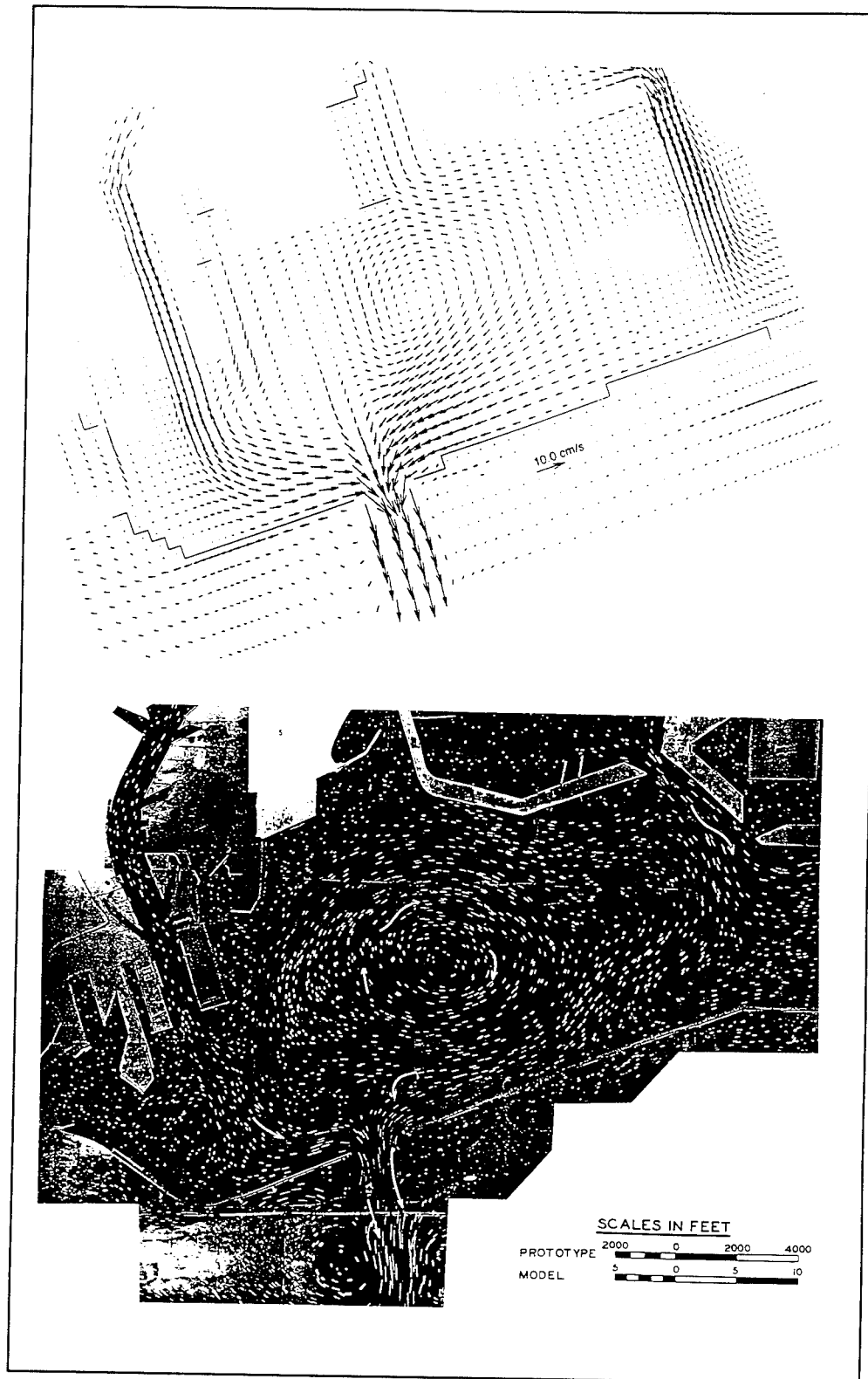
Figure 16. Numerical and physical model comparison--surface layer circulation pattern (maximum ebb current)
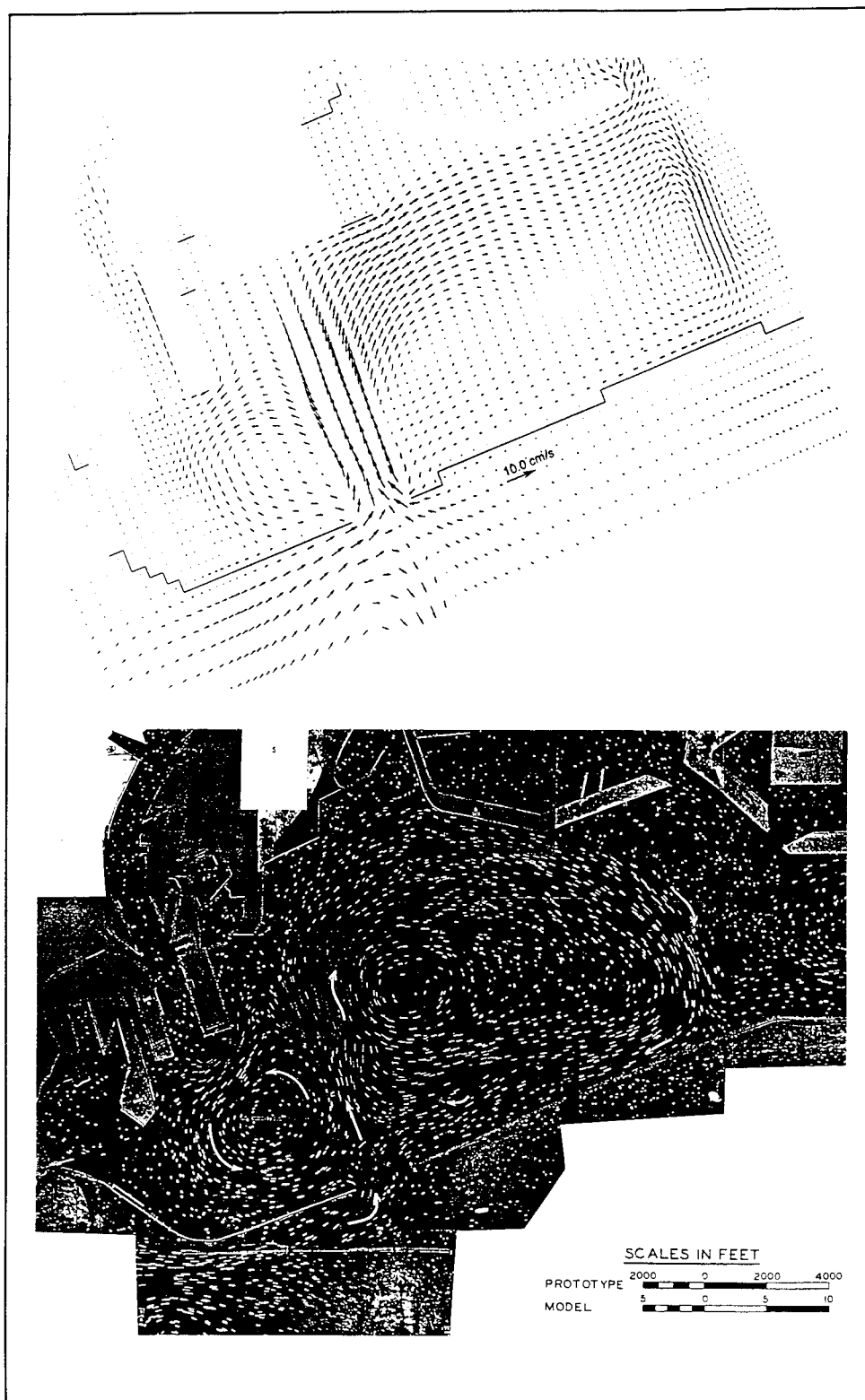
Figure 17. Numerical and physical model comparison--surface layer circulation pattern (1 hr before high tide)

4 Scenario Description and Results in Support of Water Quality Study

Under the 2020 plan, a port facility referred to as Pier 400 and its access causeway will be constructed in the central portion of the existing outer harbor. The construction may impact the water quality through the change of circulation and flushing patterns. The objective of this study is to provide hydrodynamic transport information to drive a numerical water quality model (WQM) for evaluating the changes of environmental conditions.

To achieve this goal, first a hydrodynamic model (HM) consisting of essential physical processes is developed. The HM is then coupled with WQM to ensure that the HM's transport characteristics are well preserved in WQM through an interface processor (Dortch 1990). Finally, a conservative tracer was used to verify the mass conservation for the constituent concentration.

In this report we shall consider the hydrodynamic portion of the study. Hall (1994) reports the water quality model study.

Scenario Description

Under the Los Angeles and Long Beach Harbor feasibility studies initiated in 1986, the city of Los Angeles and Los Angeles Harbor Department, identified as the Port of Los Angeles, have proposed a two-stage plan: (a) POLA stage I (hereafter referred to as POLA 1), and (b) POLA stage II (POLA 2) for the harbor expansion project.

Figure 18 shows the plan of POLA 1, under which the first stage of the two-phase construction of Pier 400 and an access causeway linked to Terminal Island will be partially completed. Associated with the harbor complex construction, the main ship channel will also be dredged to 63 ft and increment 4 of the north channel to 45 ft below mean lower low water (mllw). Figure 19 shows the plan of POLA 2, the second stage of the POLA plan, in which a full-scale model of Pier 400 and the access causeway will be

36

completed. The main channel will be dredged to 81 ft, the south channel to 75 ft, and increment 5 of the north channel to 45 ft.

Based on the above plans, the scenarios in support of the water quality model are listed in Table 1. It shows the major scenario runs comprising (a) the existing condition, (b) POLA 1, and (c) POLA 2. Hydrodynamic conditions in local areas such as Seaplane Lagoon and at the access causeway near the end of the north channel will also be analyzed.

Table 1 Scenarios for Hydrodynamic Runs in Support of the Water Quality Model
Analysis of hydrodynamic impacts from the proposed plans
1. Numerical model results for the existing condition
2. Numerical model results for POLA Stage 1 (POLA 1) condition
3. Numerical model results for POLA Stage 2 (POLA 2) condition
Analysis of local hydrodynamic conditions
1. At Seaplane Lagoon
2. At access causeway near the end of the north channel

A 31-day period in the summer was selected for the simulation corresponding to WQM beginning on August 1, 1987, and ending on August 31. The actual starting time for HM was 6 days earlier in order to allow sufficient spin-up time prior to writing out hydrodynamic data.

A total of five vertical layers were used to provide sufficient resolution. This is necessary because of the proposed deepened ship channel and the importance of the bottom layer for the WQM. The initial condition for the model is a quiescent water body, which means all velocity and surface elevations are initially set to zero. Boundary conditions used for the model run include measured ocean tidal elevation, wind stress on the water surface, and the quadratic bottom stress represented by Manning's n coefficient. Figure 20 shows the measured tidal elevation in San Pedro Harbor used as the open-boundary condition. The data show a mixture of semidiurnal (M_2), diurnal (K_1), and fortnightly (Mf) tidal constituents, typical of the Pacific coast of the United States. Figure 21a,b shows the time series of wind speed and direction. The wind is relatively quiescent (average of 2 knots) during the last week of July; then starting August 3, the wind attains moderate speed (average of 10 knots). For the purpose of examining the worst case WQM scenario, the causeway was considered to be impermeable for the entire passage when conducting studies for POLA 1 and POLA 2. In the next section of this chapter, an opening scenario will be considered in a separate discussion under local hydrodynamic conditions. Figure 22 shows that the stations used for time series presentation are station 1 (cell numbers 24 and 23) - entrance of Angel's Gate, station 2 (cells 33 and 26)- south channel, station 3 (cells 34

and 51) - west of Pier 400, and station 4 (cells 36 and 48) - north of Pier 400. To cover both spatial and temporal variabilities, the results for each of the scenarios are presented in terms of water surface elevation (time series plot), circulation pattern (vector plot), and current velocity (time series plot). Figure numbers beginning with "A" and "B" can be found in Appendices A and B, respectively.

Analysis of Hydrodynamic Impacts from Proposed Plans

Numerical model results for existing condition

Water surface elevation. Figures 23-25 compare the modeled water surface elevation with the measured ocean tide at stations 1, 2, and 4. This comparison will examine tidal transformation processes from San Pedro Bay into the harbor. It reveals that there is very little time delay and energy loss in the tidal response of the harbor to San Pedro Bay. This means that very little dissipation occurs in amplitude, and the phase response is almost simultaneous.

Circulation - vector plot. Tidal current is termed as flood when it is associated with rising water levels and as ebb when associated with falling water levels. Even though the up-and-down surface elevation looks regular and similar in pattern, the tidal current traveling in and out of the harbor through a narrow entrance during flood and ebb is far from the same and has its own distinct pattern. Figure A1(a) shows the flow during the flood tide enters from the San Pedro Bay into the harbor as a confined jet due to the interaction of tidal flow with the narrow gate of the breakwater. In comparison, Figure A1(b) shows that during the ebb tide, the flow in the harbor was drawn from all directions as a "potential flow" toward the exit.

Due to the jet flow, the flood tide has stronger velocity than the ebb tide. Table 2 shows a resultant velocity magnitude at the surface and the bottom for peak-to-peak tidal velocity at five selected stations. For all the stations, maximum flood velocities which are shown as positive values have larger magnitude than the maximum ebb velocities (negative). For example, the maximum flood velocity at the Angel's Gate (station 1) is 32 cm/s, whereas ebb current is 15 cm/s (32 percent less). From the table we also see the distribution of peak-to-peak velocity for different stations in the harbor. It appears that the largest range occurred near the entrance and decreases as it approaches further into the harbor. Compared to the surface layer, the velocity at the bottom layer is weaker in magnitude as evidenced from Table 2.

Table 2
Tidal Velocity (Peak-to-Peak) for Existing Condition

Station	Cell Number	Peak-to-Peak Velocity (cm/s)			
		Surface Velocity	Range	Bottom Velocity	Range
1. Angel's Gate	24,23	-15.0 to 32.0	(47.0)	-9.5 to 11.2	(20.7)
2. South Channel	33,26	- 3.2 to 22.4	(25.6)	-2.8 to 3.2	(6.0)
3. Pier 400 west	20,35	- 3.6 to 18.9	(22.5)	-2.3 to 3.6	(5.9)
4. Pier 400 north	34,51	- 1.4 to 16.2	(17.6)	-3.2 to 3.6	(6.8)
5. Causeway	36,48	- 2.0 to 2.6	(4.6)	-1.6 to 2.0	(3.6)

Current velocity - time series plot. Previous discussions involved comparisons of current velocity in spatial distribution. We now examine current velocity in time series. In order to examine the variation of velocity in detail, it will be helpful to resolve the velocity into u and v components from the resultant velocity. Positive u indicates a velocity component parallel to the breakwater, toward the east, while a positive v indicates the velocity component perpendicular to the breakwater, toward the north. Figures B1 through B4 show u and v current velocity variation at stations 1,2,3, and 4, respectively, from which two major points will be discussed.

First, for all the stations, the current velocity in the period July 24 - August 3 (the first period) is significantly smaller than August 3-31 (second period). The distinct pattern of weaker velocity in the first period and stronger velocity in the second period is the direct result of weaker wind (average of 2 knots) in the first period versus the strong wind (average of 10 knots) in the second period. Wind-induced current velocity can be as large as the normal tidal current (see Figures B2 and B3).

Second, the wind not only affects the magnitude of the velocity as described above, but also generates a non-tidal mean drift motion. Using Figure B2(a) for station 2 as an example, when the flow is primarily driven by the tide such as is seen in the first period, the current velocity oscillates between positive and negative velocity with zero mean (after being averaged over the tidal cycle). When the mean drift motion occurred as shown in the time series during August 7-23, the velocity shifted away from the mean zero velocity to attain a positive mean (after being averaged over the tidal cycle) u drift velocity; that is, toward the east. Figure B1(b) for station 1, as another example, shows that the velocity attains a mean positive v drift velocity during the second period, which means toward the north. The same trend was found at other stations as well. Since the wind for the second period was predominantly from the southwest, the current was toward the east and north.

Therefore, the current velocity increases in proportion to the wind speed and a mean drift motion is also established in the downwind direction. These

findings are consistent with the field measurements reported by Smith (1989). Under strong wind action, the bottom current can be the reverse of the surface current in some areas of the harbor. This condition is illustrated in the comparison of Figures C-3b and C-6b in Appendix C. Velocity vector plots for the bottom layer can be found in Appendix A.

Numerical model results from POLA Stage 1 condition

This section investigates how the hydrodynamic condition is affected by POLA 1, particularly those changes from the existing condition. Information discussed in the last section serves as baseline information for the comparison.

Water surface elevation. Figure 26 compares the water surface elevation for POLA 1 and the existing condition. It shows very little difference between the two time series, which indicates that POLA 1 does not have a significant impact on the existing water surface elevation.

Circulation - vector plot. Figure A3 shows the circulation vector plot for POLA 1 at flood and ebb tide on the surface layer. The major impact of POLA 1 on the circulation appears to be that the construction blocks the otherwise free south-north flow through the breakwater entrance, forcing it to go around the structure and conform to the shape of the local structure. Since the effect of the structure shape on the flow field is different at each location, peak-to-peak velocities taken from the plots are summarized in Table 3 for each station to assist the discussion.

Velocity direction is the direction in which the current flows, and is measured from true north. Following are the changes from the comparison between POLA 1 and the existing condition: (a) at station 1, where Pier 400 is the headland, the flow deflects more toward the east-west direction, while its magnitude decreases, (b) at station 2, the velocity changes slightly toward the east-west direction, while magnitude for both flood and ebb increases, (c) at station 3, where Pier 400 is oriented in a north-south direction, the velocity direction turns toward that direction, (d) at station 4, where Pier 400 runs from east to west, the velocity direction turns more toward the east-west, (e) at station 5, where the north-south causeway has a major influence, the velocity vector turns more toward the north-south.

Based on the changes described above, we can readily see that main variations of the velocities are the results of flow adjustment to the shape of Pier 400 at each station.

40

Table 3
Tidal Velocity (Peak-to-Peak) for POLA 1

Station	POLA 1, Peak-to-Peak Surface Velocity (cm/s)			Existing Condition, Peak-to-Peak Surface Velocity (cm/s)		
	Speed	Direction (deg)	Tide	Speed	Direction (deg)	Tide
1. Angel's Gate	12.3 26.9	191.8 42.0	Ebb Flood	15.1 32.3	184.6 21.8	Ebb Flood
2. South Channel	4.1 27.7	256.0 64.4	Ebb Flood	3.2 22.4	251.6 63.4	Ebb Flood
3. Pier 400 west	4.0 16.1	187.1 30.3	Ebb Flood	3.6 18.9	213.7 58.0	Ebb Flood
4. Pier 400 north	2.8 10.5	225.0 56.3	Ebb Flood	1.4 16.3	225.0 47.5	Ebb Flood
5. Causeway	2.2 3.1	201.8 14.9	Ebb Flood	2.0 2.6	204.0 17.7	Ebb Flood

Current velocity - time series plot. Previous discussions focussed on current variations in the spatial domain. Current variations in the time series will now be examined. Again, u and v components from the resultant velocity were used for detailed examinations.

Figures B5 - B8 show time series comparisons of POLA 1 and existing conditions at four different stations. Time series comparisons reinforce the conclusions reached in the last section. In addition, velocity responses to POLA 1 in the second period were found to have significantly larger amplitude than in period 1. For example, Figure B5(a) shows that the u velocity has a 4- to 6-cm/s net increase from the existing condition in the second period, whereas it only has a 0.5- to 1-cm/s increase in the first period. Other stations show similar patterns. In other words, with the same structure in place, the wind can induce a larger velocity fluctuation (as in the second period) than tide (as in the first period).

At stations 1 and 2, the mean drift velocity (velocity averaged over the tidal cycle) was observed to be enhanced (see Figures B5 and B6) due to the effect of a new constriction between Pier 400 and the Middle Breakwater. On the other hand, mean drift velocity at stations 3 and 4 was observed to be diminished. This is because the presence of Pier 400 effectively eliminated the fetch distance at the location and thus eliminated the possibility of wind-driven mean drift motion.

Numerical model results from POLA Stage 2 condition

Water surface elevation. Comparison of the modeled water surface elevation for POLA 2 and the existing condition shows little difference in the

41

time series record (Figure 21). This indicates, again, that the POLA 2 plan does not have a significant impact on surface height responding to the ocean tidal forcing.

Circulation - vector plot. Figure A5 shows the circulation vector plot for POLA 2 at flood and ebb tide at the surface layer. The pattern is, for the most part, similar to the response from POLA 1. That is, its main changes are the result of the flow adjustment to Pier 400 and causeway construction. However, some notable differences between POLA 1 and POLA 2 do exist.

Table 4 summarizes the peak-to-peak velocity comparison between POLA 2 and the existing condition for stations in the harbor. From the table, the following points are noted: (a) POLA 2 has a smaller magnitude of velocity than POLA 1 across the stations, except station 4; (b) At station 2, the east-west component of the velocity reduced more than the north-south component, causing the direction of the resultant velocity to align more with north-south direction; (c) At station 4, the north-south component of velocity was reduced (the east-west component was unchanged) at flood, which results in the shift of direction more toward the east-west direction. Reasons for the above changes will be further discussed in the time series analysis.

Table 4
Tidal Velocity (Peak-to-Peak) for POLA 2

Station	POLA 2, Peak-to-Peak Surface Velocity (cm/s)			Existing Condition, Peak-to-Peak Surface Velocity (cm/s)		
	Speed	Direction (deg)	Tide	Speed	Direction (deg)	Tide
1. Angel's Gate	8.1 24.8	187.1 40.1	Ebb Flood	15.1 32.2	184.6 21.8	Ebb Flood
2. South Channel	2.2 22.8	243.4 61.2	Ebb Flood	3.2 22.4	251.6 63.4	Ebb Flood
3. Pier 400 west	3.0 14.8	176.2 31.7	Ebb Flood	3.6 18.9	213.7 58.0	Ebb Flood
4. Pier 400 north	2.8 10.6	225.0 61.0	Ebb Flood	1.4 16.3	225.0 47.5	Ebb Flood
5. Causeway	1.8 2.7	206.6 17.1	Ebb Flood	2.0 2.6	204.0 17.7	Ebb Flood

Current velocity - time series plot. Figures B9 - B12 show time series plots for POLA 2. Comparing with Figures B5 - B8, we see that POLA 2 indeed has smaller velocities than POLA 1 at most stations, except station 4. This is attributed to the deepening of the ship channel, in which the main channel was deepened from 63 ft to 81 ft, the north channel from existing to 45 ft, and the south channel to 75 ft. For a given incoming volume of water, the variation in velocity will be smaller for the deeper channel (POLA 2) than for the shallower channel (POLA 1). At station 4, while all other stations

42

show a decrease, the velocity for POLA 2 is comparable to POLA 1. This is so because the overall decreasing trend was offset by the increase of velocity due to channel width reduction (between Piers 400 and 300) for POLA 2.

Analysis of Local Hydrodynamic Conditions Near Shallow Habitat

At Seaplane Lagoon

With the construction of Pier 400, a portion of the breakwater inside Seaplane Lagoon was proposed to be removed. Figure 28 shows the vector plot at maximum flood current for both the intact and the partially removed breakwater (one third of end portion removed). The velocity inside Seaplane Lagoon is fairly small, on the order of 0.5 cm/s. Velocity at the entrance is slightly larger due to the constriction effect, which is on the order of 1 cm/s. The flushing of a shallow, semi-enclosed basin is dynamically related to the rate of exchange between the basin and the water body it connects through the entrance. Primary factors that influence the flushing of a shallow basin include: astronomical tide; wind force; entrance geometry, topography and velocity; and the concentration of the receiving water body. Given the fixed amount of tracer introduced into the basin, the faster the concentration drops, the higher the flushing rate will be.

Scenario runs were conducted to investigate flushing characteristics inside the lagoon. A 100-ppt (parts per thousand) conservative tracer was introduced into Seaplane Lagoon inside the breakwater. Everywhere else in the harbor the concentration was set to 0 ppt. The concentration of the tracer was transported by the current and gradually diluted by the surrounding water. Figures 29 - 31 show the evolution of the concentration for intact and partially removed breakwaters under existing conditions, POLA 1 and POLA 2. It is obvious from all three cases that the partially removed breakwater has a higher flushing rate than its counterpart -- the intact breakwater. Of all the cases conducted, the existing condition with partially removed breakwater has the highest flushing rate.

This demonstrates that the removal of a portion of the breakwater does have an impact on increasing the flushing rate for Seaplane Lagoon. See Hall (1994) for results of a full-scale flushing experiment.

At Access Causeway

The causeway which connects Terminal Island and Pier 400 essentially cuts Seaplane Lagoon into a west basin and an east basin flanked by the Navy mole, shown in Figure 32. Questions have been raised concerning: (a) the

hydrodynamic condition in the east basin, and (b) the possible benefit of an opening in the causeway at the dead end of the north channel.

Hydrodynamic conditions near the east basin are examined first. Figures A1, A3, and A5 show the respective surface circulation for existing conditions, POLA 1 and POLA 2. The plots show that velocity around the east basin is small, generally on the order of 1-2 cm/s. Comparisons between existing conditions and POLA 1/POLA 2 show that velocity increases slightly from 0.5 cm/s for the existing condition to 1.5 cm/s for POLA 1/POLA 2 (see Figure 33).

Figure 34 shows the circulation pattern for the opened causeway. The opening at the causeway basically serves as an additional access for water to flow in and out through Long Beach Harbor. By examining velocity time series near the opening, it shows that velocity through the opening is on average -1 to 1 cm/sec for POLA 1 and -0.5 to 0.5 cm/s for POLA 2 (see Figure 35). It appears that the opening in the causeway has only local effects and it is not likely to have a major impact on the overall circulation. Additional runs were conducted to examine whether the opening in the causeway has any impact on the flushing rate in Seaplane Lagoon. Figure 36 compares the concentration evolution for the opened and closed causeway. Results show that the rate of change is only slightly affected by the opening at the causeway.
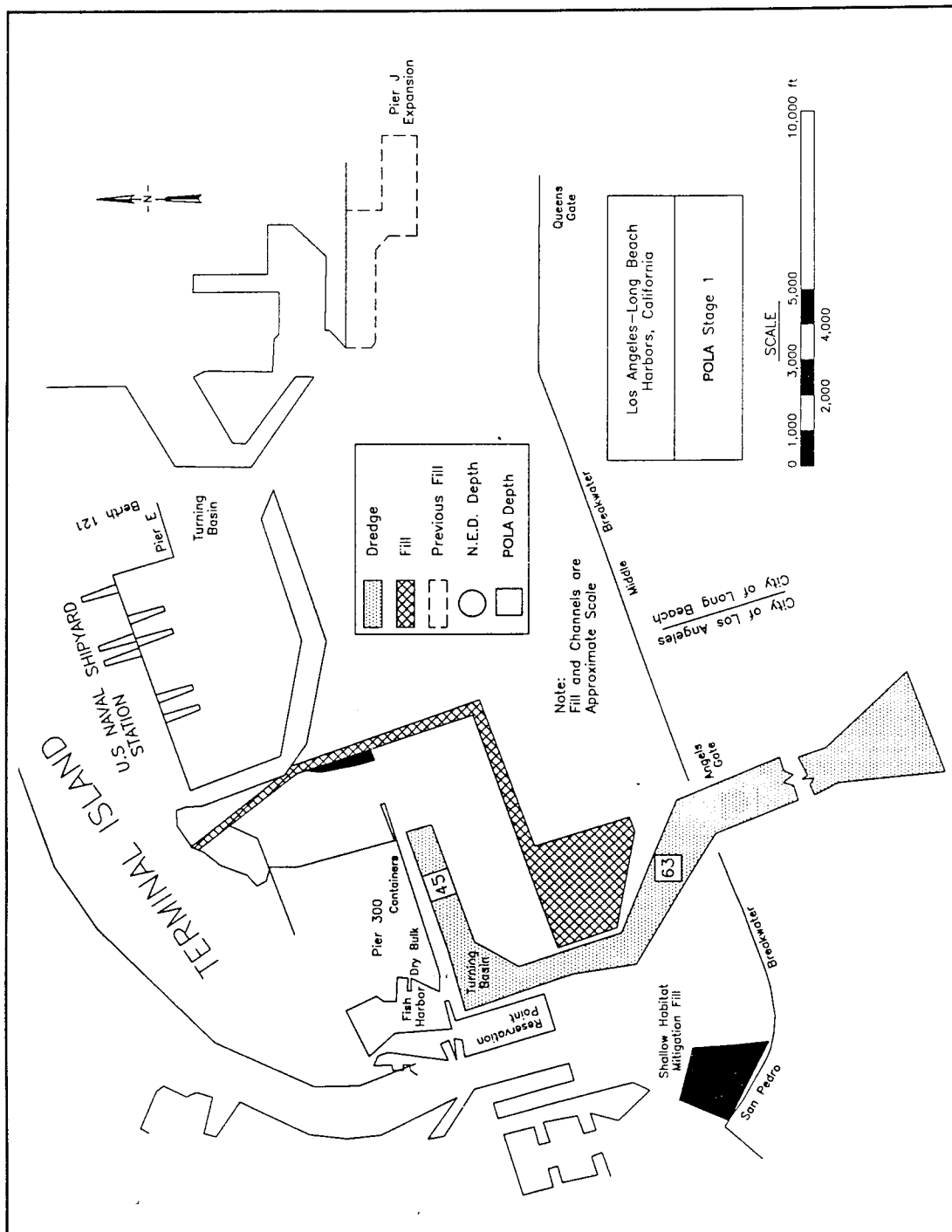
Figure 18. Proposed POLA Stage I plan

45
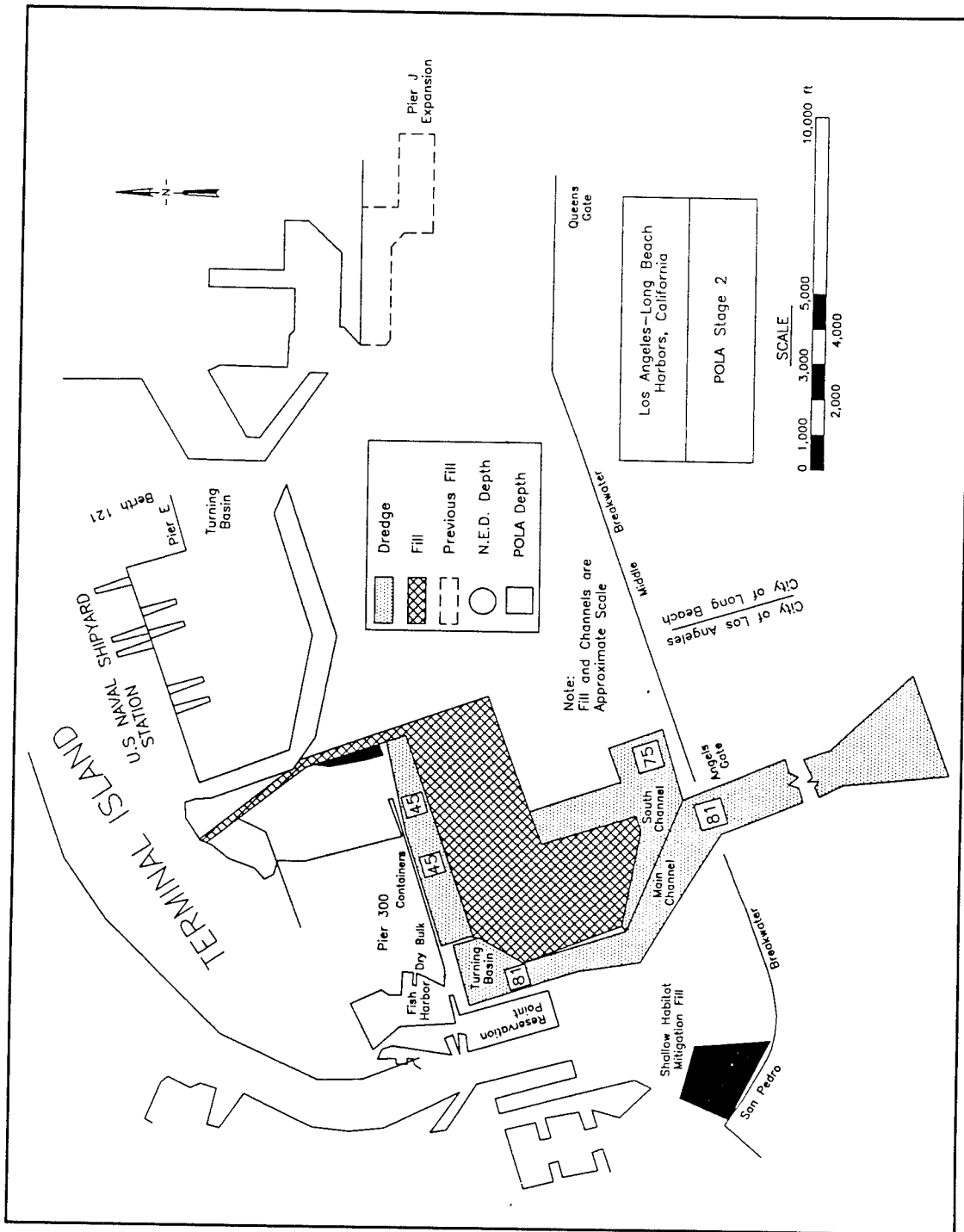
Figure 19. Proposed POLA Stage II plan

Chapter 4   Scenario Description and Results in Support of Water Quality Study
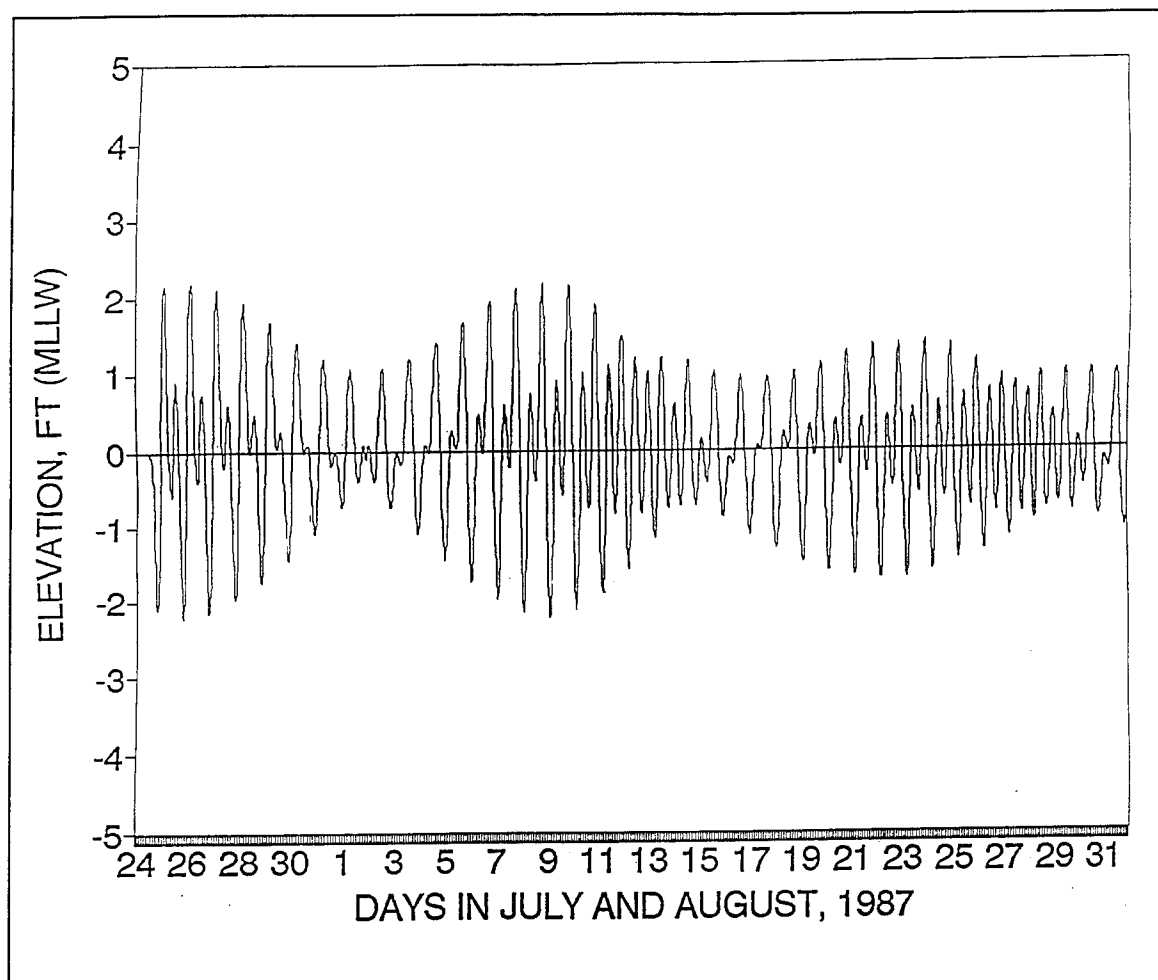
Figure 20. Measured ocean tide for boundary condition

a. Wind speed
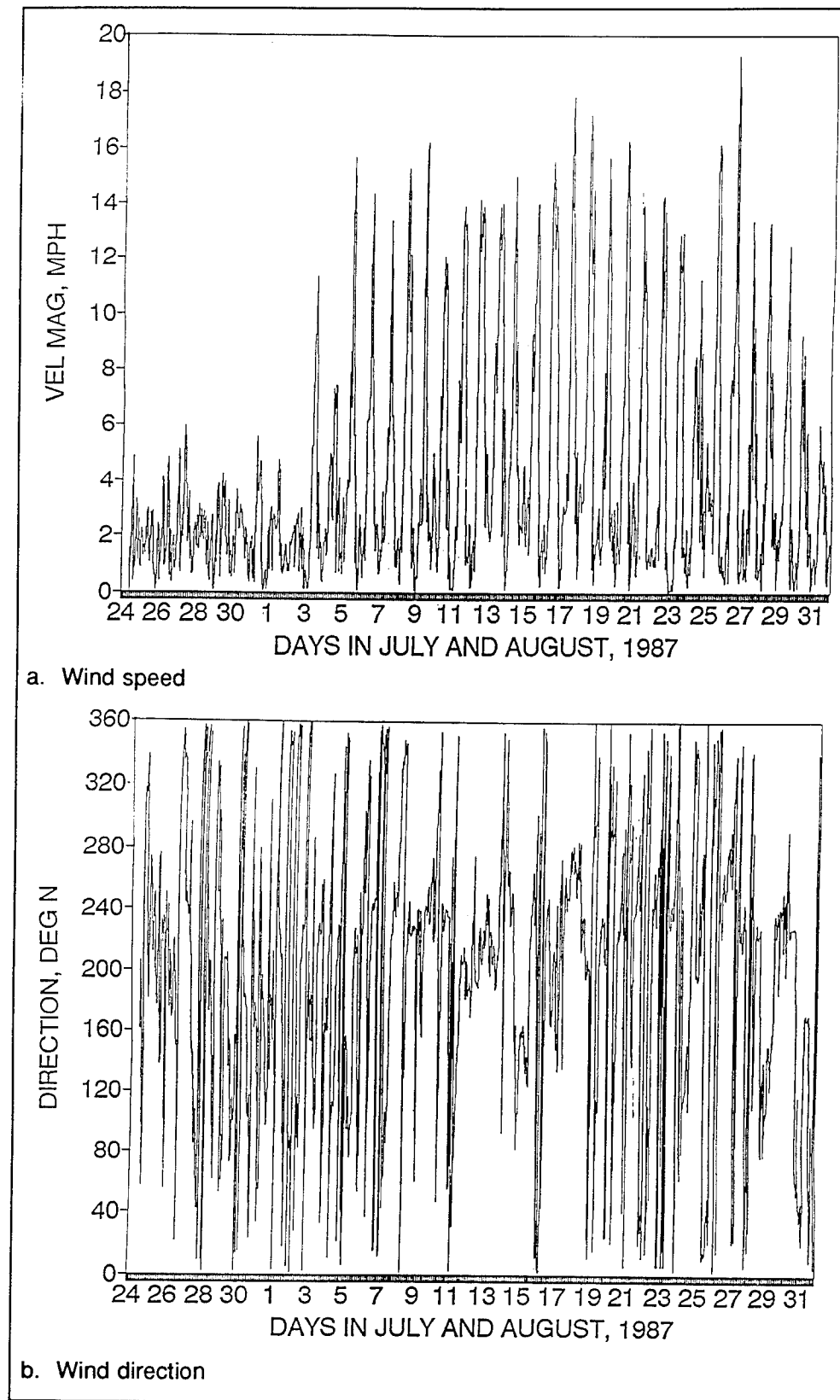
b. Wind direction

Figure 21.   Measured wind speed and direction during July 24 - August 31, 1987
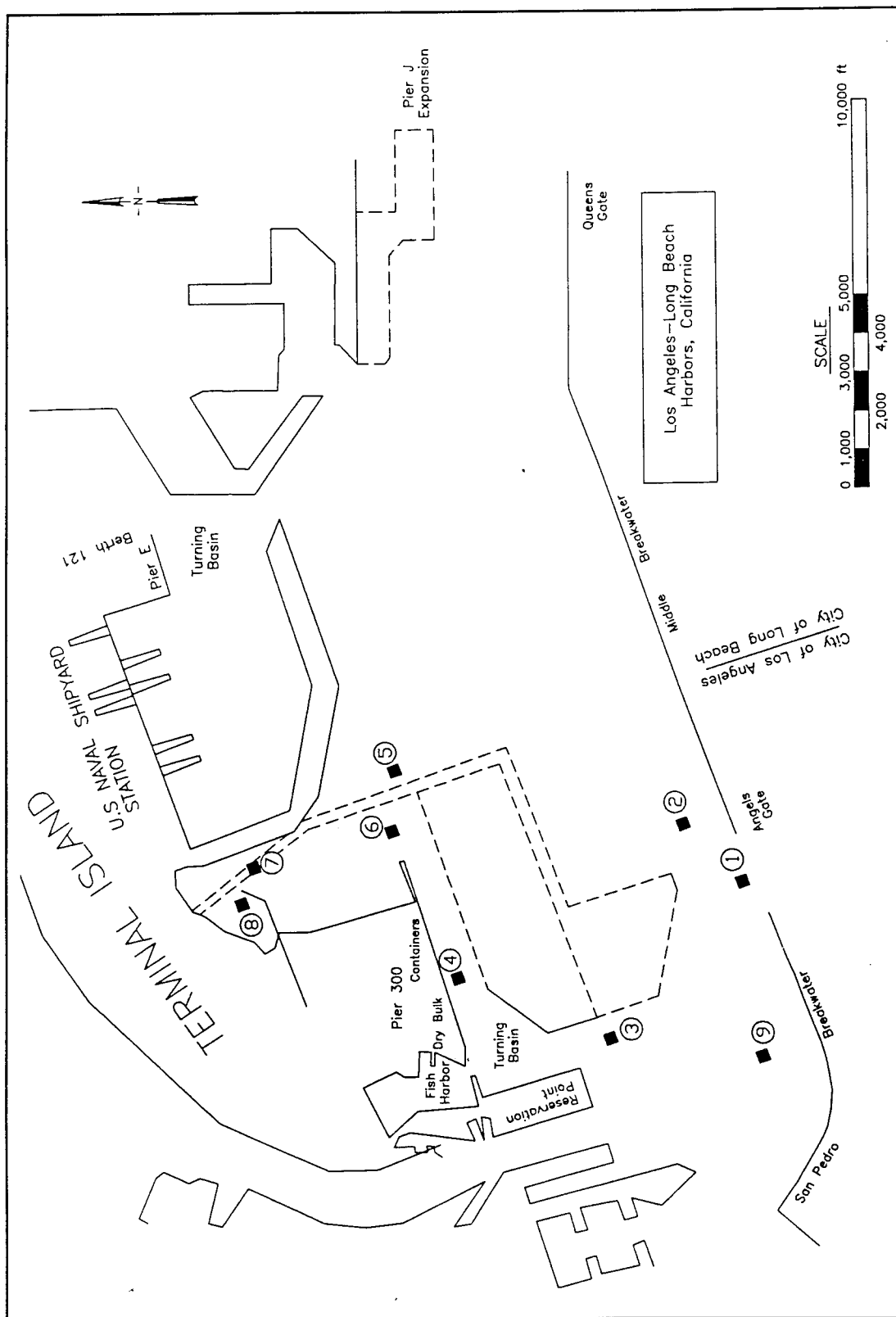
Figure 22. Station locations used for time series analysis
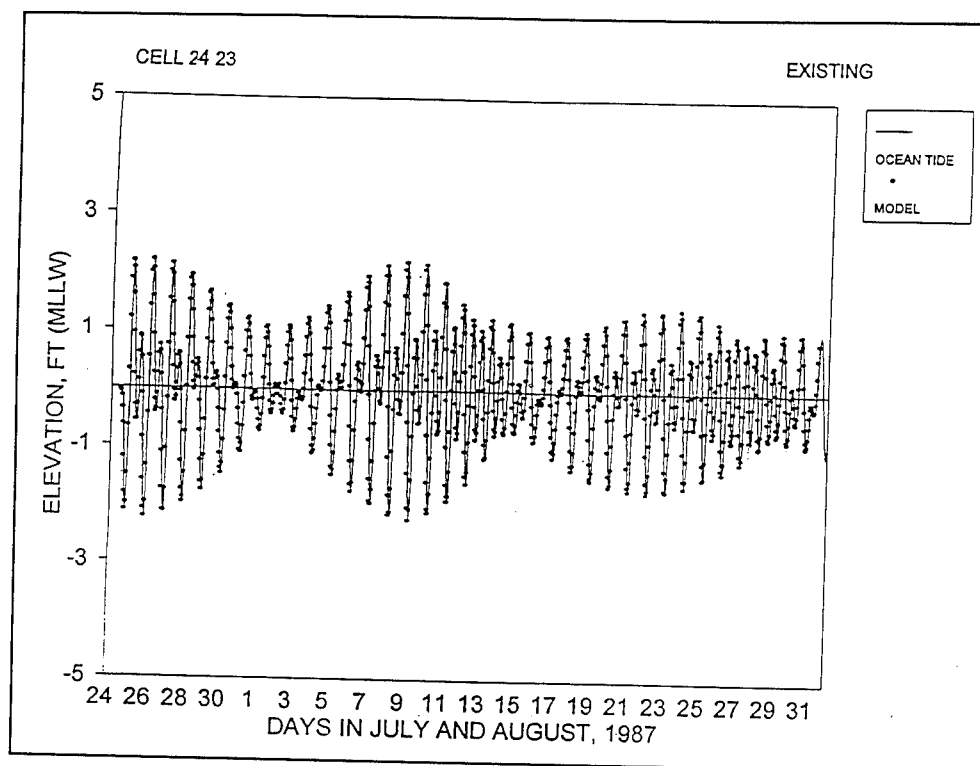
Figure 23. Calculated surface water elevation at station 1 versus measured ocean tide
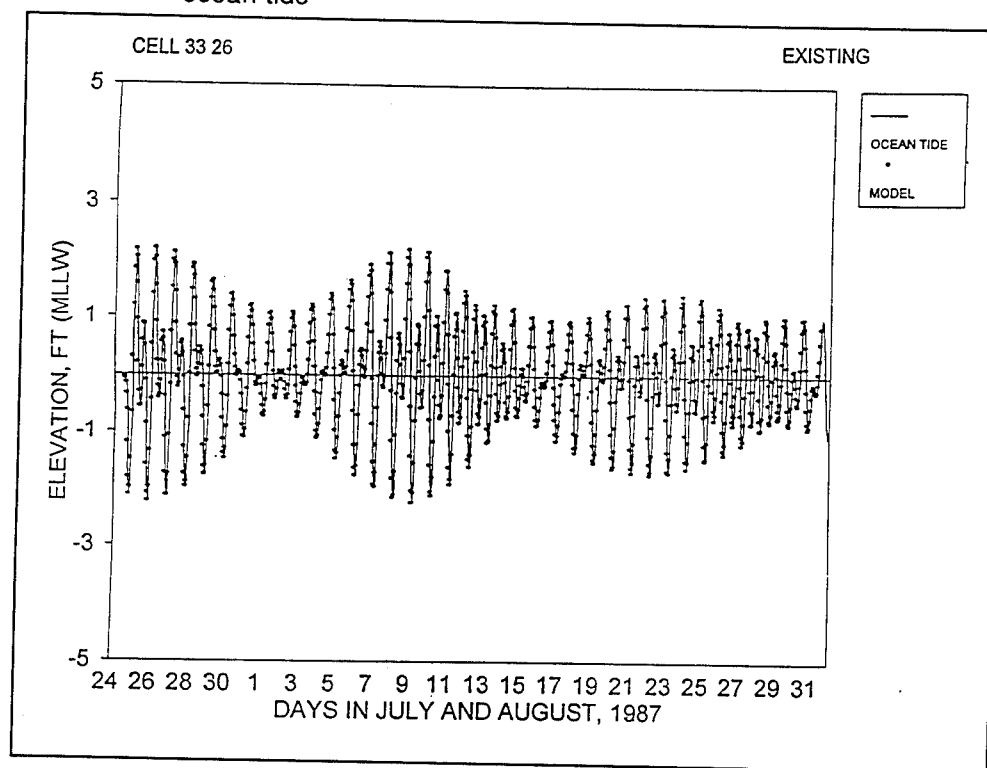
Figure 24. Calculated surface water elevation at station 2 versus measured ocean tide
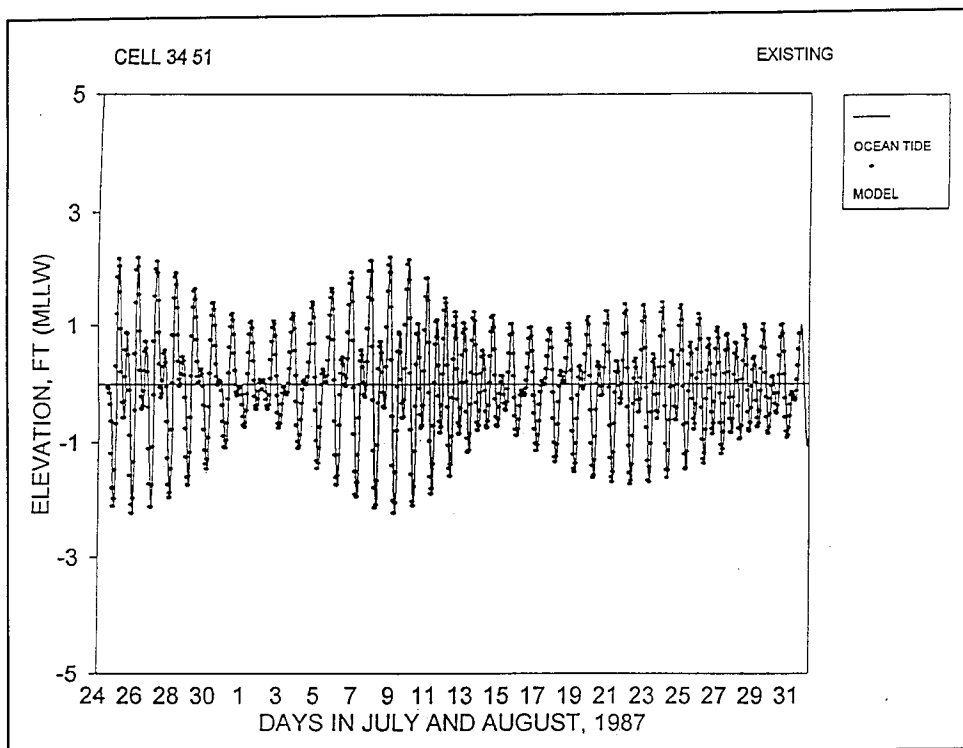
Figure 25. Calculated surface water elevation at station 6 versus measured ocean tide
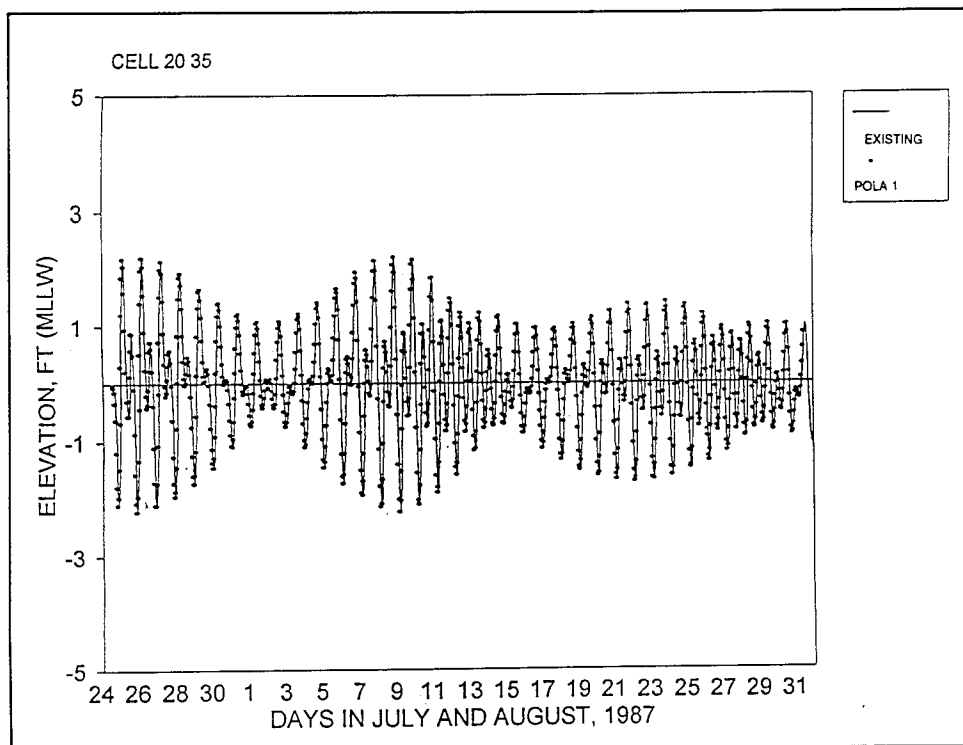
Figure 26. Calculated surface water elevation for the existing and POLA 1
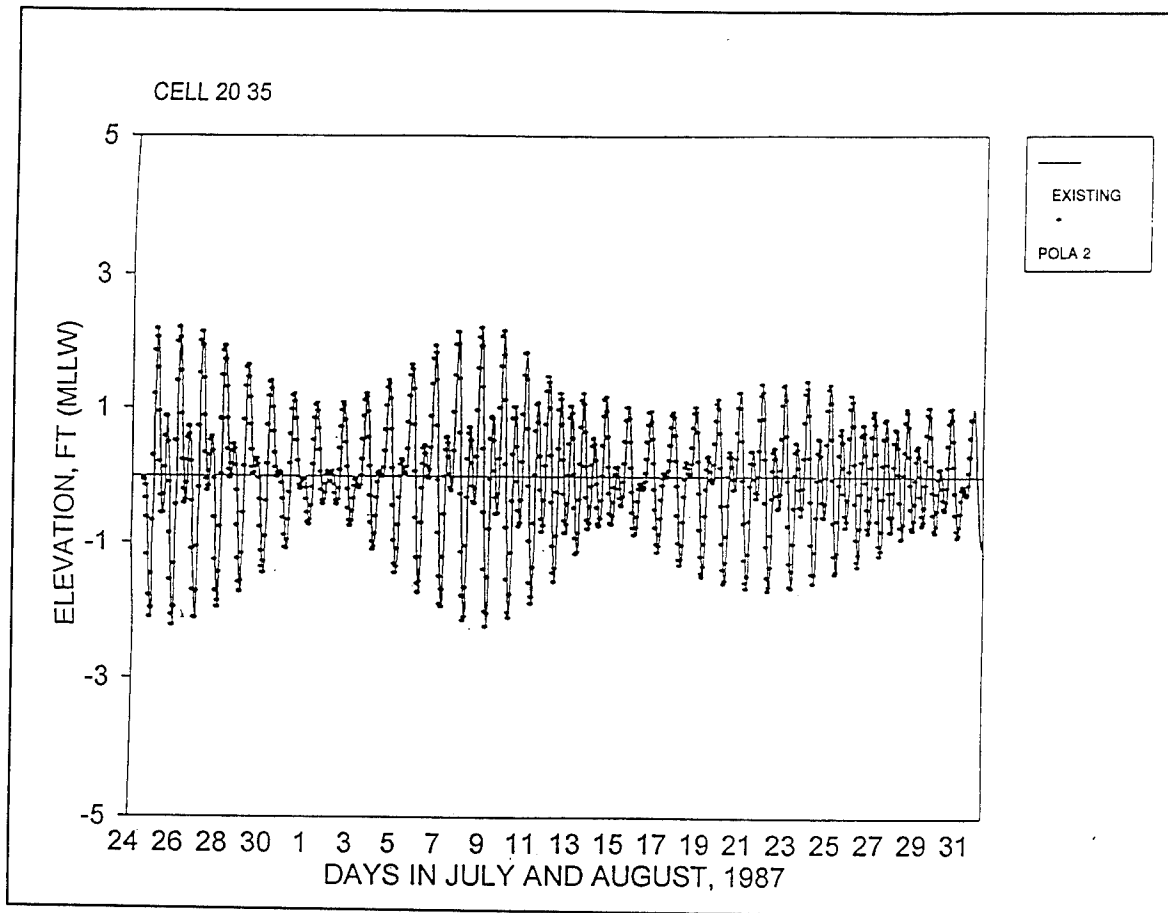
Figure 27. Calculated surface water elevation for the existing and POLA 2

a. With existing breakwater

b. Partially removed breakwater
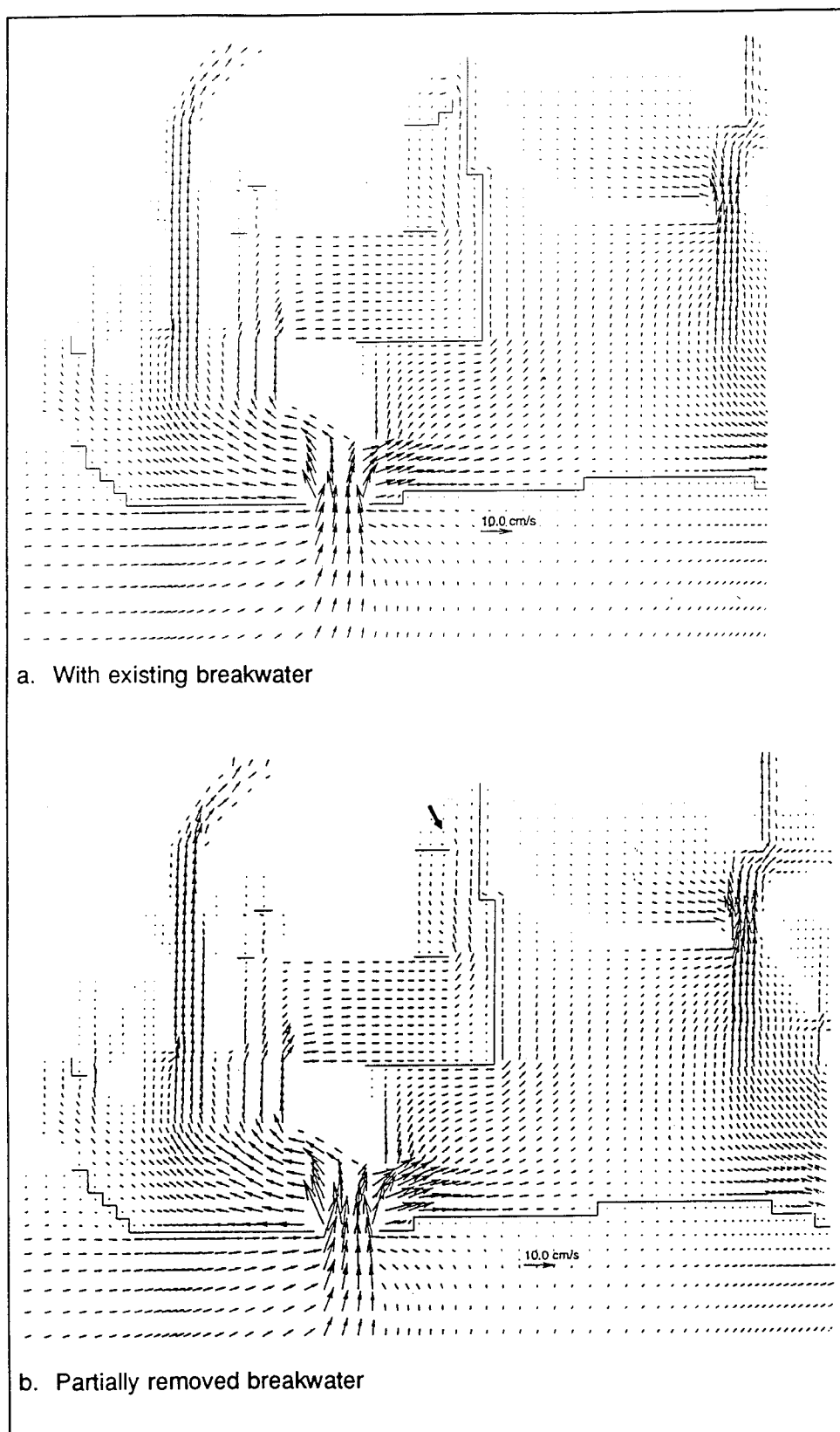
Figure 28.   Surface layer circulation for POLA 1 at maximum flood current
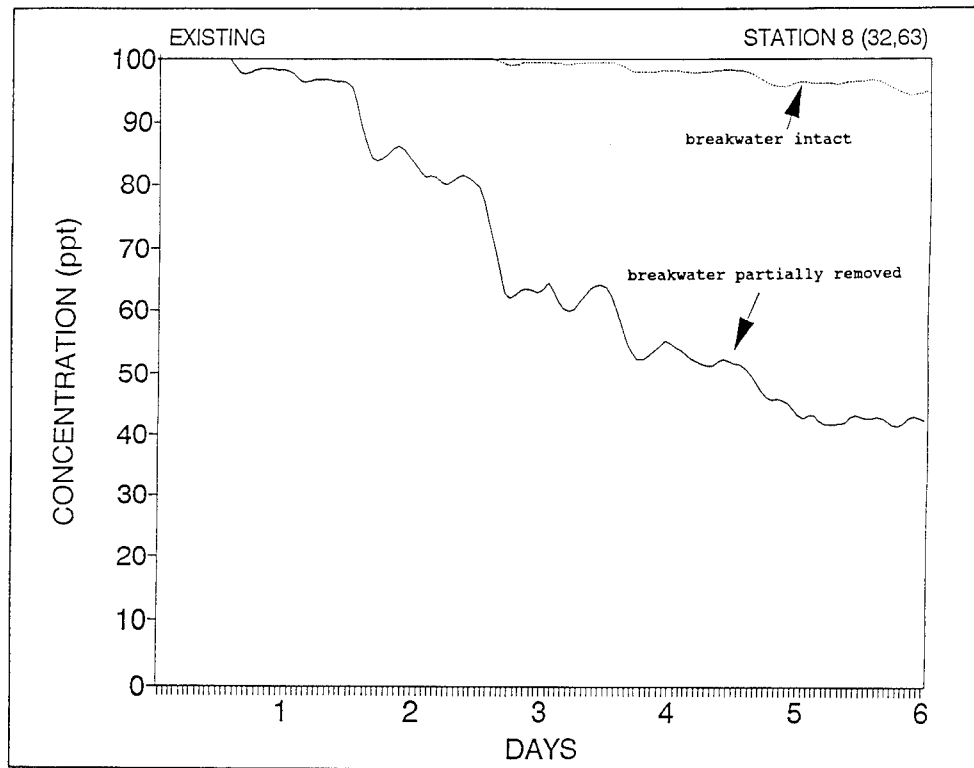
Figure 29. Time series of conservative tracer concentration for existing condition at station 8, with entire and partially removed breakwater
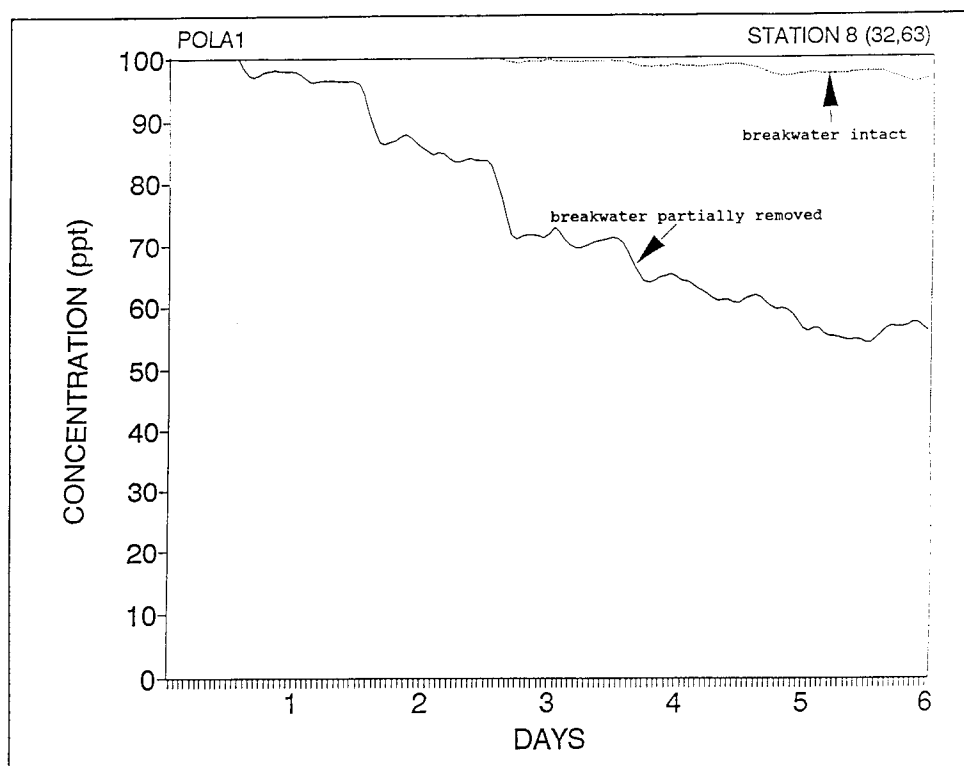
Figure 30. Time series of conservative tracer concentration for POLA 1 at station 8, with entire and partially removed breakwater
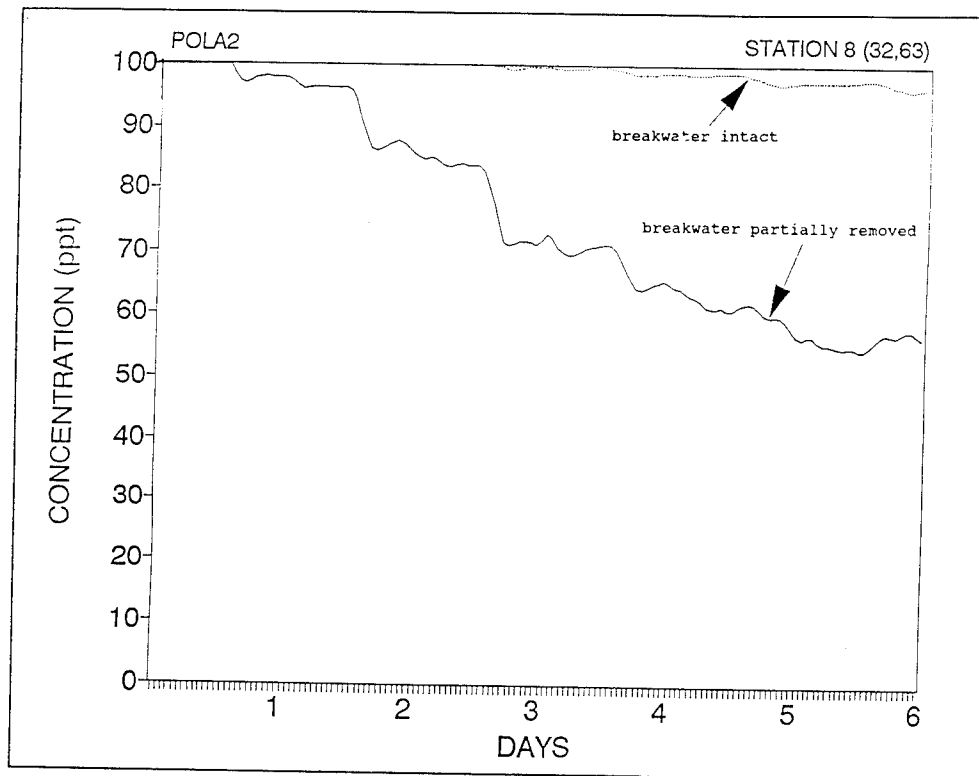
Figure 31.   Time series of conservative tracer concentration for POLA 2 at station 8, with entire and partially removed breakwater
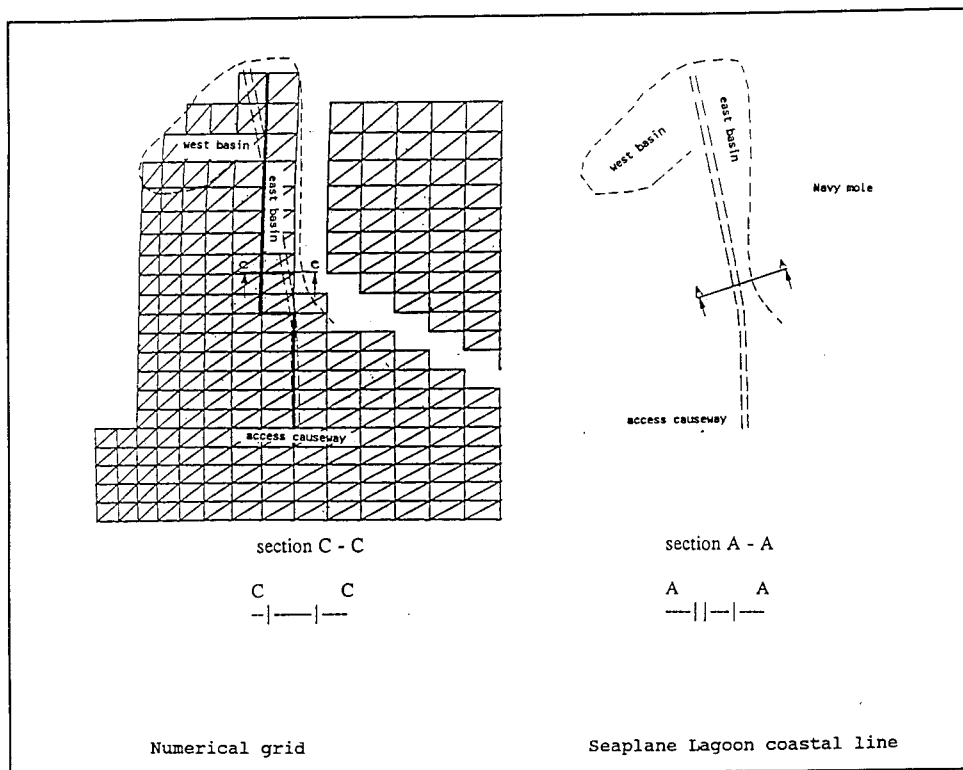
Figure 32. Geographic outline of Seaplane Lagoon, access causeway, and east and west basins
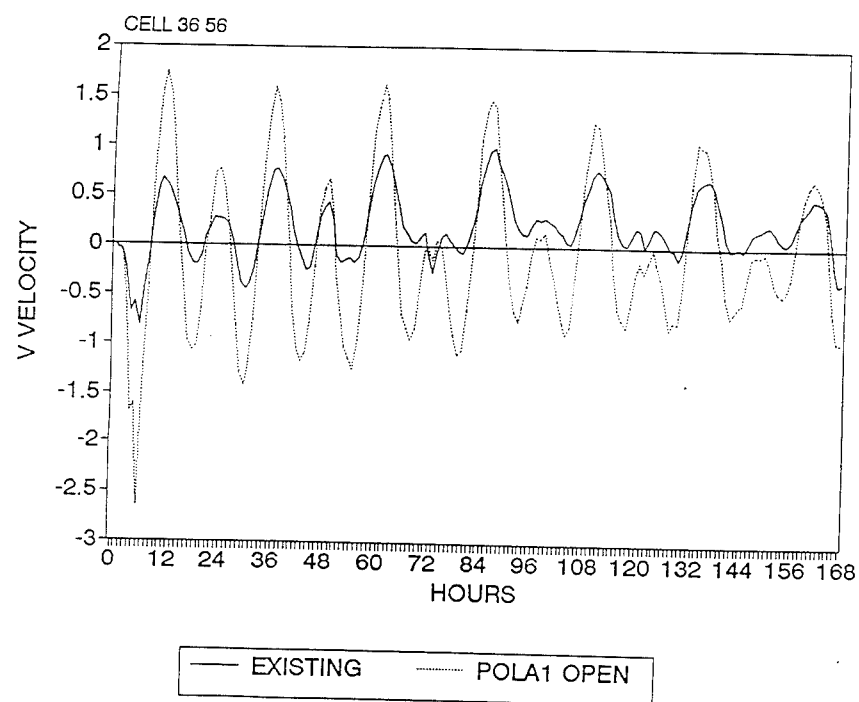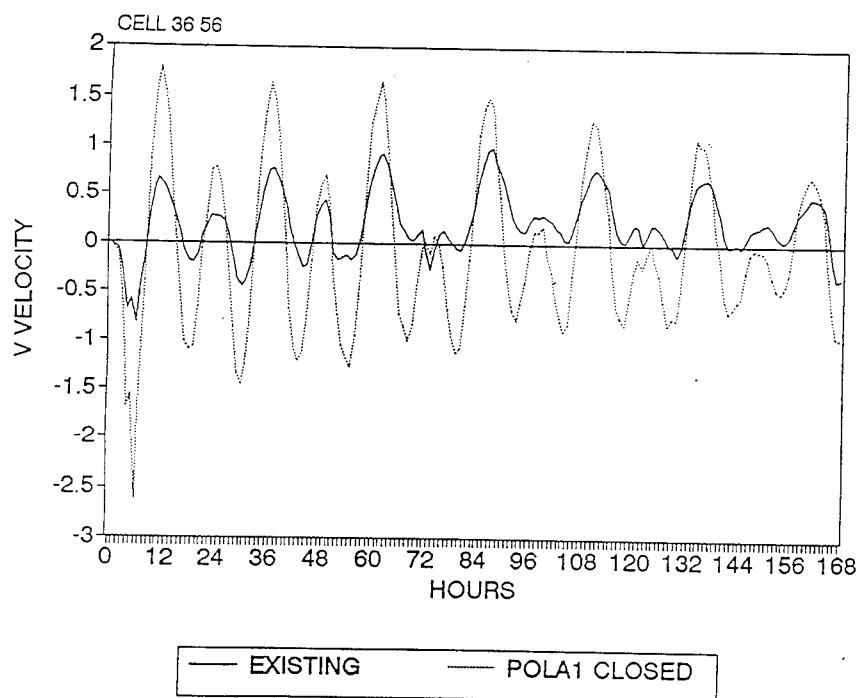
Figure 33. V velocity at the east basin with the causeway opened (a) and closed (b)

Chapter 4   Scenario Description and Results in Support of Water Quality Study

a. At maximum flood

b. At maximum ebb current
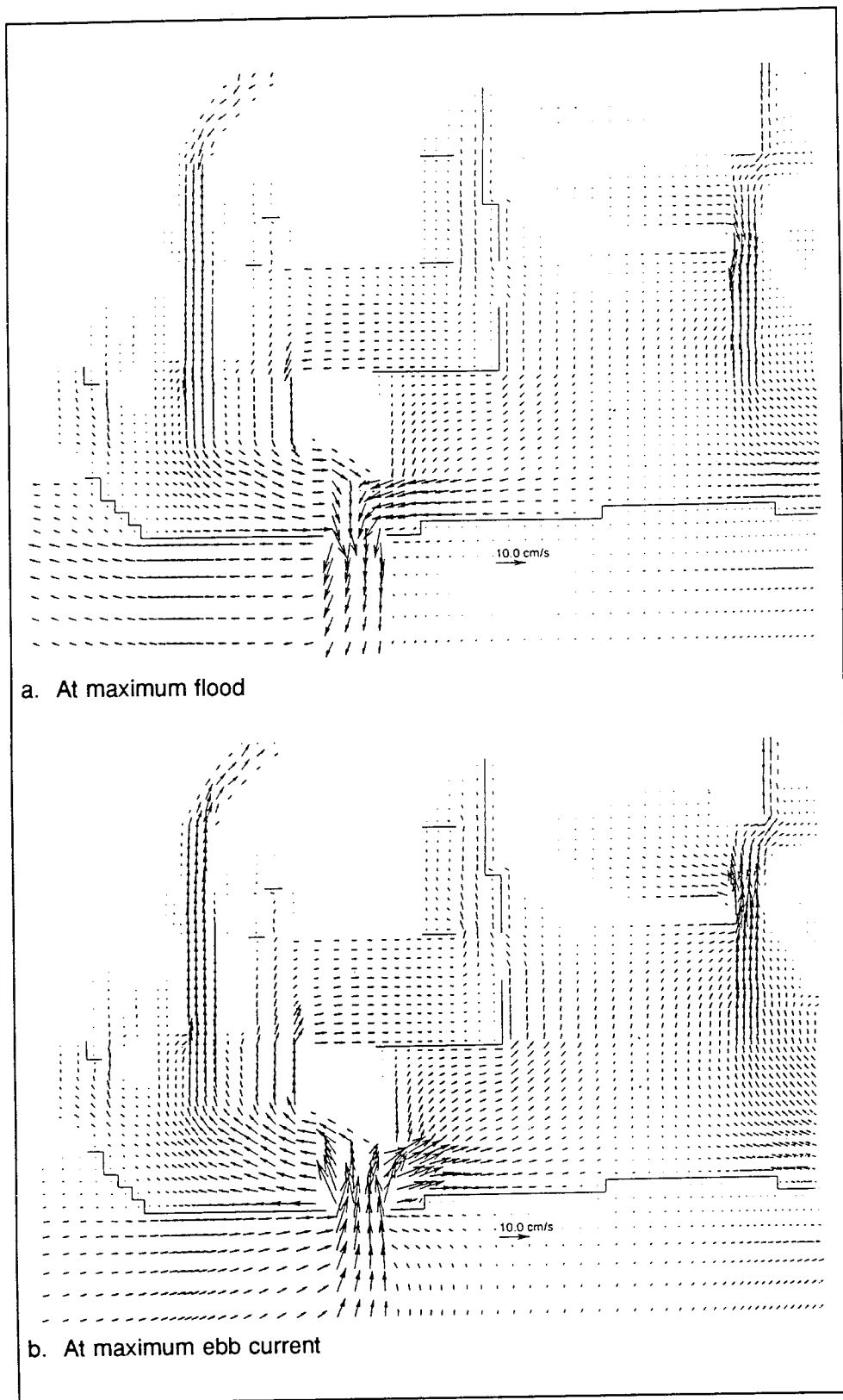
Figure 34. Surface layer circulation with opened causeway, breakwater partially removed for POLA 1, at maximum flood (a) and at maximum ebb current (b)
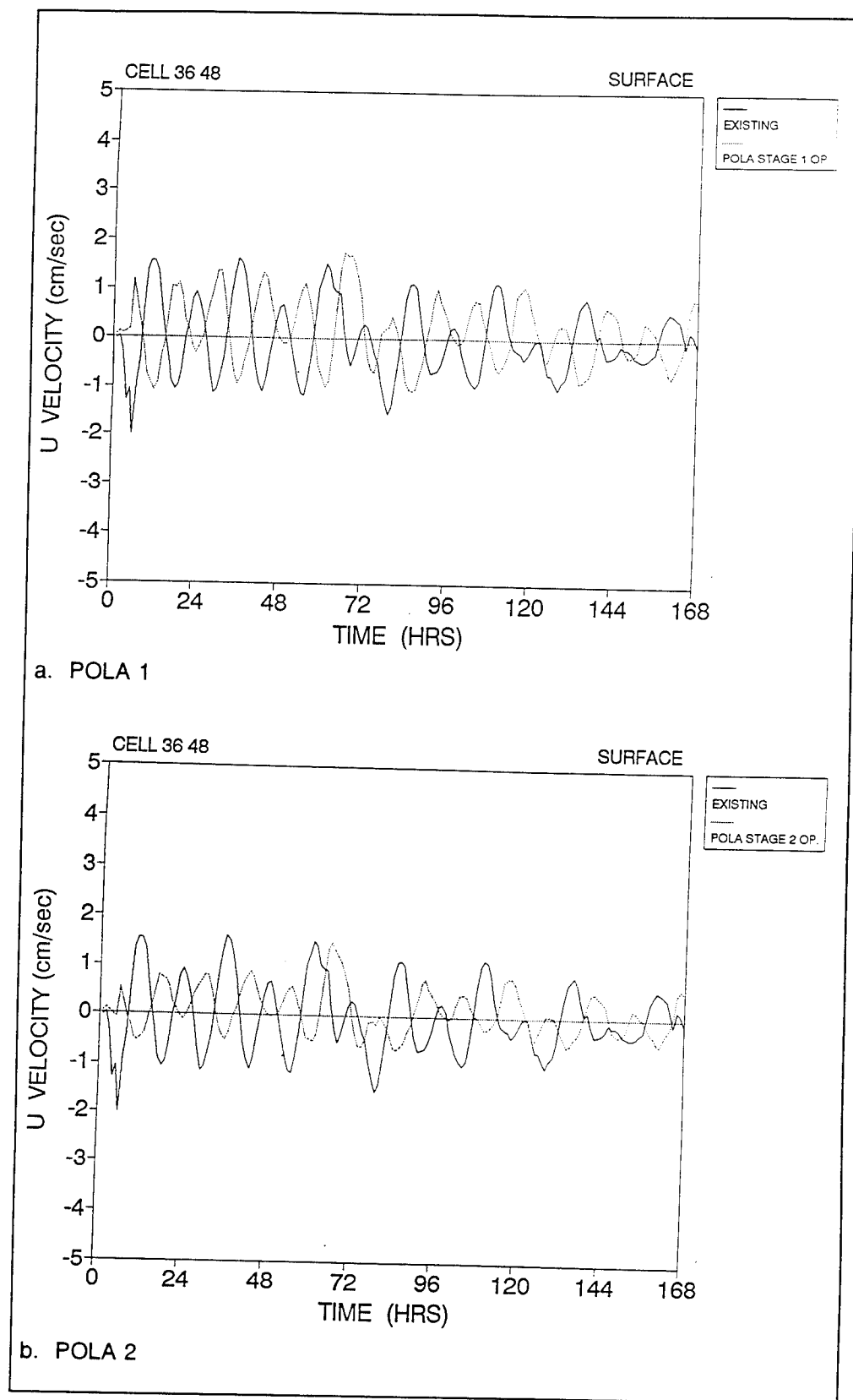
Figure 35. Time series of current velocity at station 4 for (a) POLA 1 and (b) POLA 2

Chapter 4   Scenario Description and Results in Support of Water Quality Study
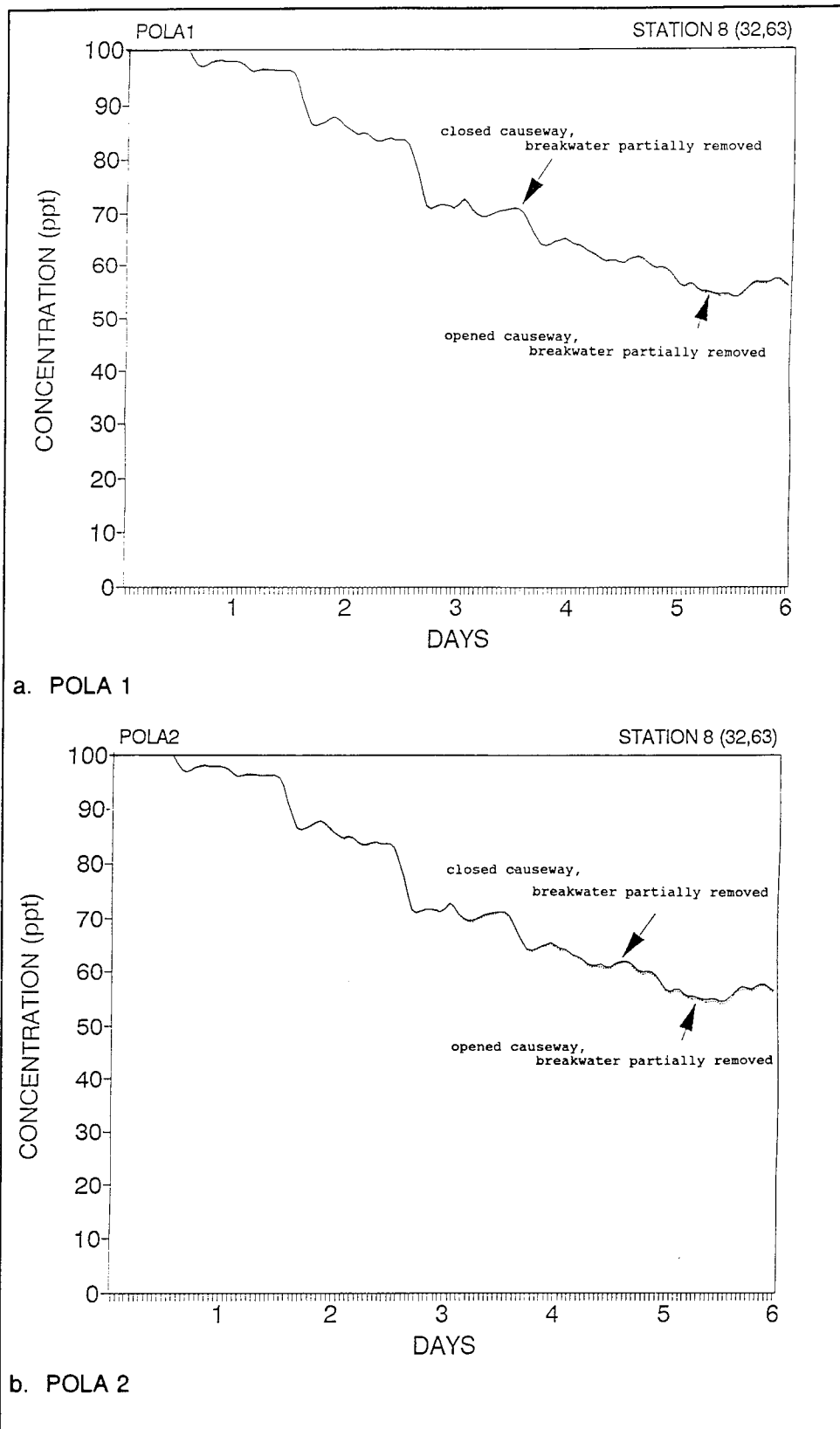
Figure 36. Time series of conservative tracer concentration at station 8, with opened and closed causeway

5 Scenario Description and Results in Support of Ship Simulation Study

Under the 2020 plan, the Port of Los Angeles is proposing an expansion program that includes navigation improvements and use of dredged material to create land for future terminals. The Recommended Federal Project at POLA calls for four increments of navigation channel improvements coupled with disposal of the dredged material at Pier 400 in the outer Los Angeles Harbor. POLA has divided the Recommended Federal Project into two stages, POLA stage I and POLA stage II. The objective of this portion of the study is to generate a database of high-resolution current velocities for use in a ship simulation model. A wind sensitivity analysis is also included. For results of ship simulation, see Hewlett (1994).

Hydrodynamic variables that are important to ship simulation must be studied on different time and space scales than those used for water quality. Resolution of the currents that affect ship navigation requires at least 5 to 6 grid cells across the ship channel. By comparison, 2 to 3 grid cells are sufficient for the WQM. The time scale must also be adjusted to take into account the rates of change of the variables of interest. Mixing of the water within the harbor causes water quality to change relatively slowly, so time scales of a week or more are appropriate to study this process. Currents that affect navigation, however, change in response to wind and tide within hours and must be evaluated on this basis. Though the same numerical model (CH3D-WES) is used for both the water quality and ship simulation studies, the computational demands are such that it is more efficient to modify the grid spacing and time-step and re-run the model than to attempt a single set of runs for both purposes.

Sensitivity Test of Grid Resolution and Critical Wind Conditions

Grid resolution

The basic grid for the water quality studies (Figure 37a) was used as the starting grid for the ship simulation studies. A finer grid system was constructed which has approximately twice the resolution of the previous grid in both the x and y directions (Figure 37b). These refinements provided eight grid cells across the main ship channel at the entrance of the breakwater; six grid cells across the south channel, and five grid cells across the north side of Pier 400. This finer resolution meets the requirements of the ship simulation studies.

Results of the hydrodynamic model, calculated on the refined grid, were compared with results from the coarser water quality grid for the same input conditions. Since the latter had been extensively verified using measured data, a favorable comparison provides validation of the fine grid model. The general circulation patterns were compared and found to be nearly identical, though the fine scale grid showed some eddy structure that was not evident in the coarse grid. Two stations, gauges 11 and 12, located in the central portion of the outer harbor (Figure 38) were used for time series comparison. Figures 39 and 40 show the comparison of current for three layers (top, middle, and bottom). The agreement is very good in all cases. The small differences in phase are due to the highly resolved topographic features in the fine grid, which make the response of the local velocity slightly different in phase from the coarse grid. Since the topographic features are real, it is assumed that the fine grid provides more accurate estimates than the coarse grid. The authors conclude that the fine grid is well-behaved numerically, provides information that is consistent with the measurements and the coarse grid, and is of sufficient accuracy and resolution to conduct a ship simulation support study.

Critical wind conditions

The wind can generate large transient currents that affect ship motions within the navigable portion of the harbor. It is, therefore, important, from a safety point of view, that the fine scale hydrodynamic model used for ship simulation studies (referred to as HMSS) be able to simulate the velocity field induced by wind. In all hydrodynamic model calculations used for water quality studies, wind inputs are from measured data. In the ship simulation application, however, wind speeds and directions will be synthesized in order to cover those conditions that are critical to prototype ship operations. Tidal currents will be included in the scenarios considered.

Ideally, it will be desirable to run as many combinations of wind and tidal conditions as possible. However, a complete test of all ranges of wind speed,

direction, and tidal conditions occurring in the harbor requires too many calculations and is not feasible. Additionally, the critical conditions selected need to be realistic enough to mimic the harbor conditions. The historical database was, therefore, used to define a manageable, yet realistic suite of critical wind conditions. Historical wind data assembled by Seaburgh et al. (1994) in the Los Angeles and Long Beach Harbor (Figure 41) were used to guide the selection. This provided the average wind condition as well as the upper bound of the wind speed and dominant wind directions. A total of 48 sensitivity test cases were conducted using 3 wind directions, 2 wind speeds, 3 layers in the water column, the vertically averaged condition, and 2 tidal conditions (Table 5).

The test was conducted in the 5-day period August 7 - 12, 1987. Since this was the period used by Vemulakonda, Chou, and Hall (1991), tidal data files were available for the period as well as actual wind measurements. After 2 days of spin-up, wind stresses were imposed on the harbor water surface steadily for 72 hr. Measured ocean tidal elevation was applied at the seaward and western boundaries. The initial condition was a quiescent water body. Results were evaluated at the end of the period.

Table 5
Wind Sensitivity Test Cases

Wind Direction	Wind Speed (knots)	Vertical Layers	Tidal Condition
Southeast	20, 30	Surface, middle, bottom vertical averaged	Maximum ebb, flood
Southwest	20, 30	Surface, middle, bottom vertical averaged	Maximum ebb, flood
West	20, 30	Surface, middle, bottom vertical averaged	Maximum ebb, flood

Figures 42-44 are surface layer circulations selected for illustration. In each case, the figure labeled "a" is for the maximum ebb tide and the figure labeled "b" is for the maximum flood tide. The base condition, using measured wind data, is shown in Figure 42. The effects of southwest winds at 20 knots and southeast winds at 20 knots are shown in Figures 43 and 44 respectively. These clearly show the offsetting influence of the wind on the surface current, in the direction of the prevailing wind. In order to better assess the sensitivity test results, a statistical analysis was performed around the entrance of the breakwater, where the flow is complicated by the interaction of wind and tidal circulation through a narrow gate.

A square area near Angel's Gate having 400 velocity grid points was selected (Figure 45) to assess current velocity response to wind forcing. Figures 46 and 47 show the distribution (direction and number of occurrences)

64

of the surface current direction and speed for southwest winds at 20 knots (Figure 46) and southeast winds at 20 knots (Figure 47) during maximum flood and ebb conditions, respectively. The current direction is the direction 'toward' while wind is the direction 'from' which it is flowing, relative to true north. The velocity direction at flood tide, for both wind conditions, is sharply concentrated in a preferential direction. In the case of the southwest wind, the current directions concentrate in a 60- to 80-deg band, and in the case of the southeast wind, they concentrate in a 300- to 320-deg band. Direction response during the ebb portion of the tidal cycle was much more variable than for the flood. The largest current generated by a 20-knot wind is in the range of 1.0 to 1.5 knots. These occurred during flood tide for winds from the southwest and during ebb tide for winds from the southeast. When wind speed was increased to 30 knots, the maximum current generated was in the range of 1.5 to 2.0 knots. Velocities in the middle and bottom layers were smaller in magnitude and direction was more diversified as opposed to the surface layer.

Following this study, it was decided to proceed with production runs using the 20-knot conditions. It was concluded that the occurrence of 30-knot winds for an extended period of time was a very rare event and would preclude the use of the channel by a prudent navigator. A ship would be more likely to await more favorable conditions before attempting an entrance. The 20-knot wind speed was selected as the maximum reasonable condition for evaluating ship motions in the channel. The west and southwest conditions were combined to west southwest to reduce the number of production runs. Second, after all three layers of current velocity, along with the vertically averaged velocity, were examined, it was felt that for deep-draft vessels, a vertically averaged velocity would be sufficient to represent the forces on the submerged portion of the ship's hull and accurate enough for conducting the ship simulation (Hewlett 1994). A complete set of velocity vector plots for different plans can be found in Appendix C, including those at the surface and bottom layer, as well as the vertically averaged condition.

Scenario Description

The two plans that the Port of Los Angeles proposed, POLA 1 and POLA 2, have been described in Chapter 4 (see Figures 18 and 19). The National Economic Development Plan Increment 2 (NED 2, Figure 48) represents the first stage of Pier 400 construction and the main ship channel deepening to 63 ft. In NED 2 and 3, the second phase of Pier 400 (with a slightly different shape at the northwest corner from POLA 2) will be completed, the main ship channel will be deepened to 71 ft, and the south channel will be deepened to 66 ft (Figure 49). In NED 2-5, the third phase of Pier 400 (resembling POLA 2) is to be completed and the north channel associated with increments 4 and 5 is also to be deepened to 45 ft (see Figure 50). In order to test the worst-case scenario (i.e., largest currents) in the north channel, a portion of the causeway at the leading end of the north channel was opened to allow flow through the otherwise dead-end channel.

The final scenarios associated with proposed harbor configurations are summarized in Table 6.

Table 6 Scenario Runs	
Harbor Construction Plan	**Critical Wind Condition**
Existing Condition	Base wind (BW) Southeast wind, 20 knots (SE20) West southwest wind, 20 knots (WSW20)
POLA Stage 1 (POLA 1)	Same as above
POLA Stage 2 (POLA 2)	Same as above
National Economic Development Increment 2 (NED 2)	Same as above
National Economic Development Increments 2 and 3 (NED 2&3)	Same as above
National Economic Development Increments 2 through 5 (NED 2-5)	Same as above

The 5-day period of August 7-12, 1987 was again selected for model runs. The initial condition is a quiescent water body. The boundary conditions include measured ocean tide elevation at the seaward and western boundaries, wind stress on the water surface, and quadratic bottom stress.

Wind stresses used in the scenario runs were: (a) the base condition in which actual measured data were used (Figure 51); (b) WSW20 -- west southwest wind, 20 knots; and (c) SE20 -- southeast wind, 20 knots. For WSW20 and SE20, rather than using 72 hr of constant steady wind, a 48-hr wind event was embedded into the background wind from day 8 to day 10. Wind direction was fixed for this entire 48-hr duration, while wind speed varied in a normal Gaussian distribution, ranging from 0 to 22.5 knots (Figures 52 and 53). After the 48 hr, wind speed and direction were restored to the background velocities. This method has several advantages for use in scenario runs. First, it more closely mimics the natural conditions during which winds increase from one direction during frontal passage and decrease to background conditions following the event. Second, the wind is a turbulent, random, unsteady motion and is more suitably treated as a stochastic process, for which normal (Gaussian) distribution can be used to acquire essential statistics. For example, during the peak 12 hr of the 48-hr event, the unsteady wind stress so constructed is statistically equivalent to the effect of 20 knots steady wind. Third, with this approach, problems in the open boundary condition can be avoided. When steady wind is imposed on the water surface for a prolonged period, instability can occur near the open boundary because of the inconsistency between the calculated water surface elevation and the prescribed

one. By using the unsteady approach, the open boundary condition became more stable, and this problem was relieved.

Based on Table 6, there are a total of six scenarios to be run. Results for the existing condition are presented first to establish baseline information in terms of circulation (vector plot) and current velocity (time series plot), followed by the five proposed harbor plans. Stations used for time series presentation are stations 1, 2, 3, 4, and 5, as shown in Figure 22.

Existing Harbor Condition Under Wind Effects

Water surface elevation

Water surface elevations for the existing harbor under BW, WSW20, and SE20 conditions are shown in Figure 54. Wind conditions in the harbor have little or no direct impact on the modeled surface elevation. Comparisons are similar for all proposed harbor plans and it can be concluded that neither wind nor proposed harbor plans has a significant impact on the surface elevation in the Los Angeles Harbor. Additional comparisons are shown in Figures D37-D41.

Circulation - vector plot

Maximum flood and ebb currents occur at half tide, i.e., half time between high and low tide. Vector plots were, therefore, selected to be presented during this period. Circulation plots for BW, WSW20, and SE20 are shown in Figures 46-44 at maximum flood and ebb current. The flood current at Angel's Gate has a larger velocity under WSW20 than under BW or SE20. In contrast, ebb current at Angel's Gate has a larger velocity under SE20 than BW or WSW20. This increased current speed is due to the addition of the wind-induced current, which can amount to 10-15 cm/s under a 20-knot wind. If the tidal current is 20 cm/s, WSW20 can add an additional 10-15 cm/s of current speed to the flood current. SE20 can add a similar amount of current speed on ebb current. This effect has implications on the maneuvering strategy under windy conditions through the entrance of the breakwater.

Whether reinforcement occurs in a particular tidal stage is determined by the relative direction of wind versus tidal velocity. During the flood, WSW20 has a vector component that coincides with the tidal flow at Angel's Gate and therefore reinforces the tidal velocity. By contrast, during the ebb, WSW20 has the opposite vector component to the ebb tide, and weakens tidal velocity. Due to the long fetch distance along the Long Beach coast, SE20 appears to be more effective in driving water from the Long Beach Harbor side into the Los Angeles Harbor. Therefore, it has a reinforcement effect on ebb tide and, conversely, a canceling effect on flood tide at Angel's Gate.

Current velocity - time series

The effect of wind on current velocities was found to be a significant addition to the tidal component at all levels in the flow. In the most extreme cases, tidal current velocities were more than doubled by the wind contribution. Nevertheless, except under extreme high-wind conditions, current velocities in the harbor are generally under 1 knot.

The complete modeled time series and velocity vectors have been saved and were provided for the ship simulation studies. Detailed analysis of velocity variations under the proposed plans and critical wind conditions can be found in Appendix E.

a. Coarse grids
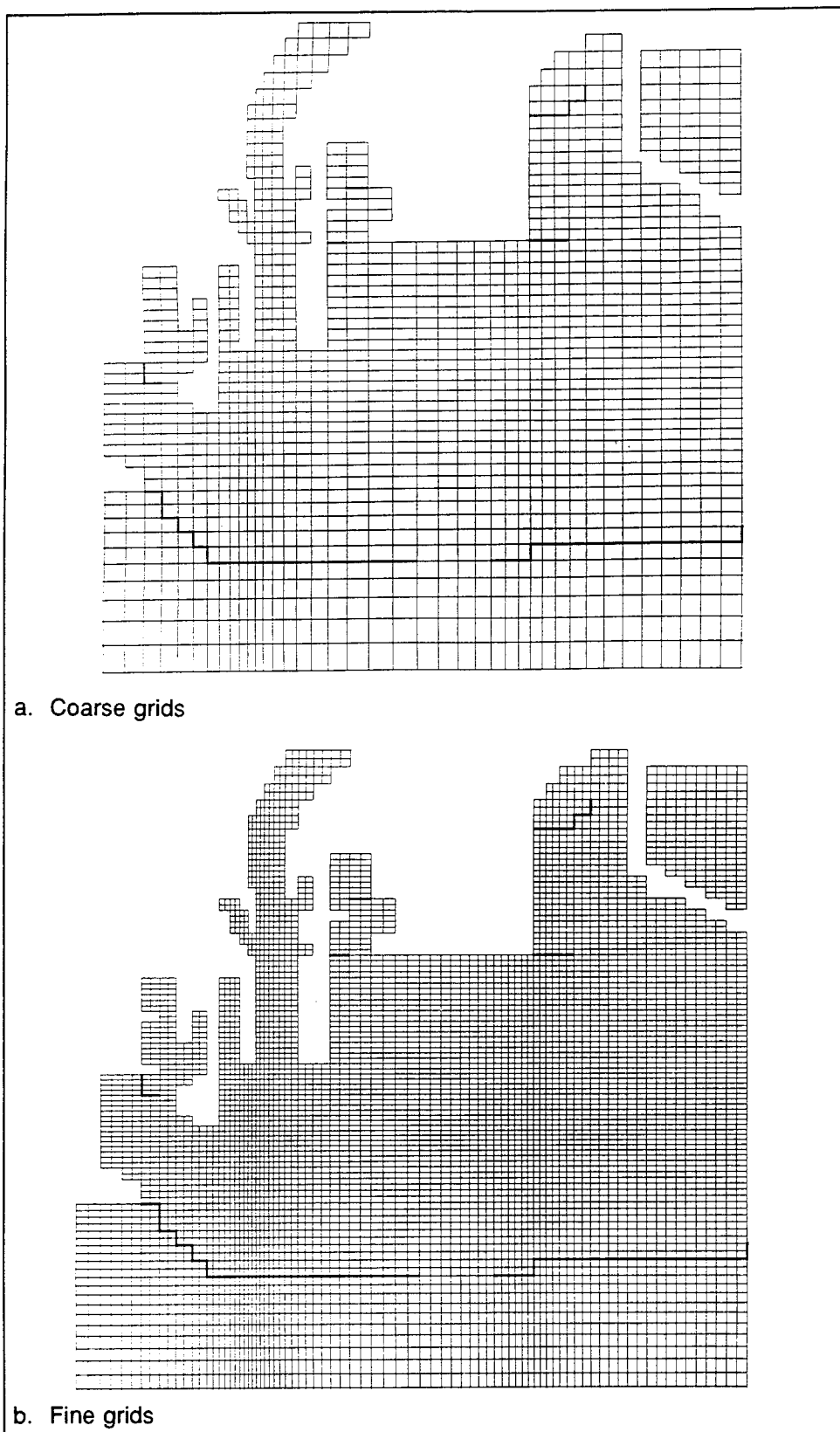
b. Fine grids

Figure 37. The numerical model
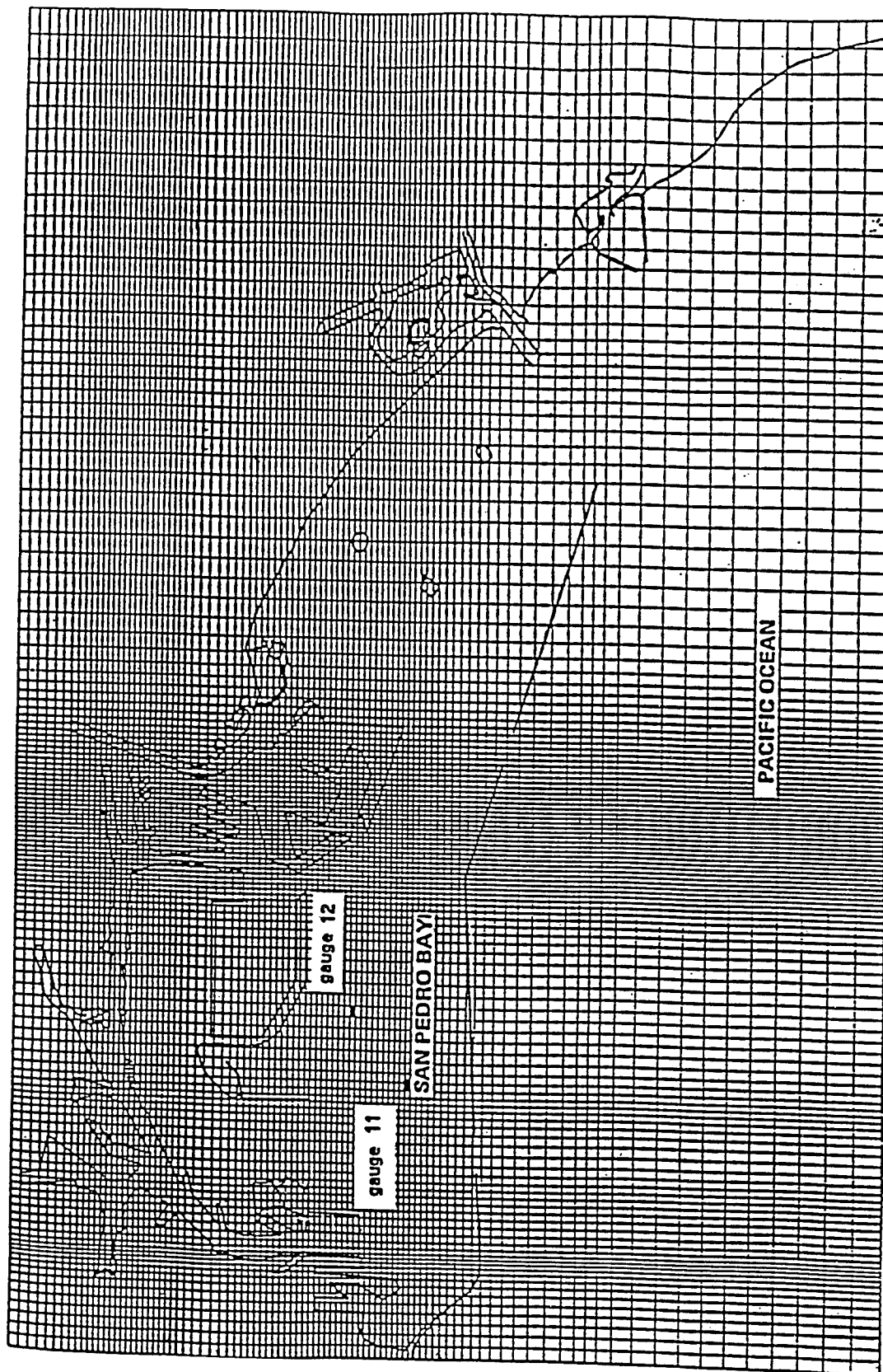
Figure 38. Station locations for gauges 11 and 12

Chapter 5   Scenario Description and Results in Support of Ship Simulation Study

a. Surface layer

b. Middle layer

c. Bottom layer
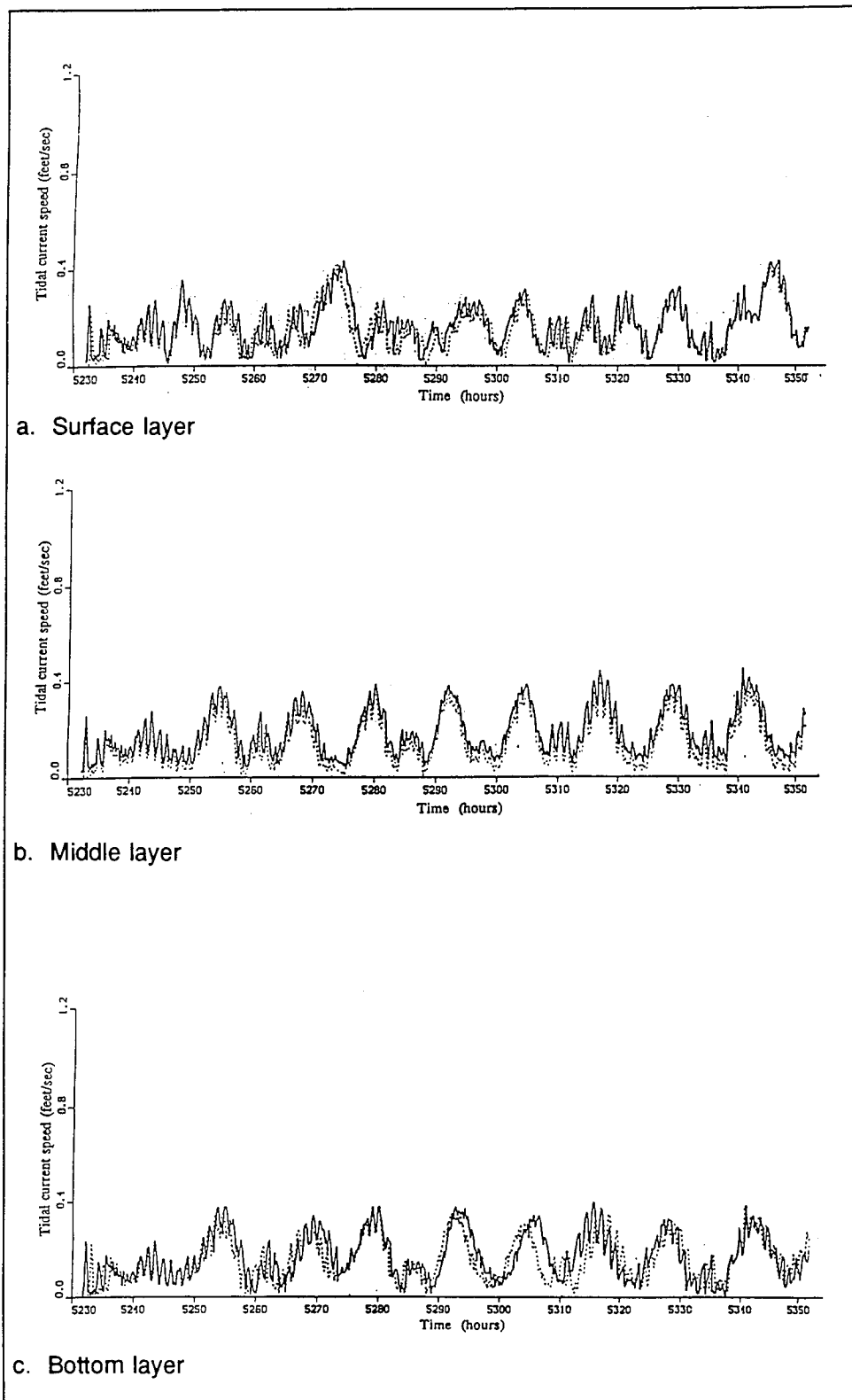
Figure 39. Comparison of tidal current speeds for fine grid (solid line) and coarse grid (broken line at gauge station 11)

a. Surface layer

b. Middle layer

c. Bottom layer
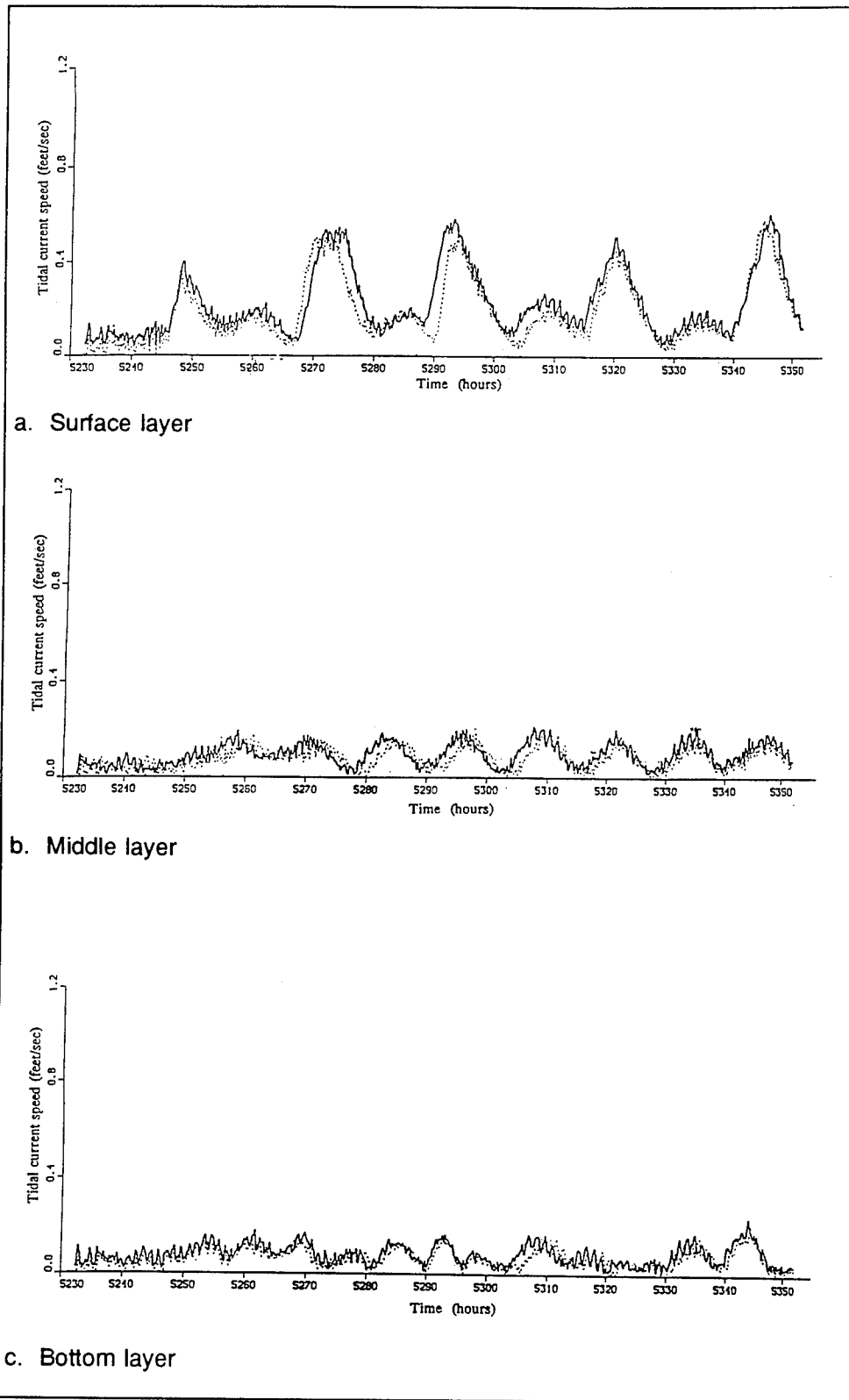
Figure 40. Comparison of tidal current speeds for fine grid (solid line) and coarse grid (broken line at gauge station 12)
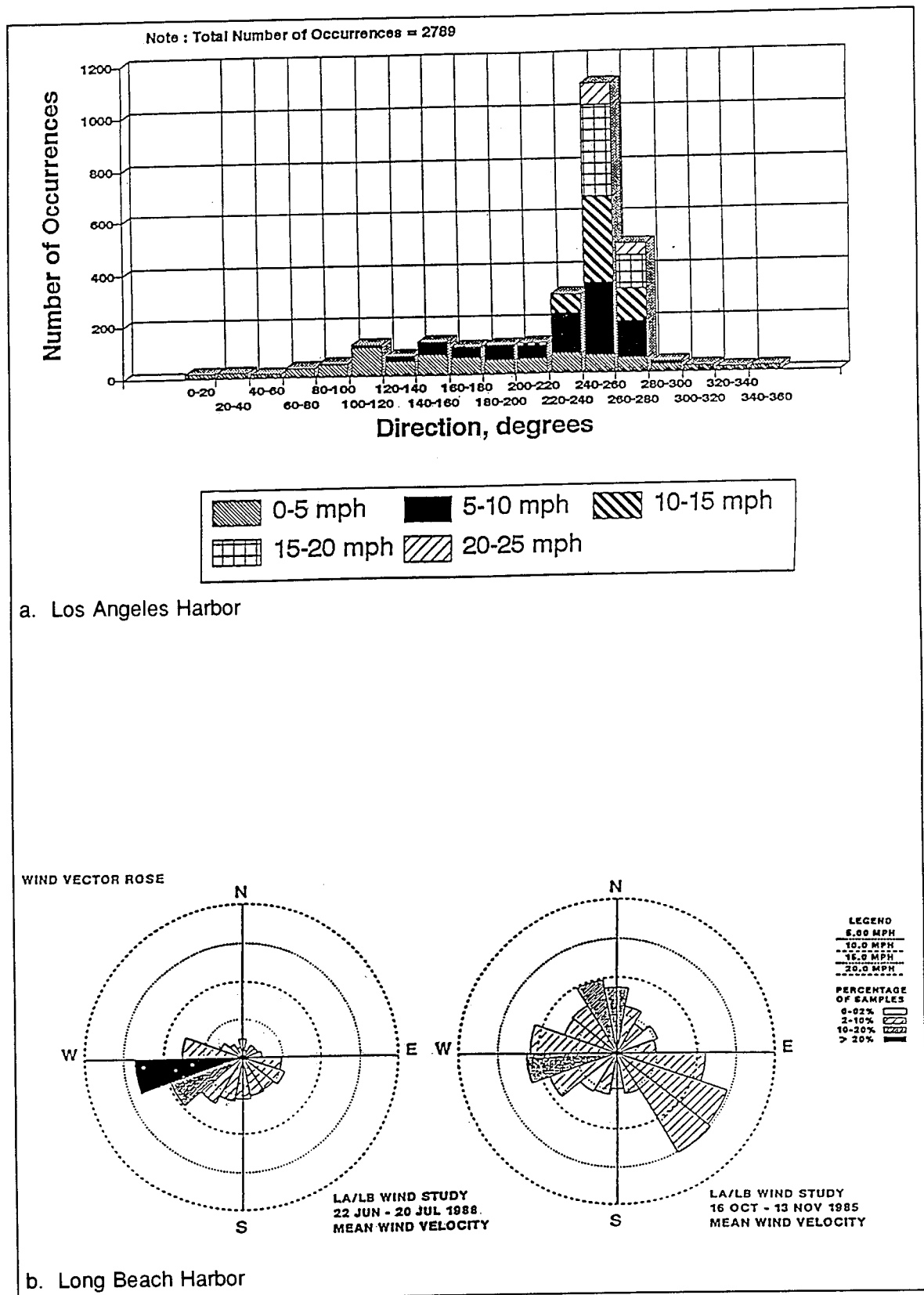
Figure 41. Historical wind records from San Pedro breakwater

Chapter 5   Scenario Description and Results in Support of Ship Simulation Study

a. During maximum ebb tide flow conditions

30.0 cm/s
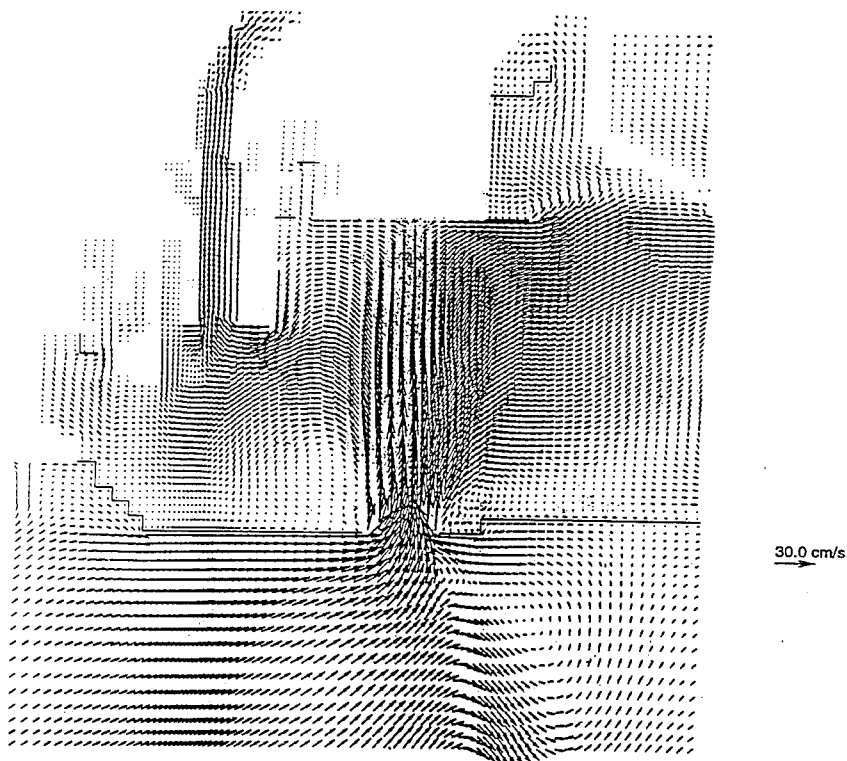
b. During flood tide flow conditions

Figure 42.   Vector plot of surface layer circulation for the existing condition under base wind condition (velocity and direction)

a. During maximum ebb tide flow conditions

30.0 cm/s

b. During flood tide flow conditions

30.0 cm/s
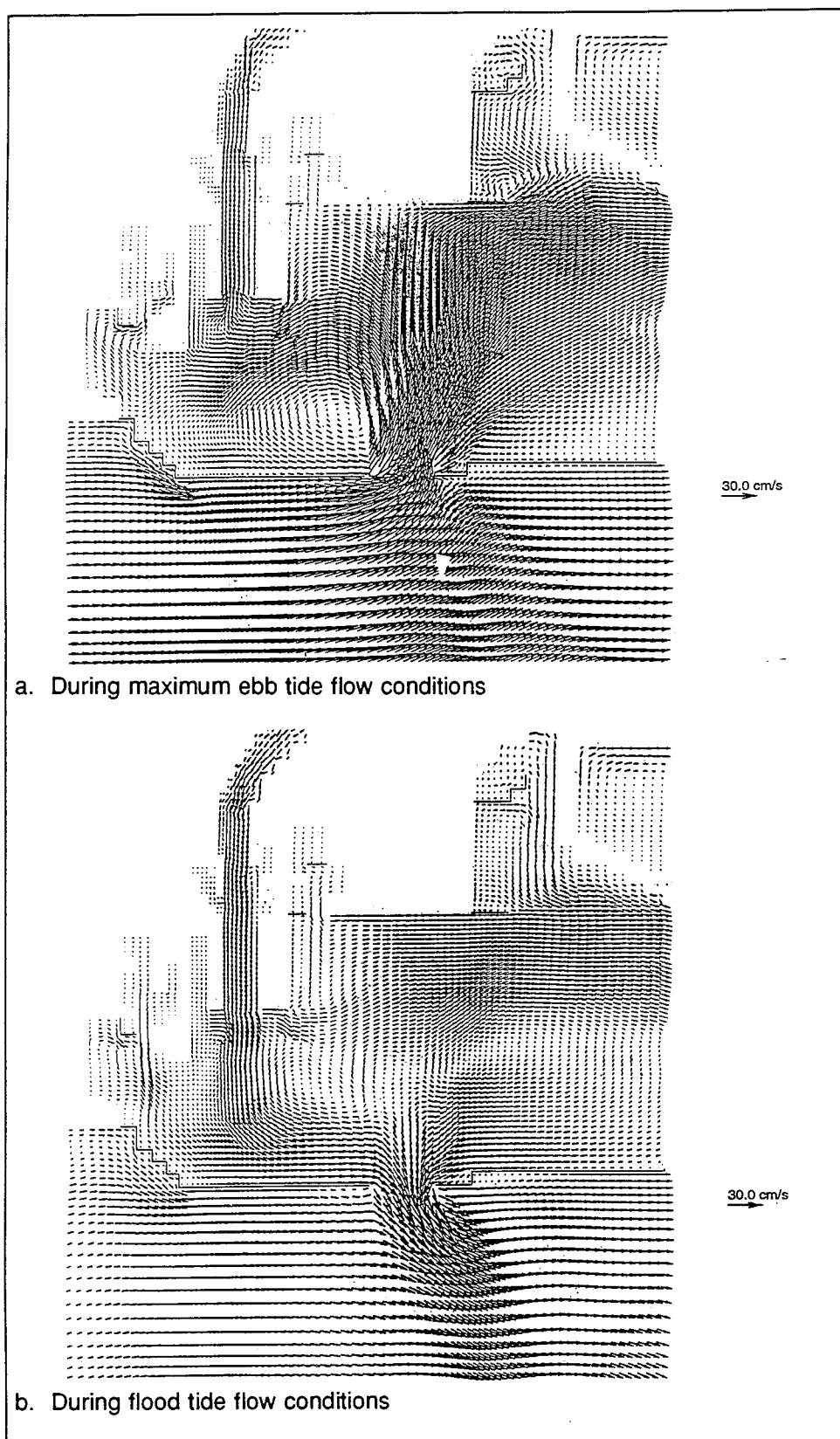
Figure 43.   Vector plot of surface layer circulation for the existing condition under winds from WSW at 20 knots

a. During maximum ebb tide flow conditions

b. During flood tide flow conditions
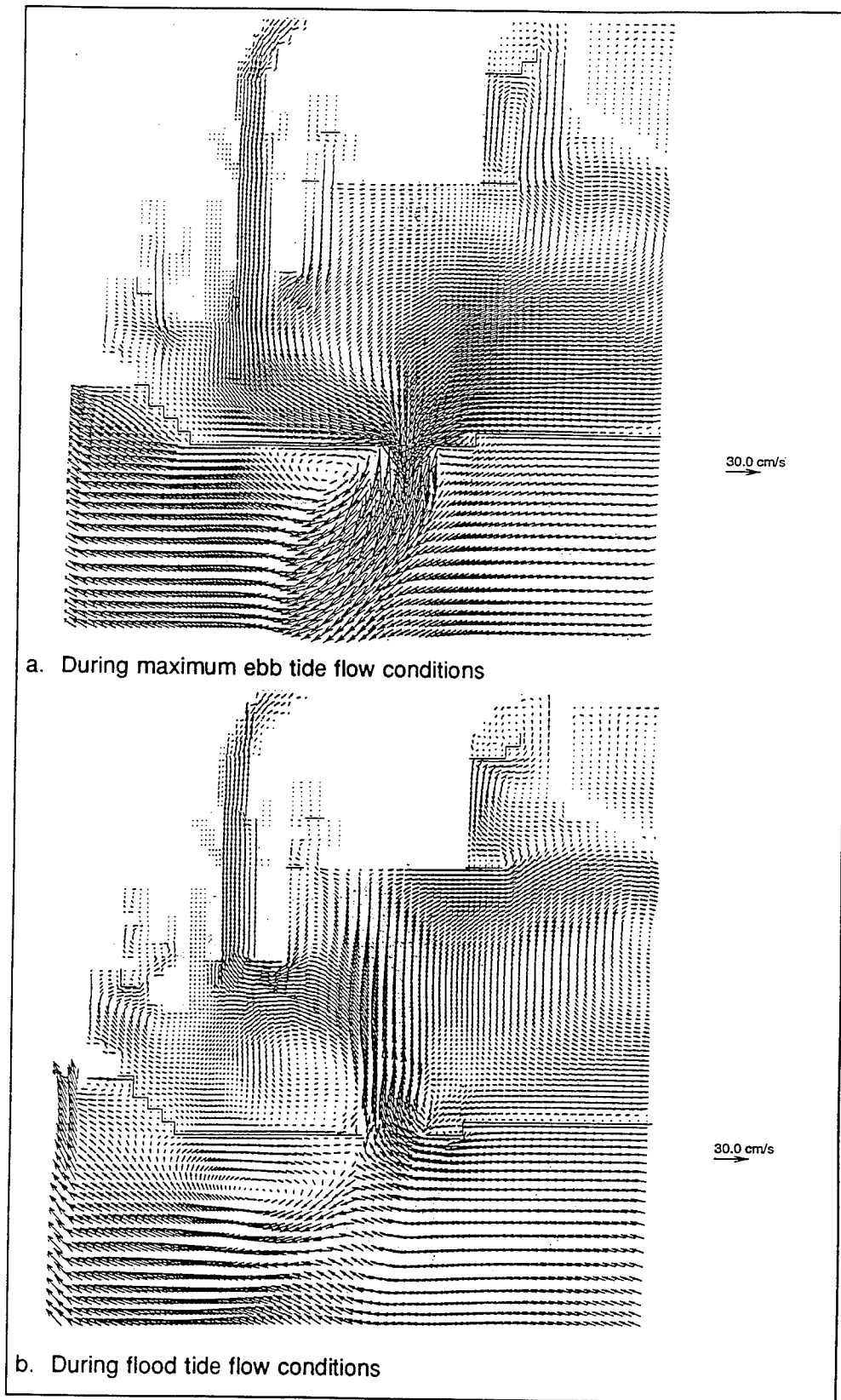
Figure 44.   Vector plot of surface layer circulation for the existing condition
under winds from SE at 20 knots
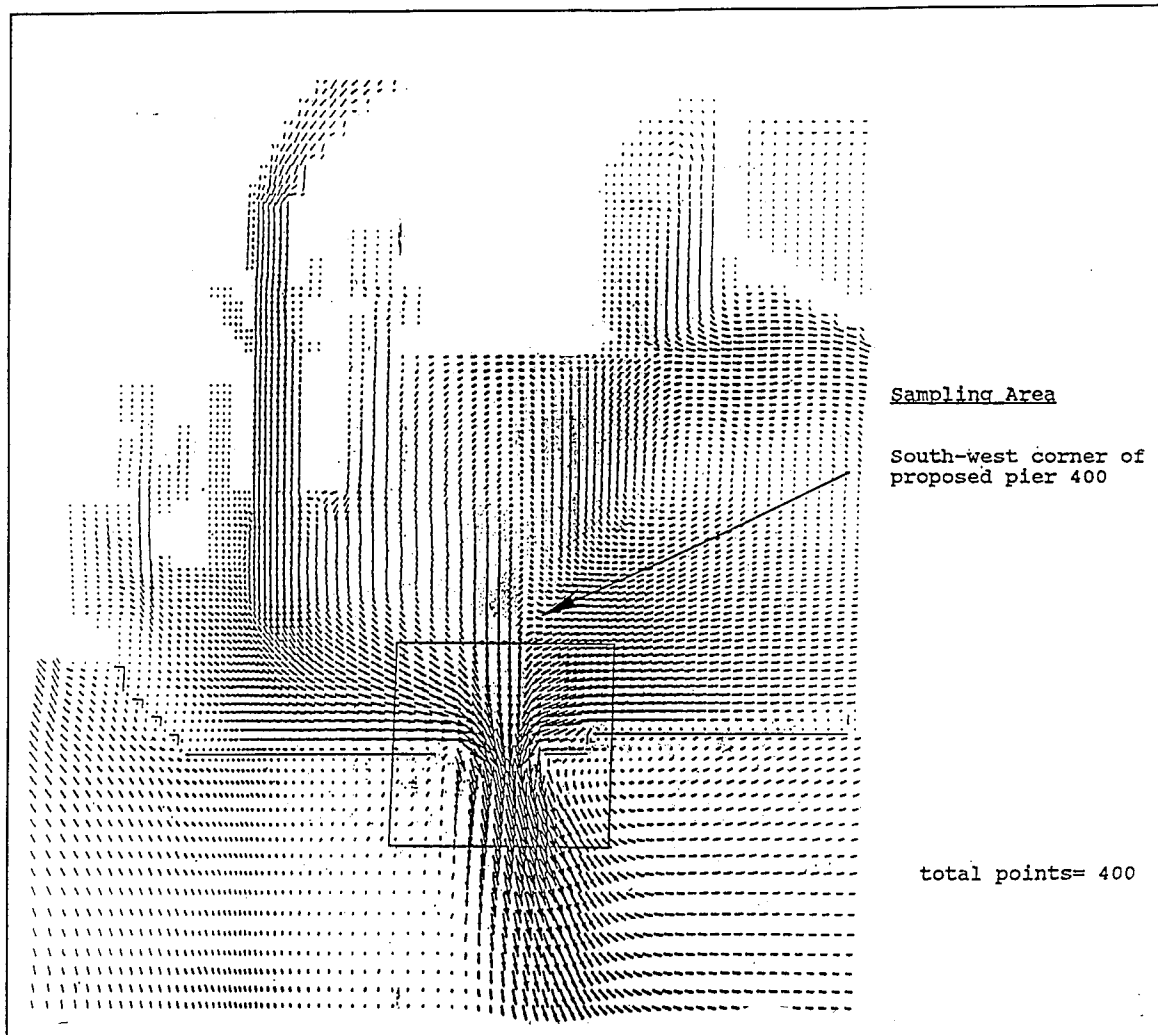
Figure 45. Enclosed area for statistical analysis. Total of 400 grid points

Figure 46. The statistical distribution of current velocity response to WSW
wind, 20 knots

Velocity Near Angel's Gate Breakwater

Note: Southeast Wind 20 knots; Surface Layer; Maximum Flood Current
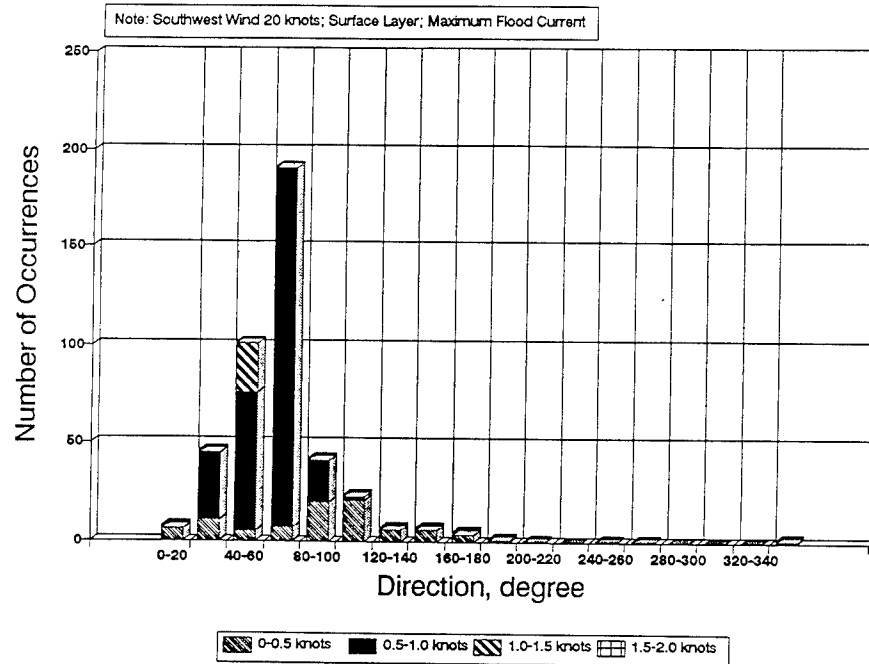
a. Maximum flood current

Velocity Near Angel's Gate Breakwater

Note: Southeast Wind 20 knots; Surface Layer; Maximum Ebb Current
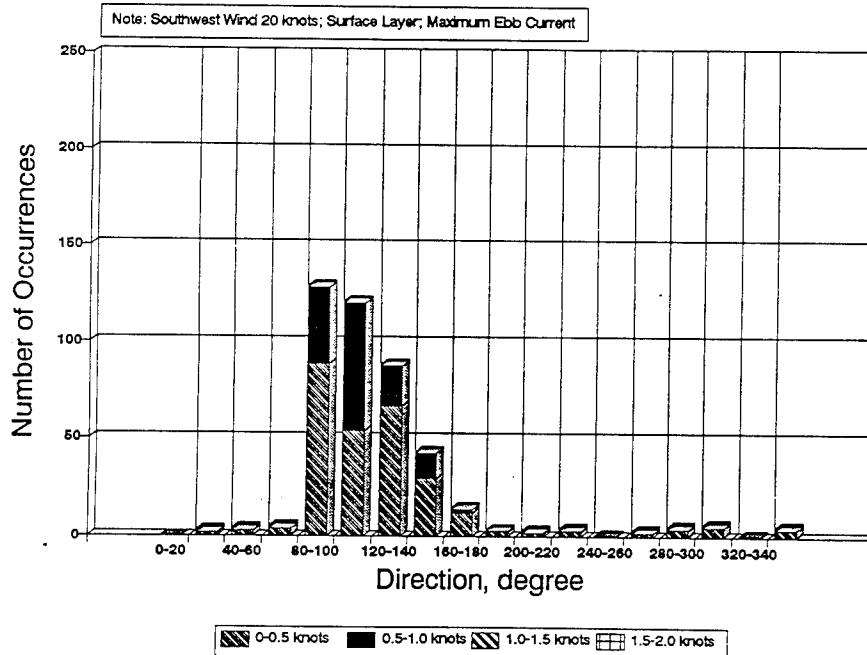
b. Maximum ebb current
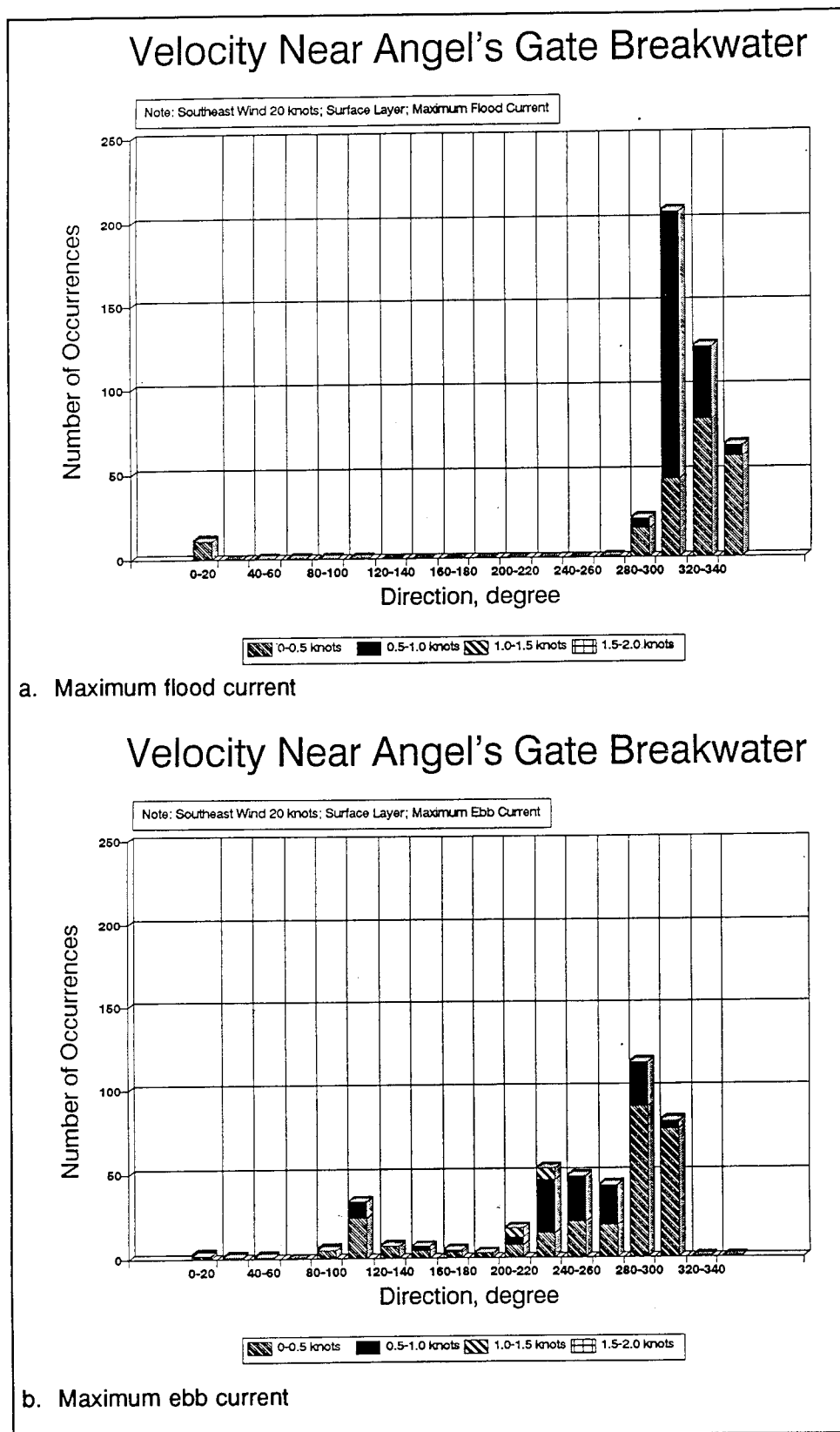
Figure 47. The statistical distribution of current velocity response to SE wind, 20 knots
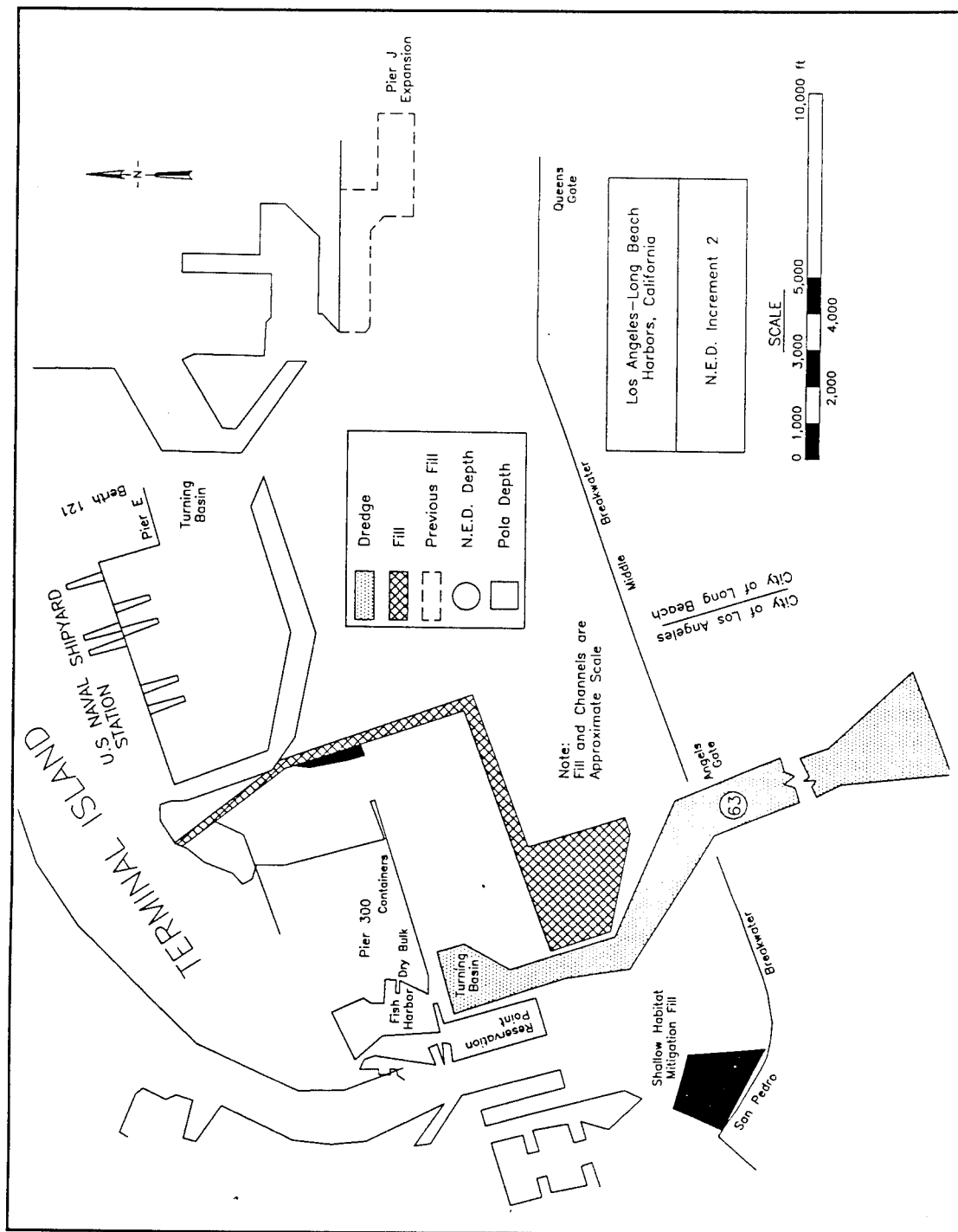
Figure 48. National Economic Development Plan, Increment 2 (NED2)

Chapter 5   Scenario Description and Results in Support of Ship Simulation Study
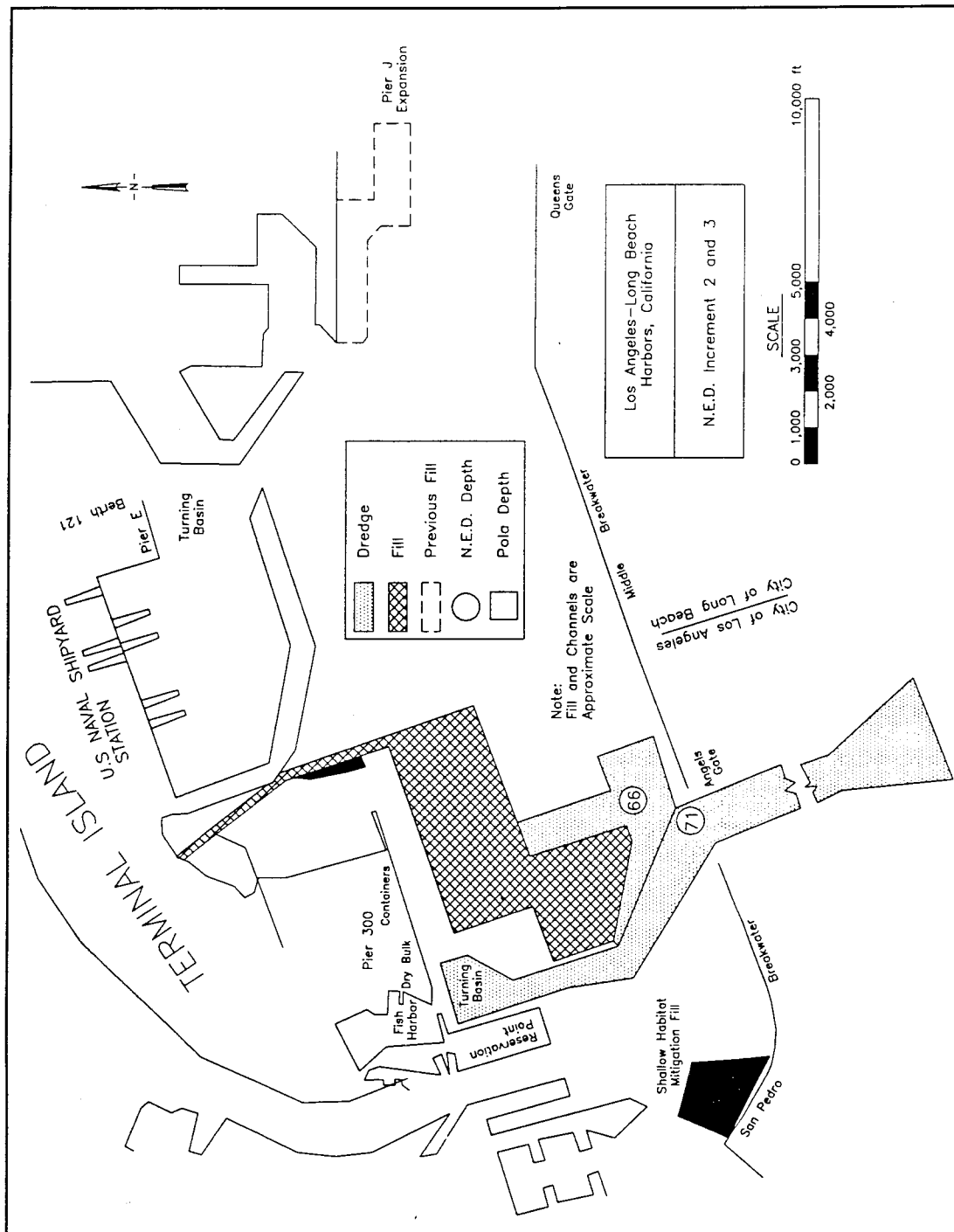
Figure 49. National Economic Development Plan, Increments 2 and 3
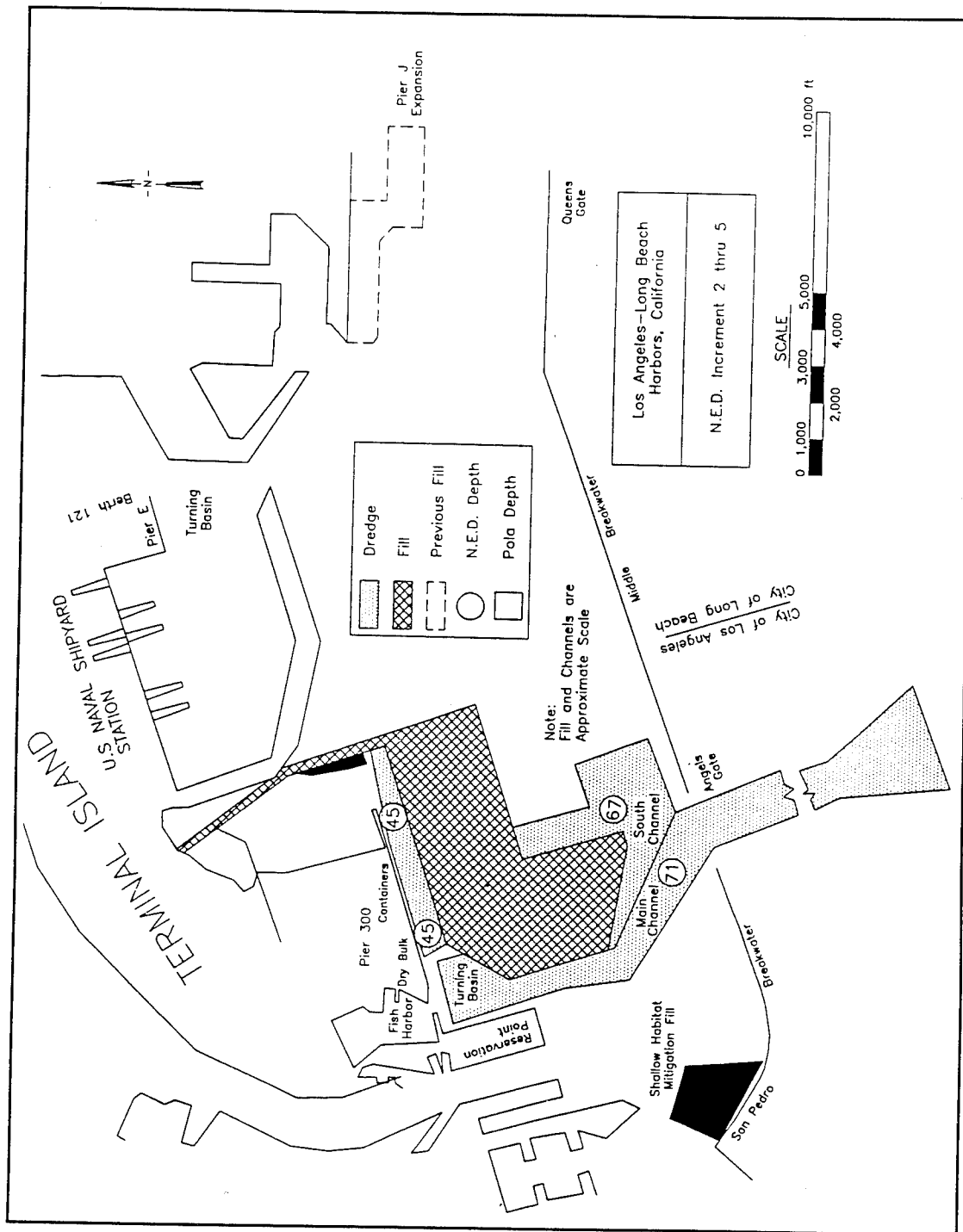
Figure 50. National Economic Development Plan, Increments 2 through 5

Chapter 5   Scenario Description and Results in Support of Ship Simulation Study

LALB_BASE

a. Wind speed

LALB_BASE
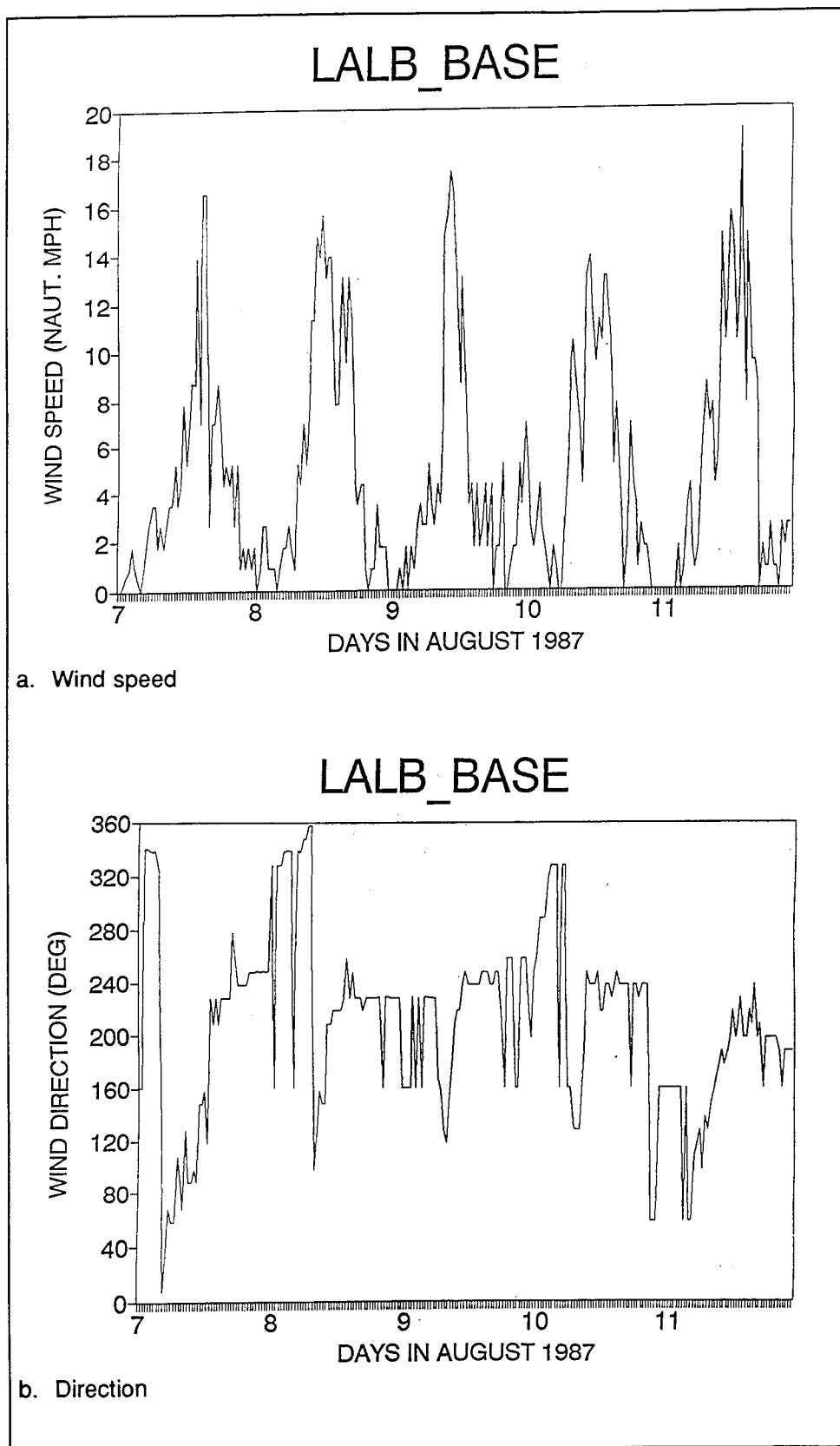
b. Direction

Figure 51. Wind speed (a) and direction (b) for the base wind condition
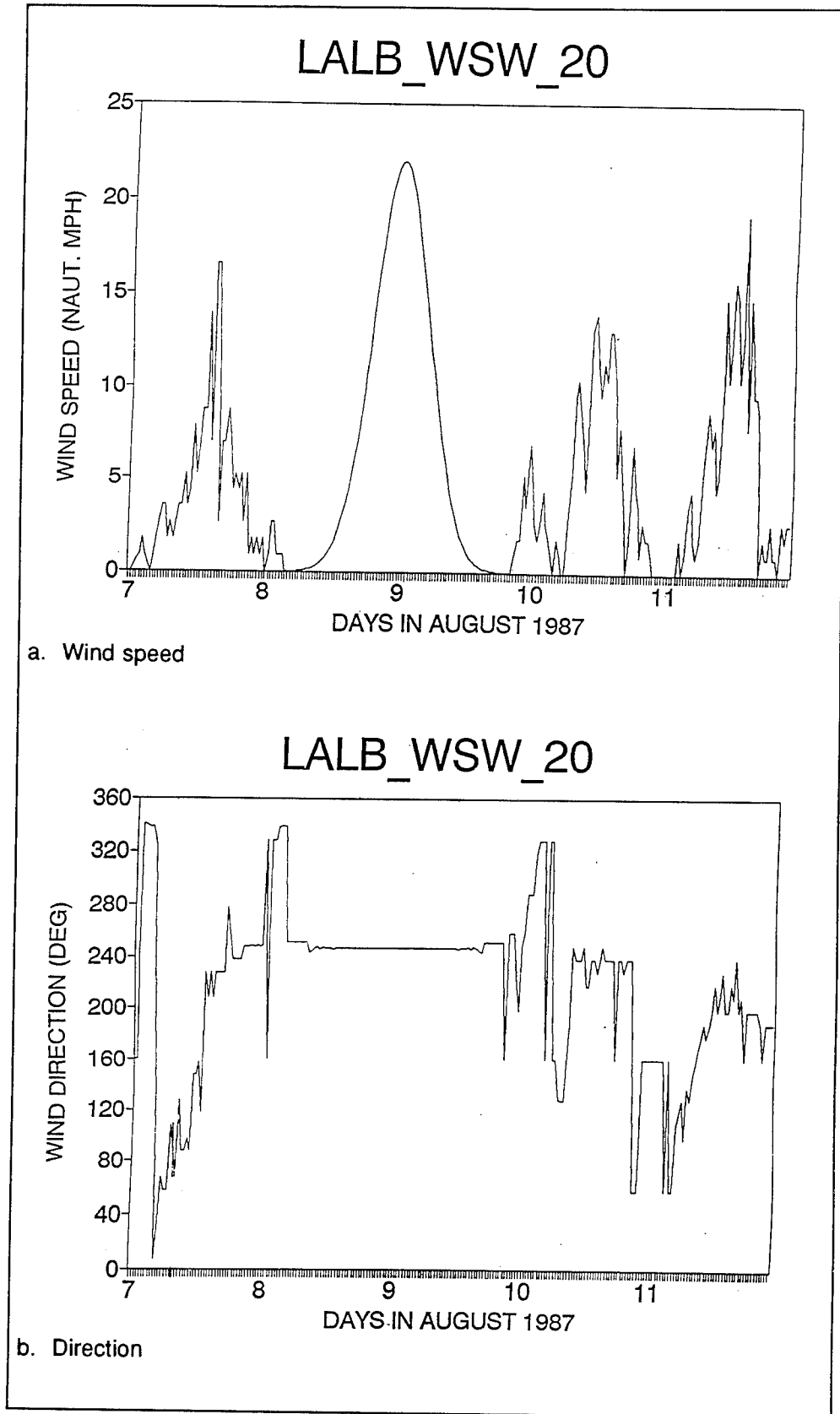
Figure 52. Wind speed and direction for winds WSW, 20 knots

LALB_SE_20

a. Wind speed

LALB_SE_20
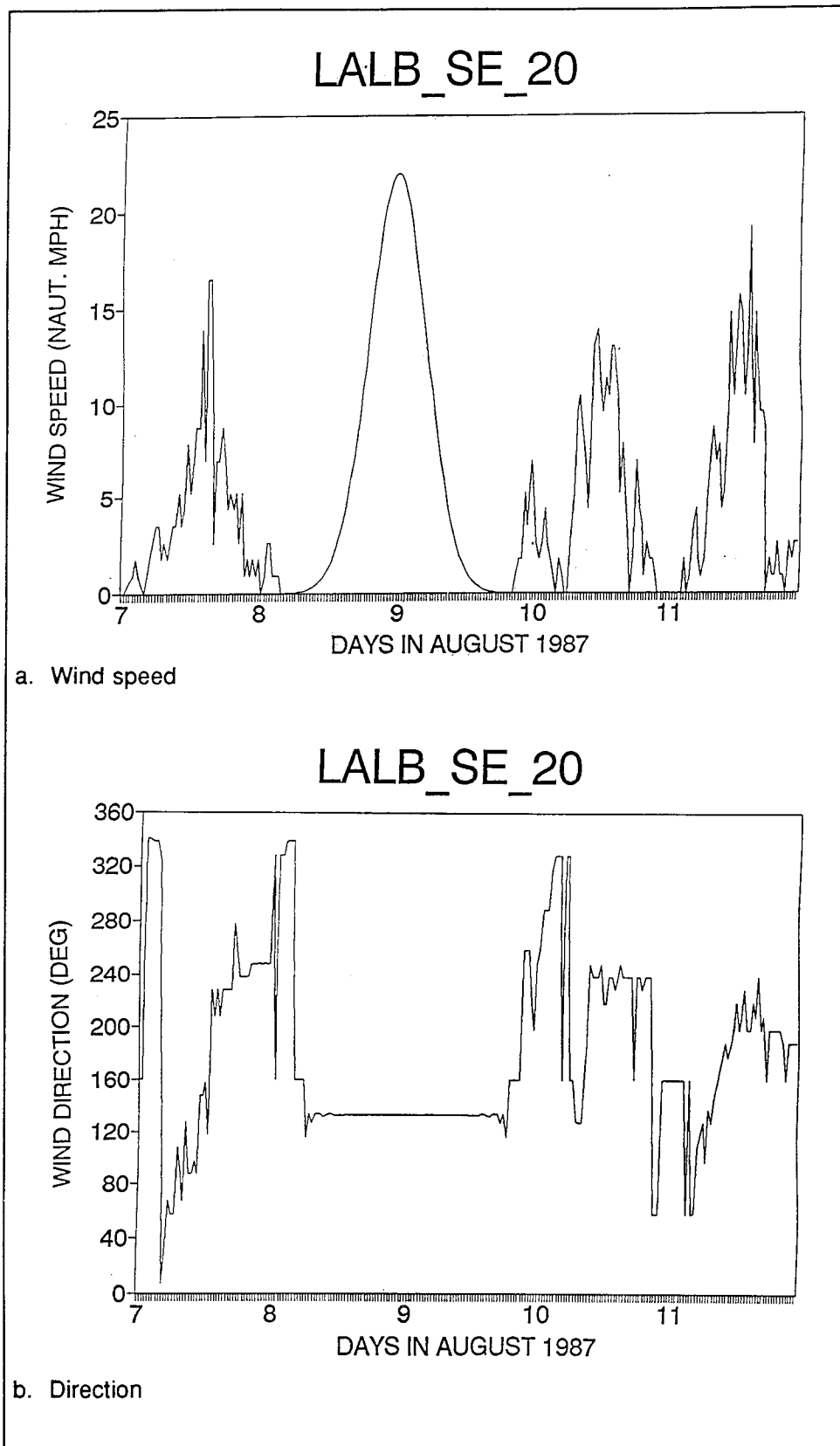
b. Direction

Figure 53. Wind speed and direction for winds SE, 20 knots
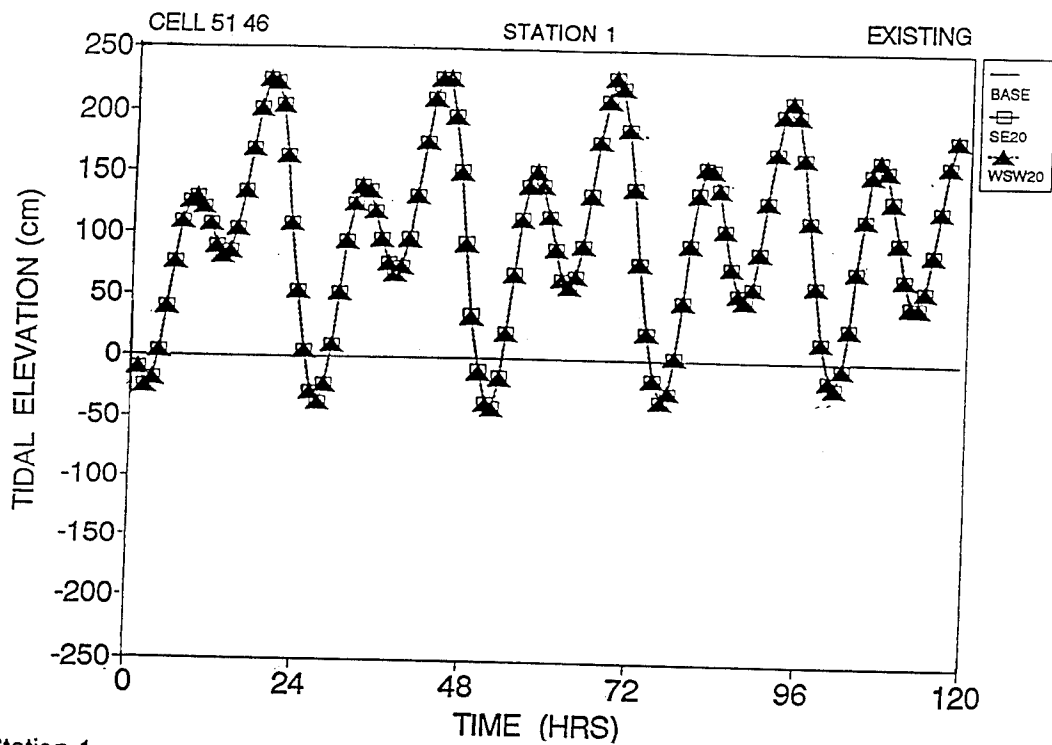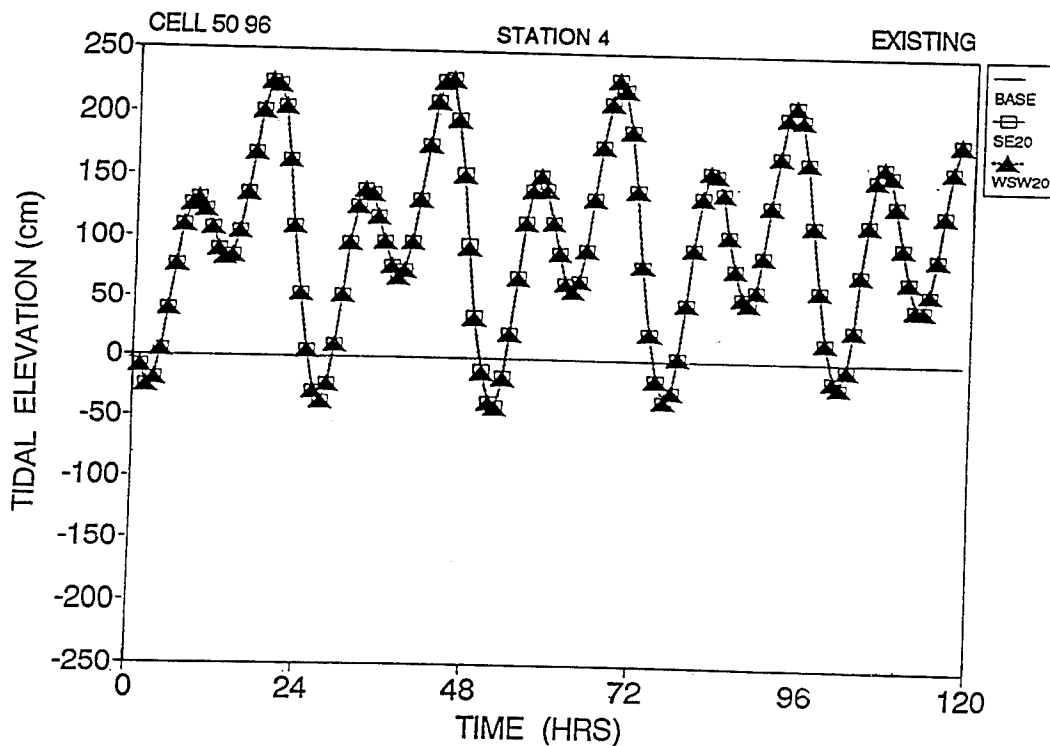
Figure 54. Water surface elevation response to wind at stations 1 and 4 in the harbor under existing conditions

6   Summary and Conclusions

A numerical model of the hydrodynamics of Los Angeles Harbor has been developed and tested against field measurements, to provide a means for predicting the impact of proposed navigation improvements and landfill under natural forcing conditions including astronomical tide and meteorological wind stress. Based on the results presented in Chapters 2 through 5, a number of conclusions regarding the performance of the numerical model can be drawn, such as the degree to which it matches field observations, and its ability to predict the hydrodynamic condition in support of the water quality model and ship simulation model under various proposed plans and wind conditions. Conclusions have been grouped according to the subject treated in each chapter.

Computational Grid

A boundary-fitted coordinate was used to generate a variable, rectilinear computational grid, which provides enhancement for fitting the complex harbor planform by locally increasing the resolution. In the vertical, a sigma stretched coordinate was used, which allowed the grid to smoothly vary with changes in topography.

For hydrodynamic modeling in support of the water quality model, a grid of 128 by 94 cells was used in the Los Angeles and Long Beach Harbor, with the finest resolution measuring 235 ft near to the main ship channel. The grid extended seaward of the middle breakwater approximately 4.2 miles, which provides a coupling of the harbor-bay system between Los Angeles Harbor and the adjacent San Pedro Bay. Five vertical layers were used in order to provide sufficient vertical resolution for the water quality model, which is critical for assessing bottom dissolved oxygen and benthic processes.

A grid system with twice the resolution was generated to fulfill the requirements of the ship simulation model. Additional comparisons were made between the calibrated coarse grid and the fine grid to ensure the model performed properly. Based on a 5-day simulation, the comparison was very good. In fact, the fine grid simulation reveals additional velocity structure in detail, which was not seen in a coarse grid result.

Performance of the Numerical Model

The numerical model has been extensively calibrated in the previous study (Vemulakondo, Chou, and Hall 1991). In the present effort, additional calibration and validation were performed as a parallel effort to ensure the model functioned correctly after changes were made in the harbor. A 5-day calibration, using two current meter stations and one tidal station, was conducted. The comparison shows that agreement between model prediction and observed data, including tidal elevation and velocity, is very good. After the calibration, the best fit of the parameters was found to be as follows:

Manning coefficient $n = 0.035\text{-}0.040$

Horizontal mixing coefficient $A_H = 1000 \text{ cm}^2/\text{sec}$

Base vertical mixing coefficient $A_V = 10 \text{ cm}^2/\text{sec}$

Wind drag coefficient $C = (0.075 + 0.67 \text{ W}) \text{x } 10^{-3}$, where W is wind speed in m/sec

During validation, comparison of model calculations with measured field data reinforced the conclusion drawn from calibration comparisons, and in addition, highlighted the importance of the wind-driven circulation. A comparison between the numerical model and physical model was also conducted to verify the spatial variability resulting from the interaction of tidal flow with the narrow entrance. The model accurately predicted jet recirculation in the harbor.

Hydrodynamic Results Supporting the Water Quality Model

The main objective of the hydrodynamic study in support of WQM was to assess the impact of landfill and deepening of the channel on existing harbor conditions. Scenarios were conducted for POLA 1 and POLA 2, with the following results:

a. Water surface elevation was not affected by either deepening of the channel or construction of Pier 400.

b. The existing flow condition in the harbor is characterized by a free-flowing jet and associated features such as recirculation in the flood tide and a potential flow in the ebb. When Pier 400 was introduced in the harbor, it blocked the free-flowing jet and forced the flow to go around and conform to the shape of the structure.

c.   Current magnitude generally decreases from the entrance toward the harbor. Wind not only increased the current velocity in proportion to its speed, but also generated a mean drift motion toward the direction it traveled. Nevertheless, except under extreme high wind, current velocities were generally under 1 knot.

d.   Flow in Seaplane Lagoon has magnitude on the order of 0.5 - 1.5 cm/s. Velocity in the east basin between the causeway and the Navy mole is between 1.0 - 2.0 cm/s. These velocities are all small in magnitude. By introducing the conservative tracer into Seaplane Lagoon and recording the concentration history, it was found that the removal of a portion of the breakwater had a significant impact on the flushing rate. Local velocity at the opening of the causeway averaged 2 cm/s. When the causeway was opened, it only slightly increased the flushing rate in Seaplane Lagoon.

Hydrodynamic Results Supporting Ship Simulation

Conditions selected for ship simulation studies were considered to be near the maximum for which channel navigation should be attempted. These conditions can be the combination effect of (a) harbor configuration, and (b) natural forcing including tide and wind. Under a 20-knot wind, total current velocity can reach between 1.0 and 1.5 knots. Sensitivity tests were conducted using wind speeds of 20 and 30 knots combined with wind direction from the west, southwest, and southeast to test its effect on current velocity. It was found that near the entrance of the breakwater, directions of the current velocity were more concentrated during flood than during ebb. A west wind has the effect of reinforcing the flood tide, while a southeast wind has the effect of reinforcing ebb tide. Based on historical data, BW, WSW20, and SE20 winds were chosen along with five plans; i.e., POLA 1, POLA 2, NED 2, NED 2&3, and NED 2-5 for the scenario runs. Findings are as follows:

a.   For all five plans, the presence of Pier 400 and the causeway has a blocking effect on the velocity field, which makes the flow conform to the shape of the local structure and go around it.

b.   For POLA 2, due to its deeper dredged ship channel, changes from the existing condition are smaller compared to those of POLA 1. The only exception is at station 4, where the velocity for POLA 1 is comparable to POLA 2. Comparisons between NED 2 and NED 2&3 show that at most of the stations, the u velocity for NED 2 has a slightly larger magnitude than NED 2&3. Comparisons between NED 2-5 and NED 2&3 show that for most of the stations, the velocity for NED 2-5 has a phase lag of 5 min behind that of NED 2&3. The only exception is at station 4, where u velocity of NED 2-5 is almost identical to that of NED 2.

c.   Under critical wind conditions, the wind can induce additional velocity
     fluctuation to the variation already created by the harbor configuration.
     In the scenario runs under the influence of WSW20 and SE20, wind-
     induced velocity could be as large as its tidal velocity and in some
     cases, even change the phase of the background velocity. The general
     tendency of the wind's effect is to drive the water into its prevailing
     wind direction. This effect is particularly pronounced when the created
     harbor structure makes a narrow constriction such as in the area
     between Pier 400 and the middle breakwater, and the area between
     Pier 400 and Pier 300. In this case, a mean drift velocity is likely to be
     generated.

References

Donaldson, C. dup. (1973). "Atmospheric turbulence and the dispersal of atmospheric pollutants." *Workshop on micrometeorology*. D. A. Haugen, ed., American Meteorological Society, Science Press, Boston, 313-90.

Dortch, M. S. (1990). "Three-dimensional, Lagrangian residual transport computed from an intratidal hydrodynamic model," Technical Report EL-90-11, U.S. Army Engineer Waterways Experiment Station, Vicksburg, MS.

Edinger, J. E., Brady, D. K., and Geyer, J. C. (1974). "Heat exchange and transport in the environment," Report 14, EPRI Publication No. 74-049-00-3, prepared for Electric Power Research Institute, Palo Alto, CA.

Garratt, J. R. (1977). "Review of drag coefficients over oceans and continents," *Monthly Weather Review* 105, 915-29.

Hall, R. W. "Numerical water quality model study for the Pier 400 project," in preparation, U.S. Army Engineer Waterways Experiment Station, Vicksburg, MS.

Hewlett, J. C. "Ship navigation simulation study, Los Angeles Harbor, Los Angeles, California," in preparation, U.S. Army Engineer Waterways Experiment Station, Vicksburg, MS.

Johnson, B. H. (1980). "VAHM - A vertically averaged hydrodynamic model using boundary-fitted coordinates," Miscellaneous Paper HL-80-3, U.S. Army Engineer Waterways Experiment Station, Vicksburg, MS.

Johnson, B. H., Kim, K. W., Heath, R. E., and Butler, H. L. (1991). "User's guide for the Chesapeake Bay three-dimensional numerical hydrodynamic model," Technical Report HL-91-1, U.S. Army Engineer Waterways Experiment Station, Vicksburg, MS.

Leonard, B. P. (1979). "A stable and accurate convective modeling procedure based on upstream interpolation," *Computer Methods in Applied Mechanics and Engineering*, 19, 59-98.

Lewellen, W. S. (1977). "Use of invariant modeling." *Handbook of turbulence.* W. Frost, ed., Plenum Press, New York, 1, 237-80.

McAnally, W. H., Jr. (1975). "Los Angeles and Long Beach Harbors model study; Report 5: Tidal verification and base circulation tests," Technical Report H-75-4, U.S. Army Engineer Waterways Experiment Station, Vicksburg, MS.

McGehee, D. D., McKinney, J. P., and Dickey, M. S. (1989). "Los Angeles and Long Beach Harbors model enhancement program -- tidal circulation prototype data collection effort," U.S. Army Engineer Waterways Experiment Station, Vicksburg, MS.

Outlaw, D. G., and Raney, D. C. (1979). "Numerical analysis of tidal circulation for Long Beach Outer Harbor proposed landfill," Miscellaneous Paper H-79-5, U.S. Army Engineer Waterways Experiment Station, Vicksburg, MS.

Raney, D. C. (1976). "Numerical analysis of tidal circulation for Long Beach Harbor; Report 1: Existing conditions and alternate plans for Pier J completion and tanker terminal study," Miscellaneous Paper H-76-4, U.S. Army Engineer Waterways Experiment Station, Vicksburg, MS.

Seabergh, W. C., and Outlaw, D. G. (1984). "Los Angeles and Long Beach Harbors model study: Numerical analysis of tidal circulation for the 2020 master plan," Miscellaneous Paper CERC-84-5, U.S. Army Engineer Waterways Experiment Station, Vicksburg, MS.

Seabergh, W C., Vemulakonda, S. R., Chou, L. W., and Mark, D. J. (1994). "Los Angleles and Long Beach Harbors, model enhancement program, effect of wind on circulation in Los Angeles-Long Beach Harbors," Techical Report CERC-94-7, U.S. Army Engineer Waterways Experiment Station, Vicksburg, MS.

Sheng, Y. P. (1982). "Hydraulic applications of a second-order closure model of turbulent transport." *Applying Research to Hydraulic Practice.* P. Smith, ed., American Society of Civil Engineers, New York, 106-19.

_____. (1986). "A three-dimensional mathematical model of coastal, estuarine and lake currents using boundary fitted grid," Report N. 585, A.R.A.P Group of Titan Systems, New Jersey, Princeton, NJ.

_____. (1990). "A simplified second order closure model of turbulent transport," Unpublished paper prepared for U.S. Army Engineer Waterways Experiment Station, Vicksburg, MS.

Smith, E. R. (1989). "Los Angeles and Long Beach Harbor Model Enhancement Program: Current, tide and wind data summary for 1983, "Miscellaneous Paper CERC-89-4, U.S. Army Engineer Waterways Experiment Station, Vicksburg, MS.

Vemulakonda, S. R. (1990). "Los Angeles and Long Beach Harbors Model Enhancement Program: Three-dimensional numerical model testing of tidal circulation," Technical Report CERC-90-16, U.S. Army Engineer Waterways Experiment Station, Vicksburg, MS.

Vemulakonda, S. R., Chou, L. W., and Hall, R. W. (1991). "Los Angeles and Long Beach Harbors additional plan testing: Numerical modeling of tidal circulation and water quality," Technical Report CERC-91-2, U.S. Army Engineer Waterways Experiment Station, Vicksburg, MS.

Appendix A
Velocity Vector Plots in Support of the Water Quality Model

a. at maximum flood current

b. at maximum ebb current
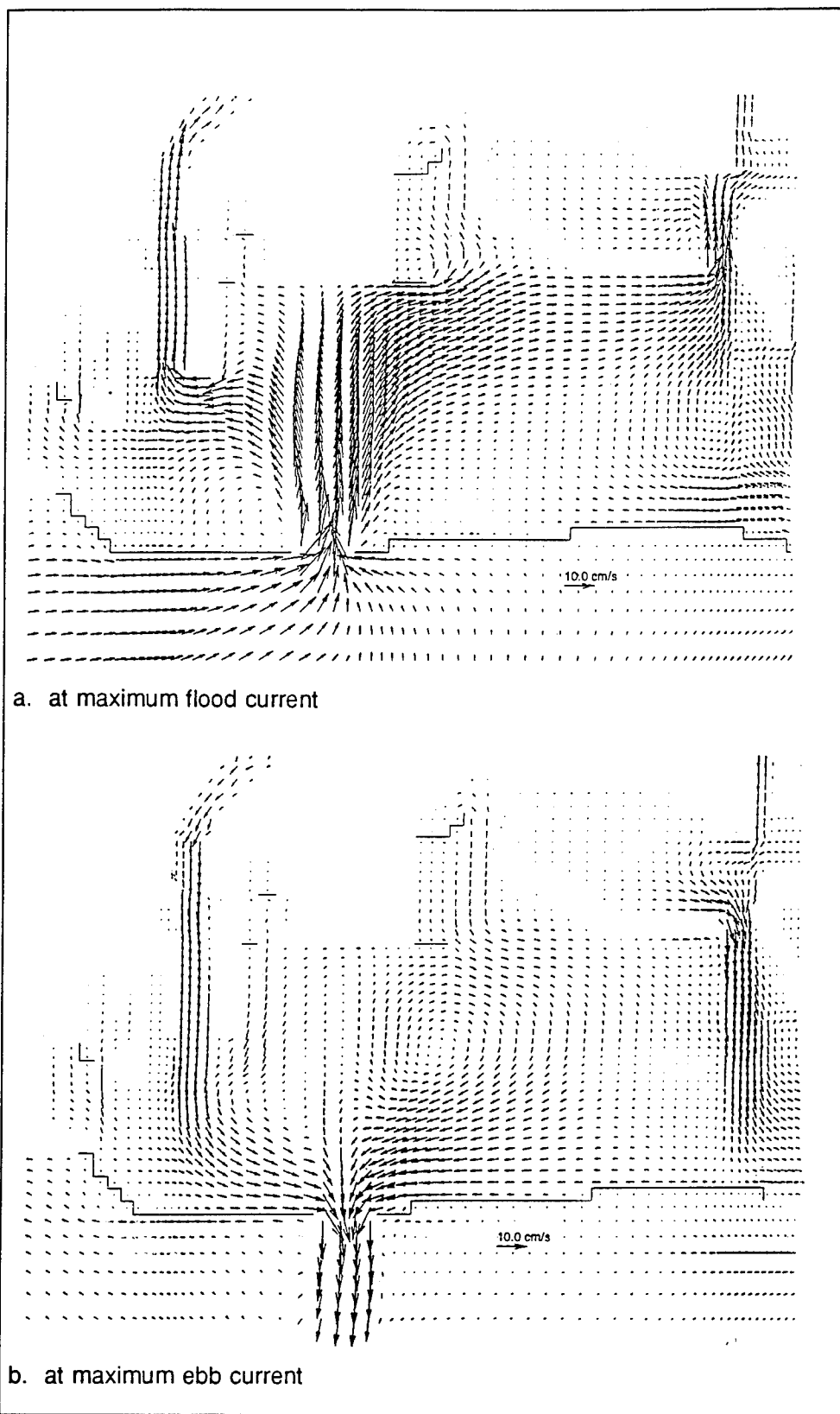
Figure A1. Surface layer circulation of existing condition

a. at maximum flood current

b. at maximum ebb current
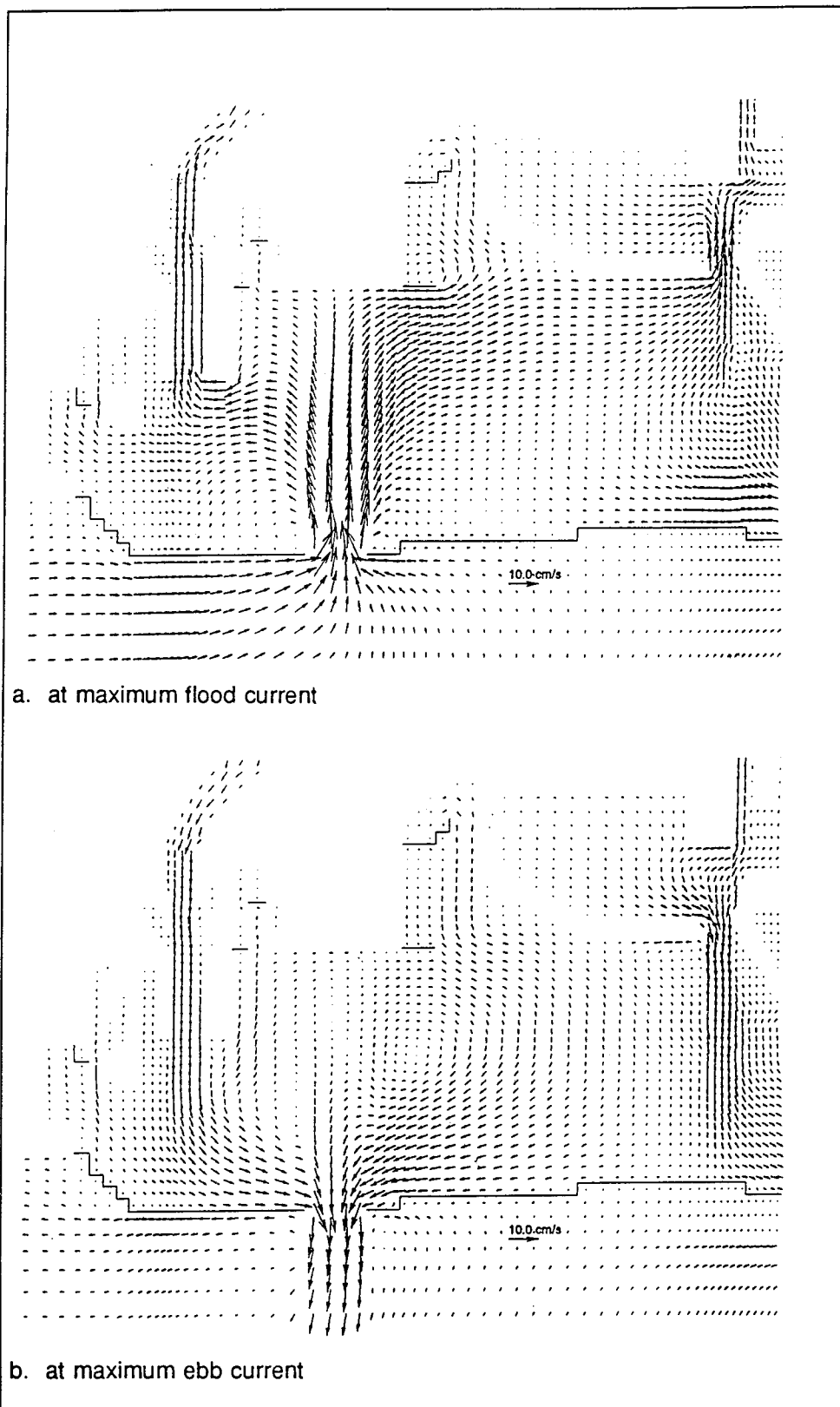
Figure A2. Bottom layer circulation of existing condition

a. at maximum flood current

b. at maximum ebb current
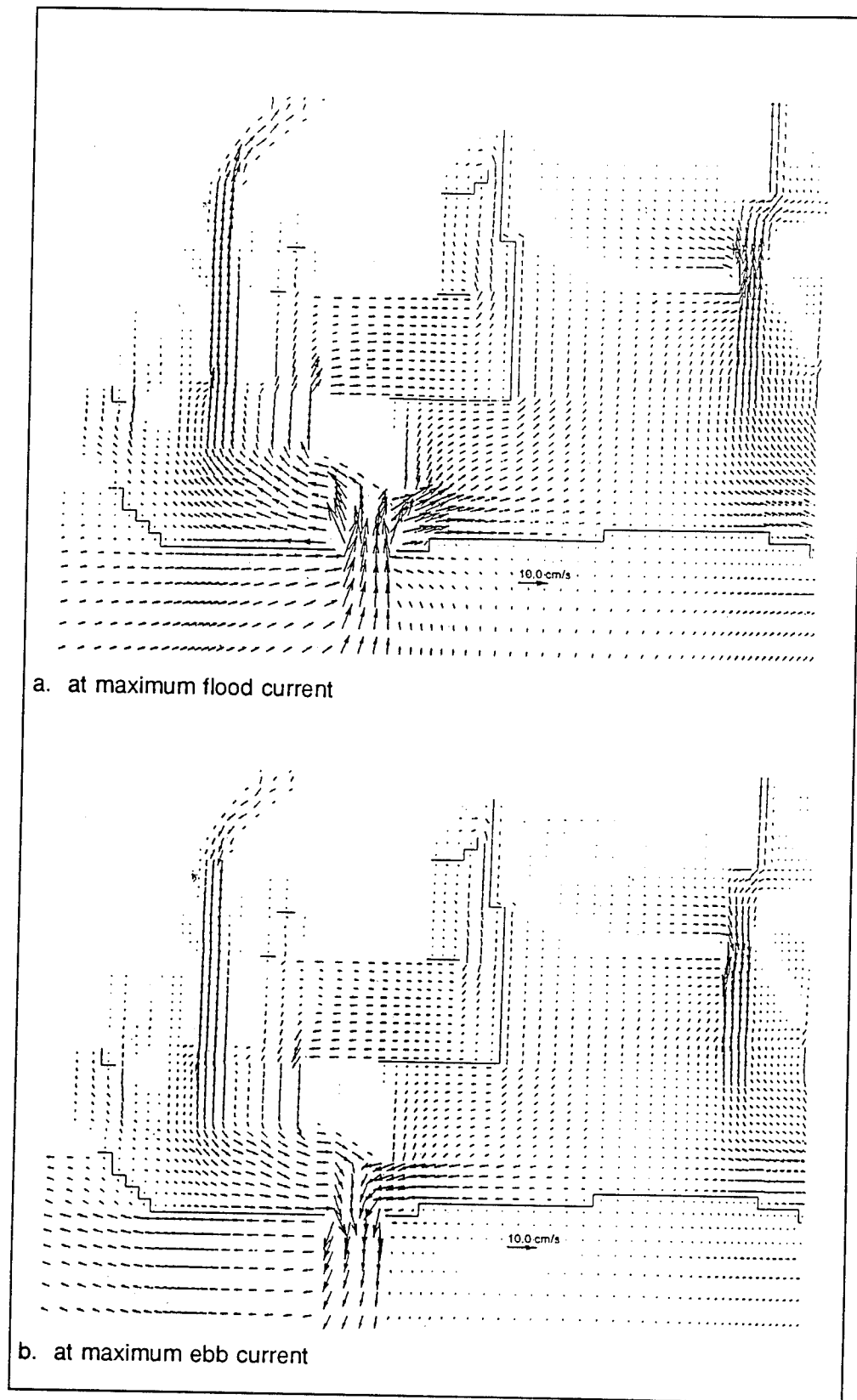
Figure A3. Surface layer circulation for POLA 1

a. at maximum flood current

b. at maximum ebb current
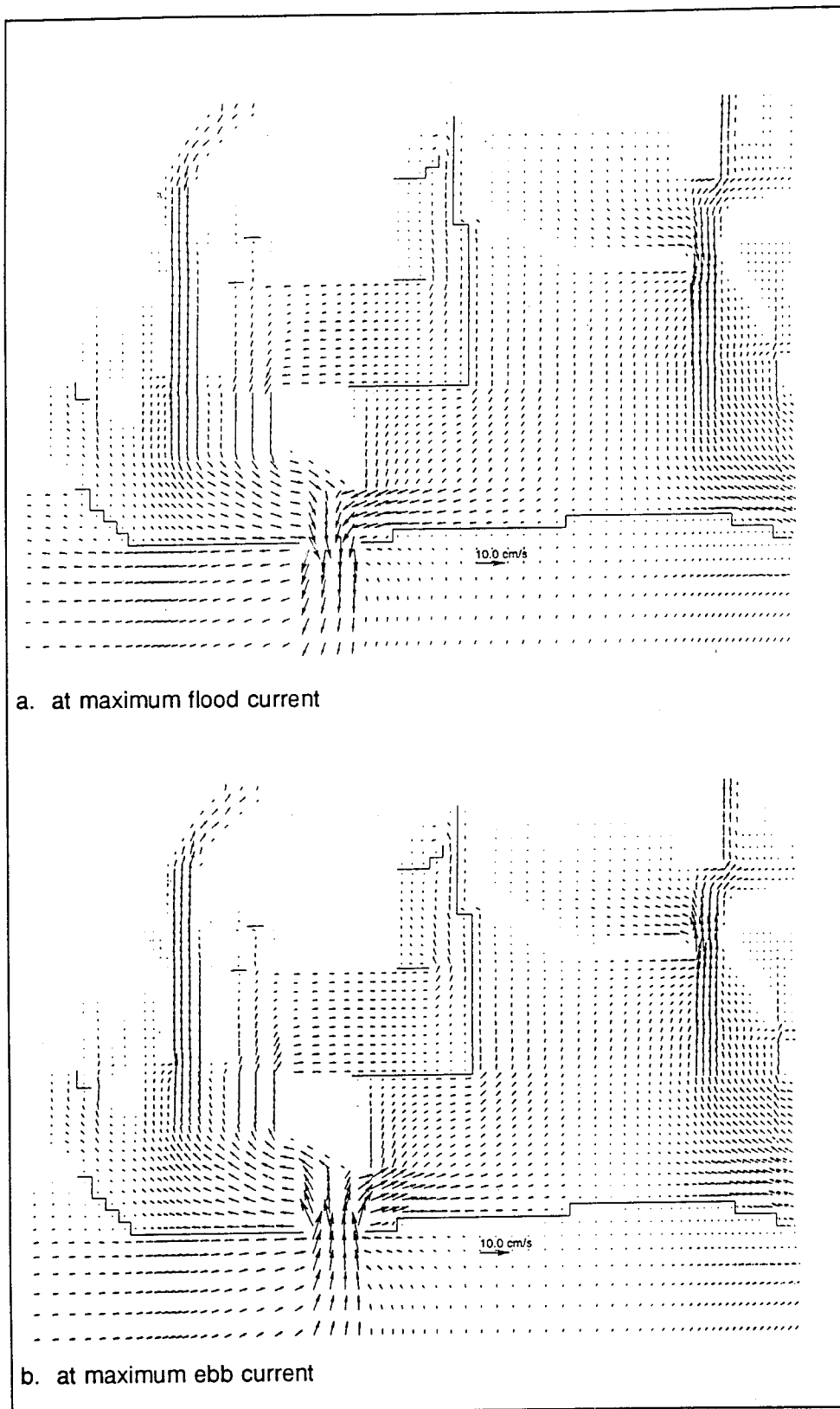
Figure A4. Bottom layer circulation for POLA 1

a. at maximum flood current

b. at maximum ebb current
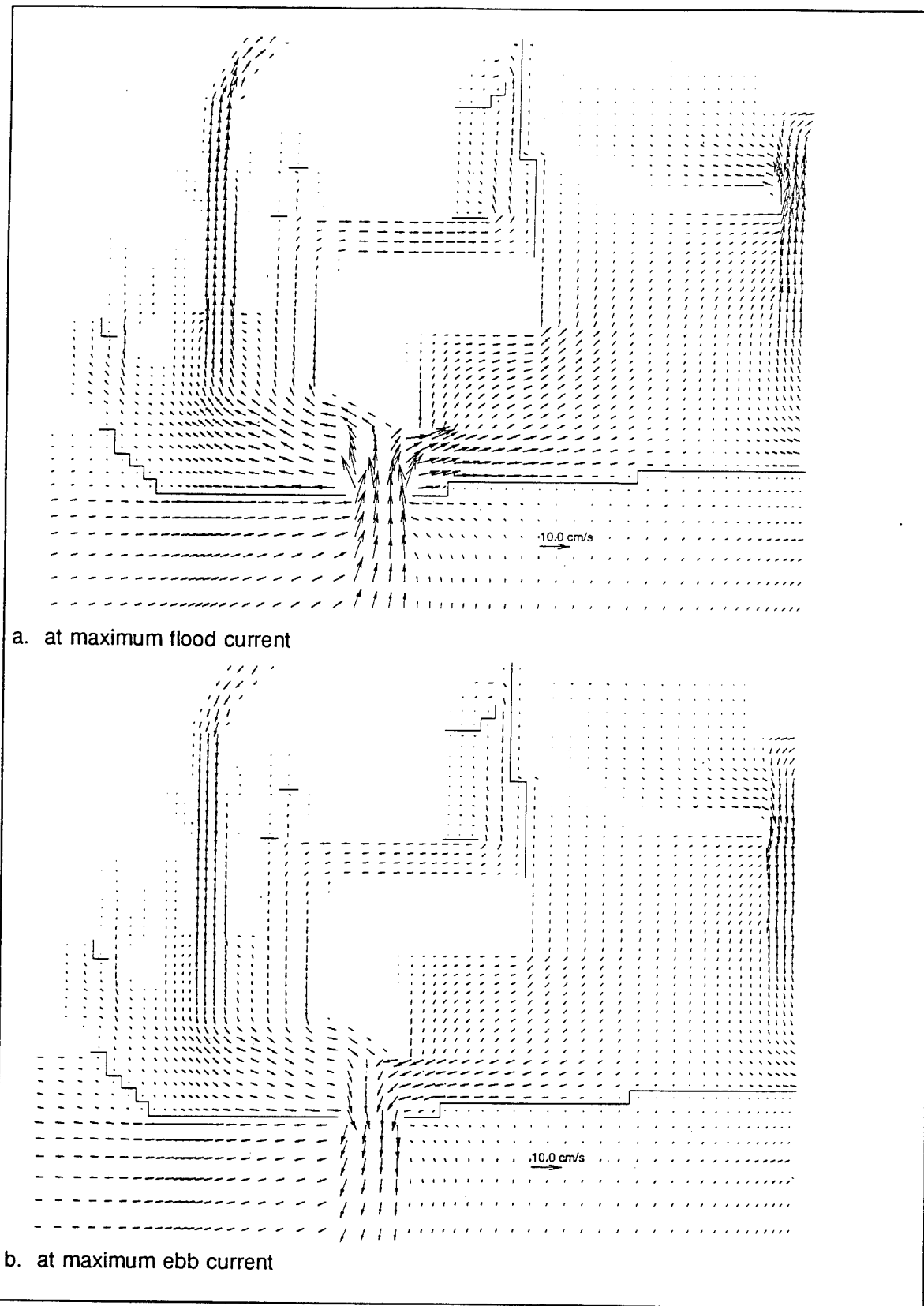
Figure A5. Surface layer circulation for POLA 2

a. at maximum flood current

b. at maximum ebb current
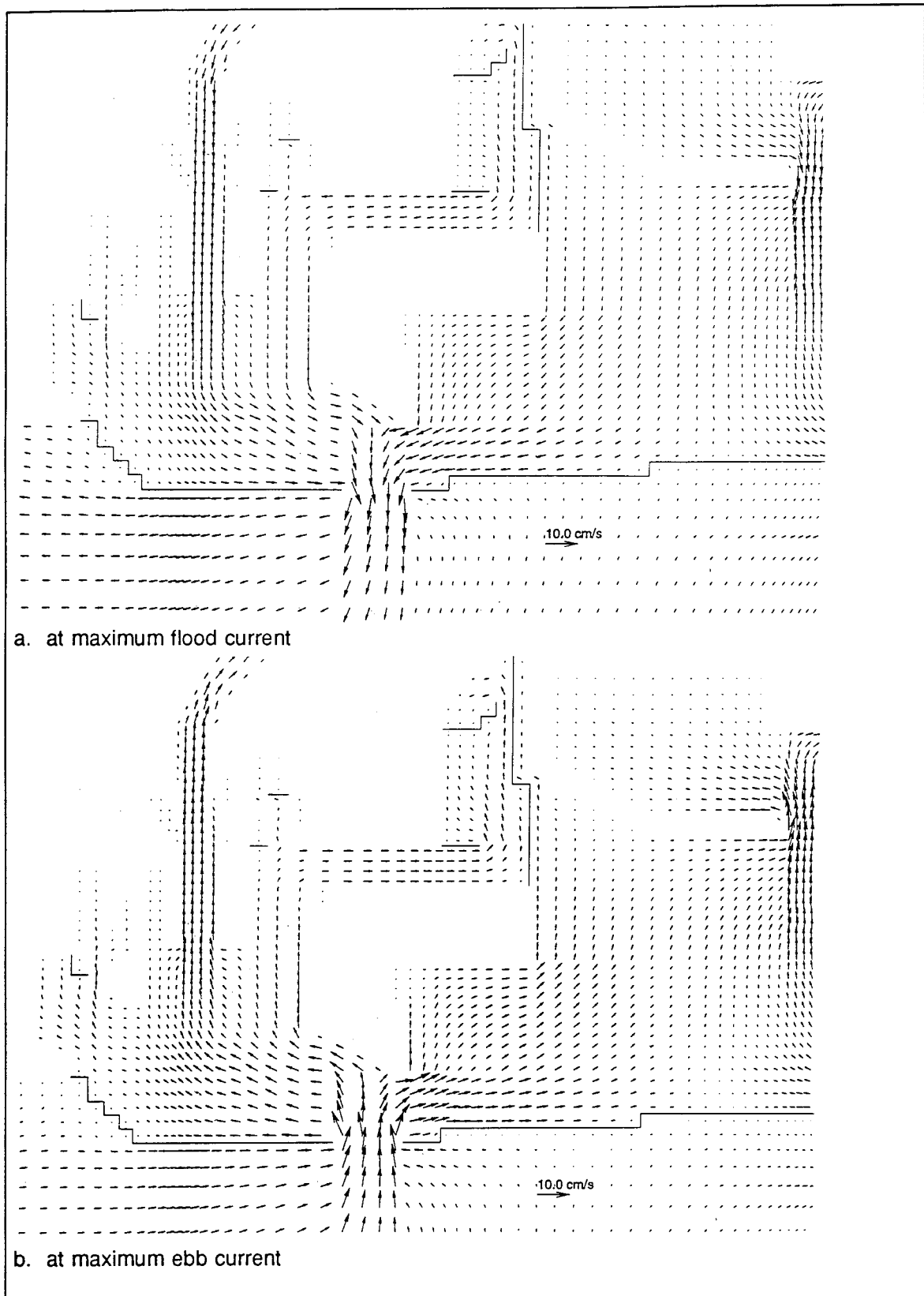
Figure A6. Bottom layer circulation for POLA 2

Appendix B
Time Series Plots in Support of the Water Quality Model

STATION 1 (24,23) — **SURFACE** — EXISTING

U VELOCITY (cm/sec) vs DAYS IN JULY AND AUGUST, 1987

a.

STATION 1 (24,23) — **SURFACE** — EXISTING

V VELOCITY (cm/sec) vs DAYS IN JULY AND AUGUST, 1987

b.
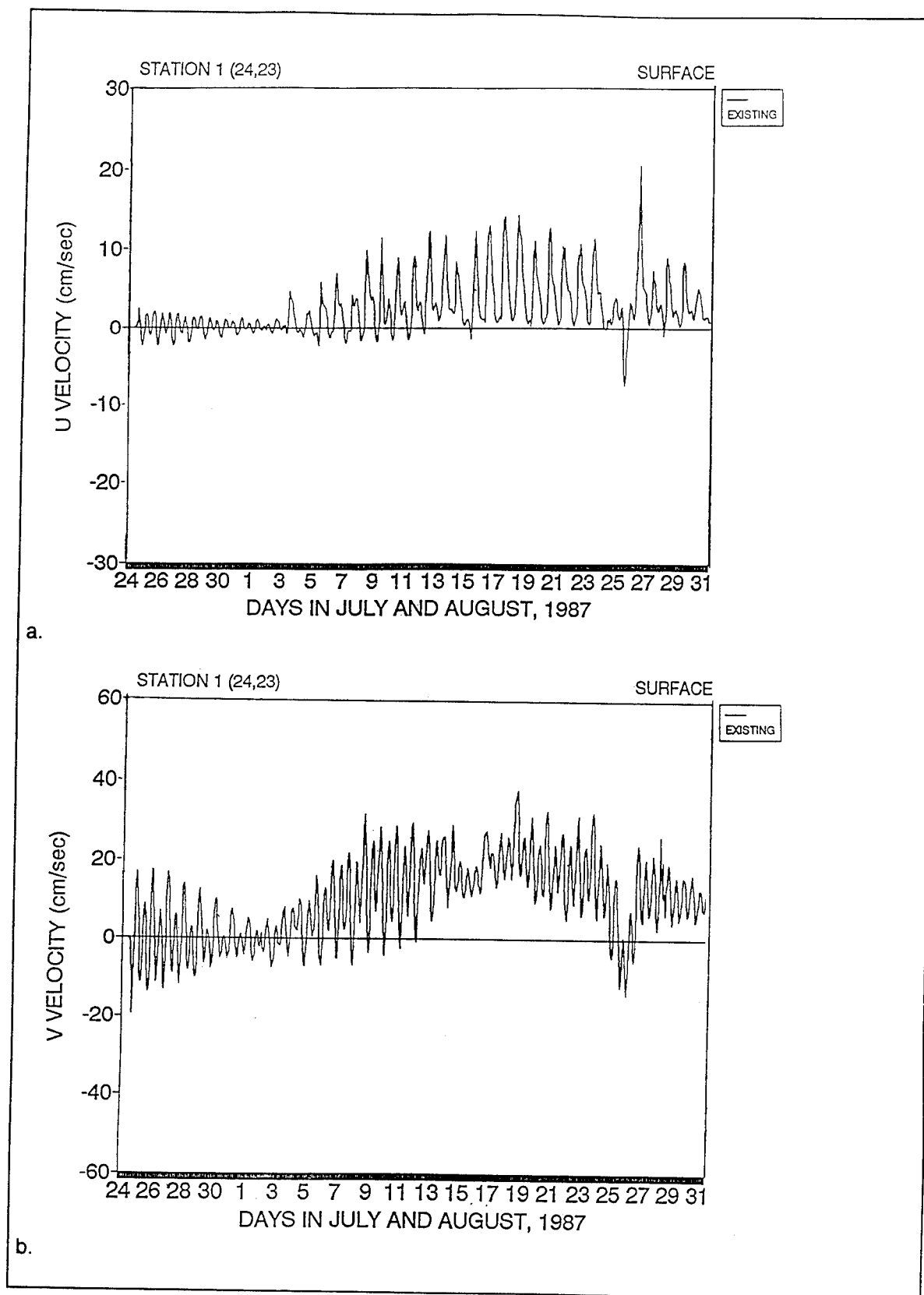
Figure B1. Time series of current velocity for the existing condition at station 1

a.

b.
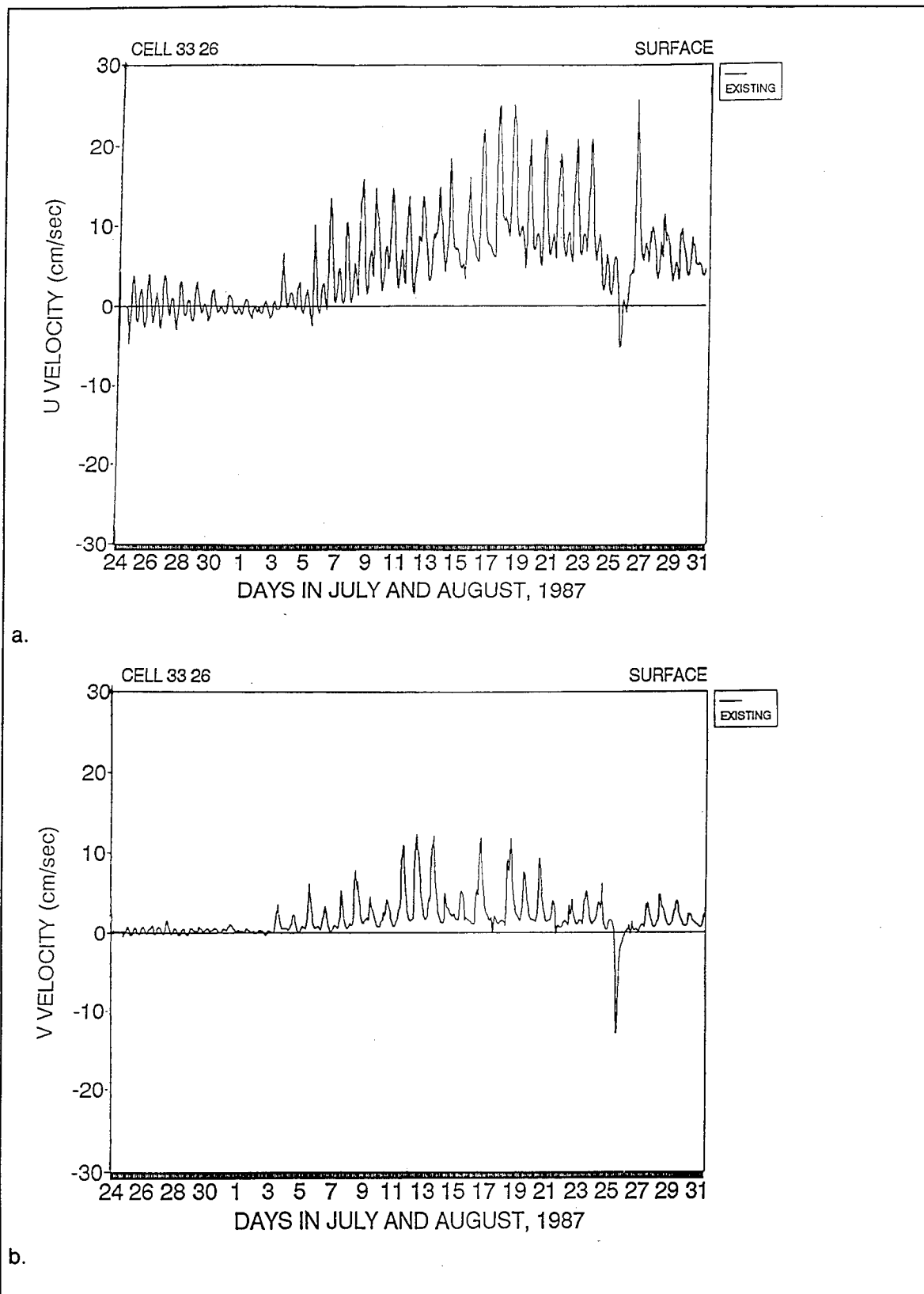
Figure B2. Time series of current velocity for the existing condition at station 2
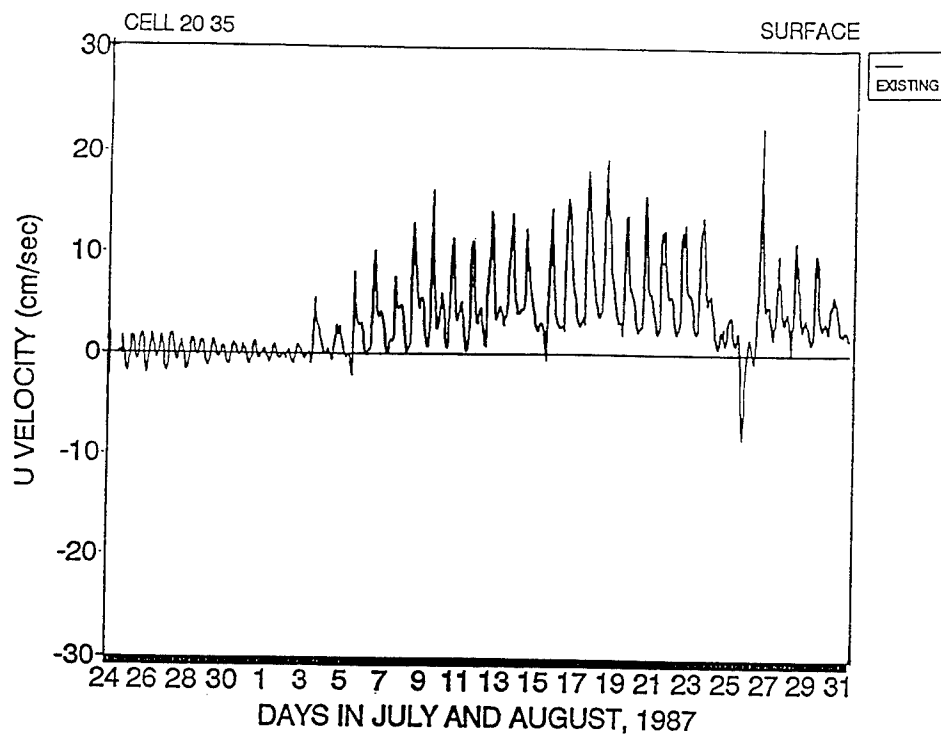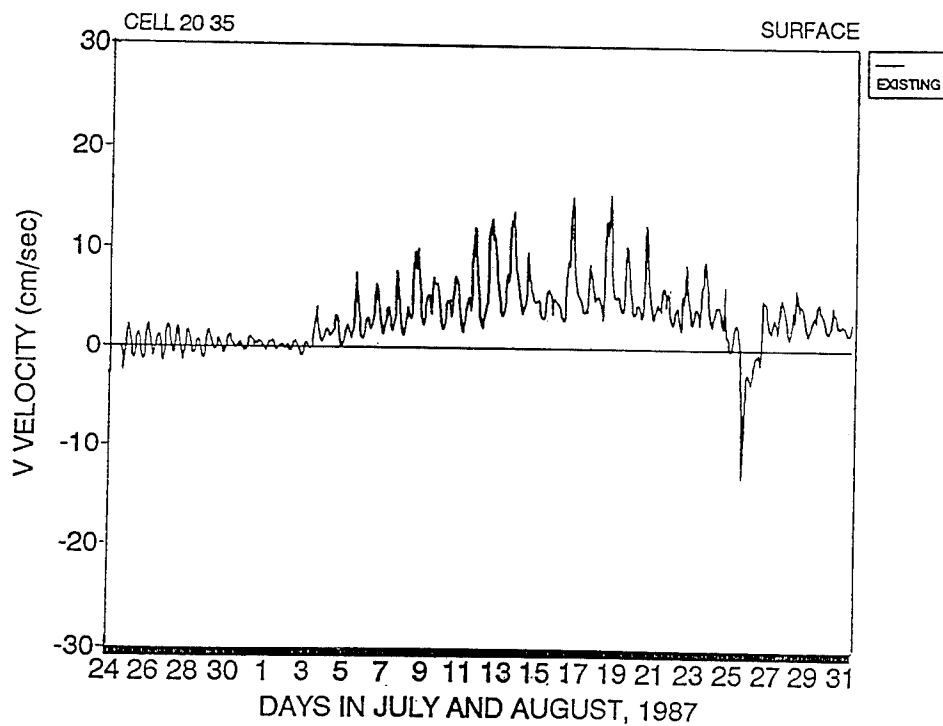
Figure B3. Time series of current velocity for the existing condition at station 3

a.

b.
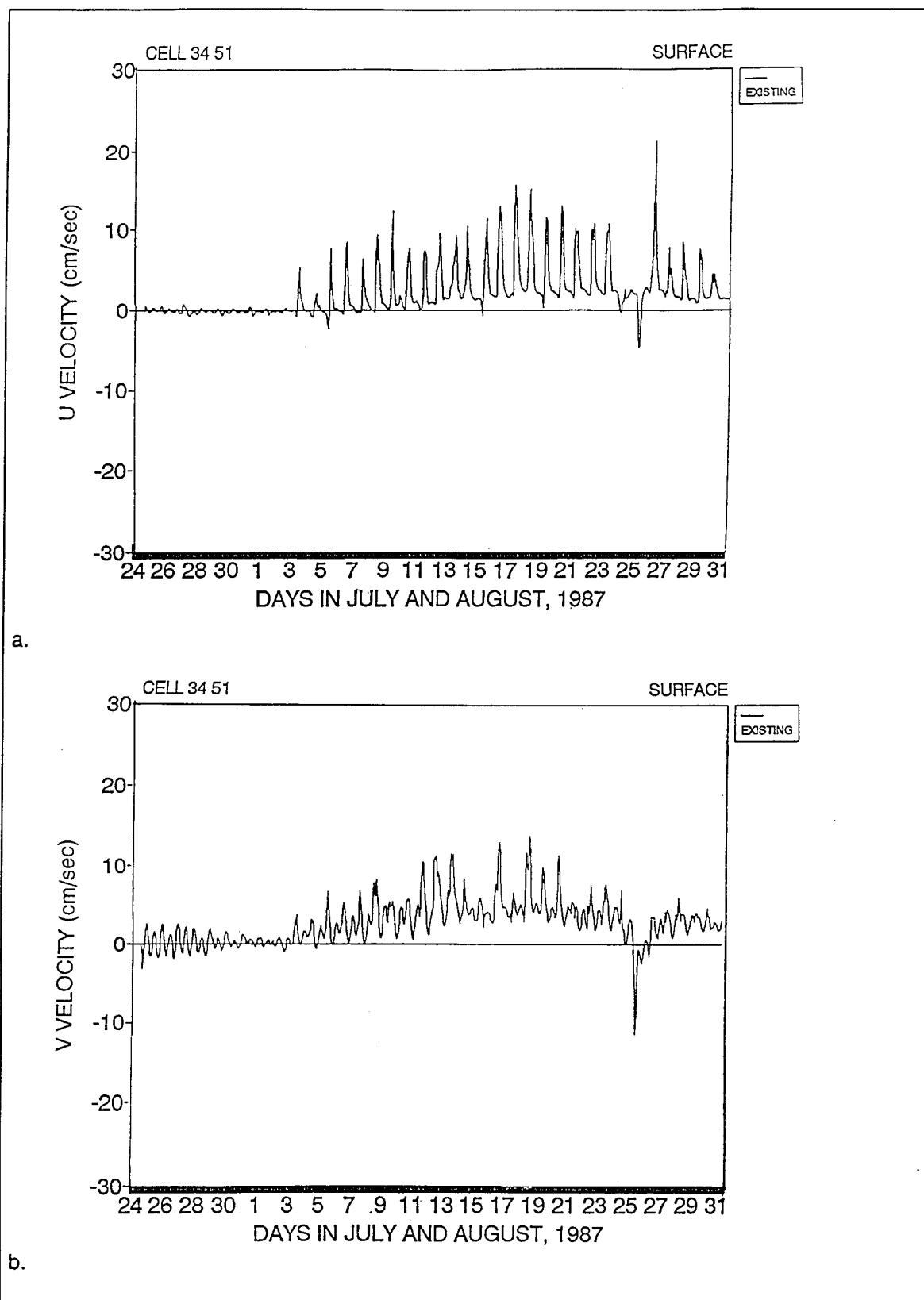
Figure B4. Time series of current velocity for the existing condition at station 4
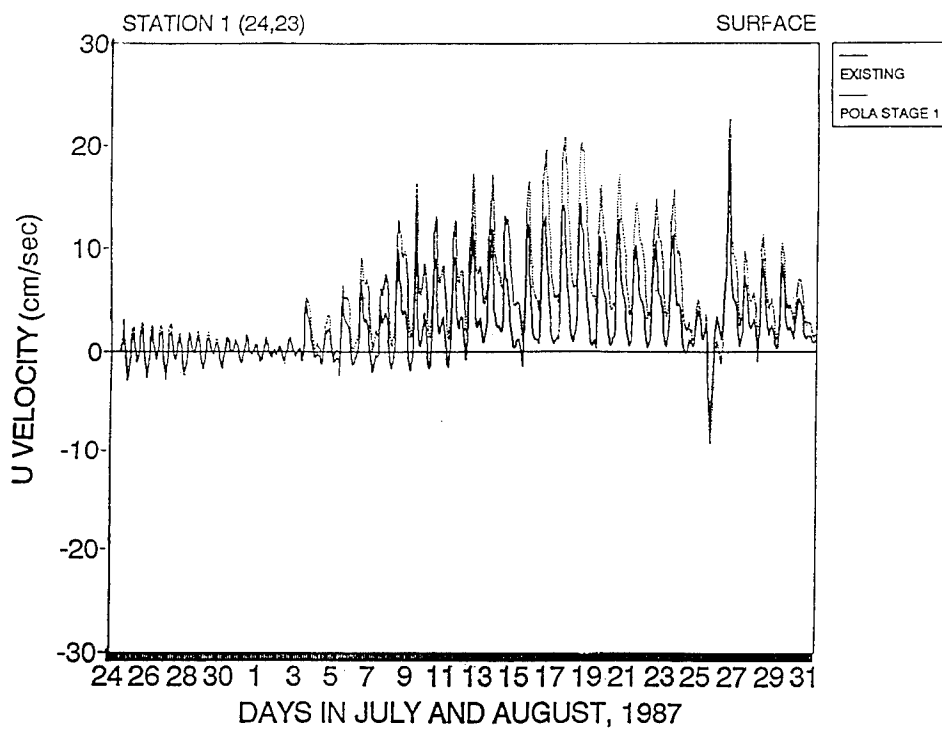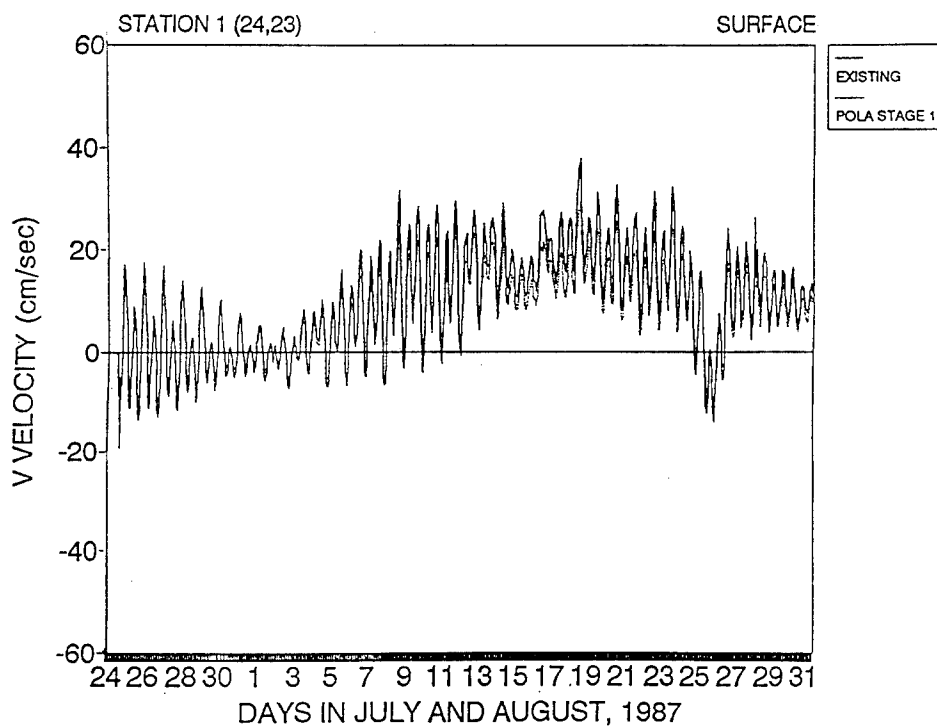
Figure B5. Time series of current velocity for POLA 1 at station 1
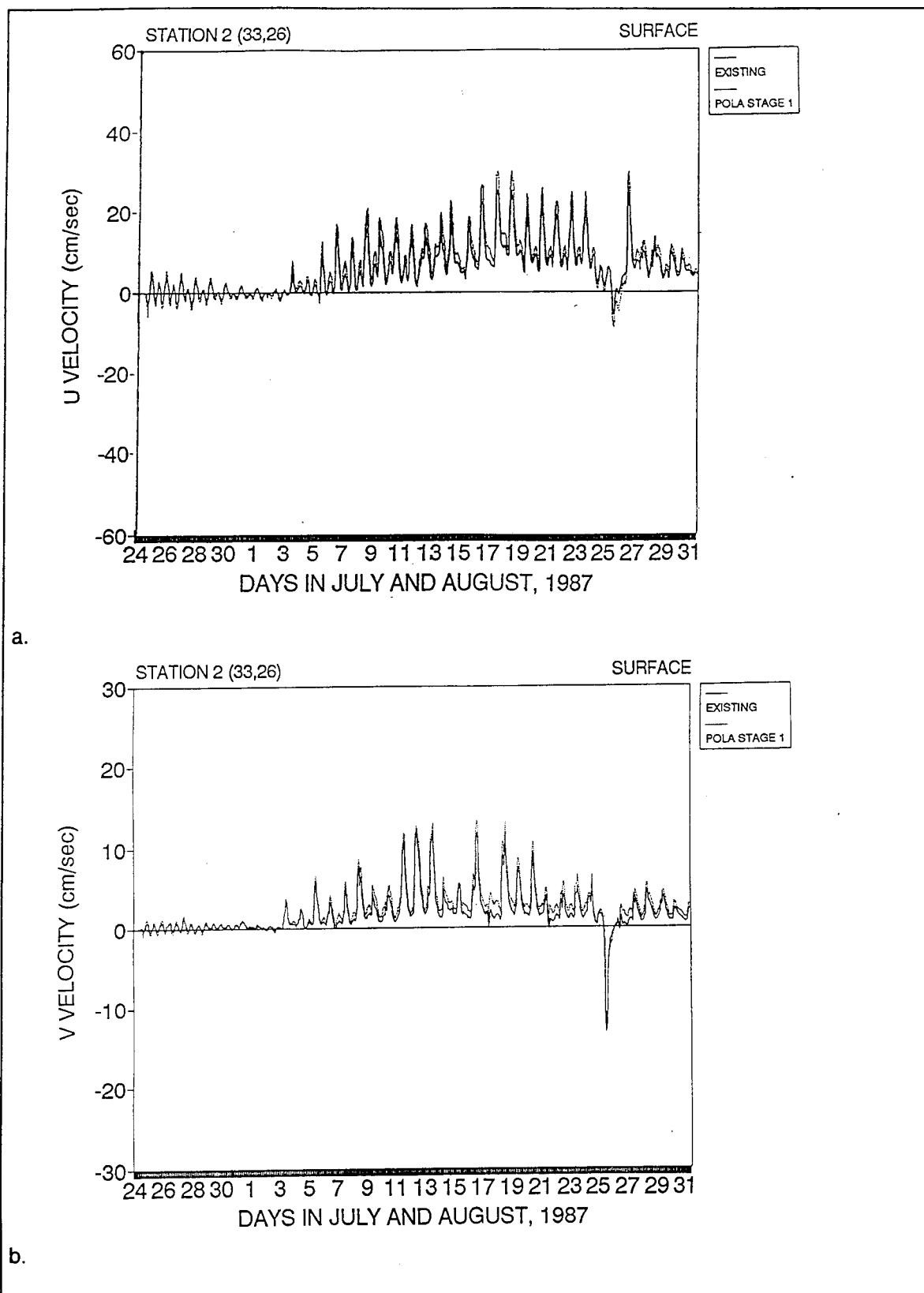
Figure B6. Time series of current velocity for POLA 1 at station 2
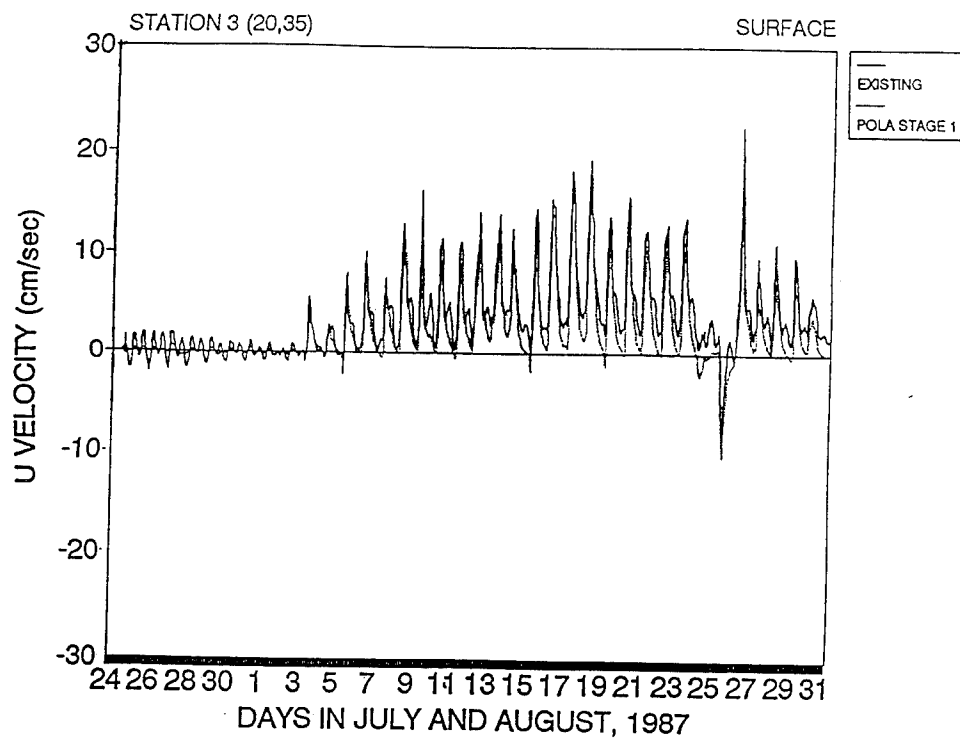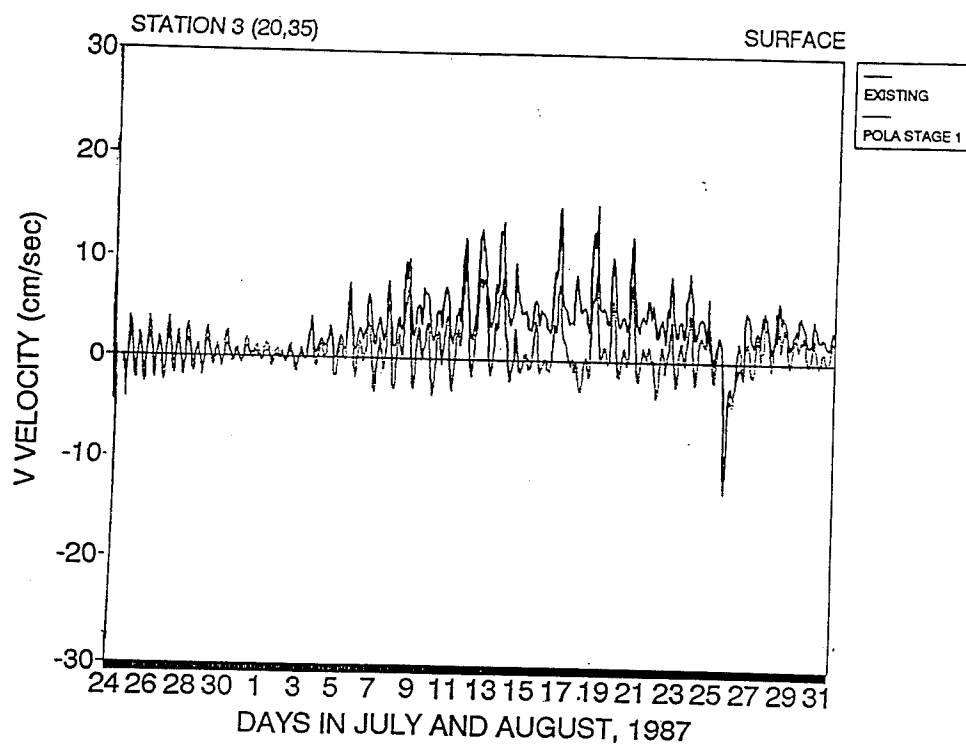
Figure B7. Time series of current velocity for POLA 1 at station 3
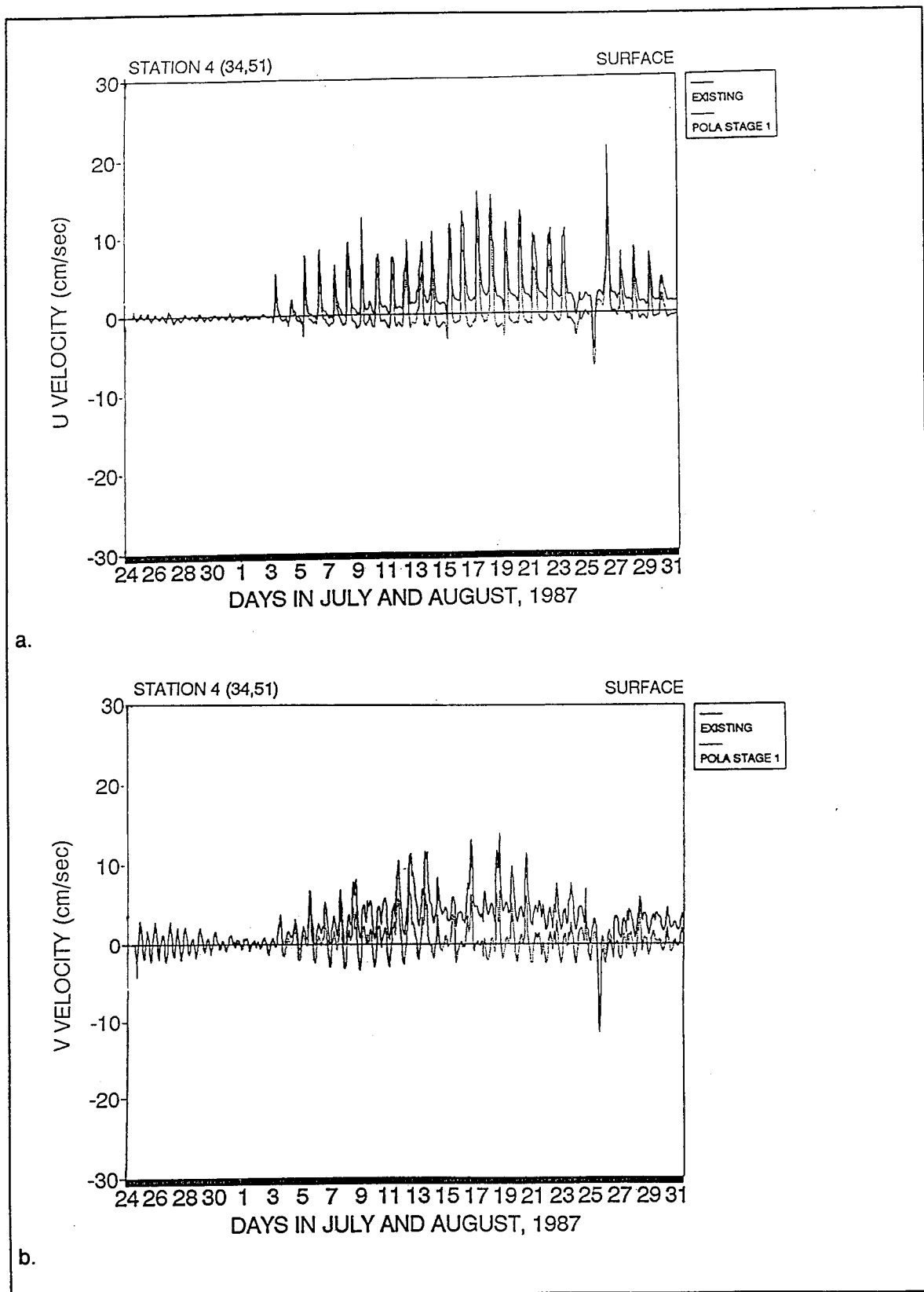
Figure B8. Time series of current velocity for POLA 1 at station 4
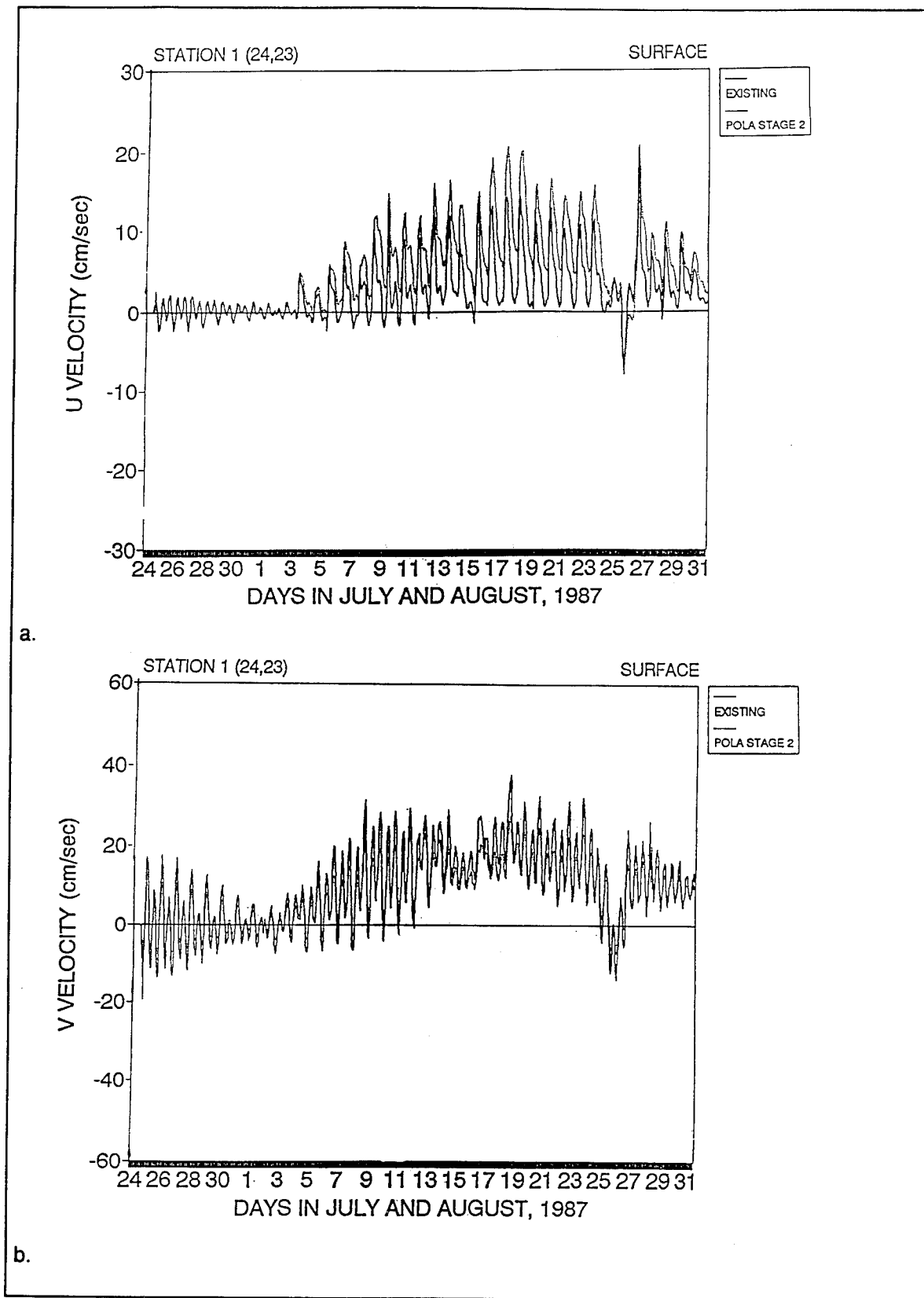
Figure B9. Time series of current velocity for POLA 2 at station 1
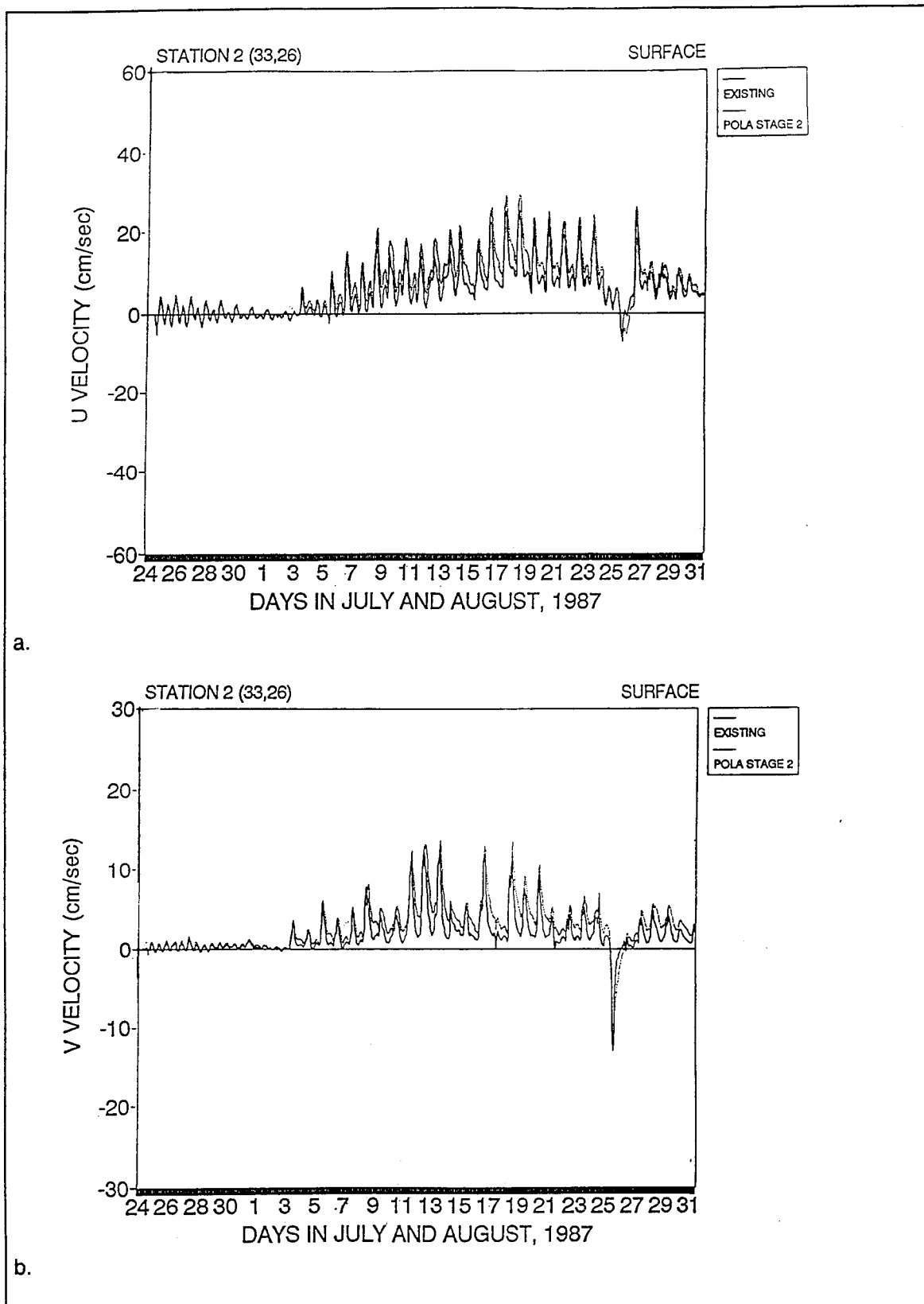
Figure B10. Time series of current velocity for POLA 2 at station 2
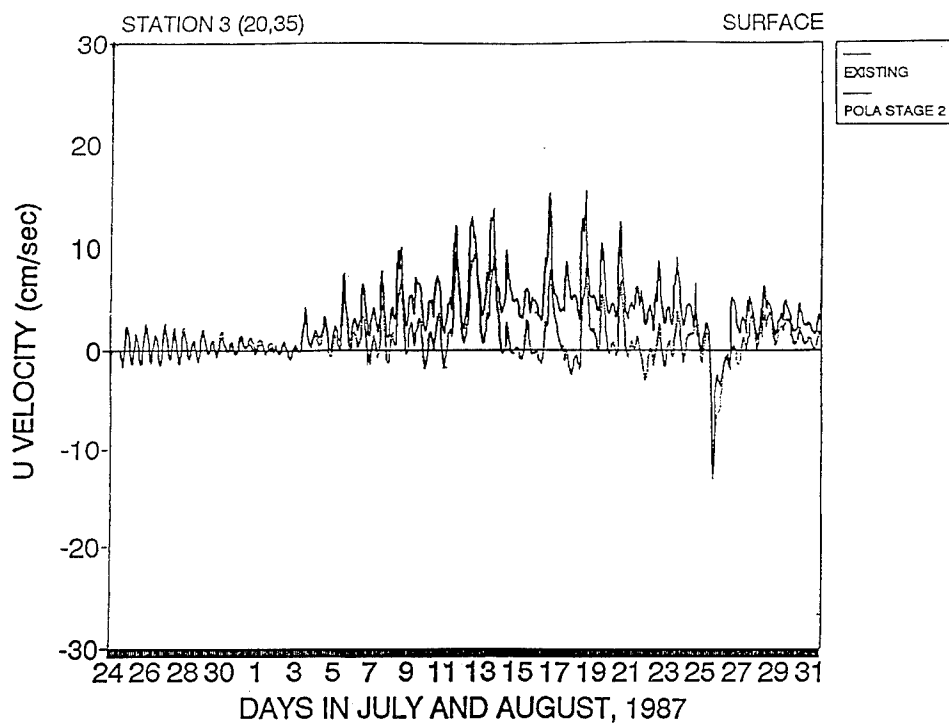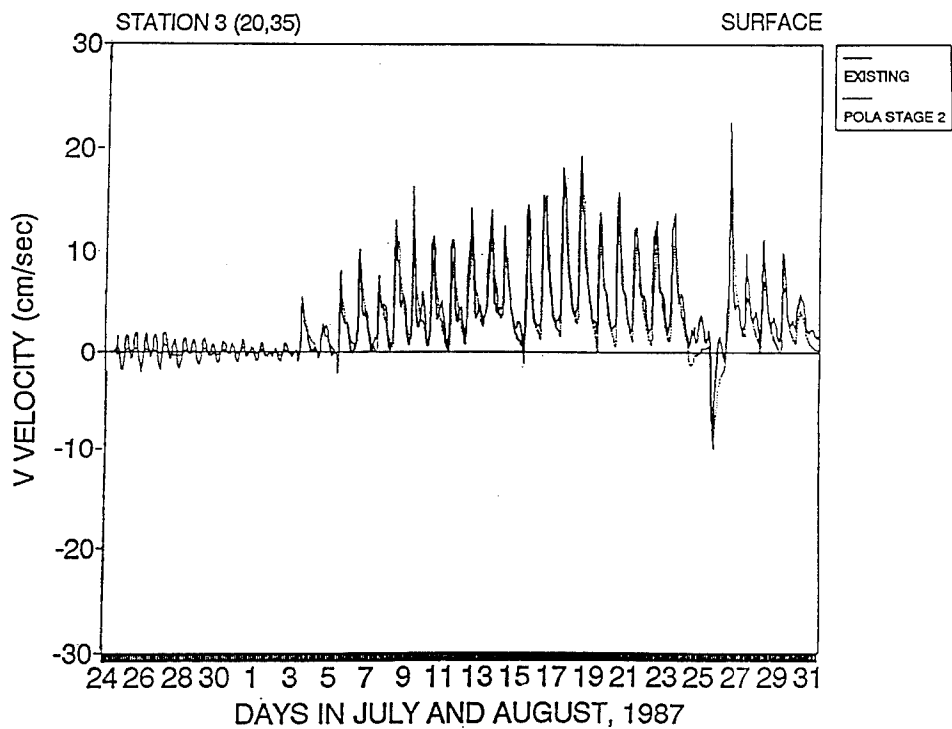
Figure B11. Time series of current velocity for POLA 2 at station 3
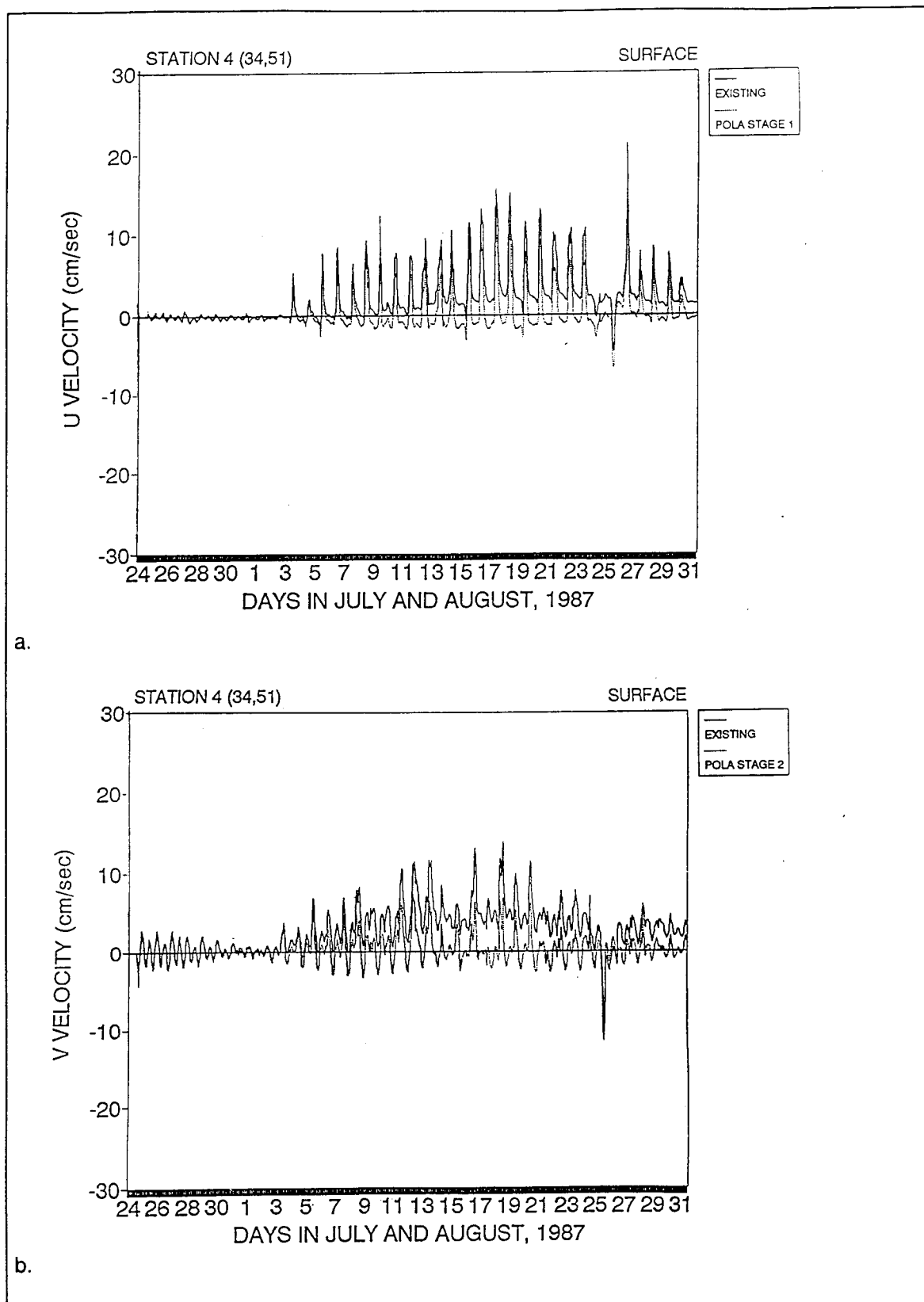
Figure B12. Time series of current velocity for POLA 2 at station 4

Appendix C
Velocity Vector Plots in Support of the Ship Simulation Model

30.0 cm/s

a. at maximum flood current

30.0 cm/s

b. maximum ebb current
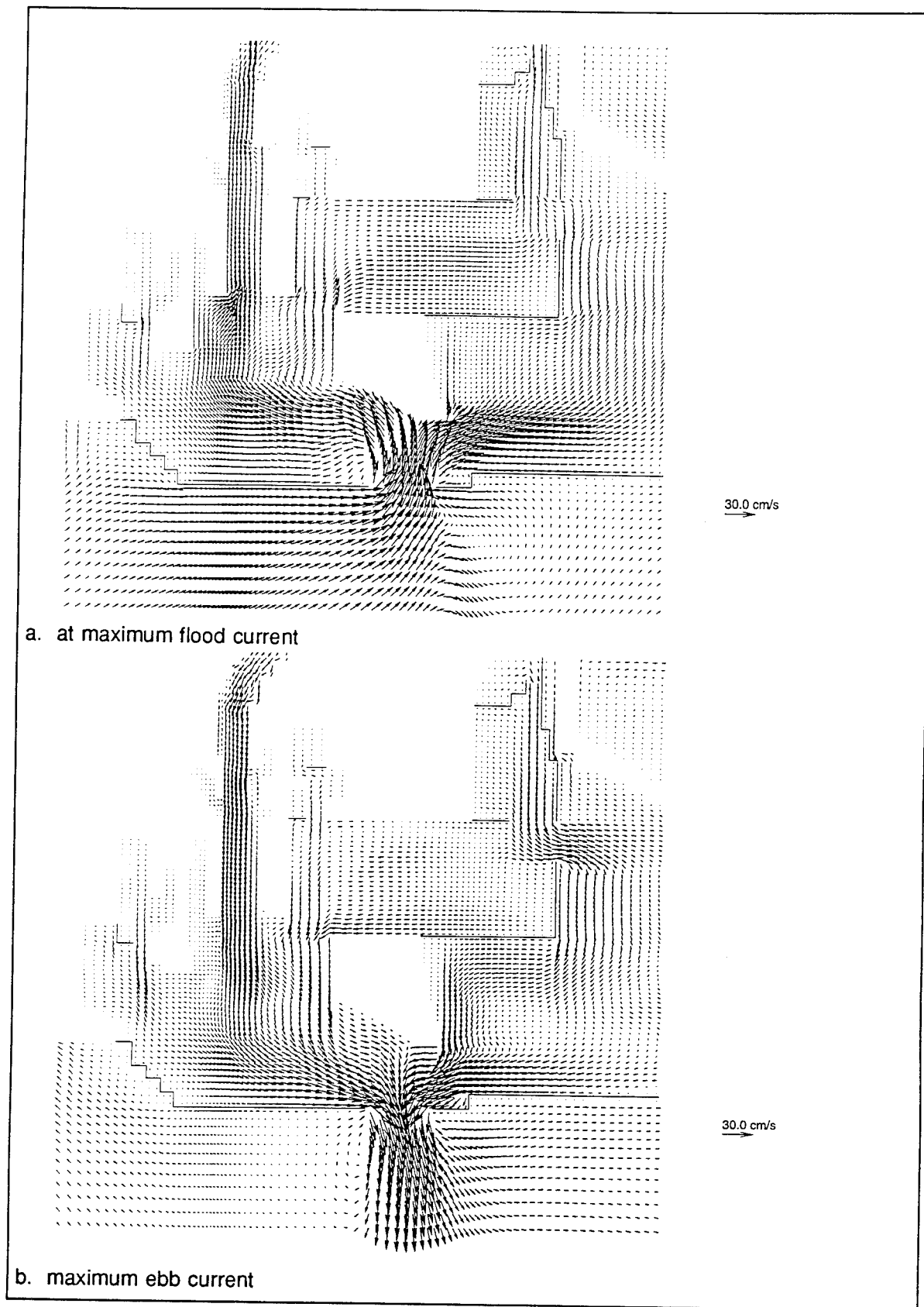
Figure C1. Vector plot of POLA 1 surface layer circulation under BW

30.0 cm/s

a. at maximum flood current

30.0 cm/s

b. maximum ebb current
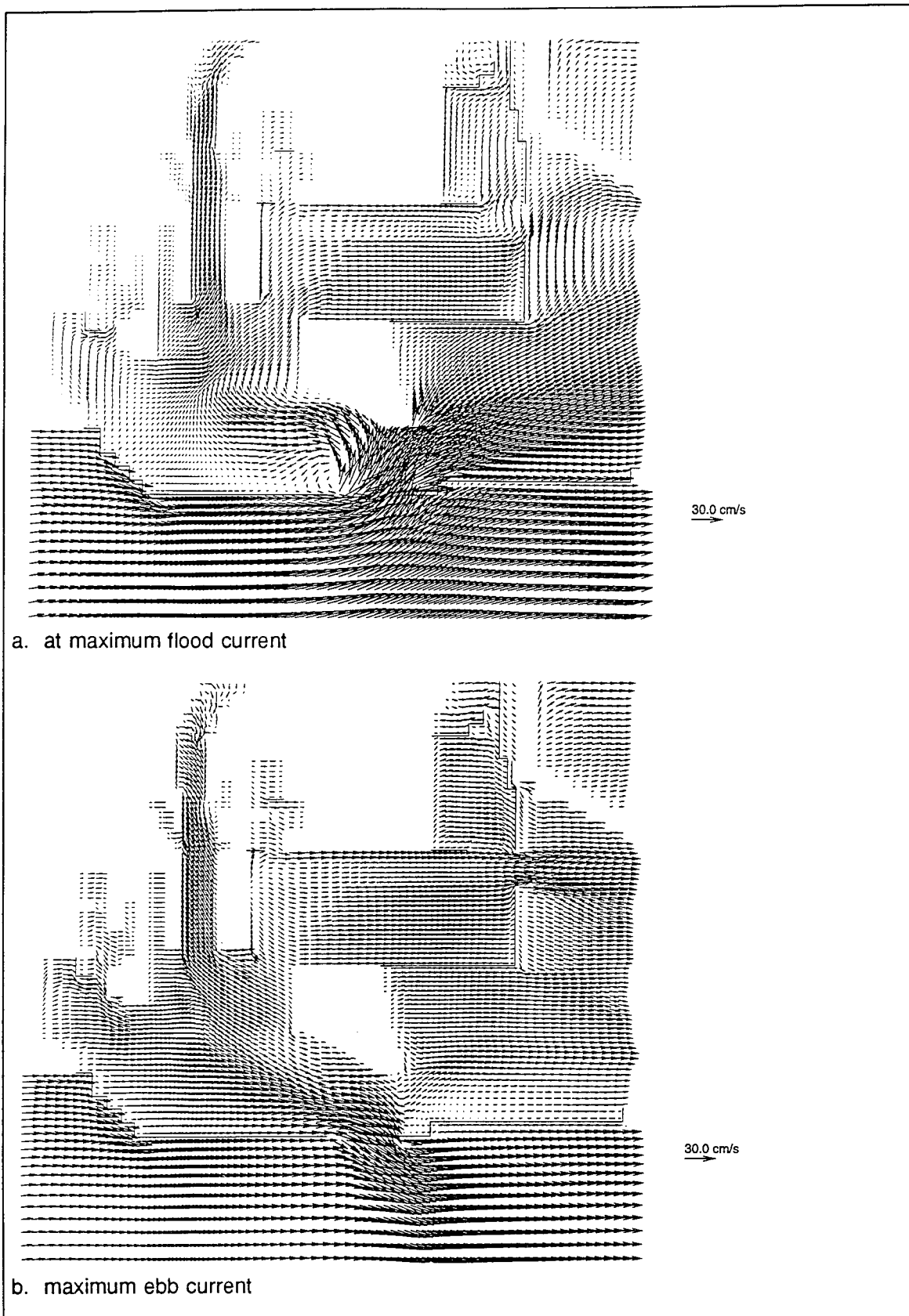
Figure C2. Vector plot of POLA 1 surface layer circulation under WSW20

30.0 cm/s

a. at maximum flood current

30.0 cm/s

b. maximum ebb current
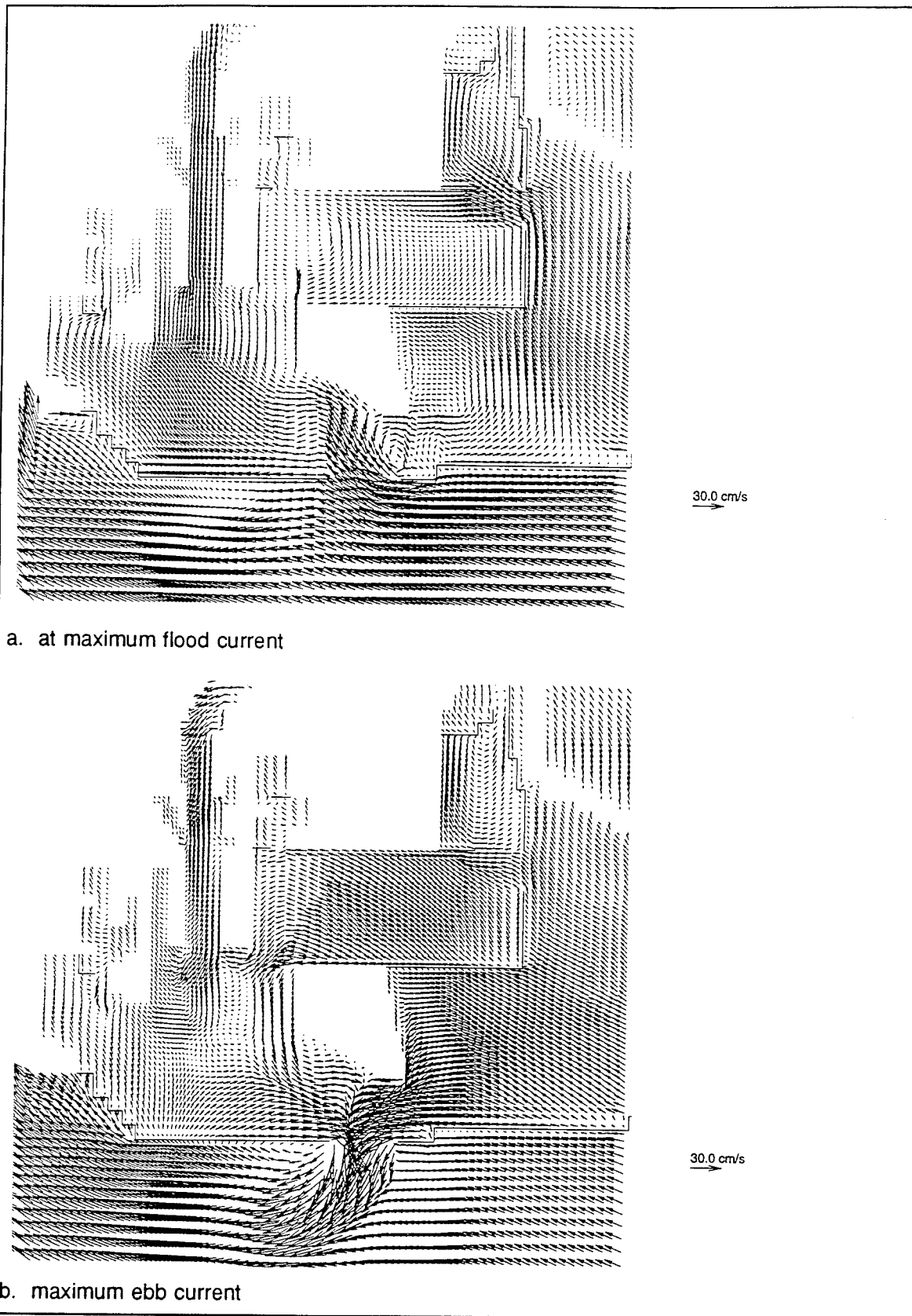
Figure C3. Vector plot of POLA 1 surface layer circulation under SE20

C4

30.0 cm/s

a. at maximum flood current

30.0 cm/s

b. maximum ebb current
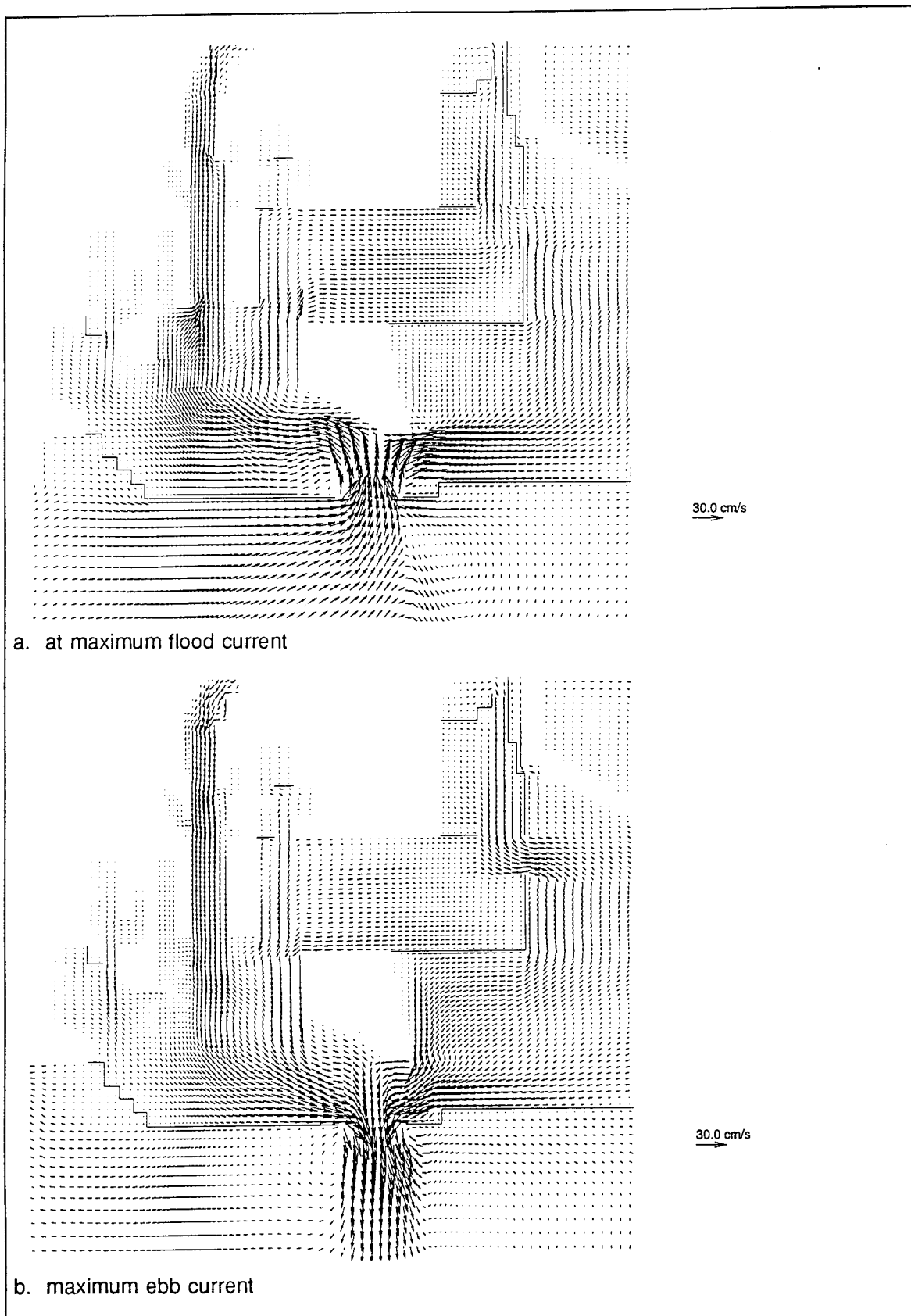
Figure C4. Vector plot of POLA 1 bottom layer circulation under BW

30.0 cm/s

a. at maximum flood current

30.0 cm/s
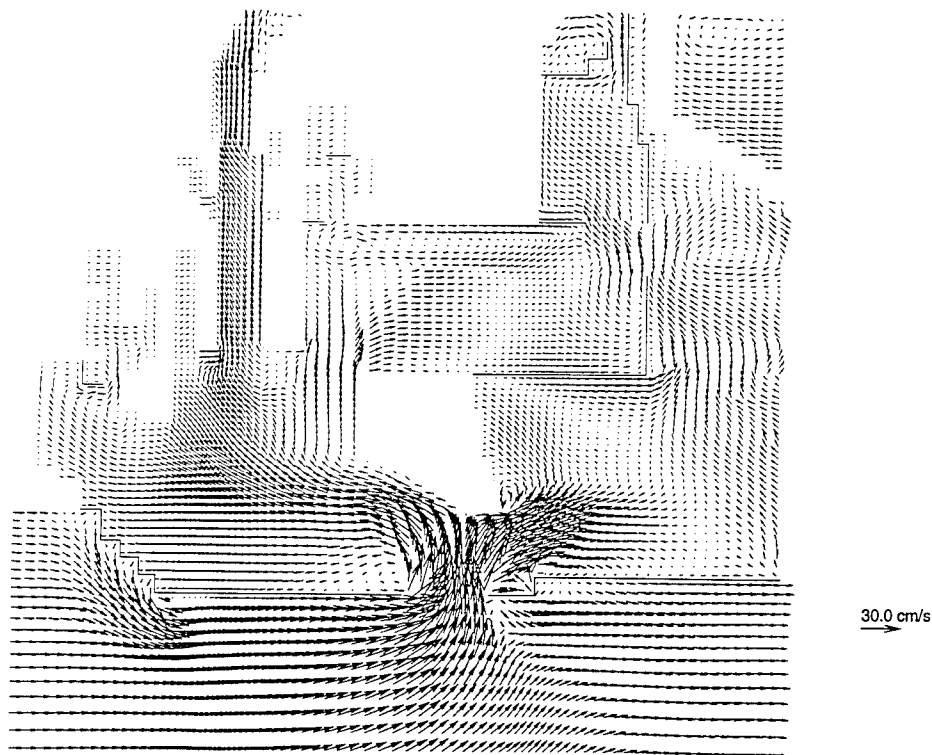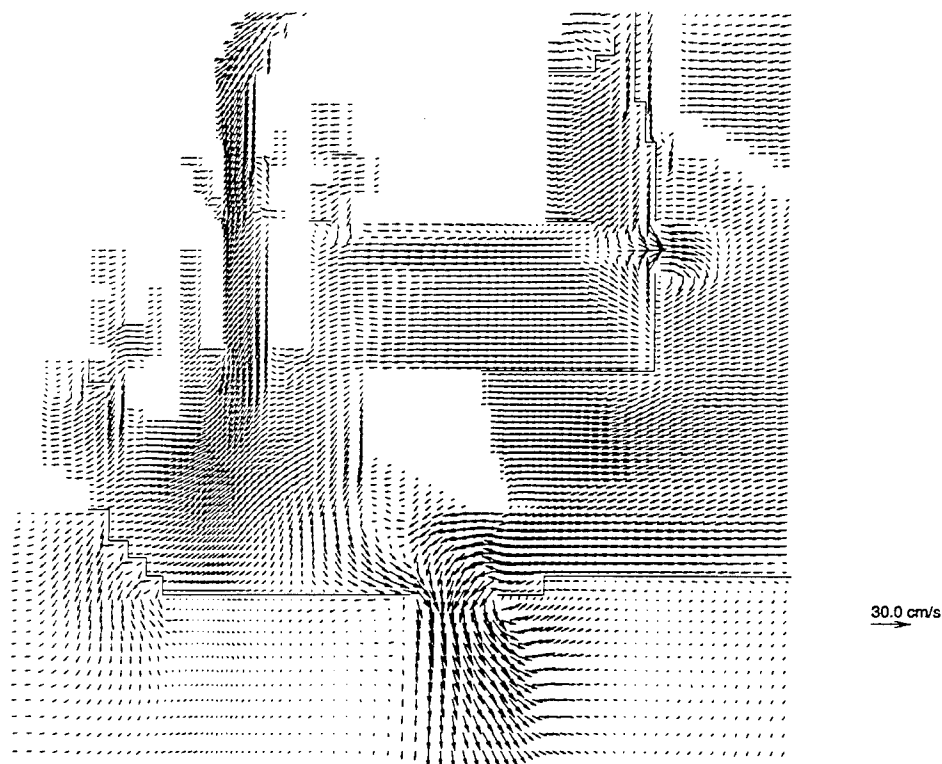
b. maximum ebb current

Figure C5. Vector plot of POLA 1 bottom layer circulation under WSW20

C6

a. at maximum flood current

30.0 cm/s

b. maximum ebb current

30.0 cm/s
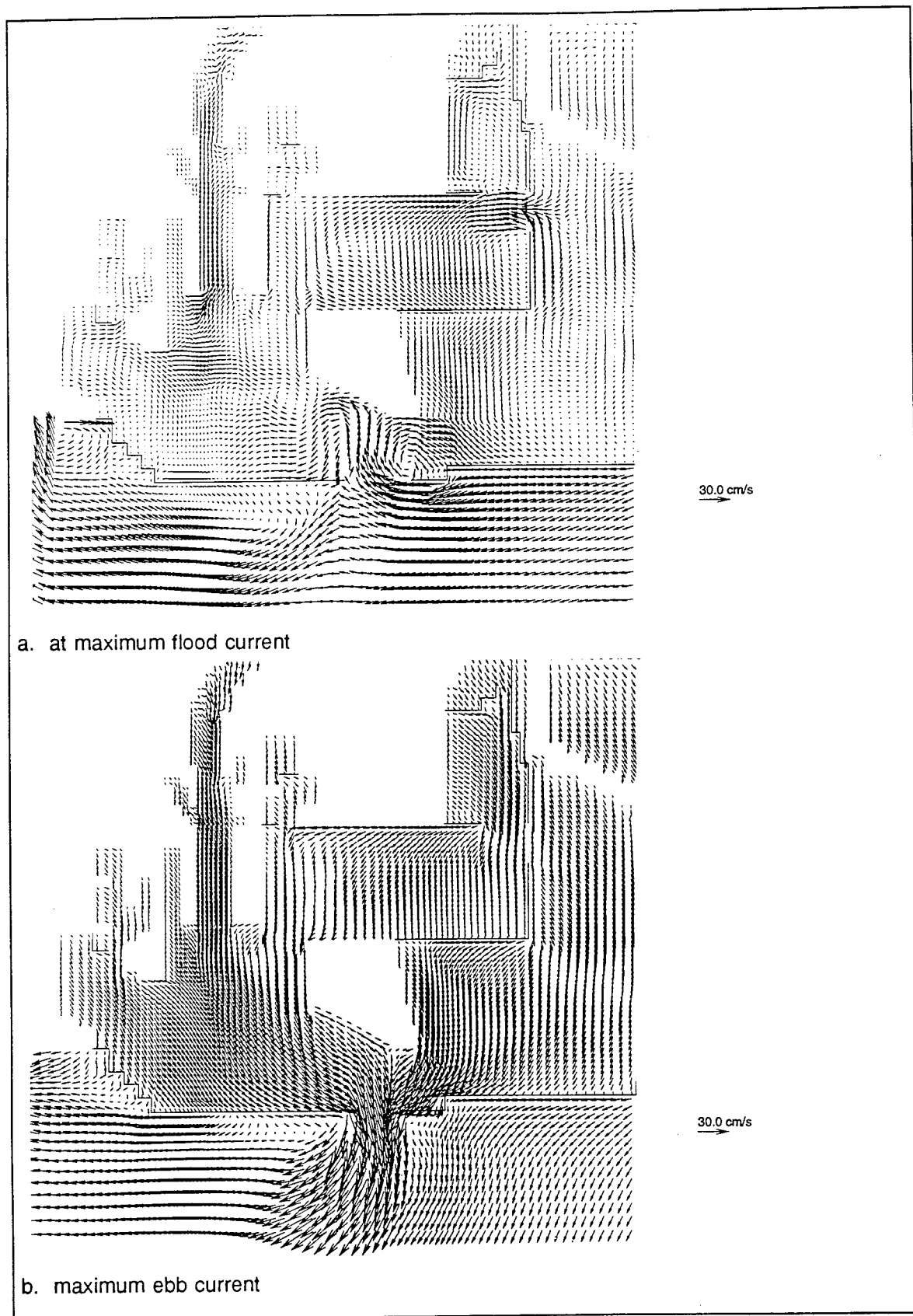
Figure C6. Vector plot of POLA 1 bottom layer circulation under SE20

a. at maximum flood current

30.0 cm/s

b. maximum ebb current

30.0 cm/s
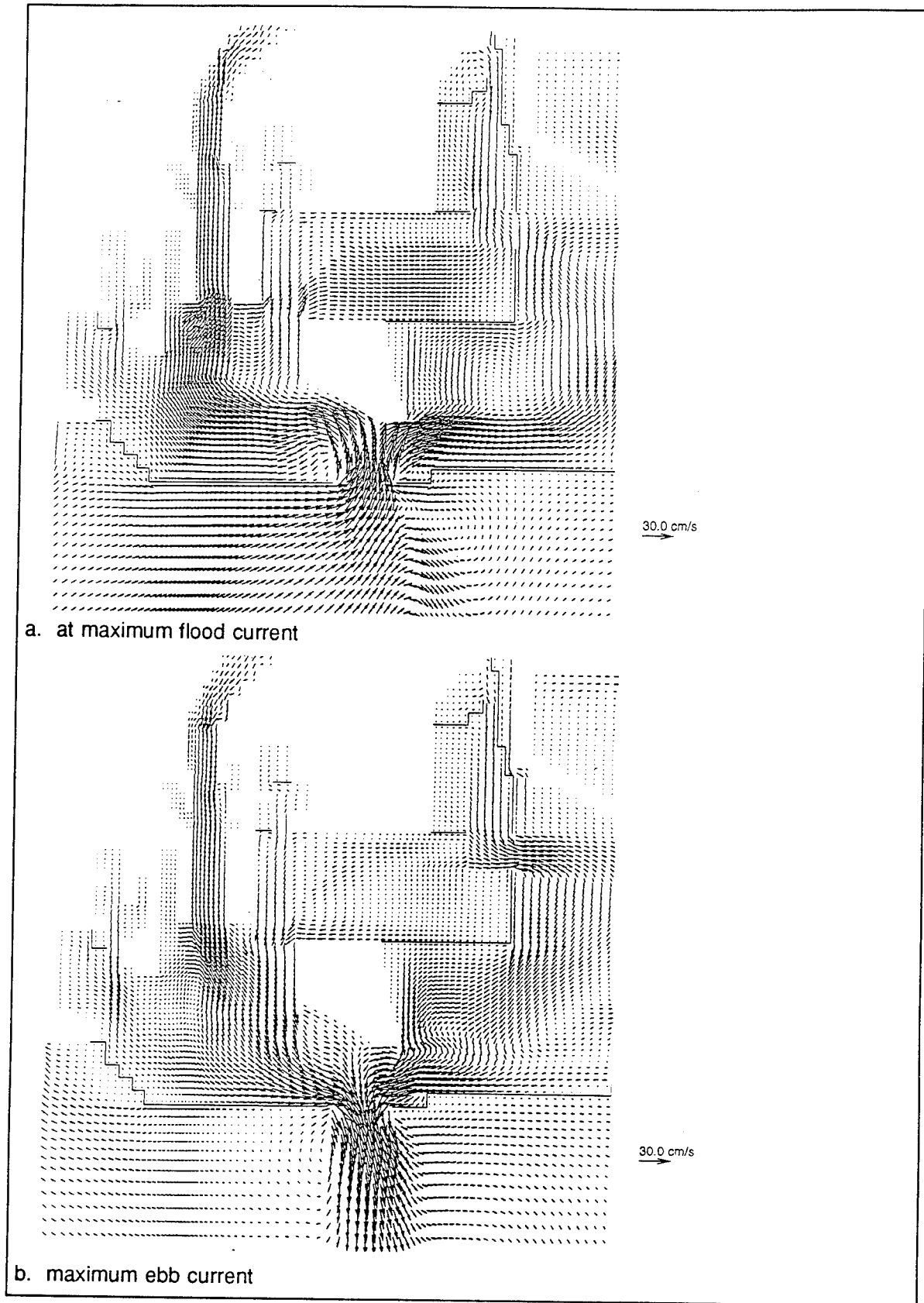
Figure C7. Vector plot of POLA 1 vertical averaged circulation under BW

30.0 cm/s

a. at maximum flood current

b. maximum ebb current
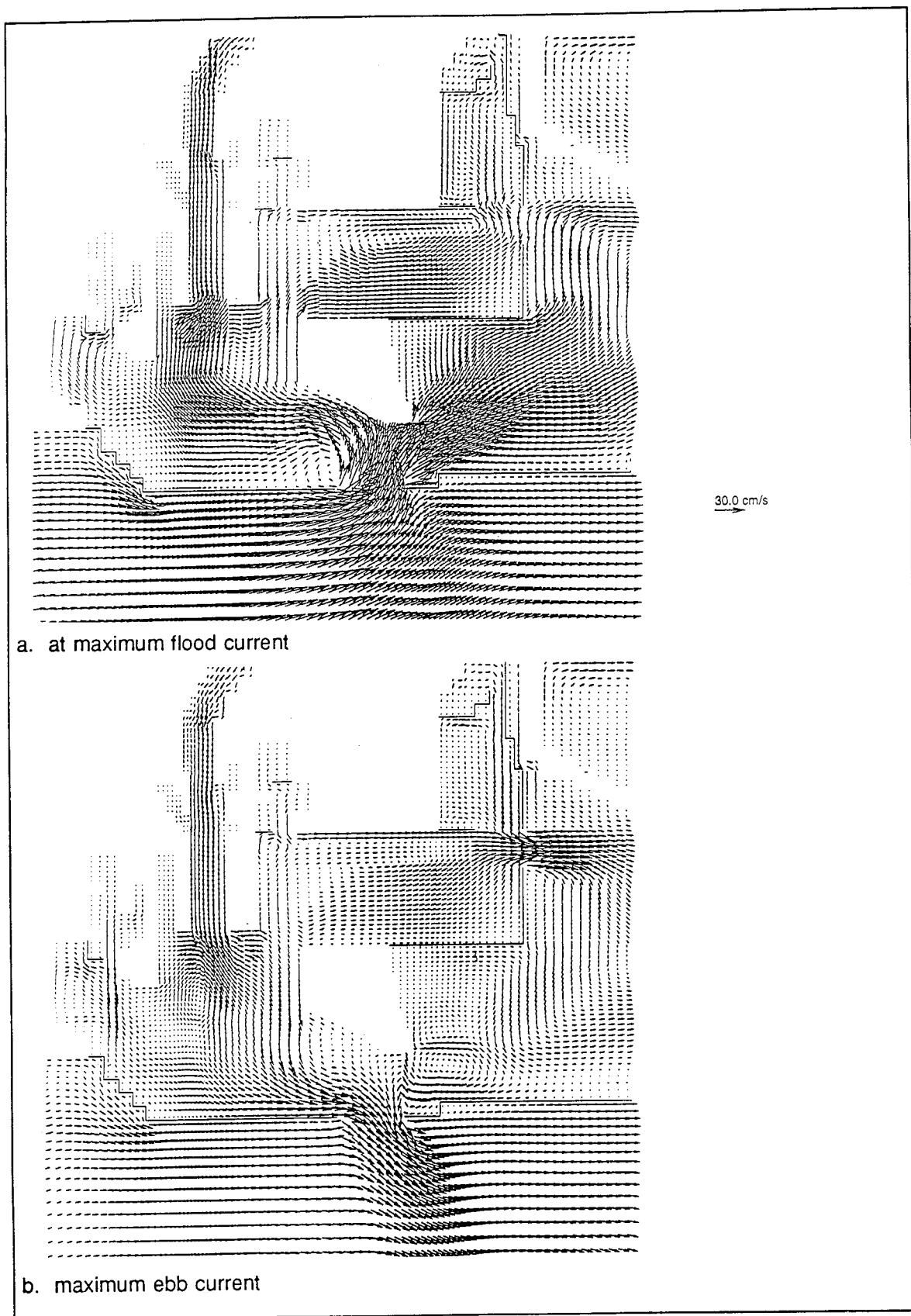
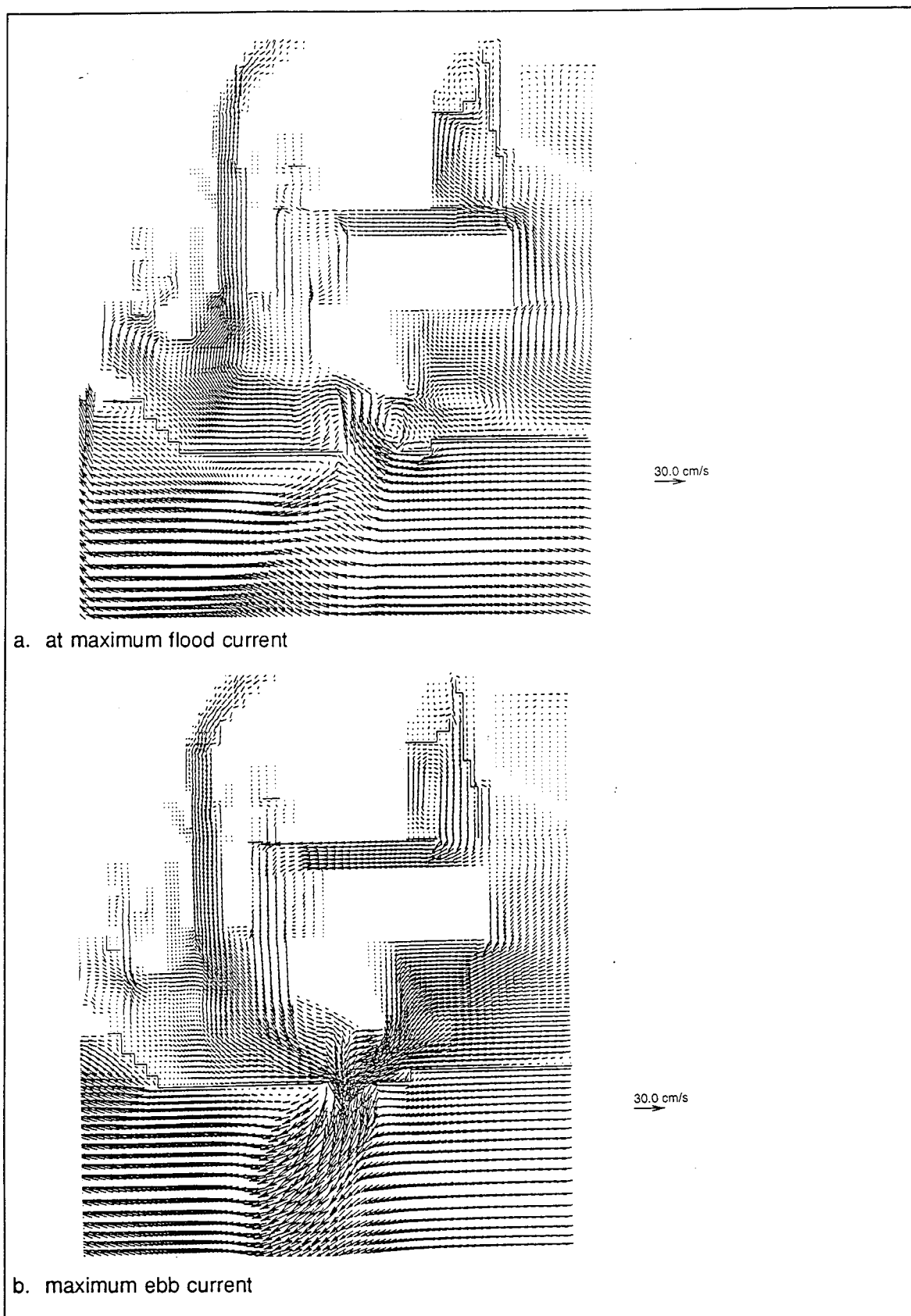Figure C8. Vector plot of POLA 1 vertical averaged circulation under WSW20

30.0 cm/s

a. at maximum flood current

30.0 cm/s
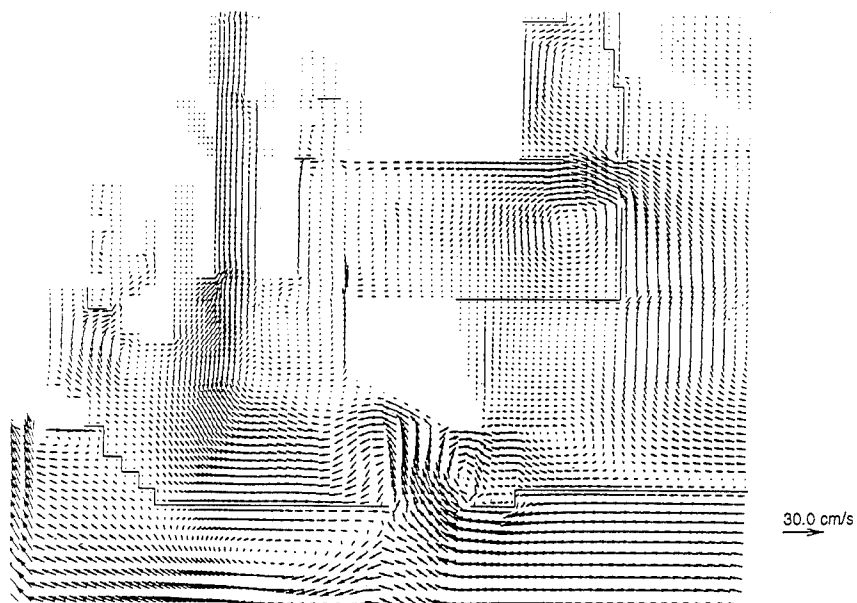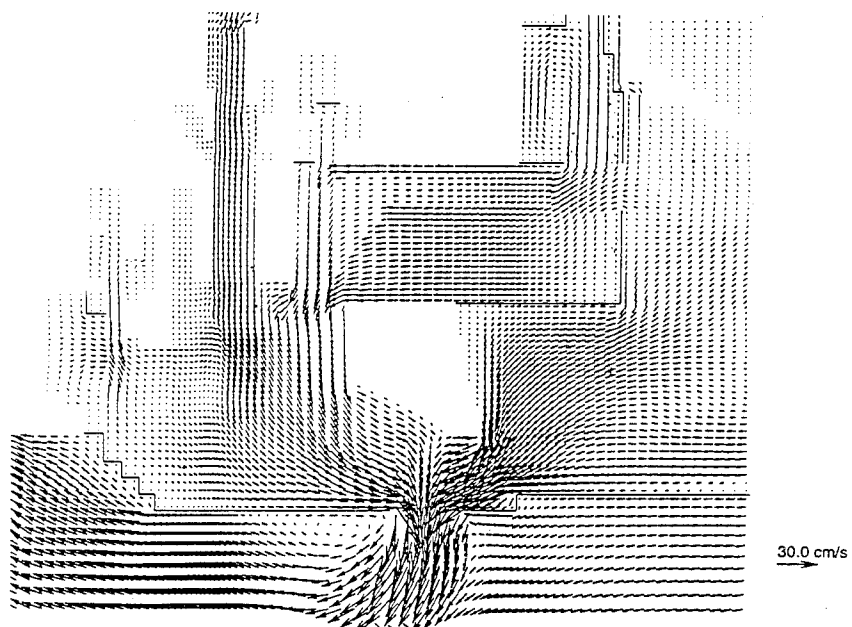
b. maximum ebb current

Figure C9. Vector plot of POLA 1 vertical averaged circulation under SE20

C10

a. at maximum flood current

30.0 cm/s

b. maximum ebb current

30.0 cm/s
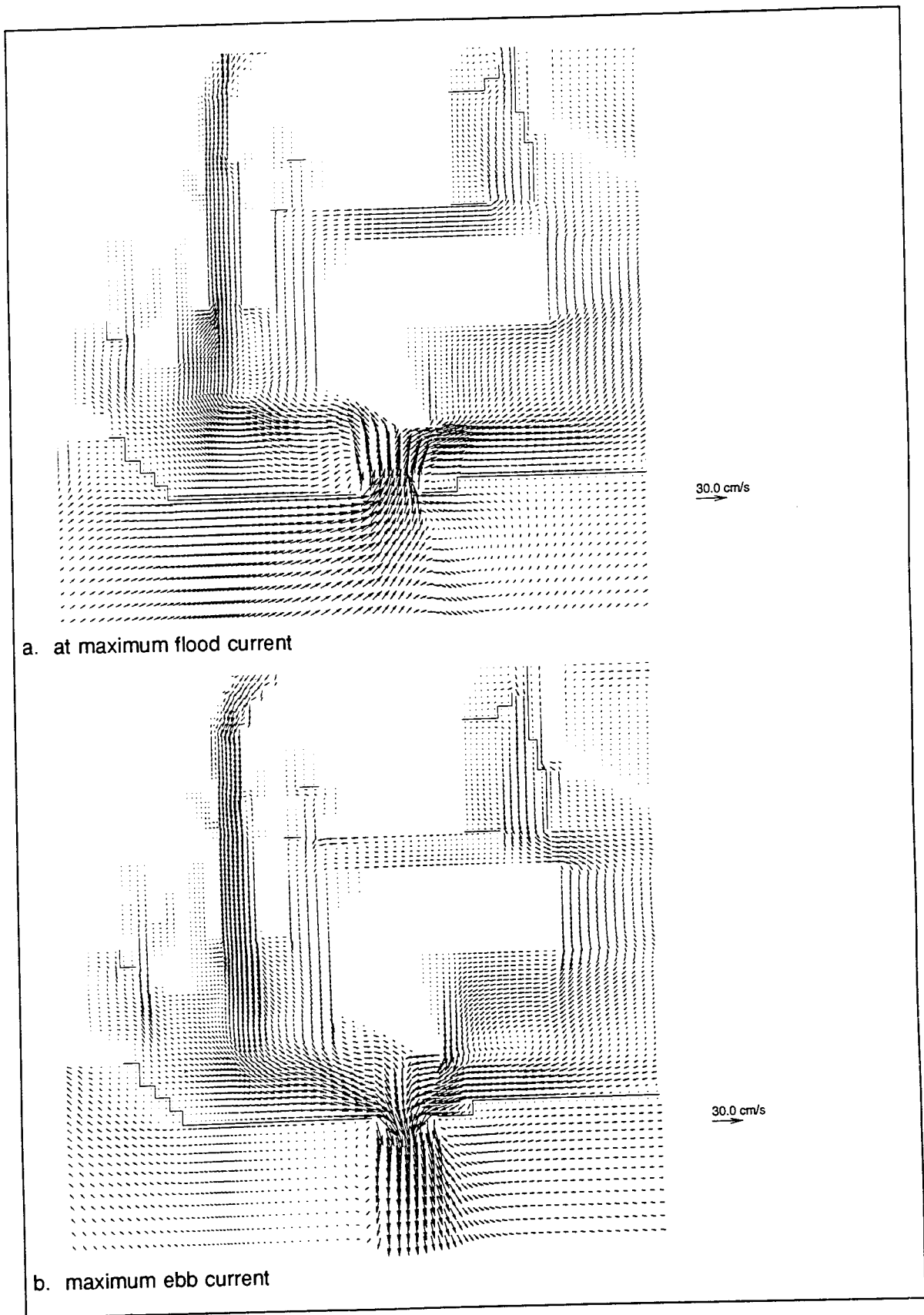
Figure C10. Vector plot of POLA 2 surface layer circulation under BW

Appendix C   Velocity Vector Plots in Support of the Ship Simulation Model
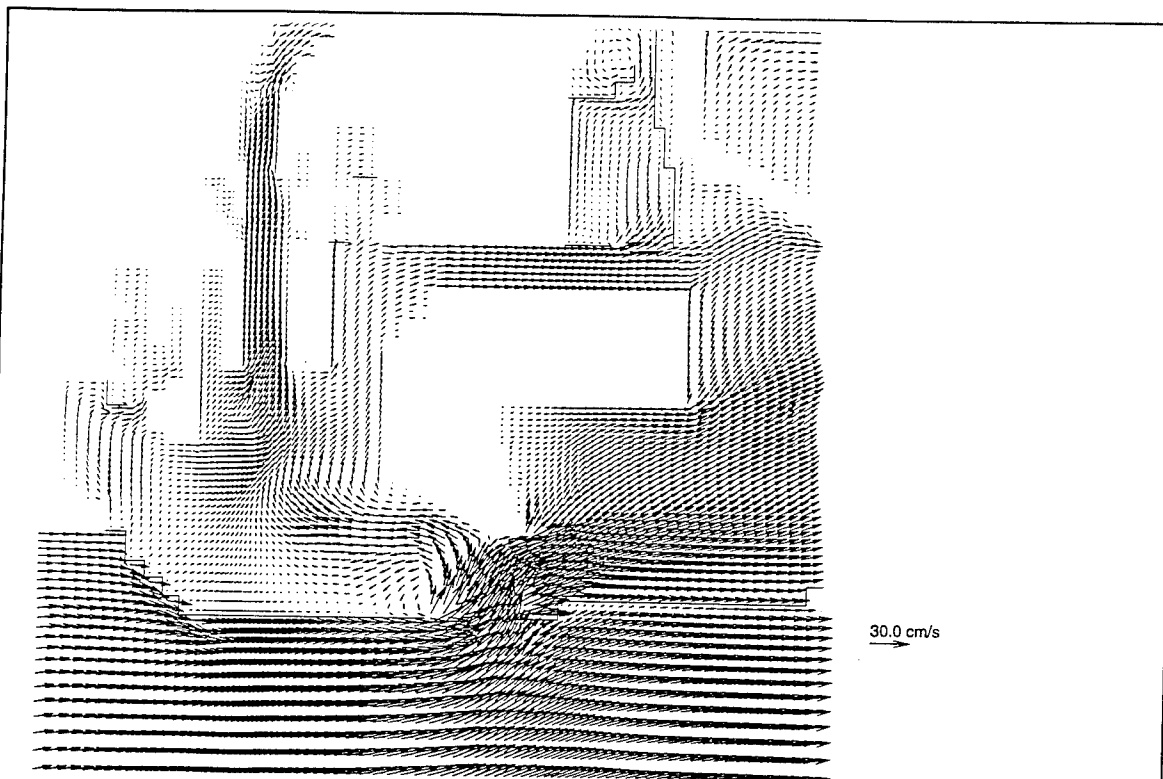
a. at maximum flood current
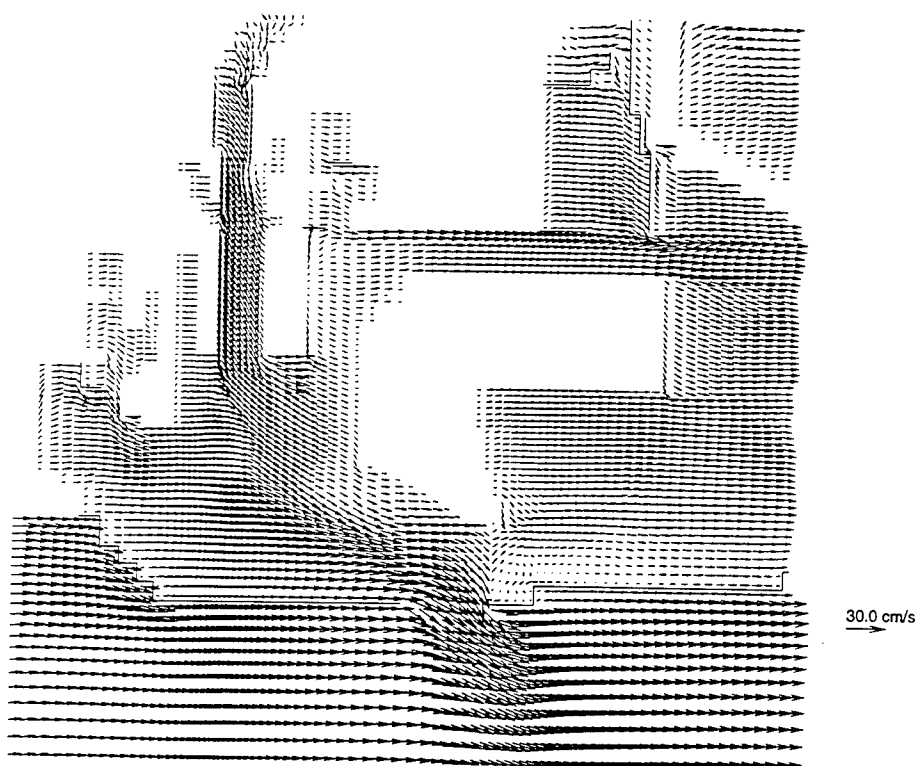
b. maximum ebb current

Figure C11. Vector plot of POLA 2 surface layer circulation under WSW20

a. at maximum flood current

30.0 cm/s

b. maximum ebb current

30.0 cm/s
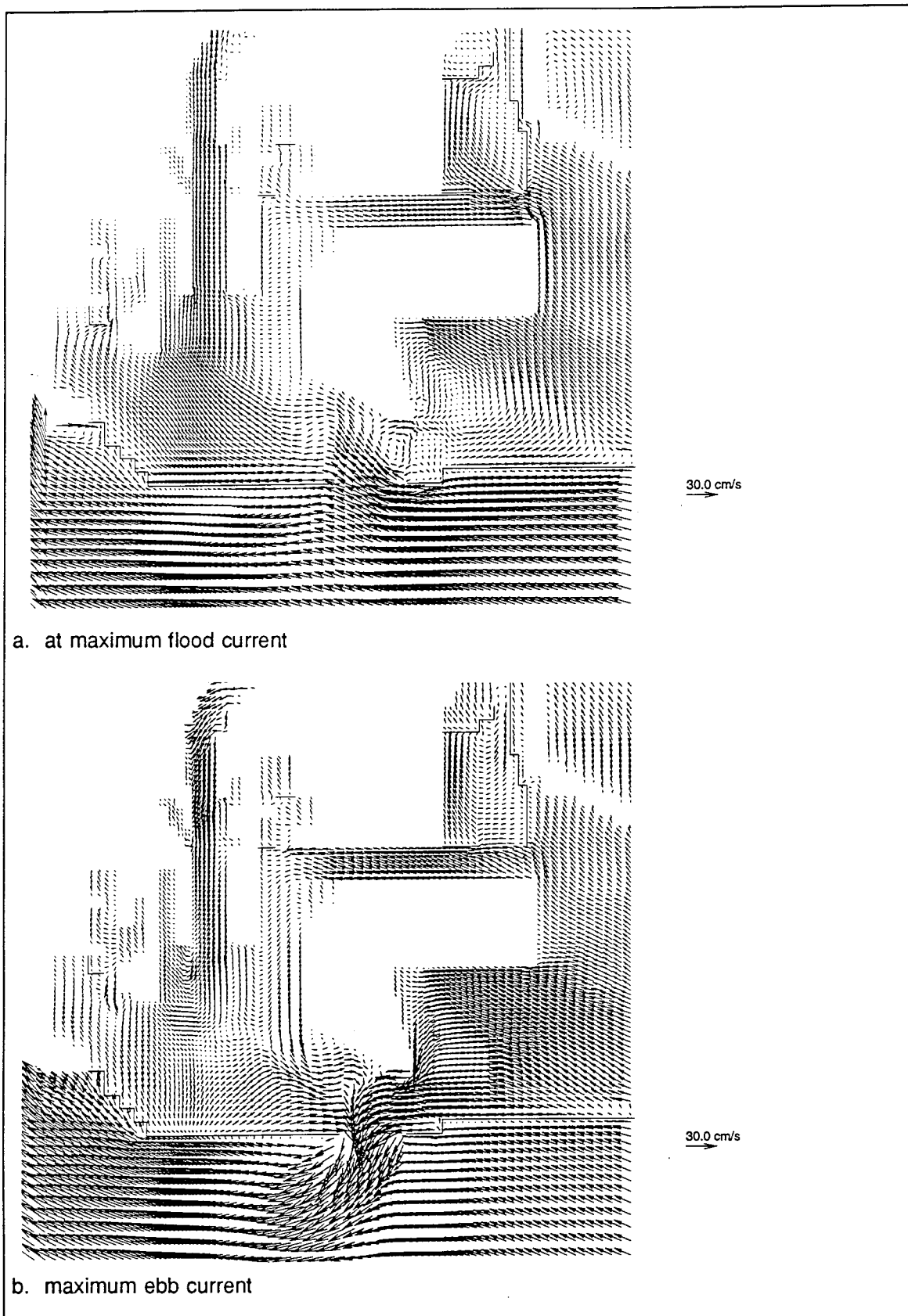
Figure C12. Vector plot of POLA 2 surface layer circulation under SE20

a. at maximum flood current

30.0 cm/s

b. maximum ebb current

30.0 cm/s
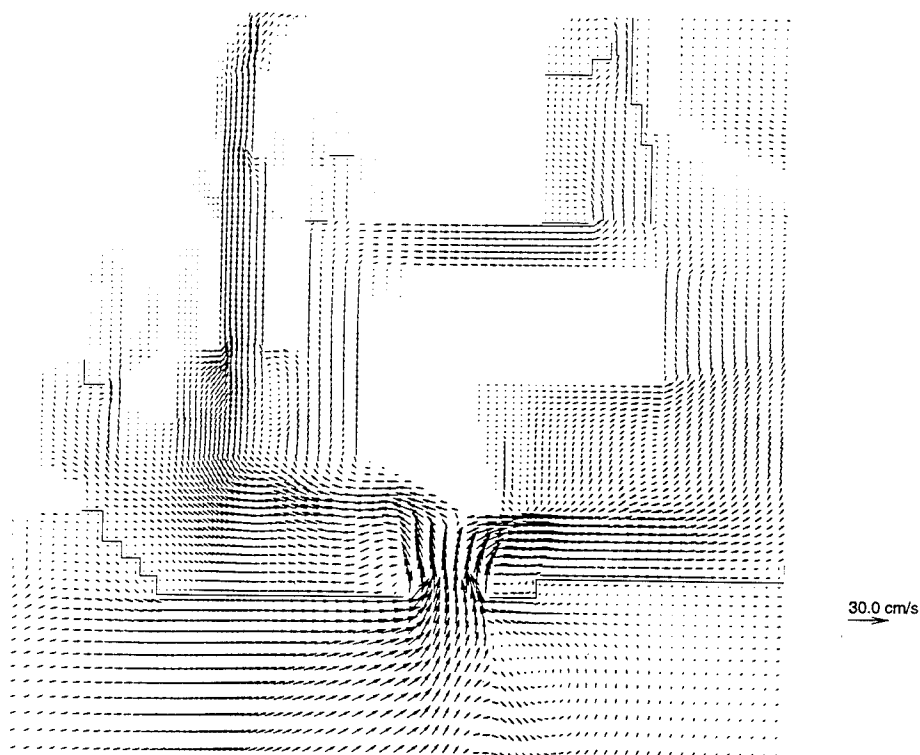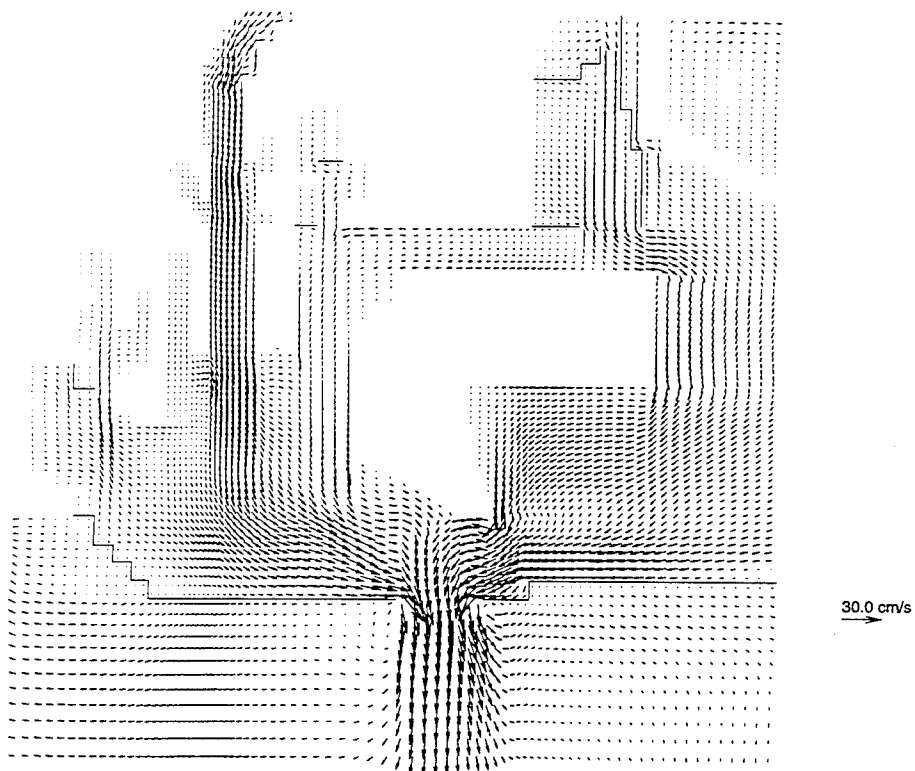
Figure C13. Vector plot of POLA 2 bottom layer circulation under BW

C14

a. at maximum flood current

b. maximum ebb current
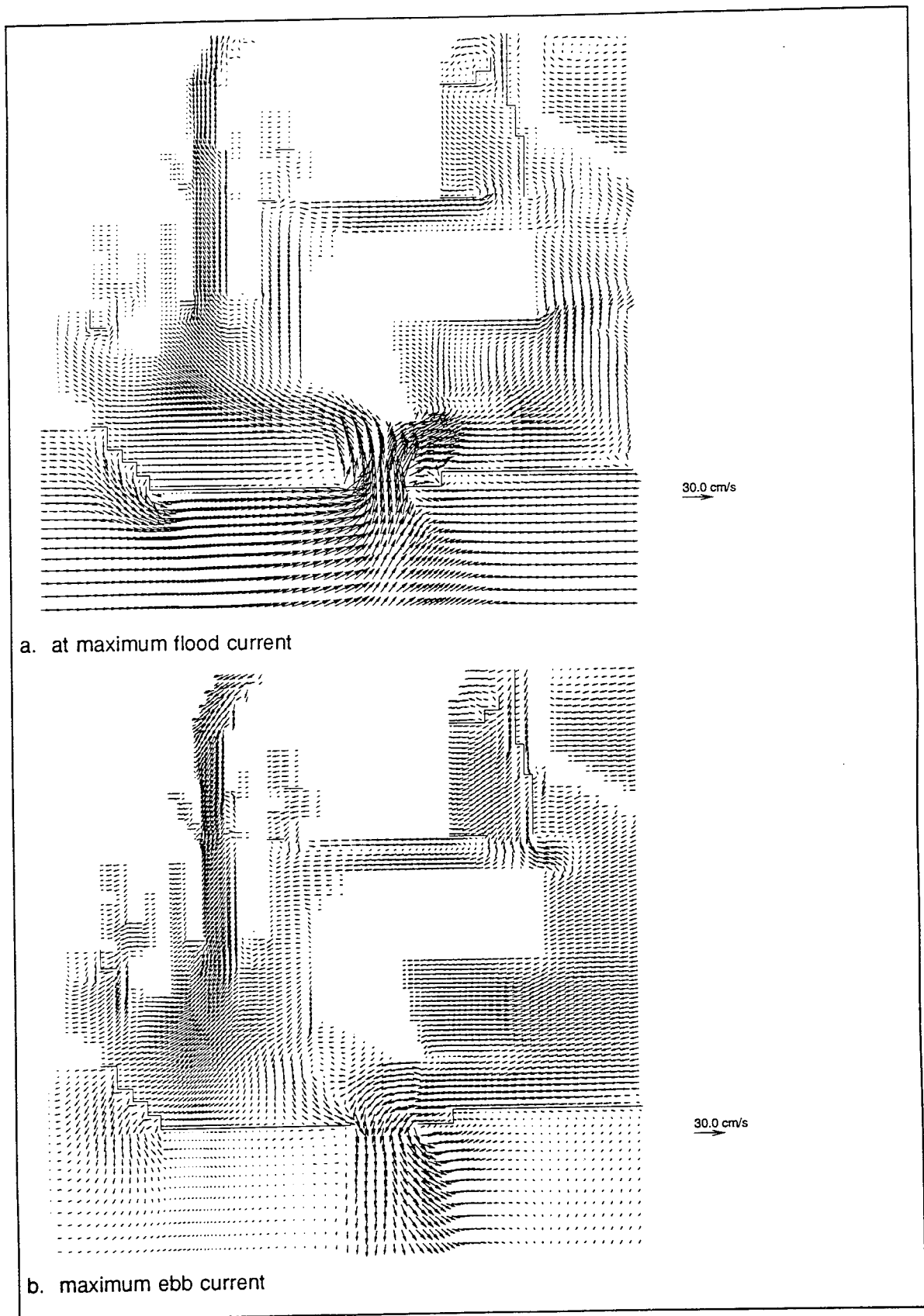
Figure C14. Vector plot of POLA 2 bottom layer circulation under WSW20

Appendix C   Velocity Vector Plots in Support of the Ship Simulation Model

30.0 cm/s

a. at maximum flood current

30.0 cm/s

b. maximum ebb current
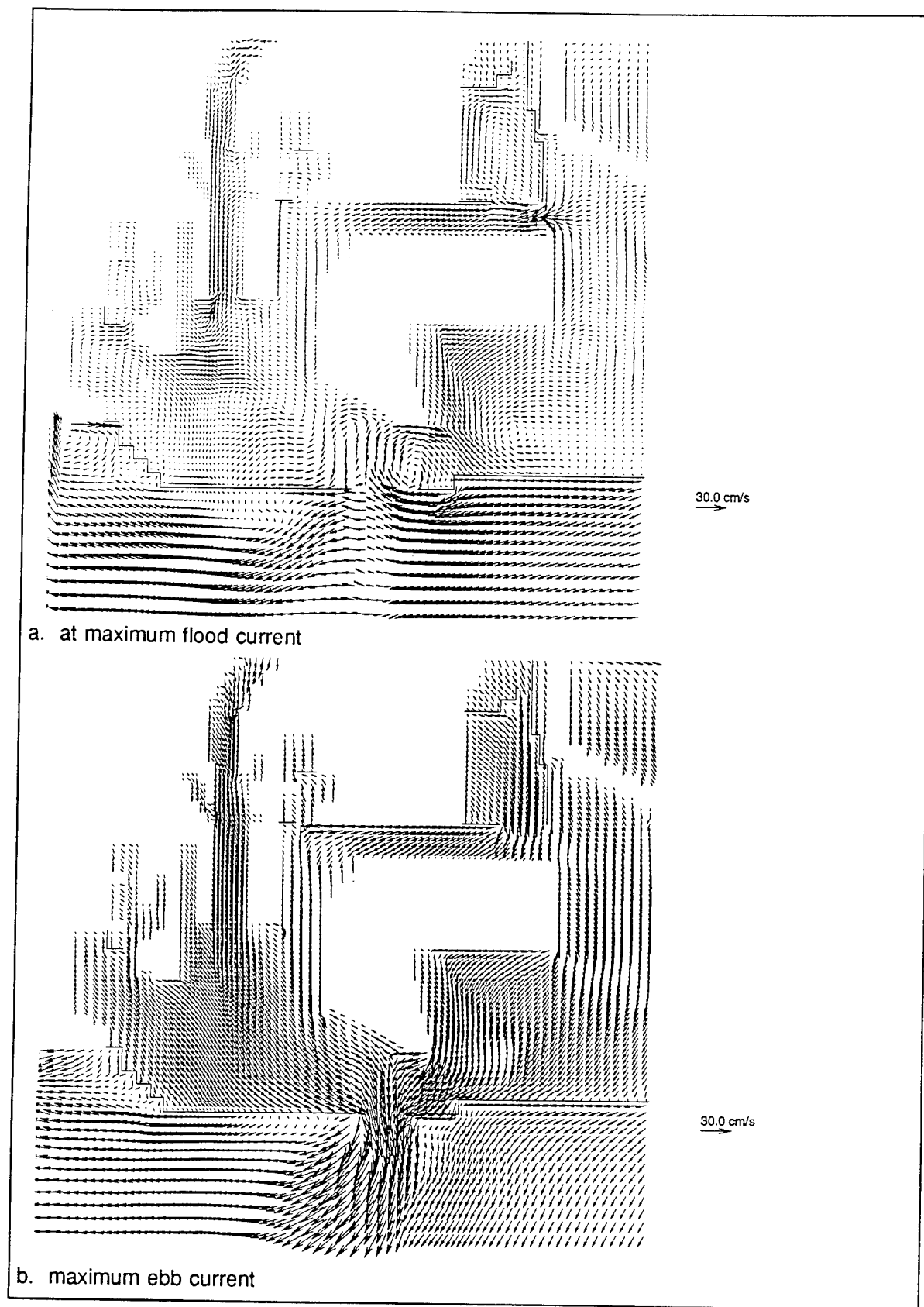
Figure C15. Vector plot of POLA 2 bottom layer circulation under SE20

C16

30.0 cm/s

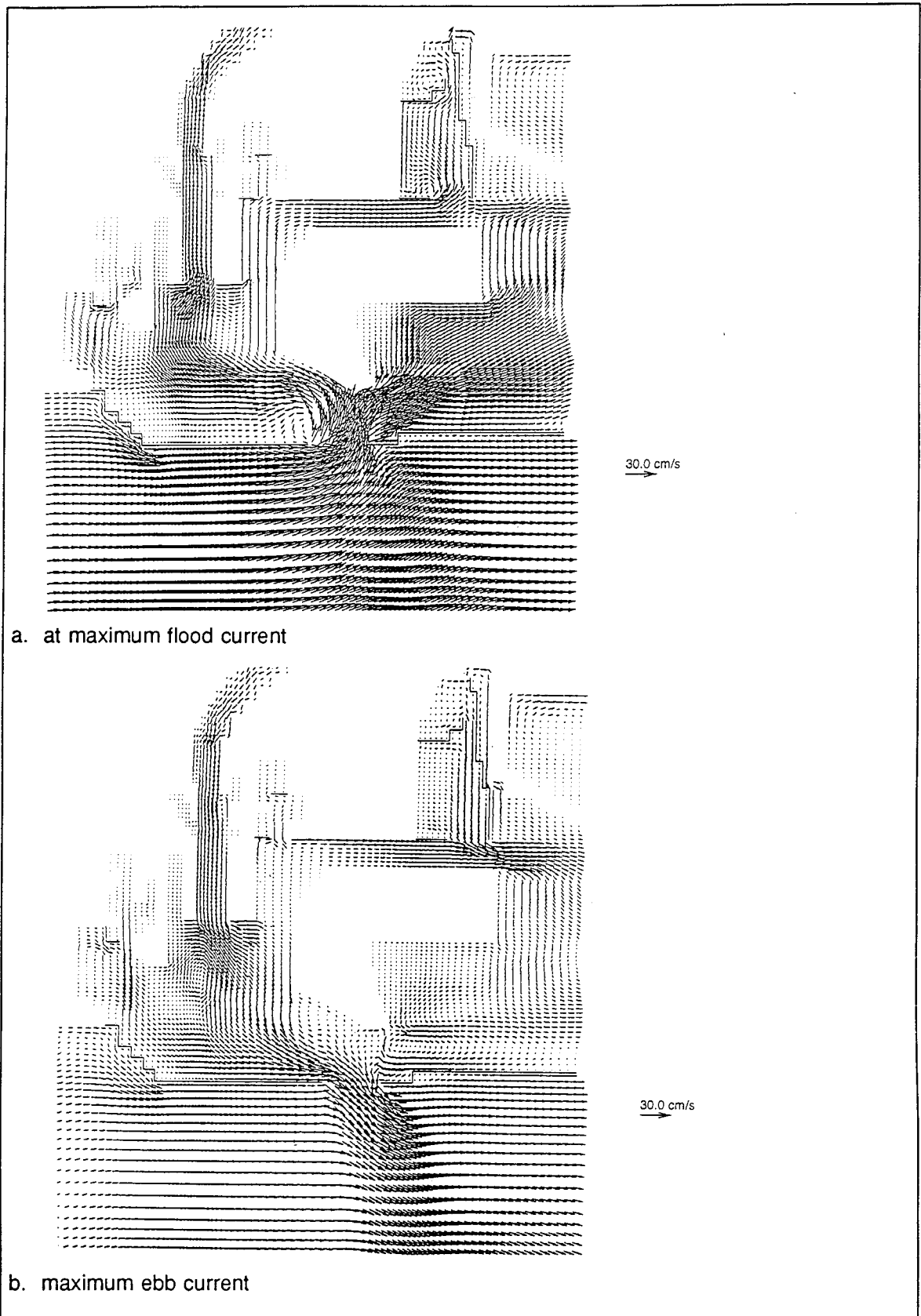a. at maximum flood current

30.0 cm/s

b. maximum ebb current
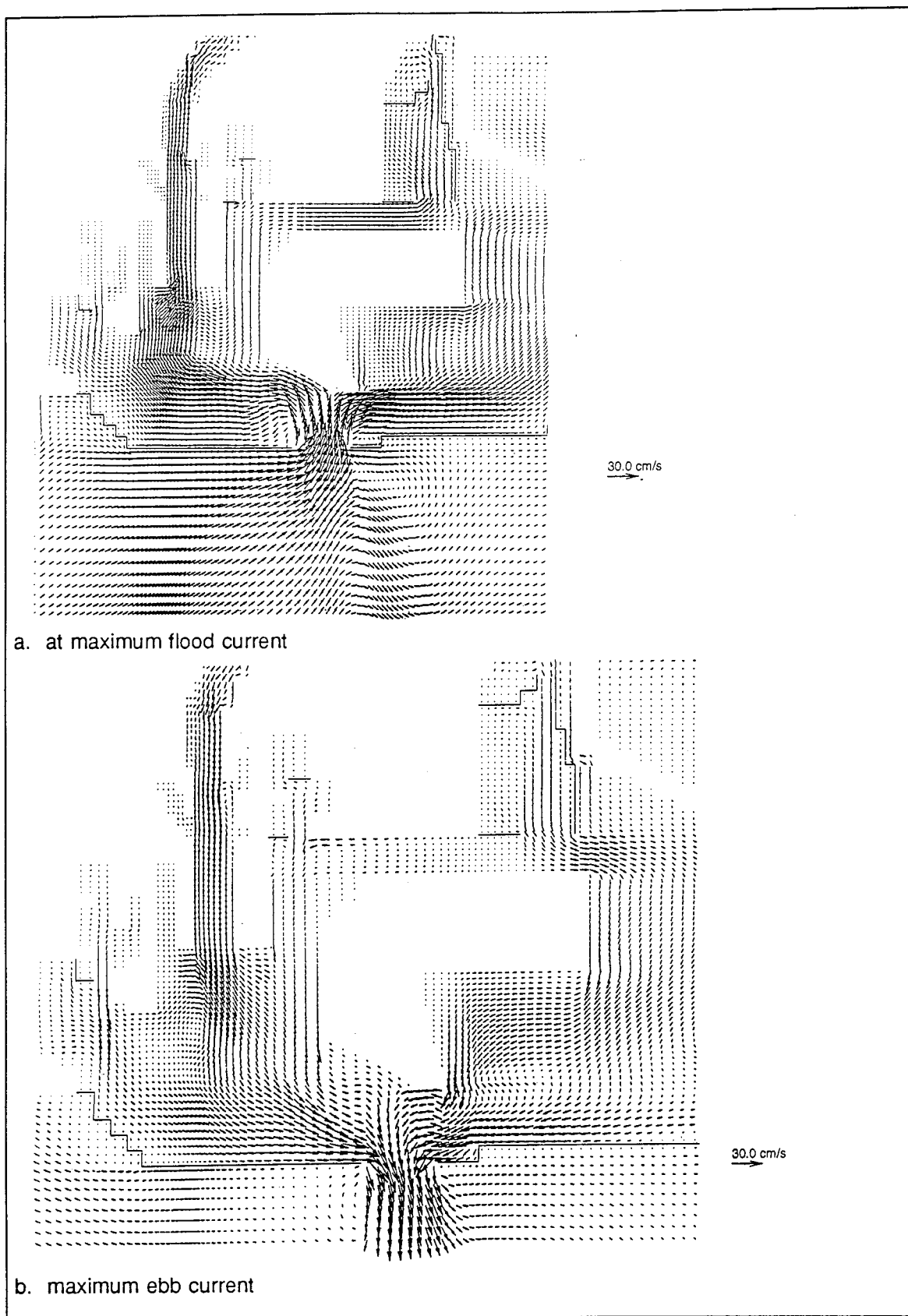
Figure C16. Vector plot of POLA 2 vertical averaged circulation under BW

30.0 cm/s

a. at maximum flood current

30.0 cm/s
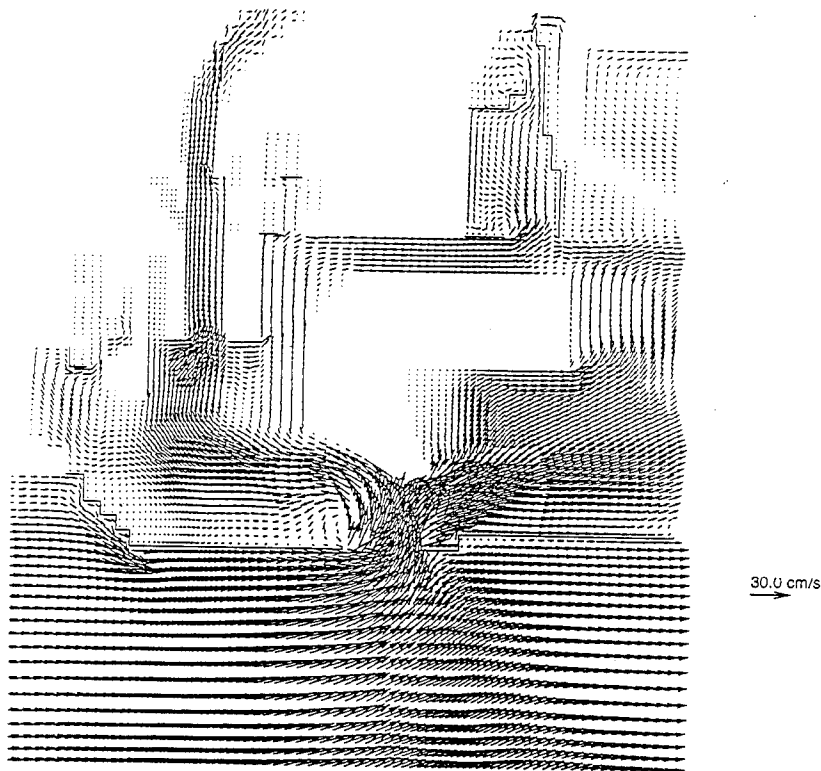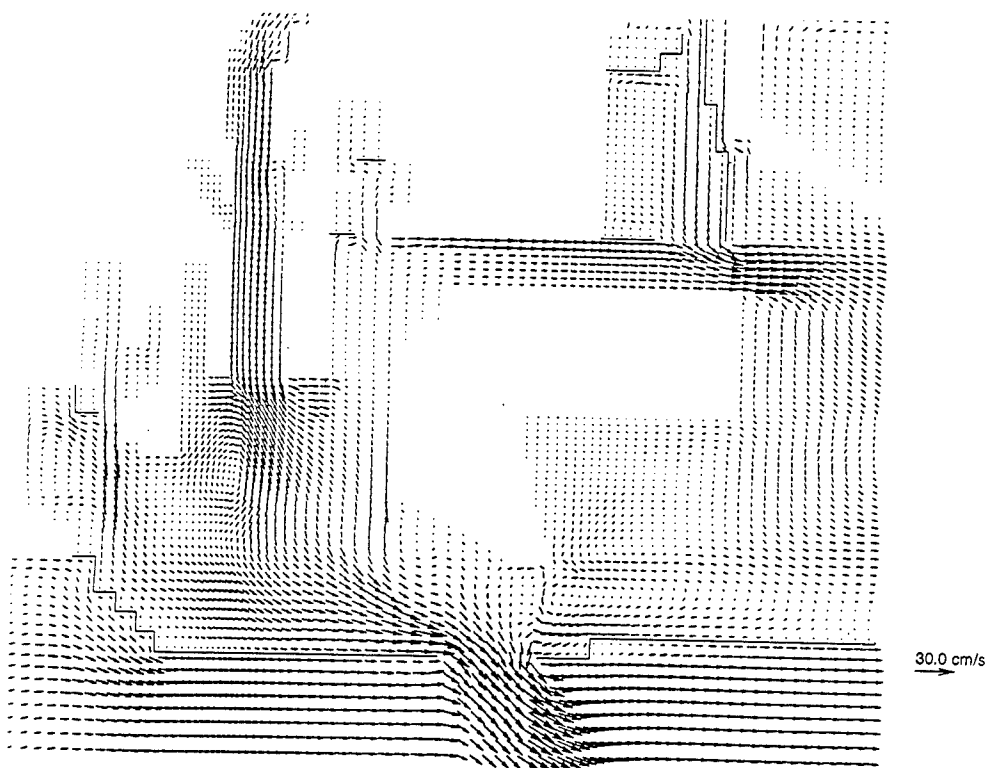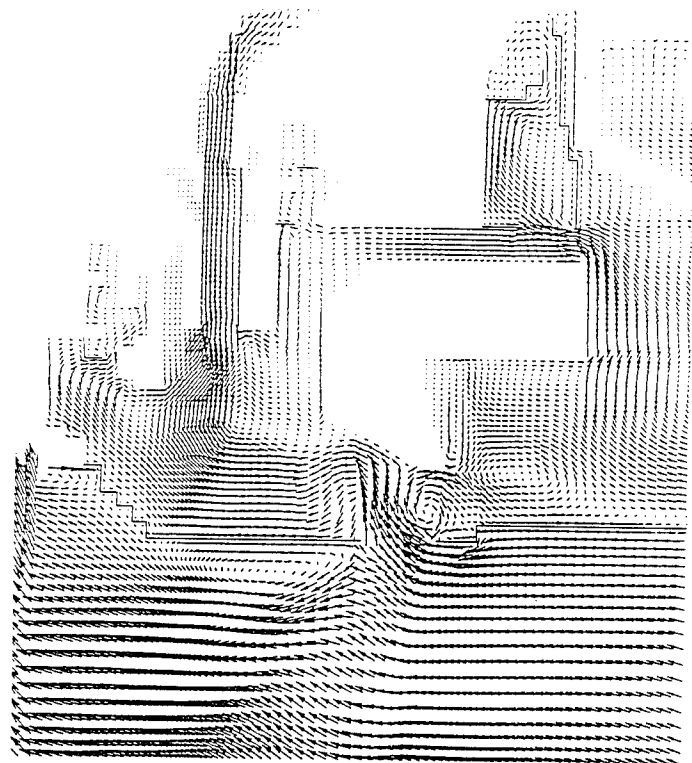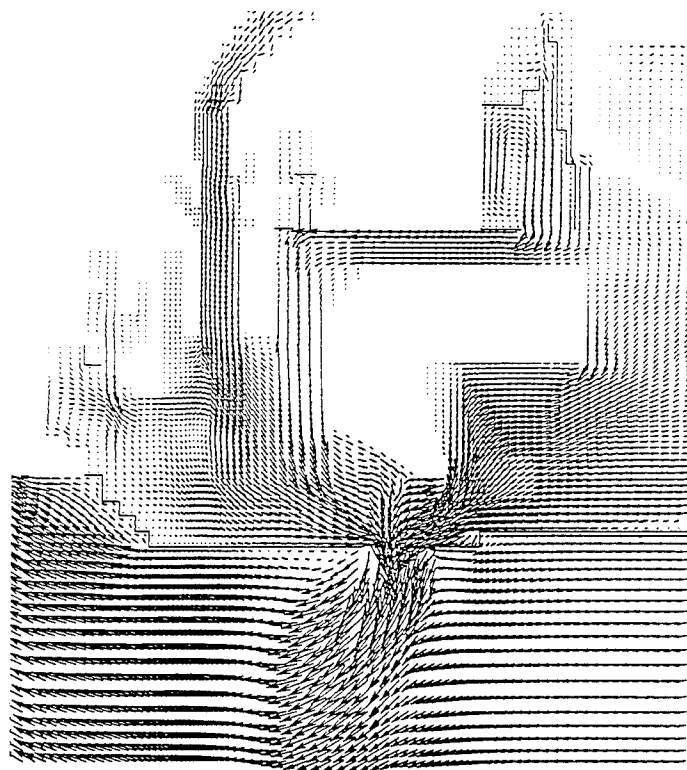
b. maximum ebb current

Figure C17. Vector plot of POLA 2 vertical averaged circulation under WSW20

C18

30.0 cm/s

a. at maximum flood current

30.0 cm/s

b. maximum ebb current
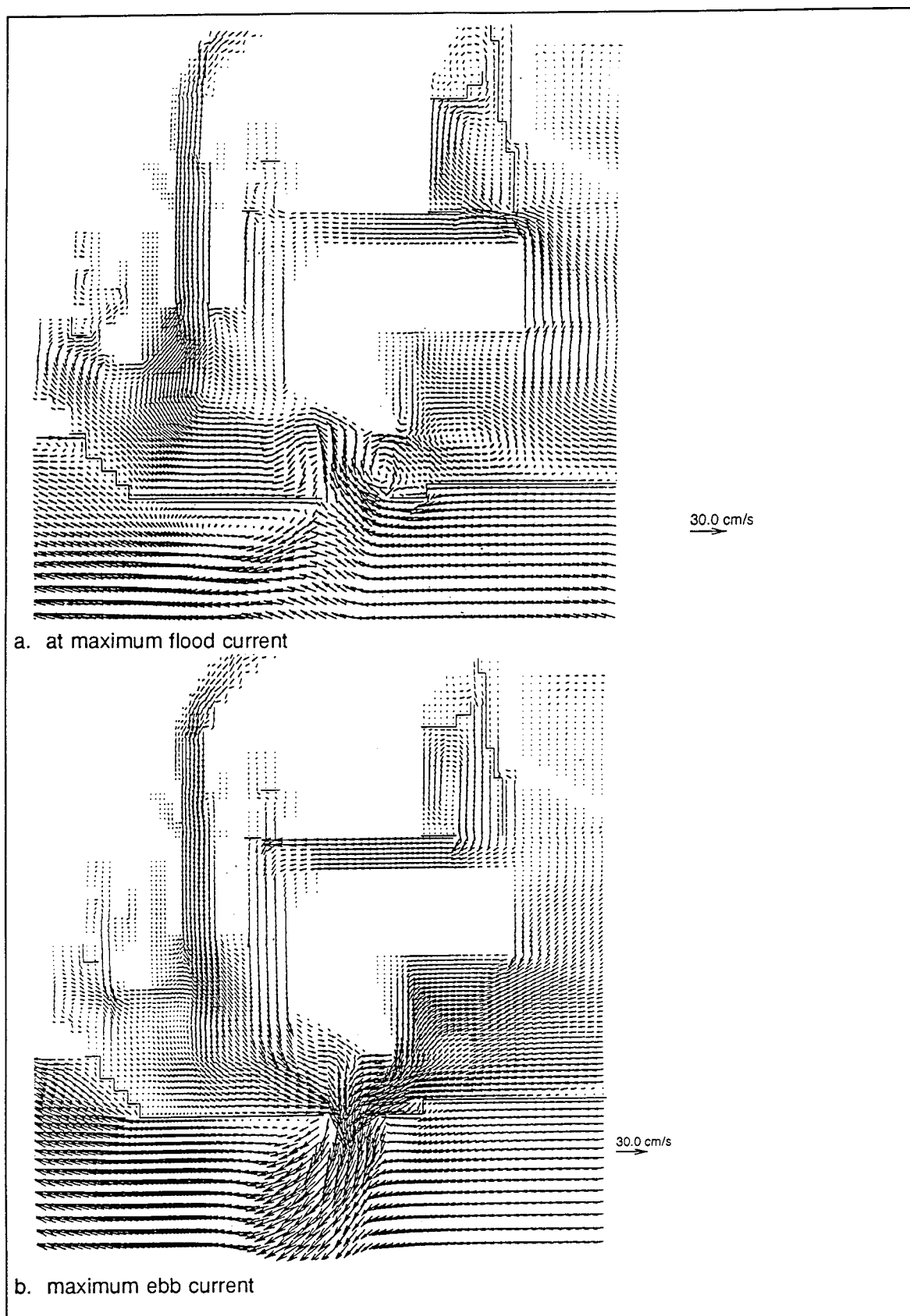
Figure C18. Vector plot of POLA 2 vertical averaged circulation under SE20

30.0 cm/s

a. at maximum flood current

30.0 cm/s

b. maximum ebb current
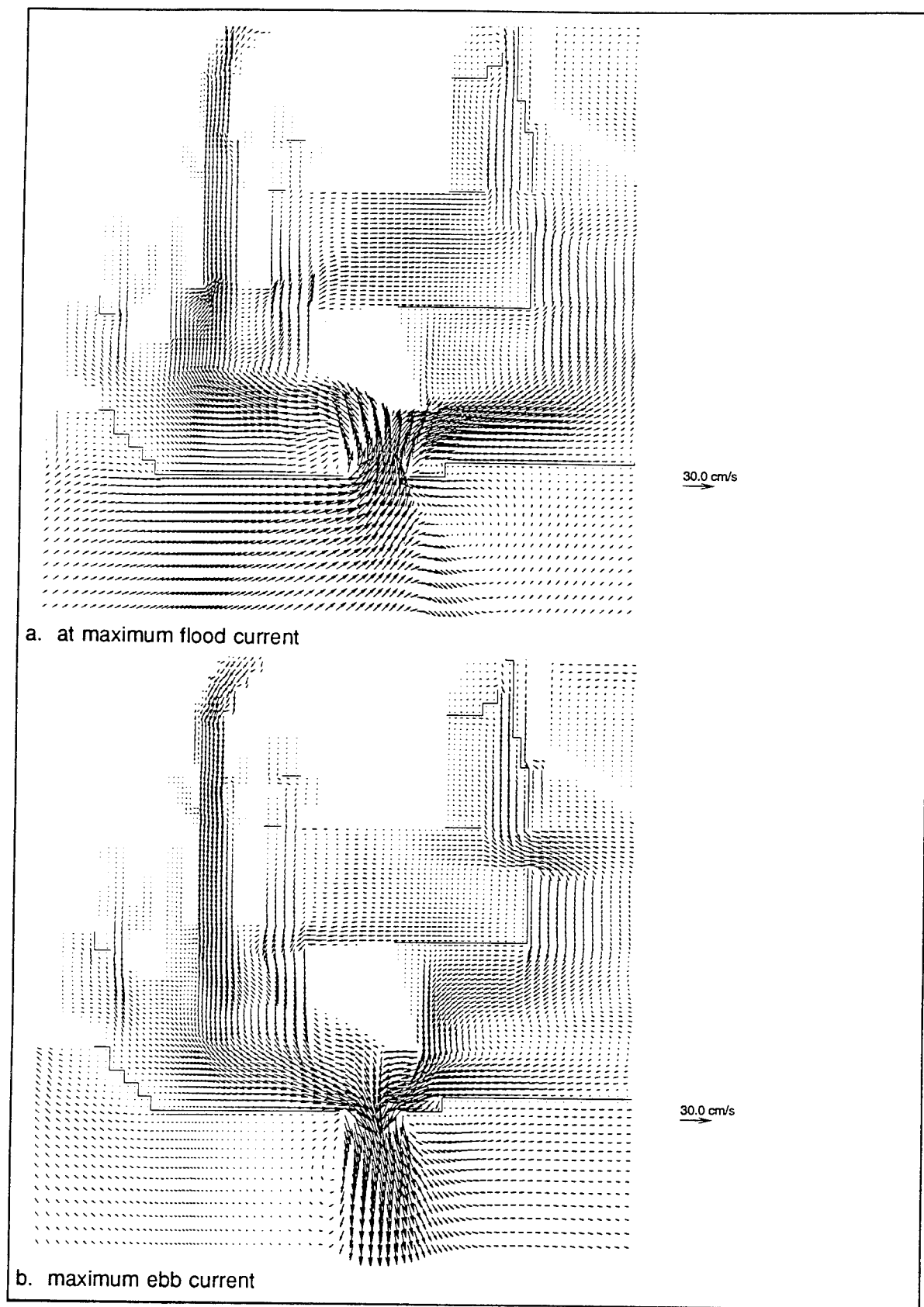
Figure C19. Vector plot of NED2 surface layer circulation under BW

a. at maximum flood current

b. maximum ebb current
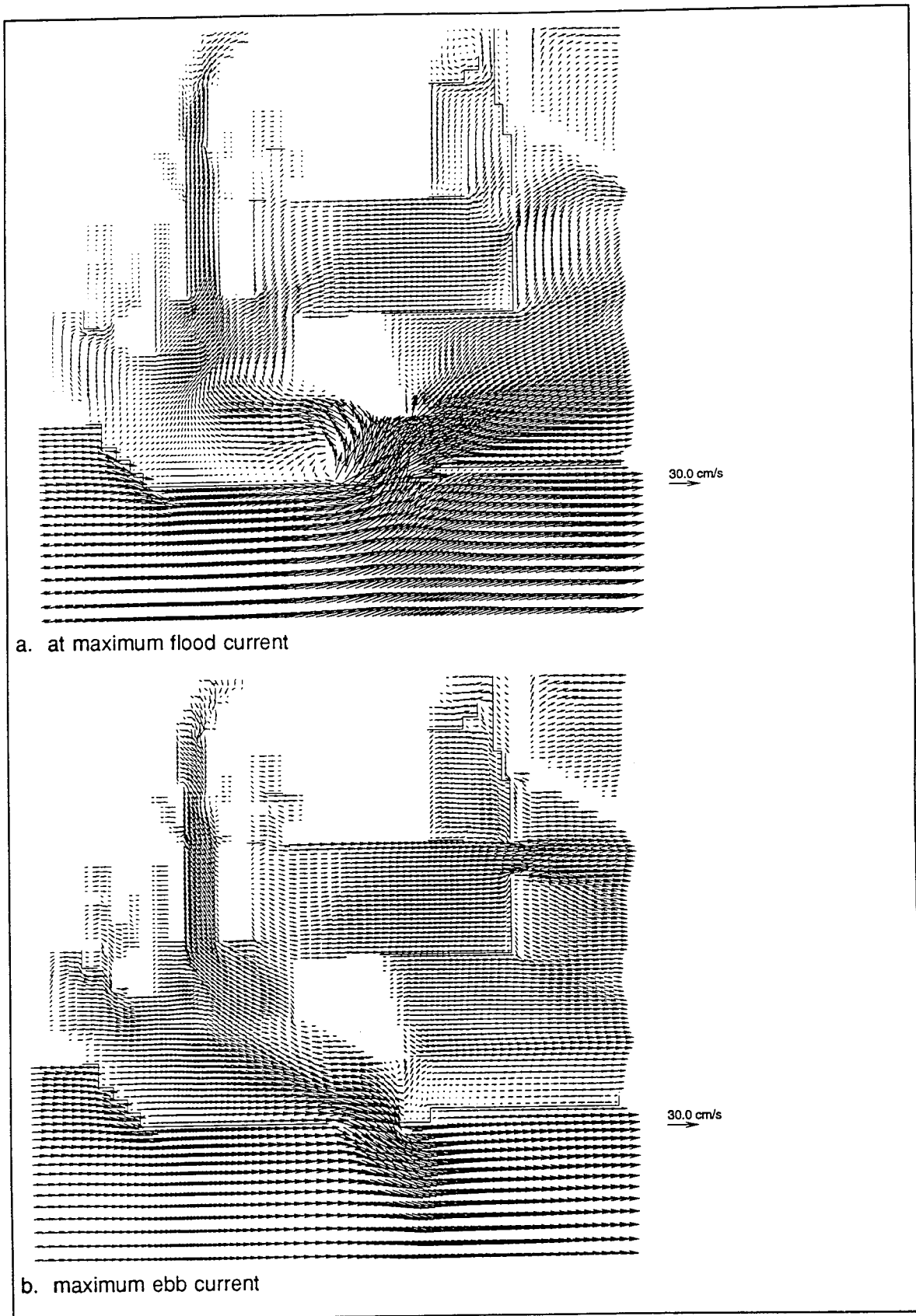
Figure C20. Vector plot of NED2 surface layer circulation under WSW20

a. at maximum flood current

b. maximum ebb current
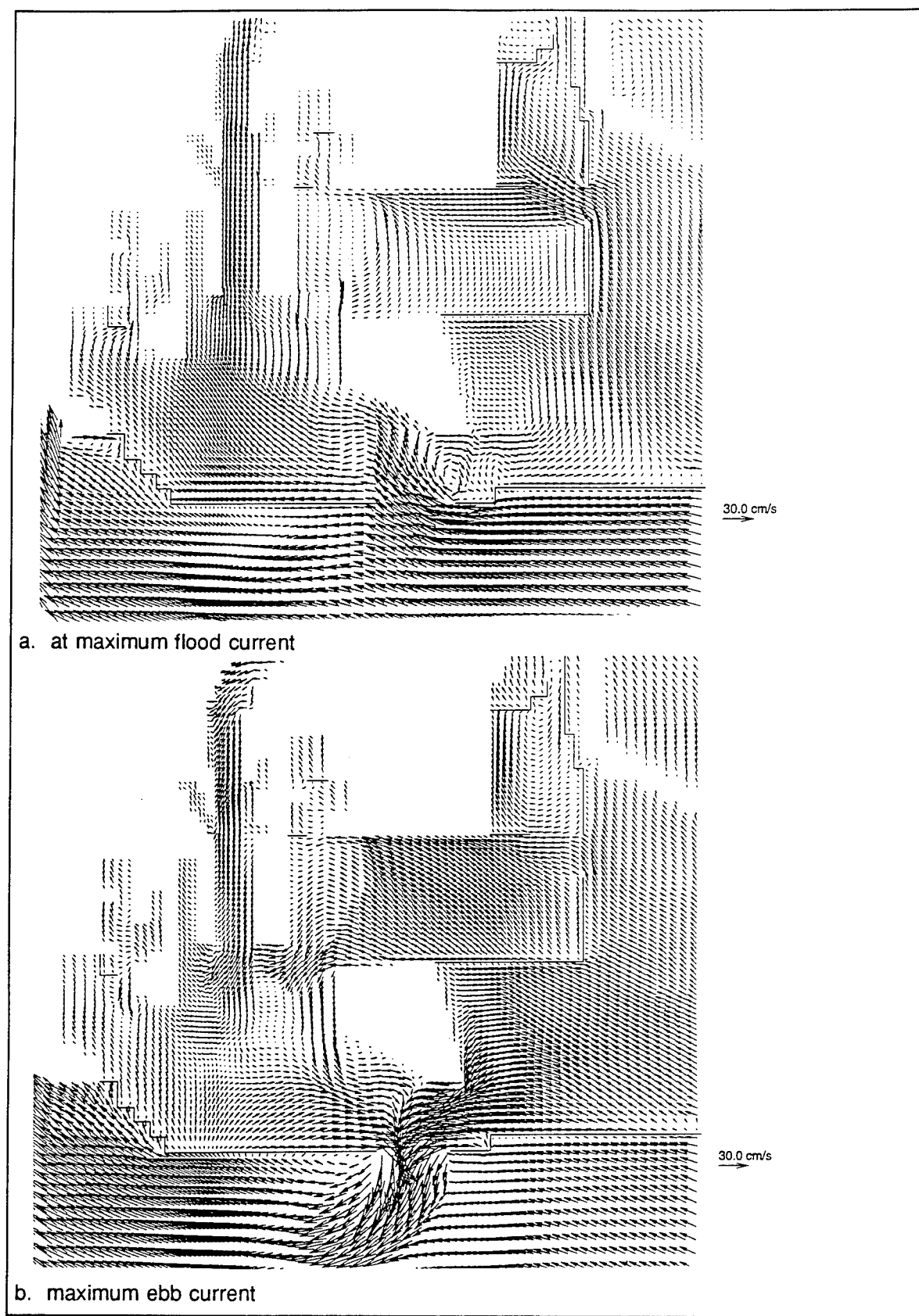
Figure C21. Vector plot of NED2 surface layer circulation under SE20

a. at maximum flood current

b. maximum ebb current
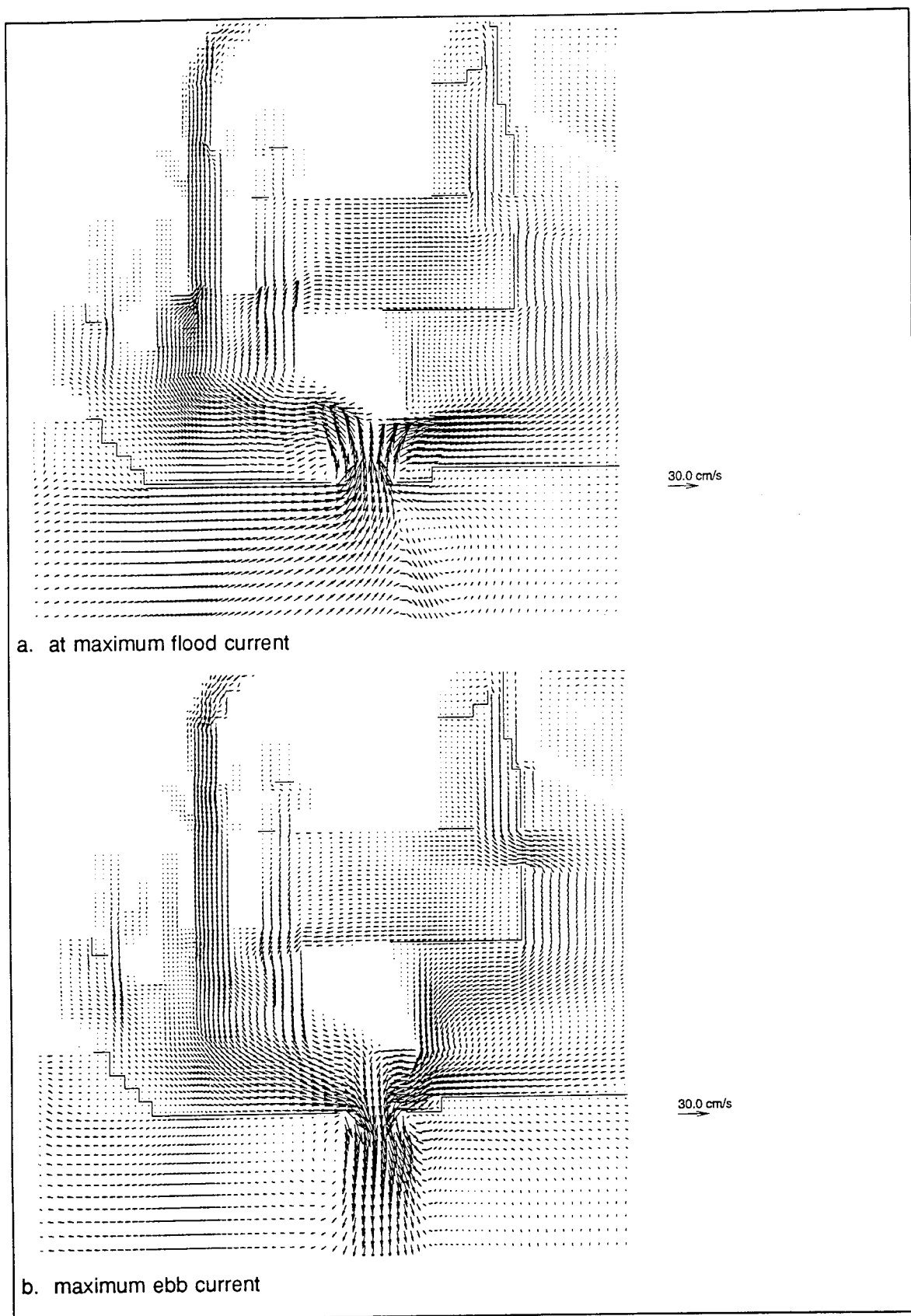
Figure C22. Vector plot of NED2 bottom layer circulation under BW

Appendix C   Velocity Vector Plots in Support of the Ship Simulation Model

30.0 cm/s

a. at maximum flood current

30.0 cm/s

b. maximum ebb current
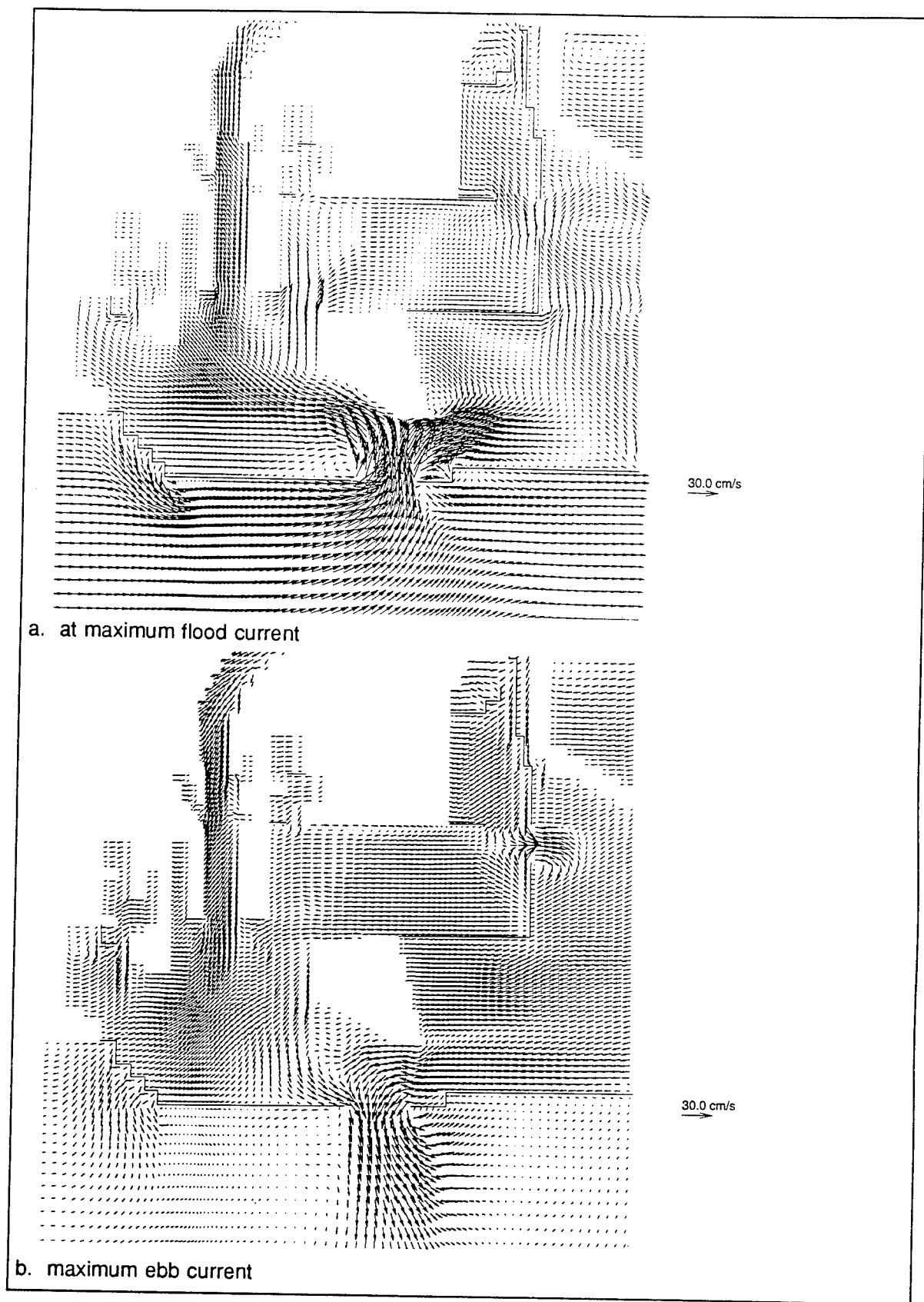
Figure C23. Vector plot of NED2 bottom layer circulation under WSW20

C24

30.0 cm/s

a. at maximum flood current

30.0 cm/s

b. maximum ebb current
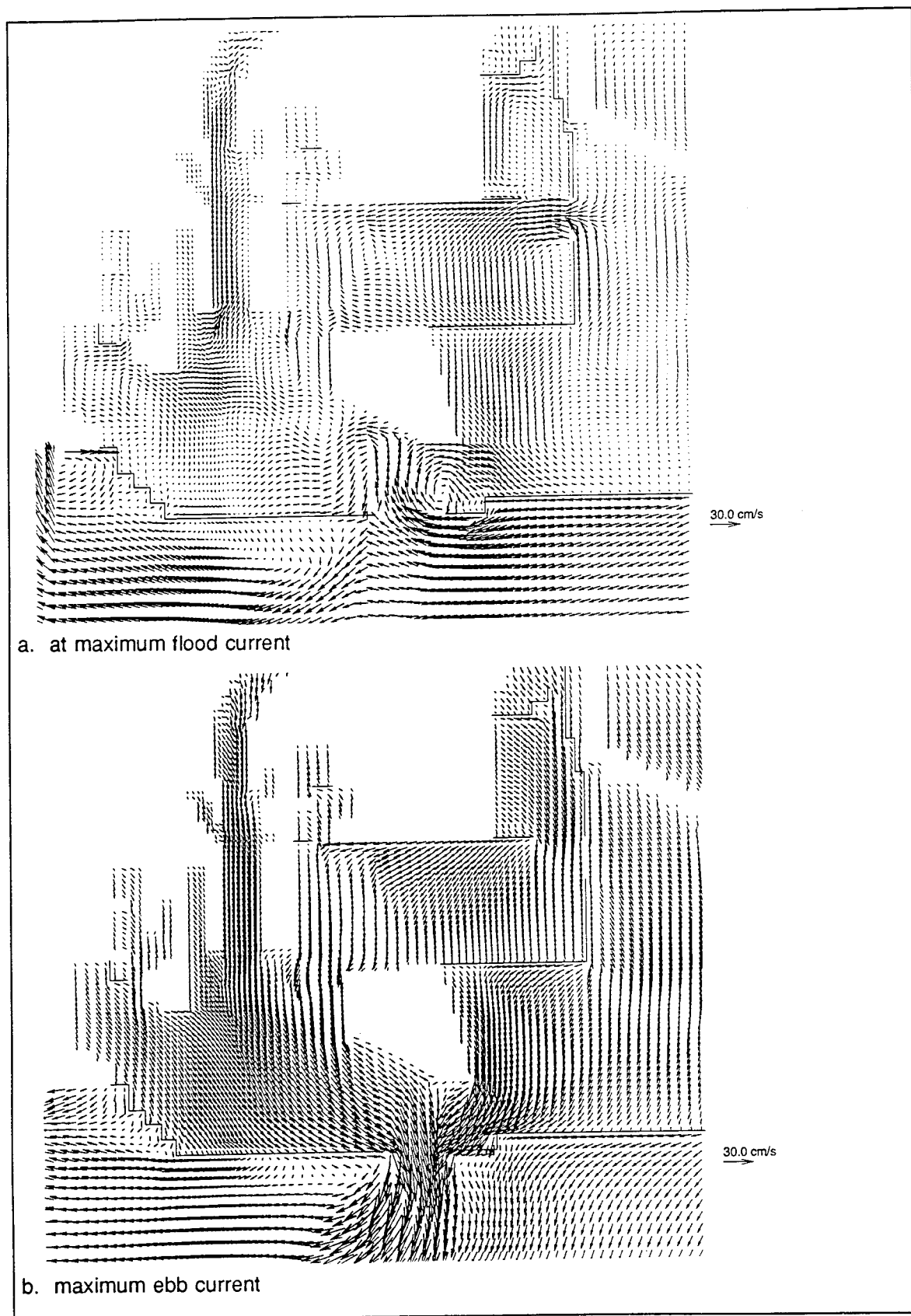
Figure C24. Vector plot of NED2 bottom layer circulation under SE20

C25

a. at maximum flood current

b. maximum ebb current
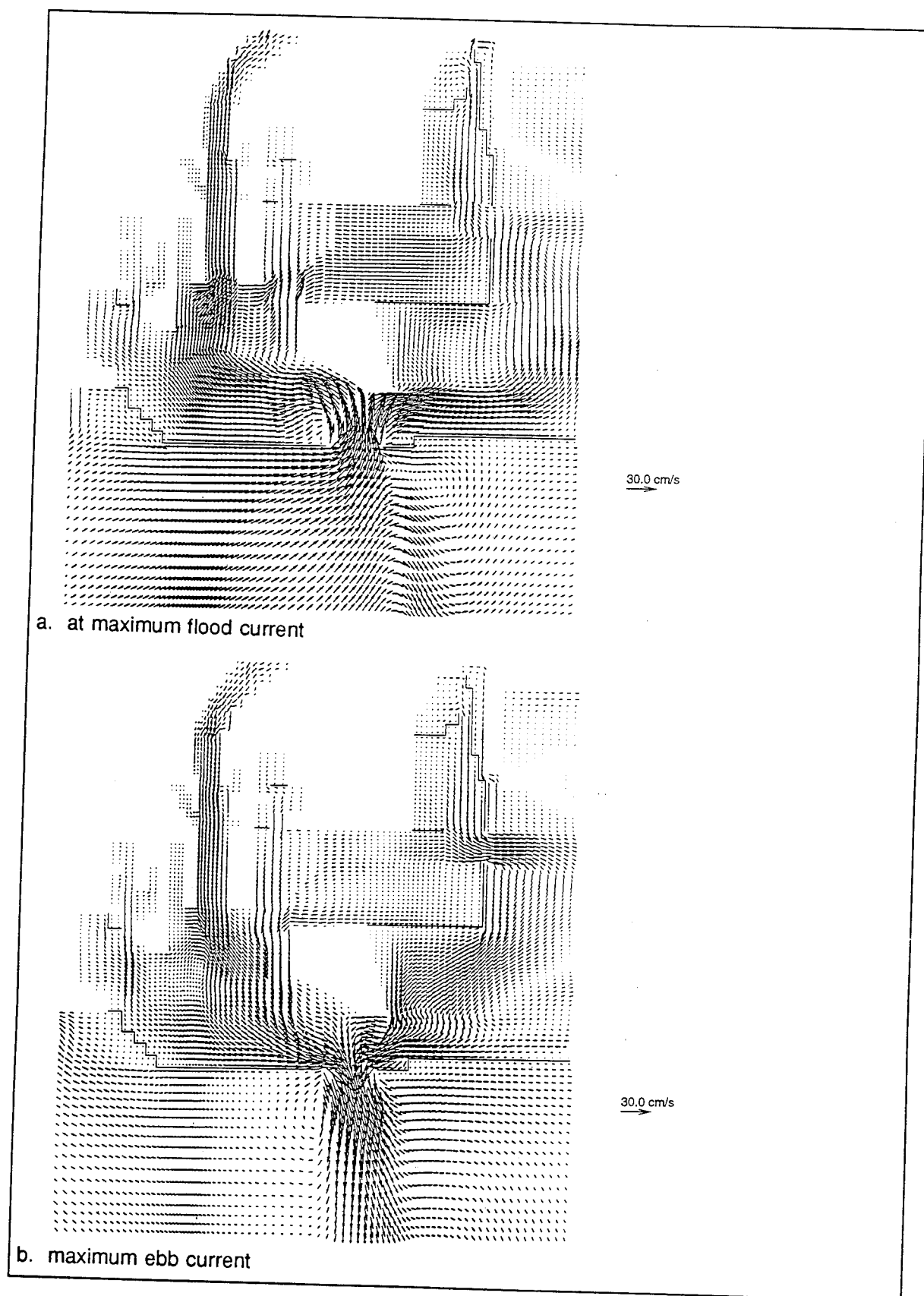
Figure C25. Vector plot of NED2 vertical averaged circulation under BW

30.0 cm/s

a. at maximum flood current

30.0 cm/s

b. maximum ebb current
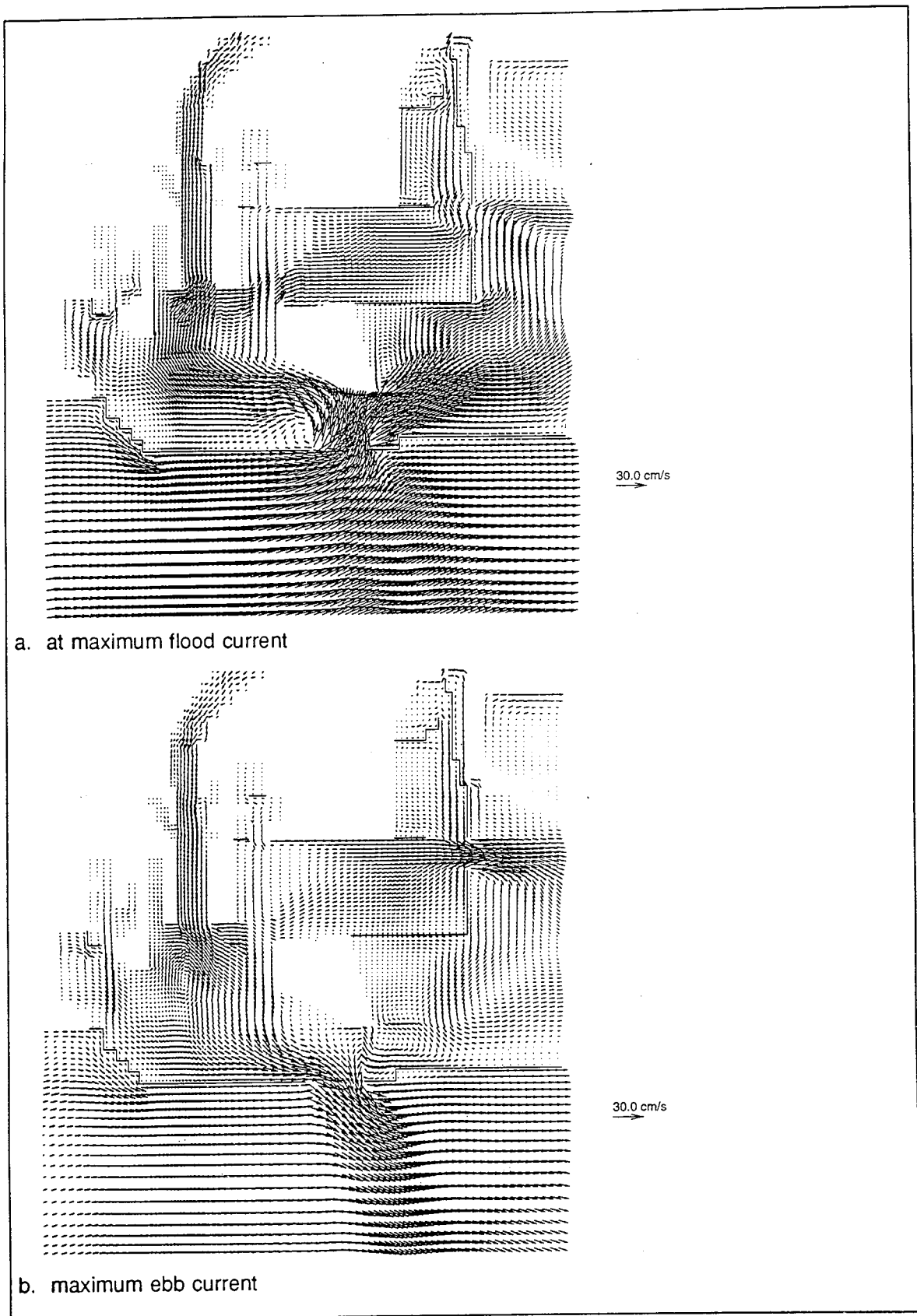
Figure C26. Vector plot of NED2 vertical averaged circulation under WSW20

a. at maximum flood current

b. maximum ebb current
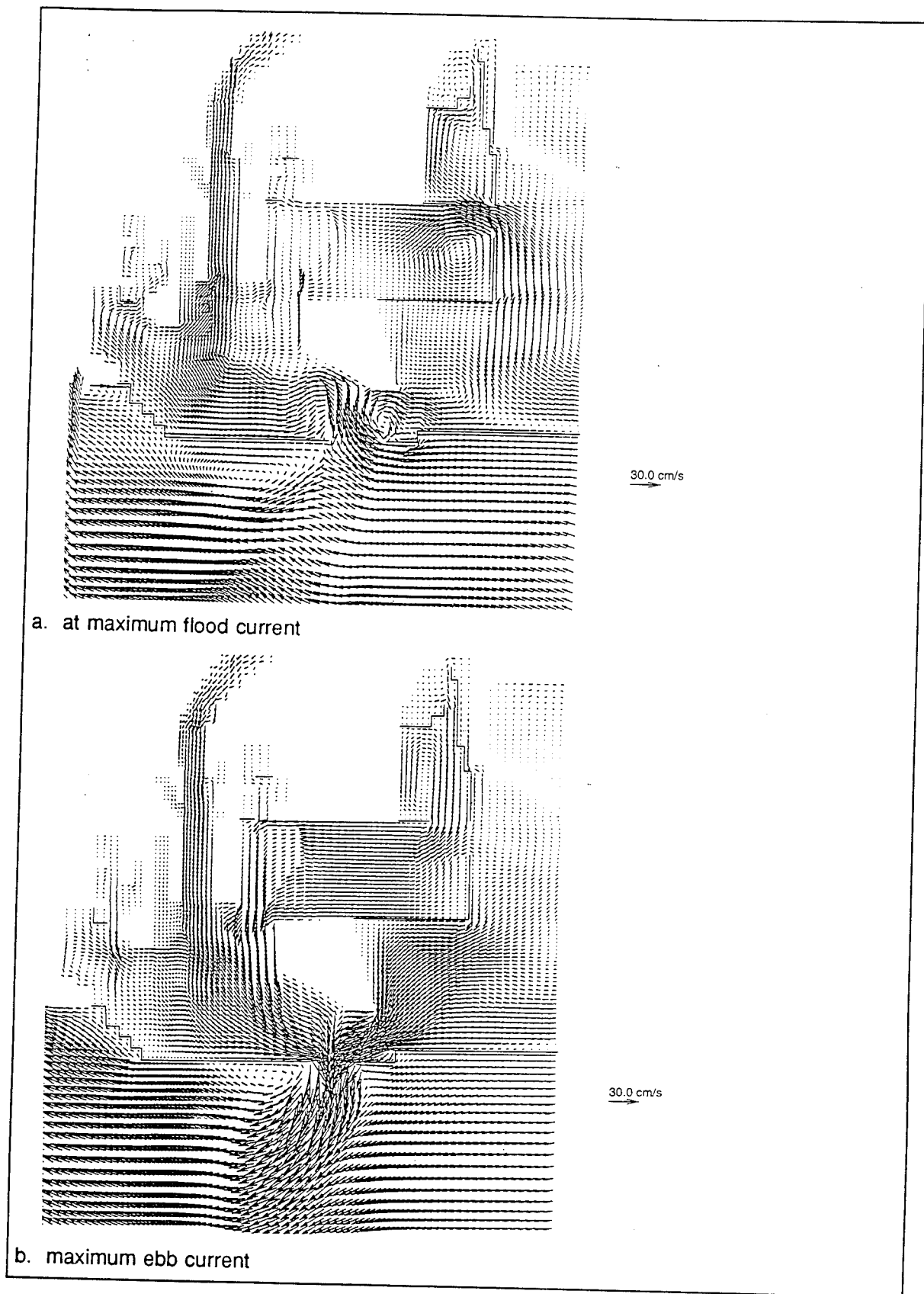
Figure C27. Vector plot of NED2 vertical averaged circulation under SE20

C28

a. at maximum flood current

30.0 cm/s

b. maximum ebb current

30.0 cm/s
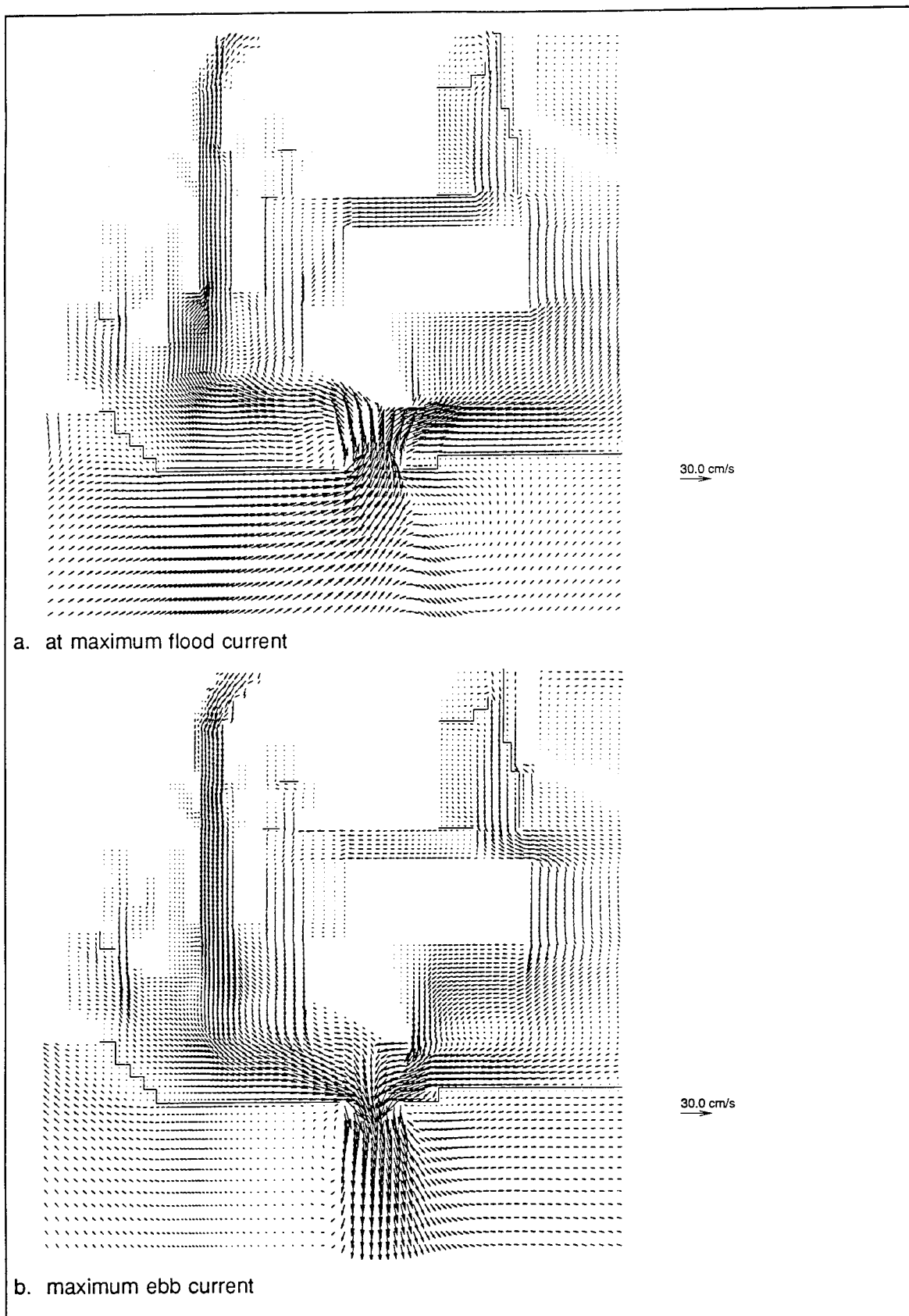
Figure C28. Vector plot of NED2&3 surface layer circulation under BW
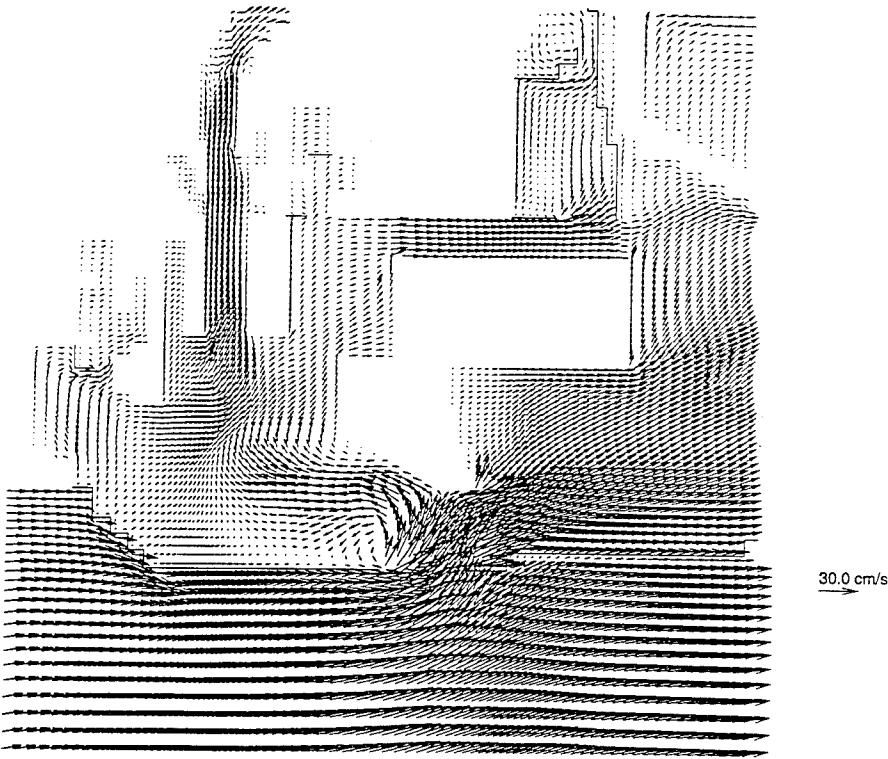
a. at maximum flood current
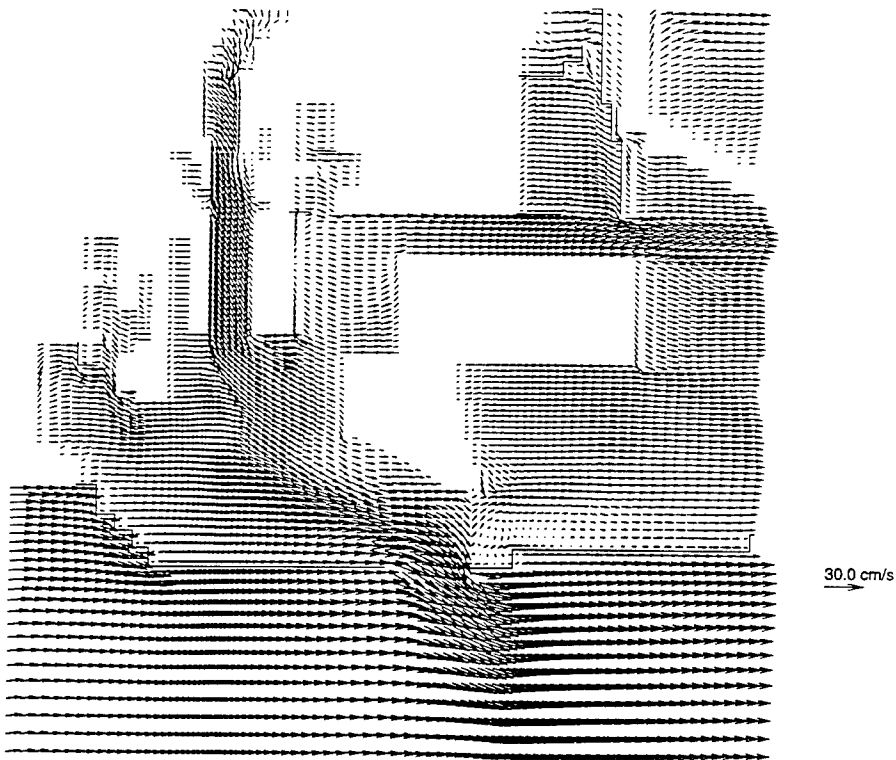
b. maximum ebb current

Figure C29. Vector plot of NED2&3 surface layer circulation under WSW20

a. at maximum flood current

b. maximum ebb current
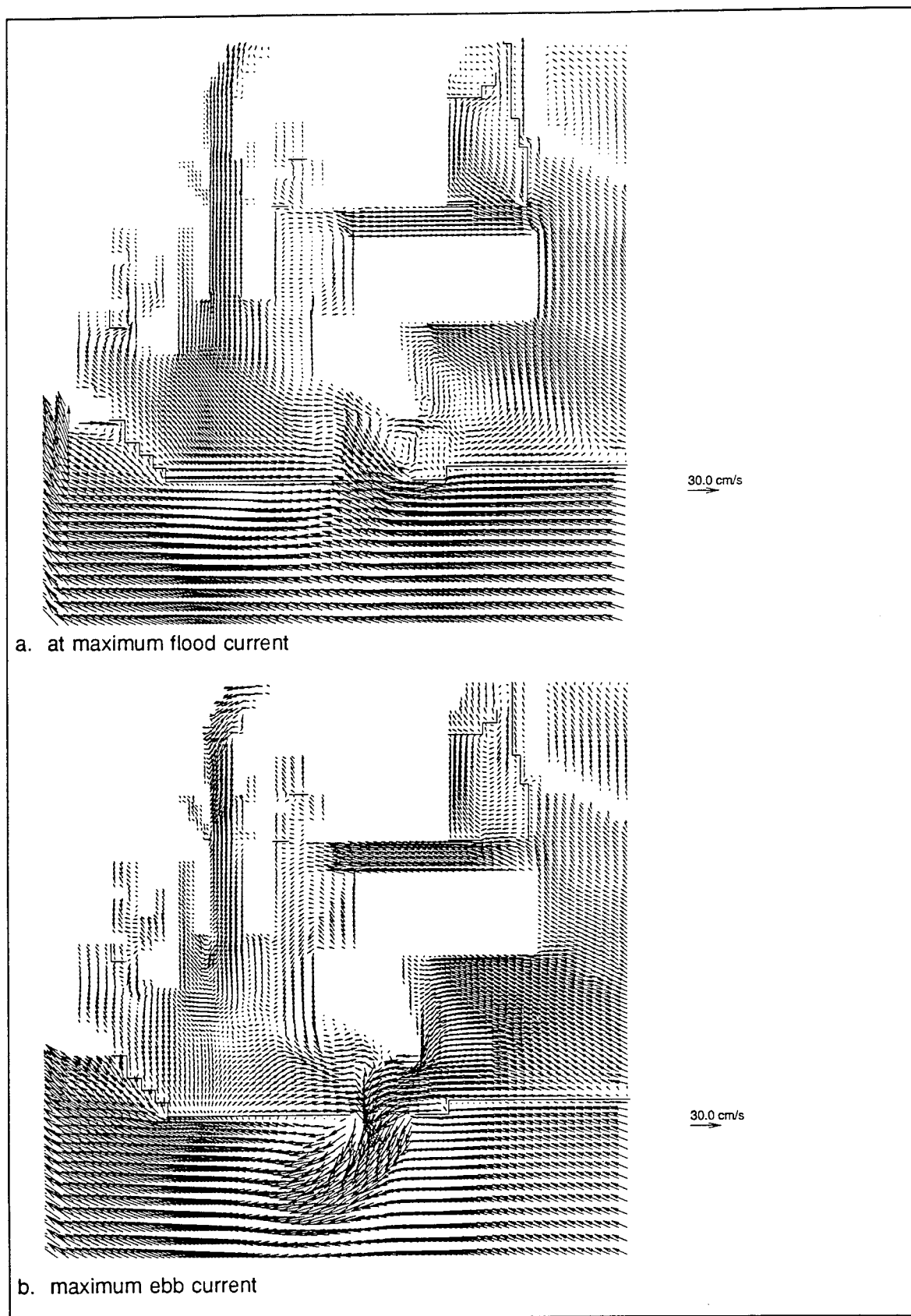
Figure C30. Vector plot of NED2&3 surface layer circulation under SE20

30.0 cm/s

a. at maximum flood current

30.0 cm/s

b. maximum ebb current
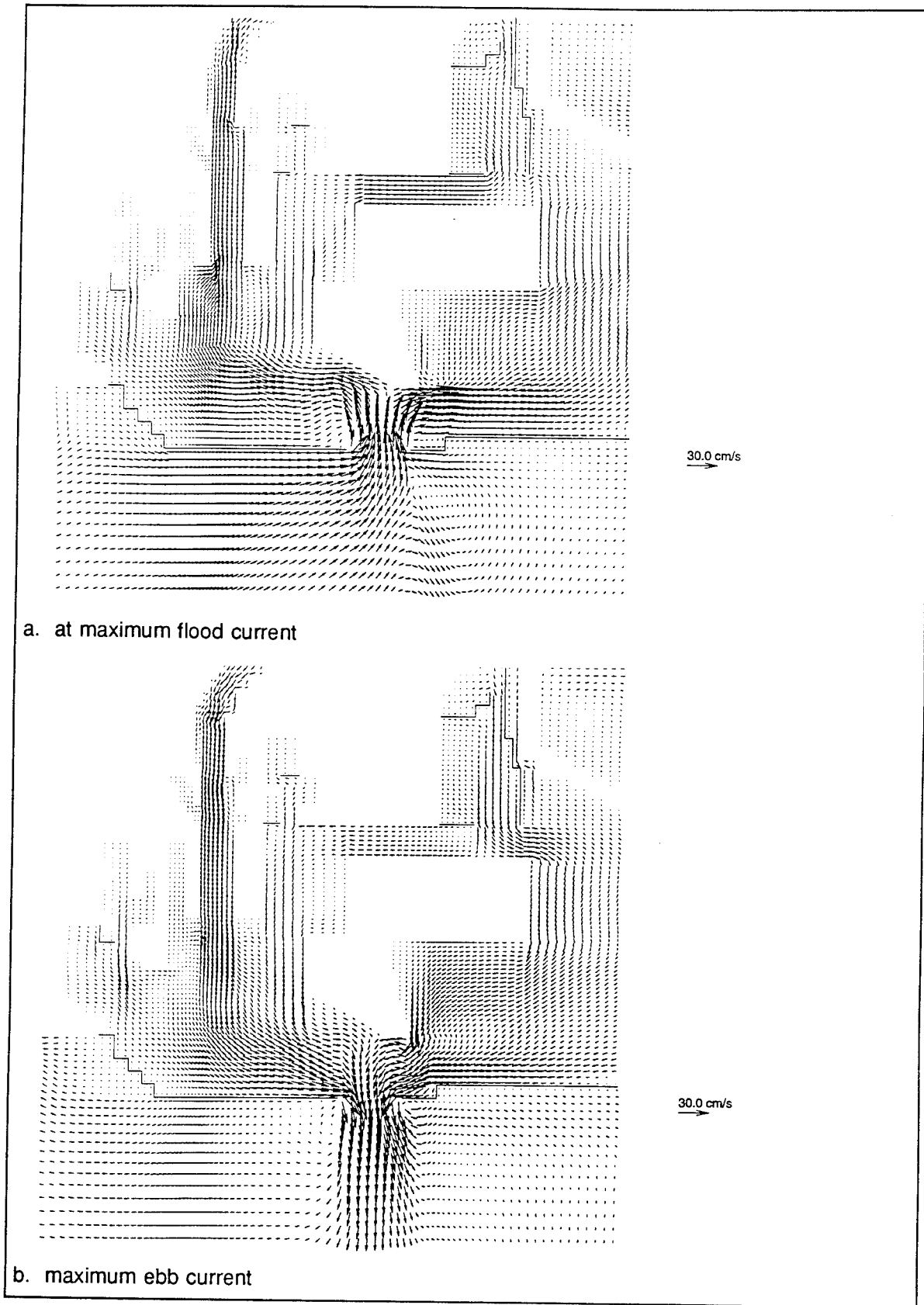
Figure C31. Vector plot of NED2&3 bottom layer circulation under BW

C32

a. at maximum flood current

30.0 cm/s

b. maximum ebb current

30.0 cm/s
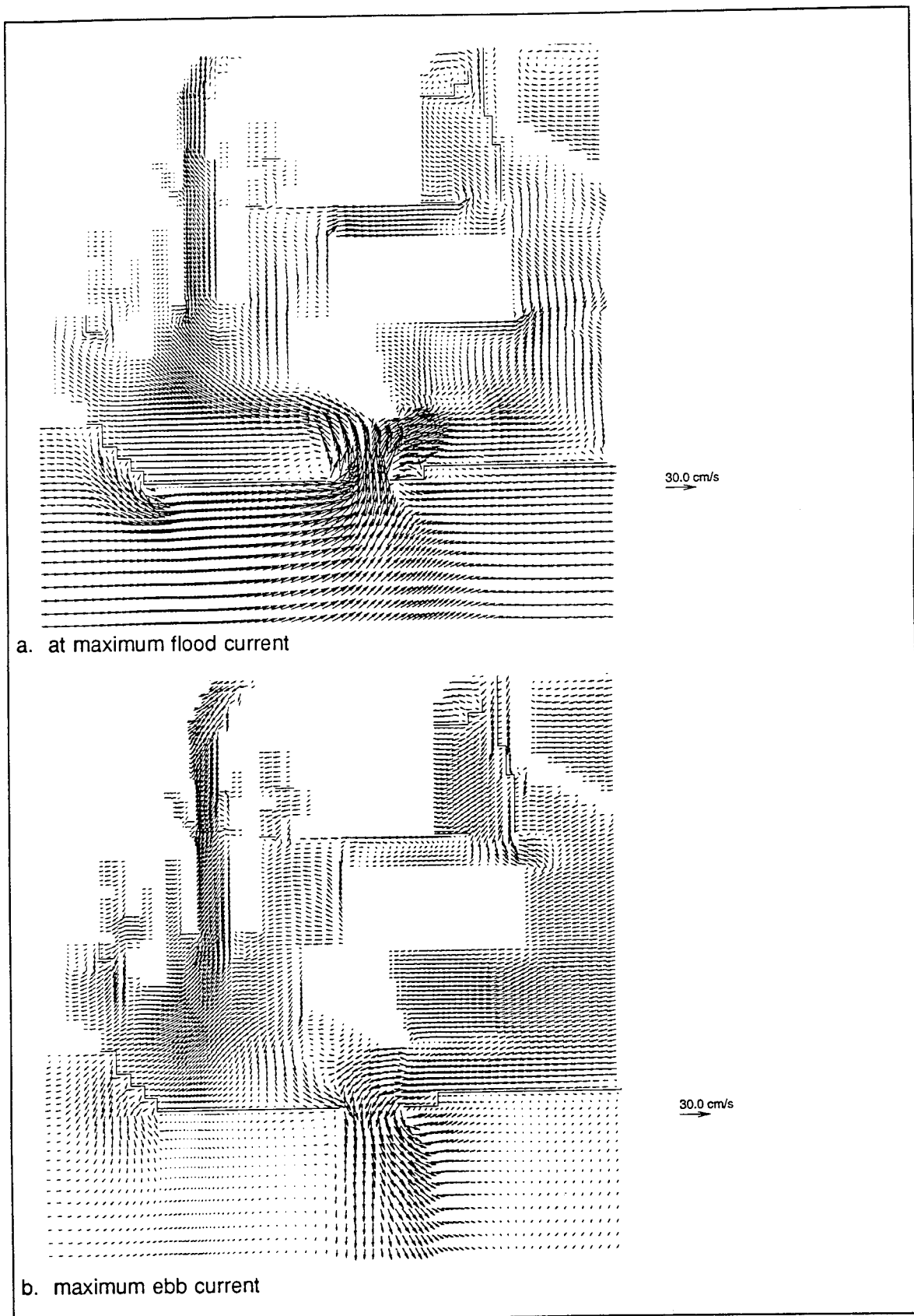
Figure C32. Vector plot of NED2&3 bottom layer circulation under WSW20
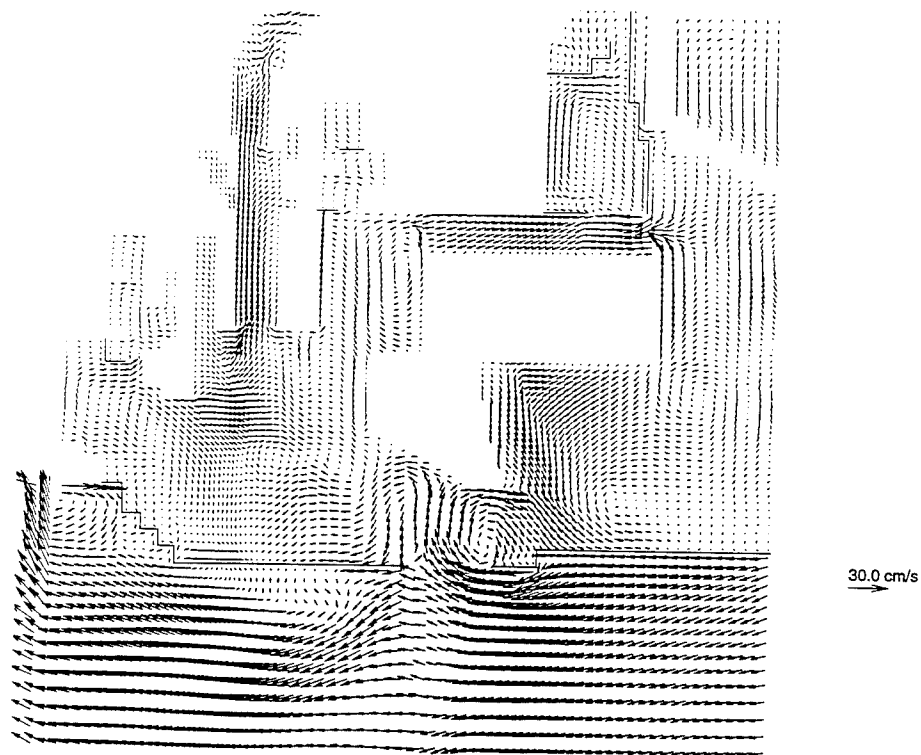
a. at maximum flood current
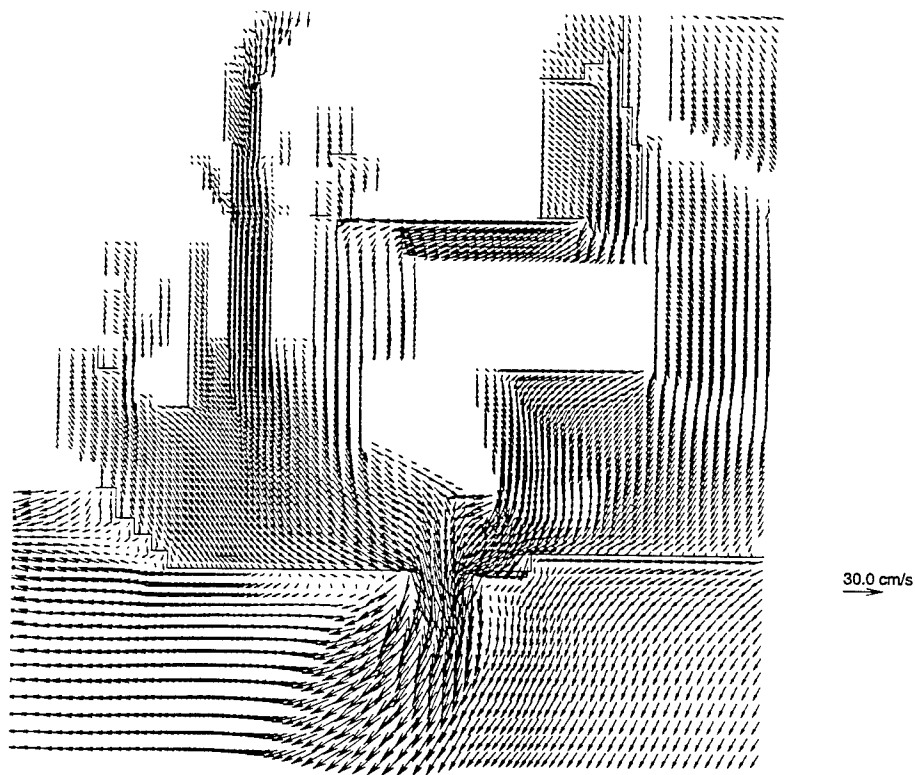
b. maximum ebb current

Figure C33. Vector plot of NED2&3 bottom layer circulation under SE20

C34

a. at maximum flood current

30.0 cm/s

b. maximum ebb current

30.0 cm/s
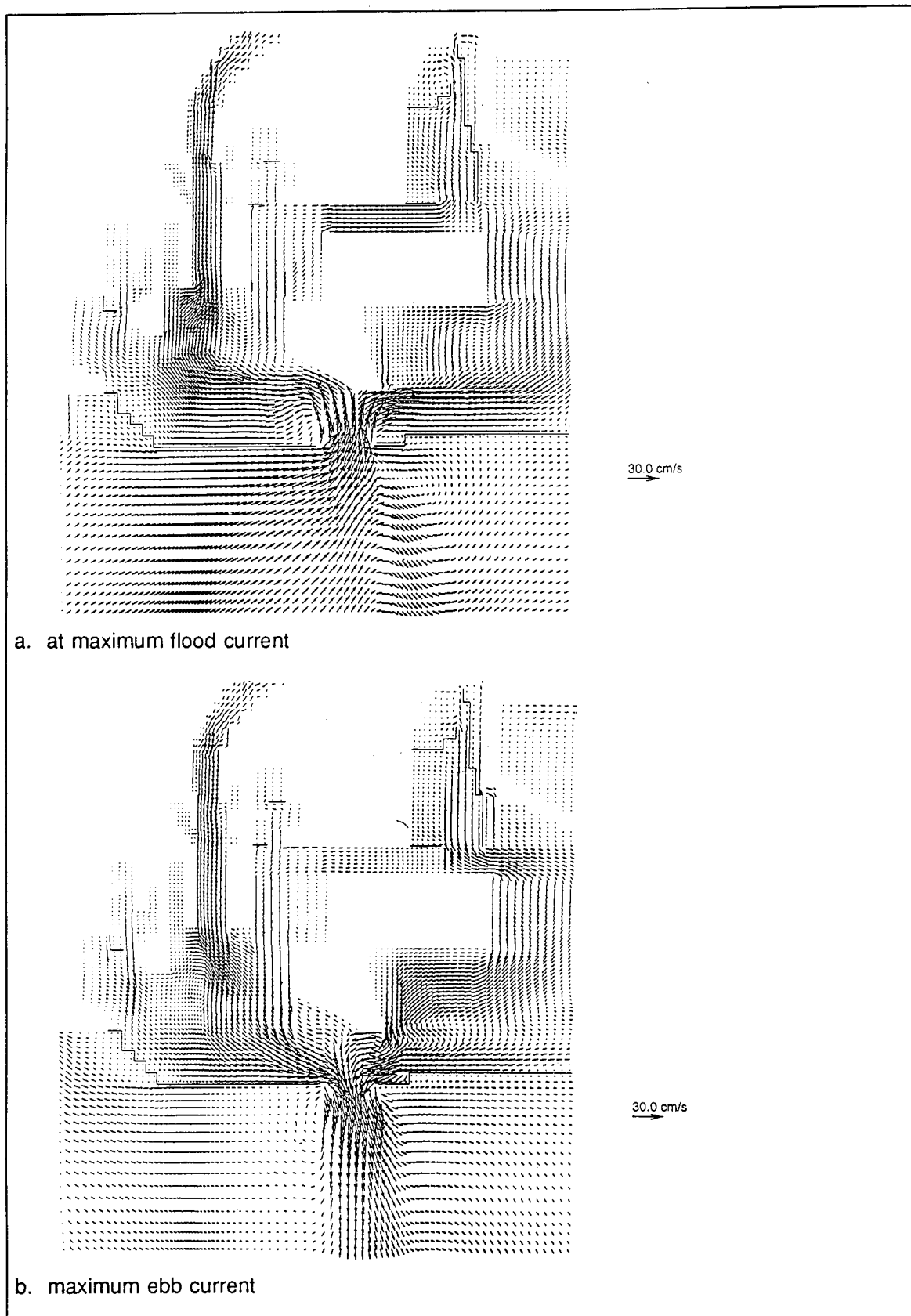
Figure C34. Vector plot of NED2&3 vertical averaged circulation under BW

a. at maximum flood current

30.0 cm/s

b. maximum ebb current

30.0 cm/s
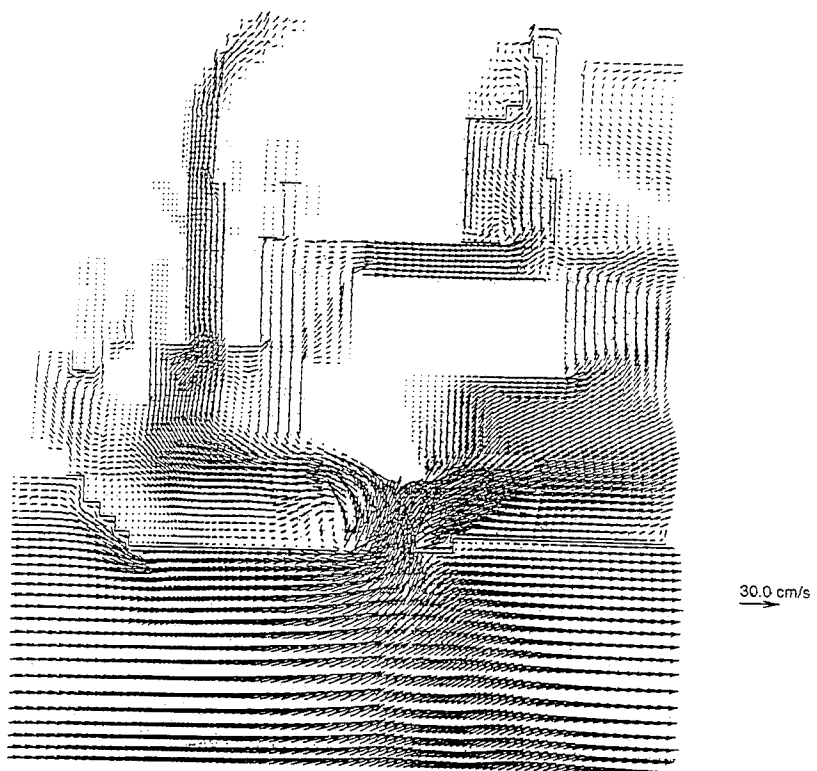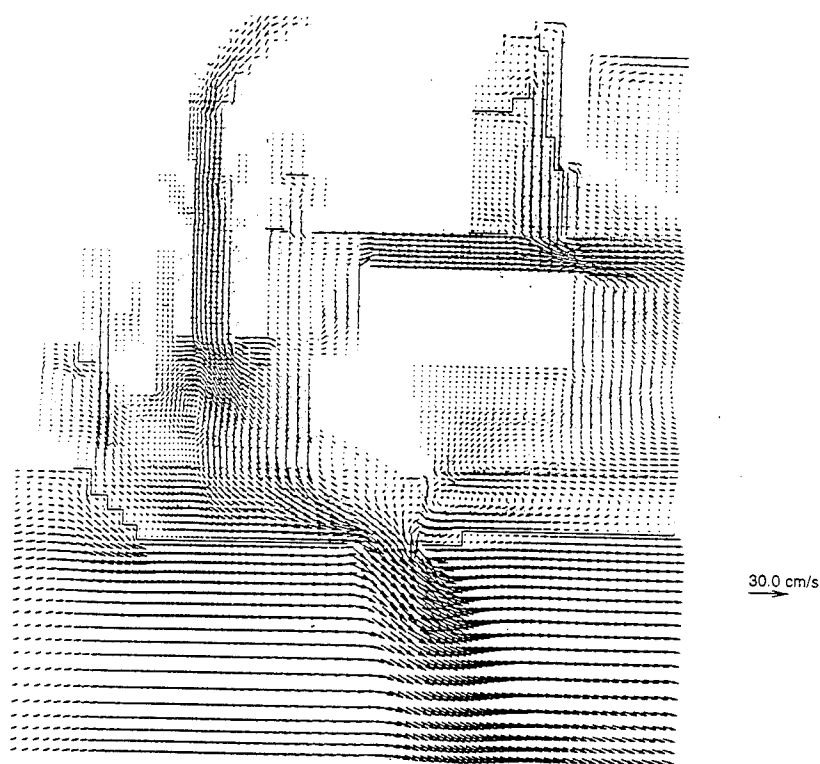
Figure C35. Vector plot of NED2&3 vertical averaged circulation under WSW20

a. at maximum flood current

30.0 cm/s

b. maximum ebb current

30.0 cm/s

Figure C36. Vector plot of NED2&3 vertical averaged circulation under SE20

30.0 cm/s

a. at maximum flood current

30.0 cm/s

b. maximum ebb current
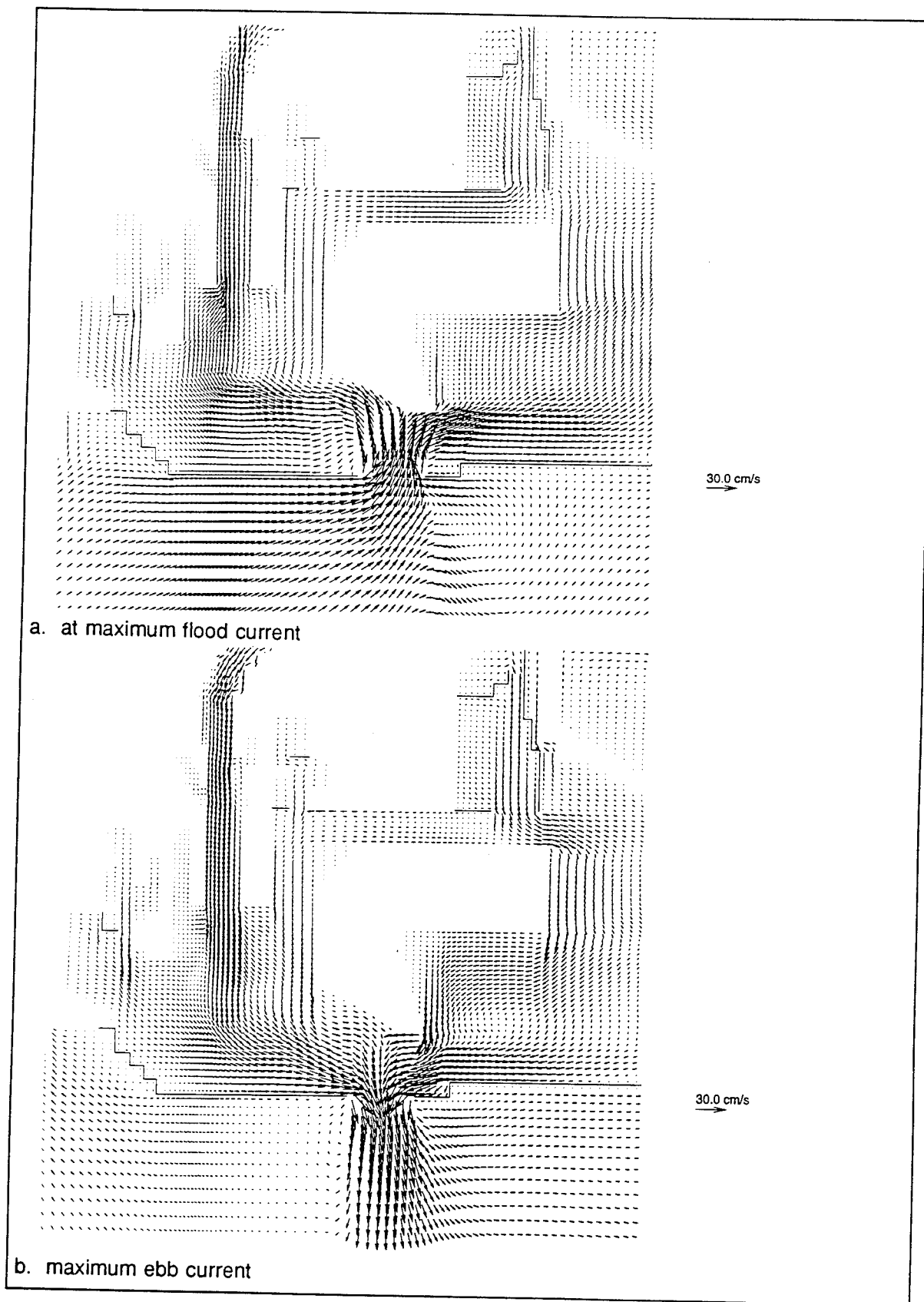
Figure C37. Vector plot of NED2-5 surface layer circulation under BW

C38

a. at maximum flood current

b. maximum ebb current
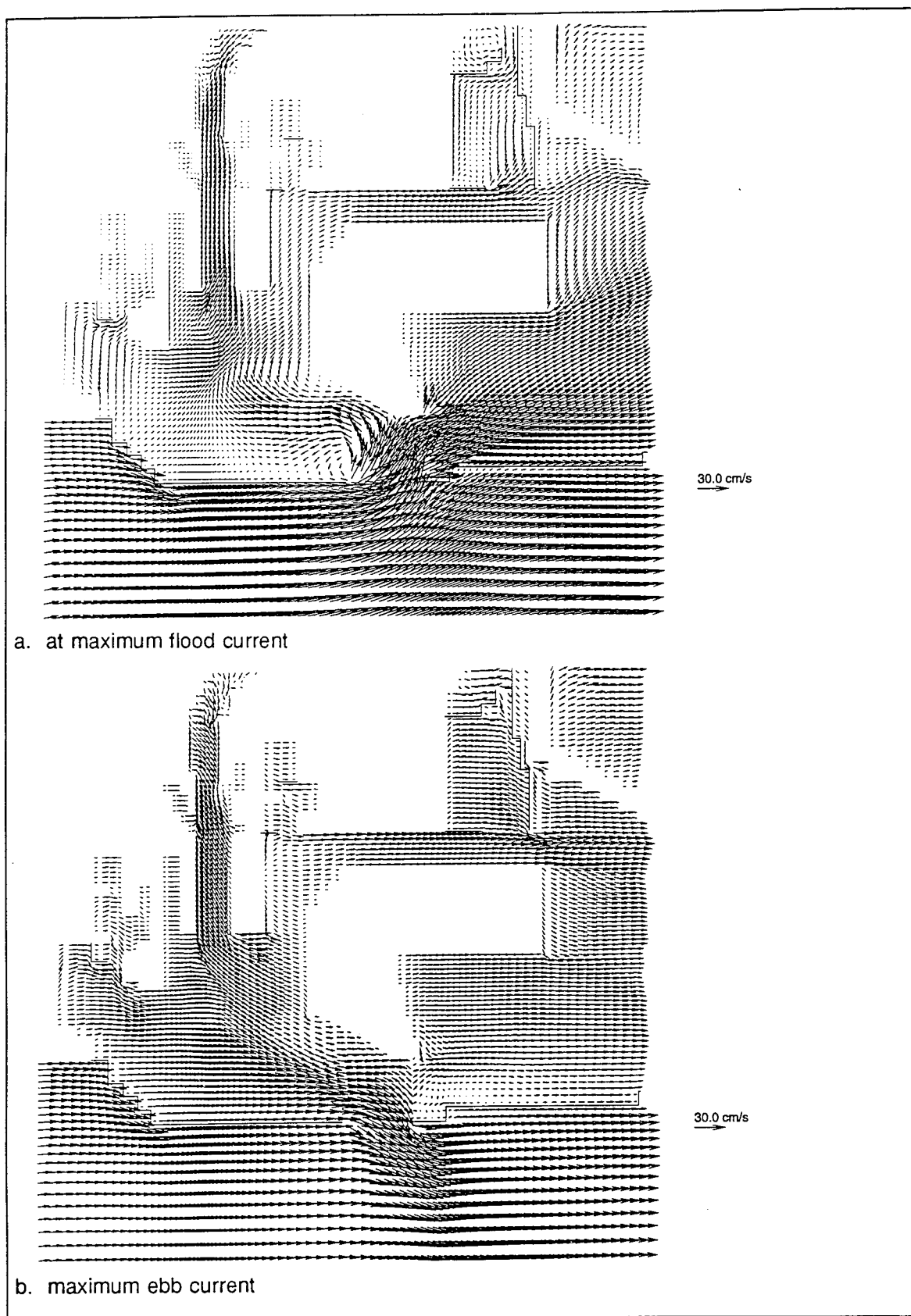
Figure C38. Vector plot of NED2-5 surface layer circulation under WSW20

Appendix C   Velocity Vector Plots in Support of the Ship Simulation Model

30.0 cm/s

a. at maximum flood current

30.0 cm/s

b. maximum ebb current
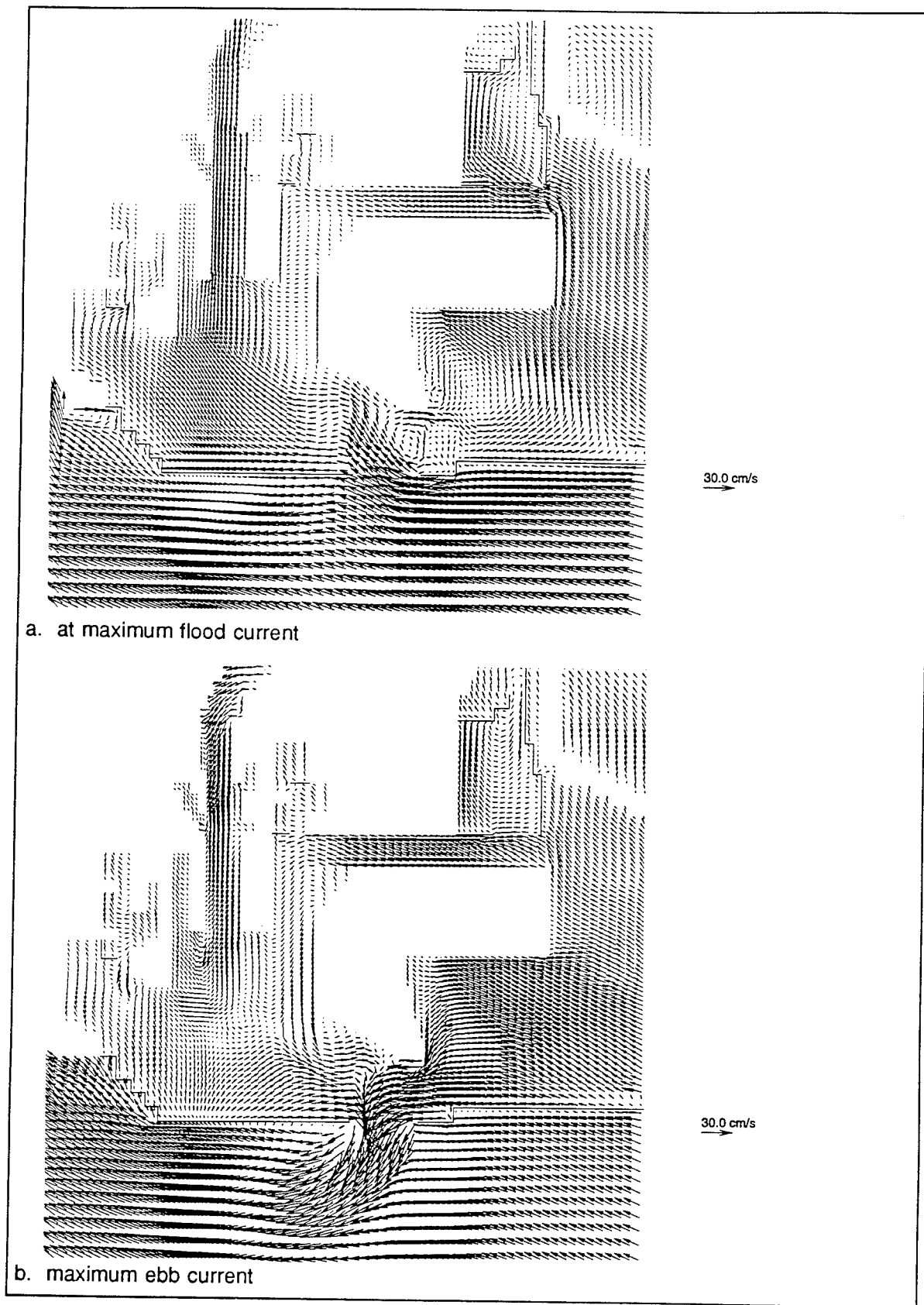
Figure C39. Vector plot of NED2-5 surface layer circulation under SE20

C40

a. at maximum flood current

30.0 cm/s

b. maximum ebb current

30.0 cm/s
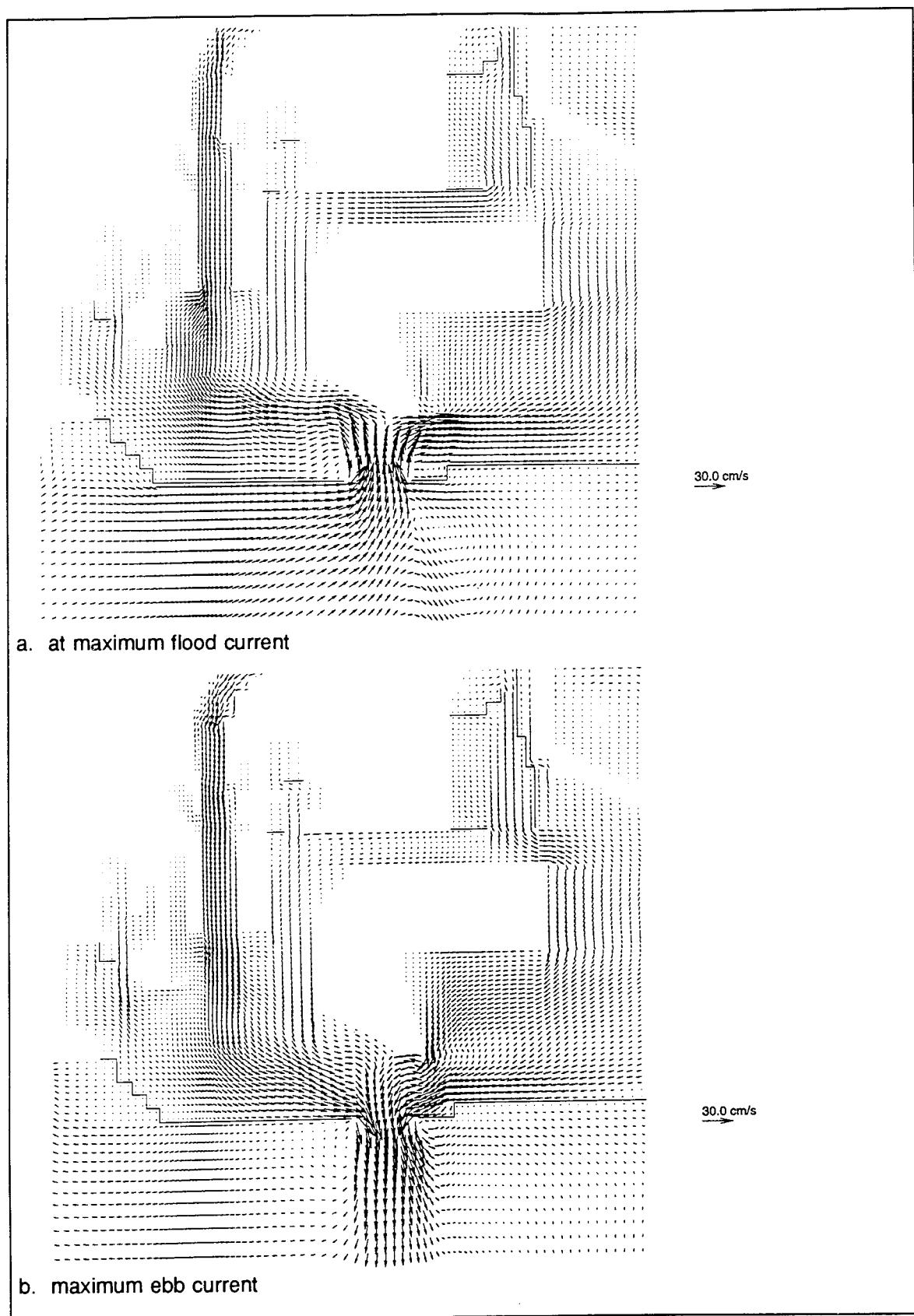
Figure C40. Vector plot of NED2-5 bottom layer circulation under BW

Appendix C   Velocity Vector Plots in Support of the Ship Simulation Model

30.0 cm/s

a. at maximum flood current

30.0 cm/s

b. maximum ebb current
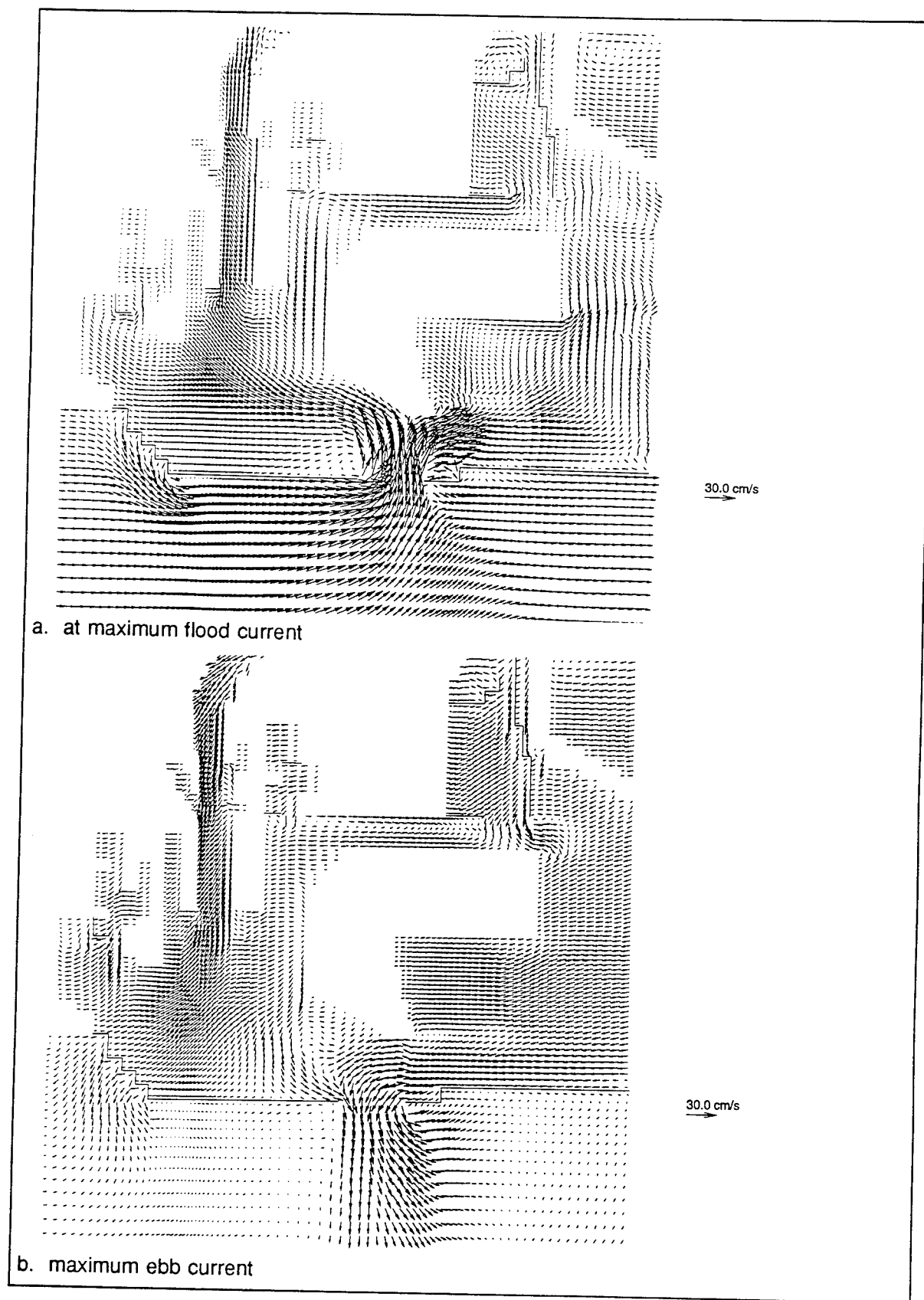
Figure C41. Vector plot of NED2-5 bottom layer circulation under WSW20

C42

30.0 cm/s

a. at maximum flood current

30.0 cm/s

b. maximum ebb current
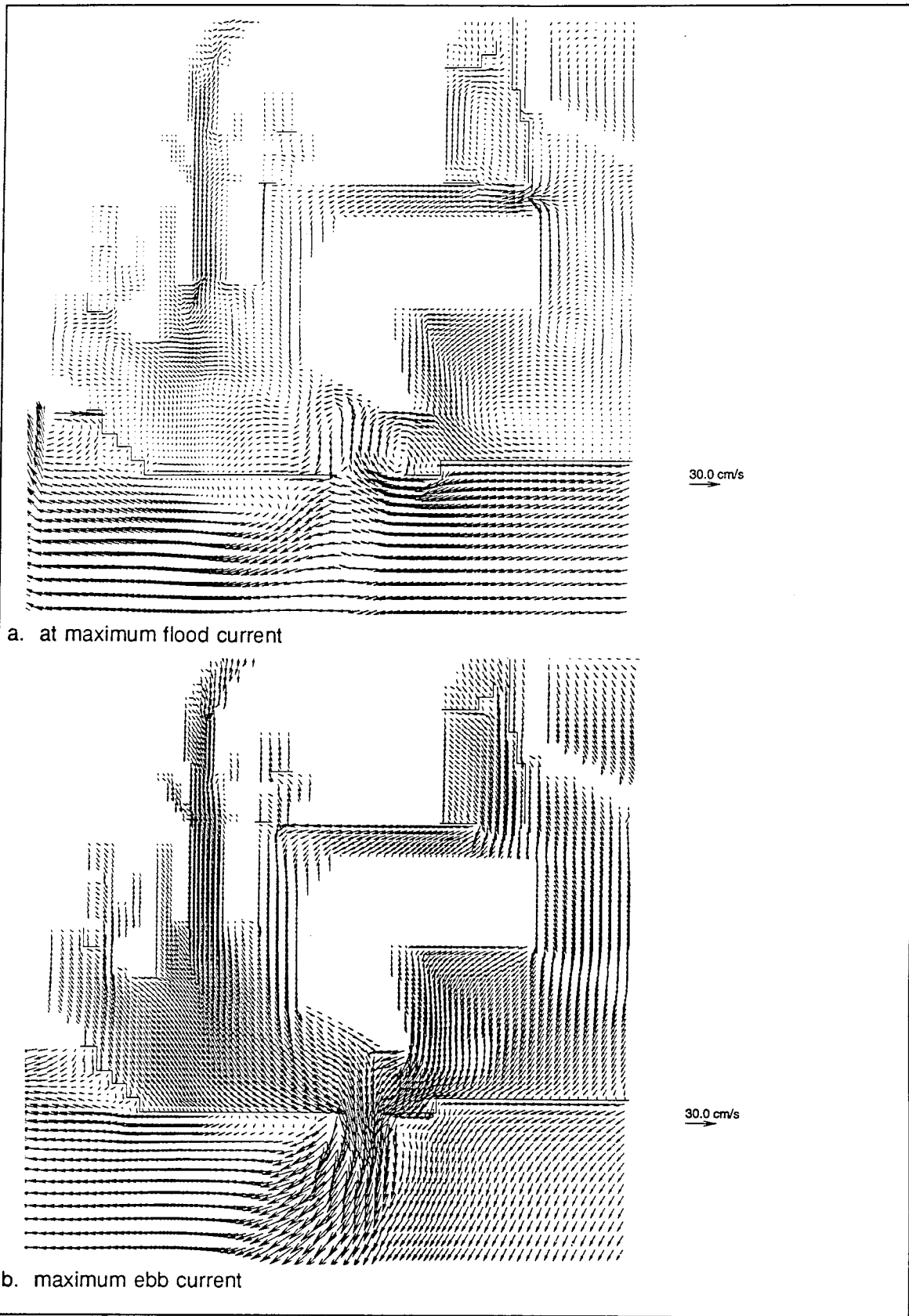
Figure C42. Vector plot of NED2-5 bottom layer circulation under SE20

a. at maximum flood current

30.0 cm/s

b. maximum ebb current
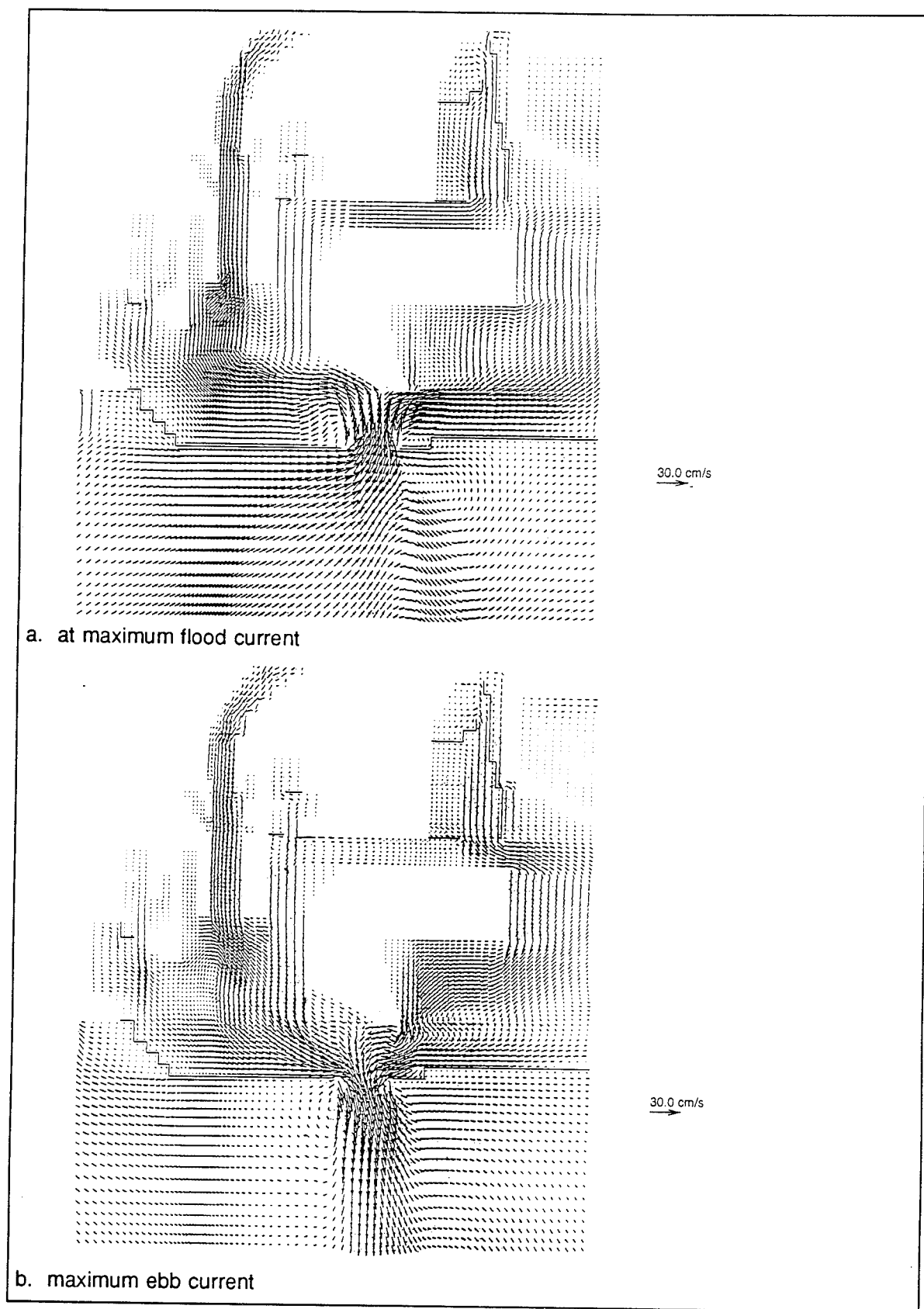
30.0 cm/s

Figure C43. Vector plot of NED2-5 vertical averaged circulation under BW

a. at maximum flood current

30.0 cm/s

b. maximum ebb current

30.0 cm/s

Figure C44. Vector plot of NED2-5 vertical averaged circulation under WSW20

30.0 cm/s

a. at maximum flood current

30.0 cm/s

b. maximum ebb current

Figure C45. Vector plot of NED2-5 vertical averaged circulation under SE20

Appendix D
Time Series Plots in Support
of the Ship Simulation Model
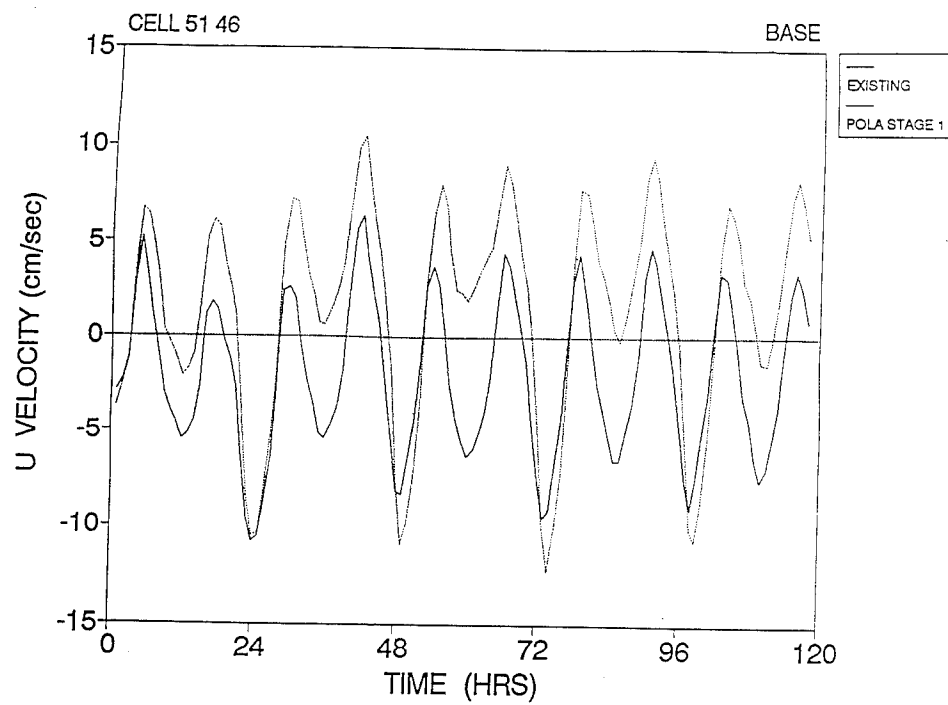
a. u under BW at station 1
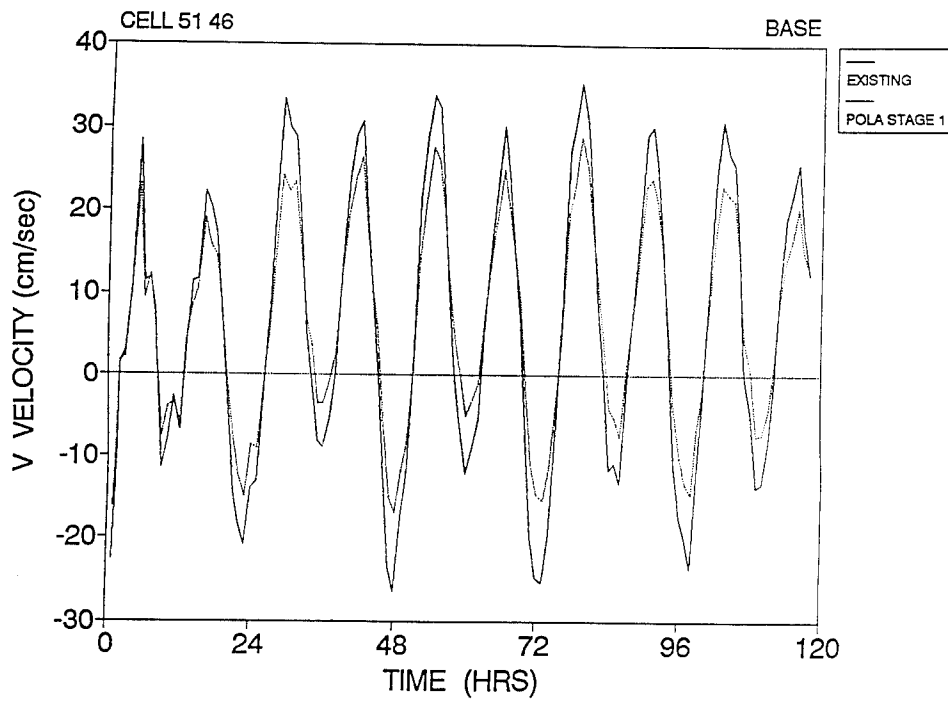
b. v under BW at station 1

Figure D1. Time series of POLA 1 current velocity

a. u under BW at station 2

b. v under BW at station 2
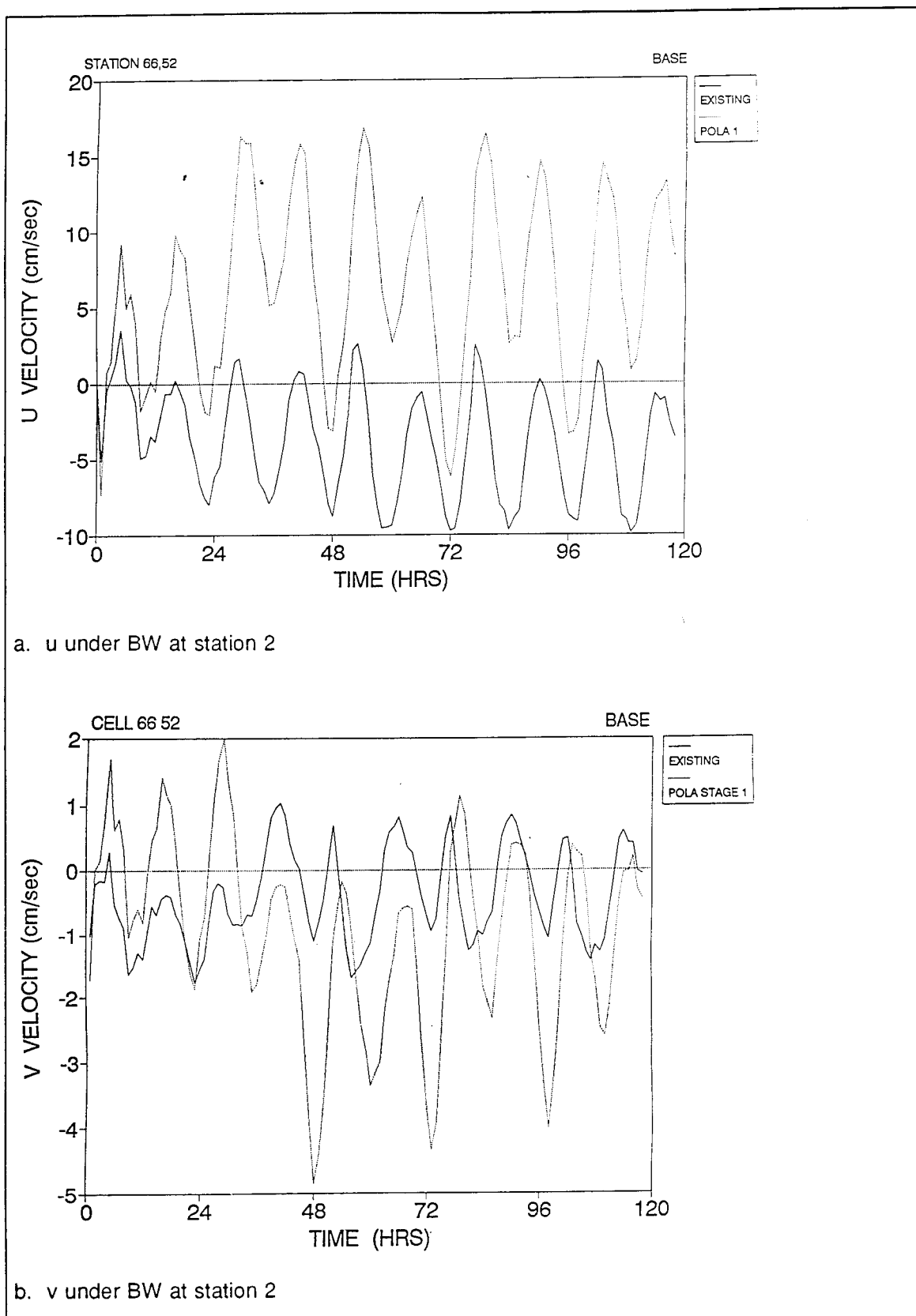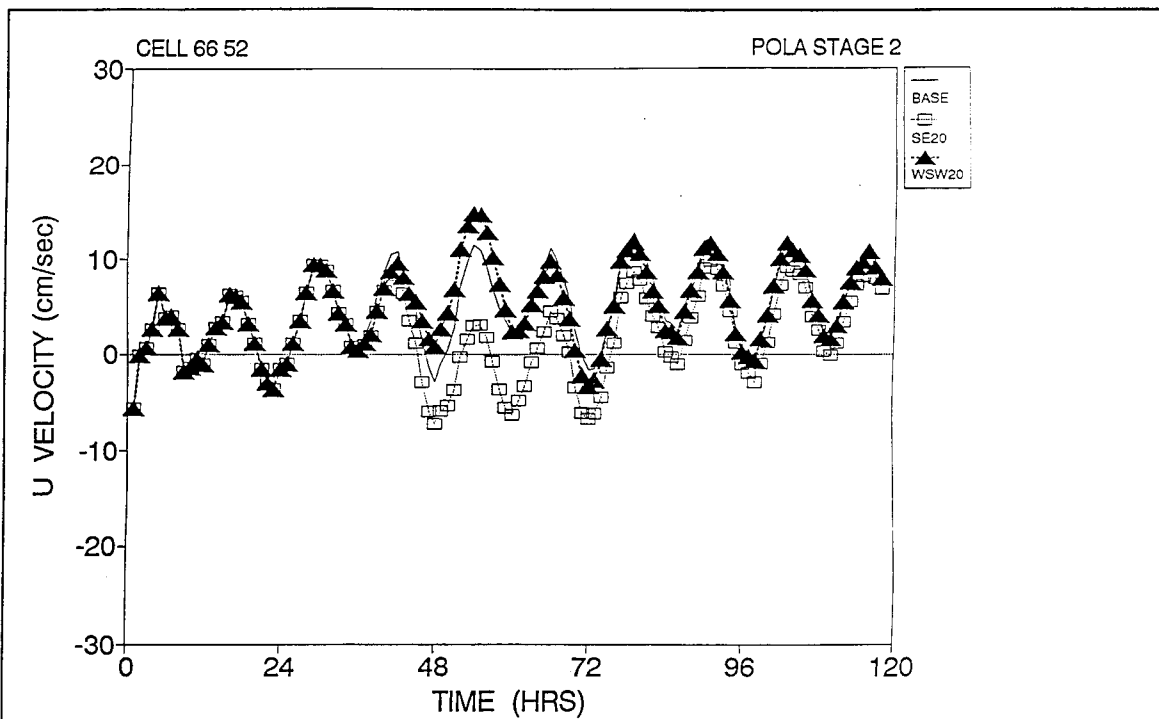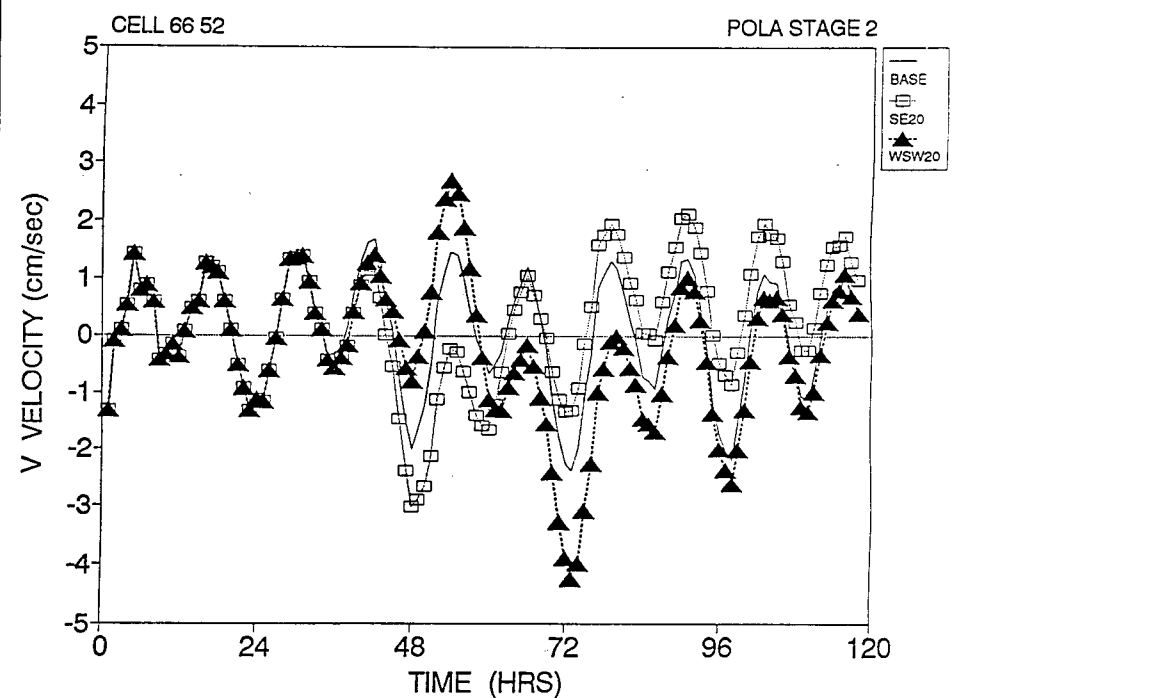
Figure D2. Time series of POLA 1 current velocity
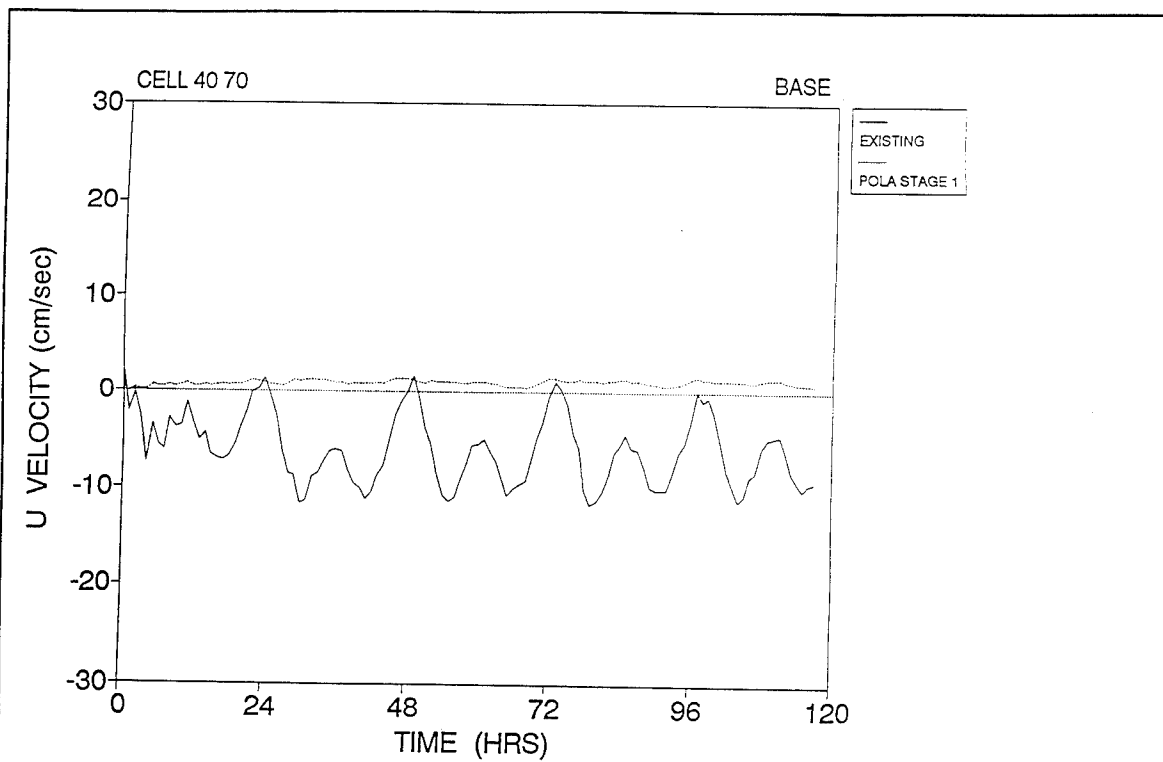
a. u under BW at station 3
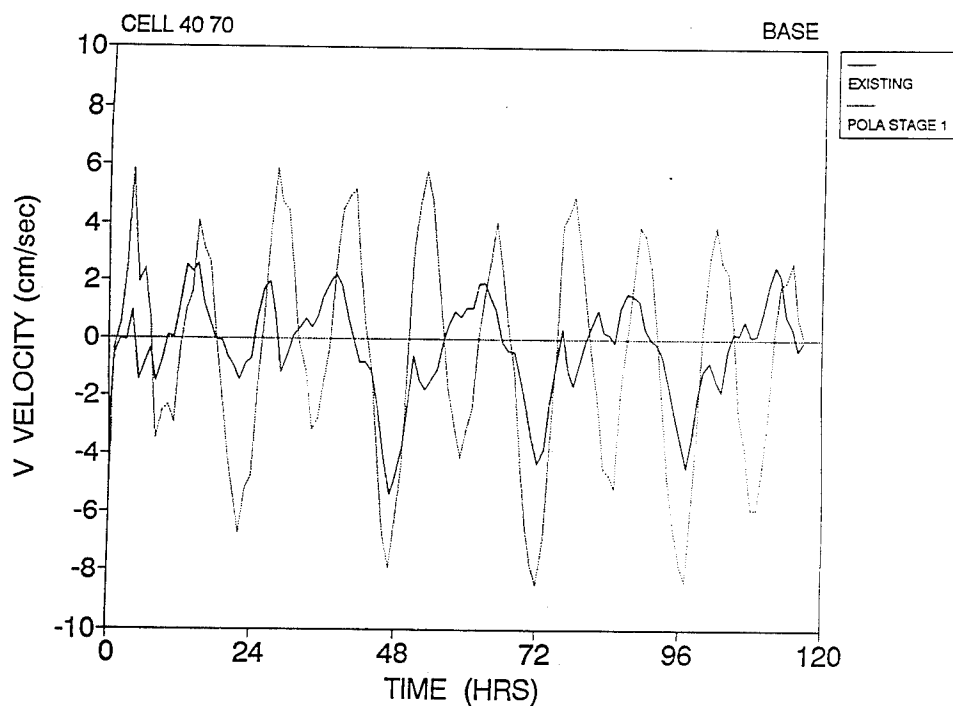
b. v under BW at station 3

Figure D3. Time series of POLA 1 current velocity

a. u under BW at station 4

b. v under BW at station 4
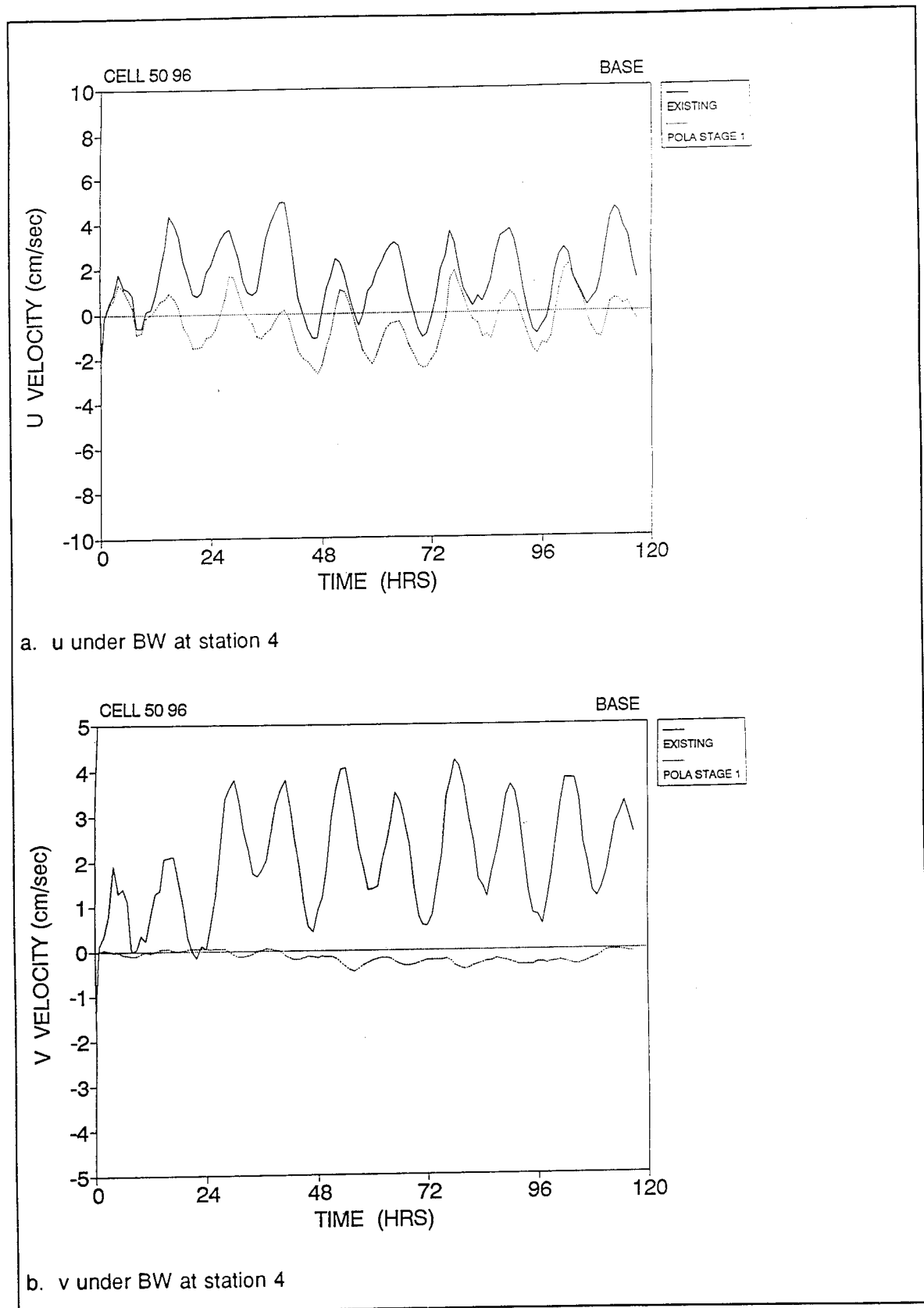
Figure D4. Time series of POLA 1 current velocity

Appendix D   Time Series Plots in Support of the Ship Simulation Model
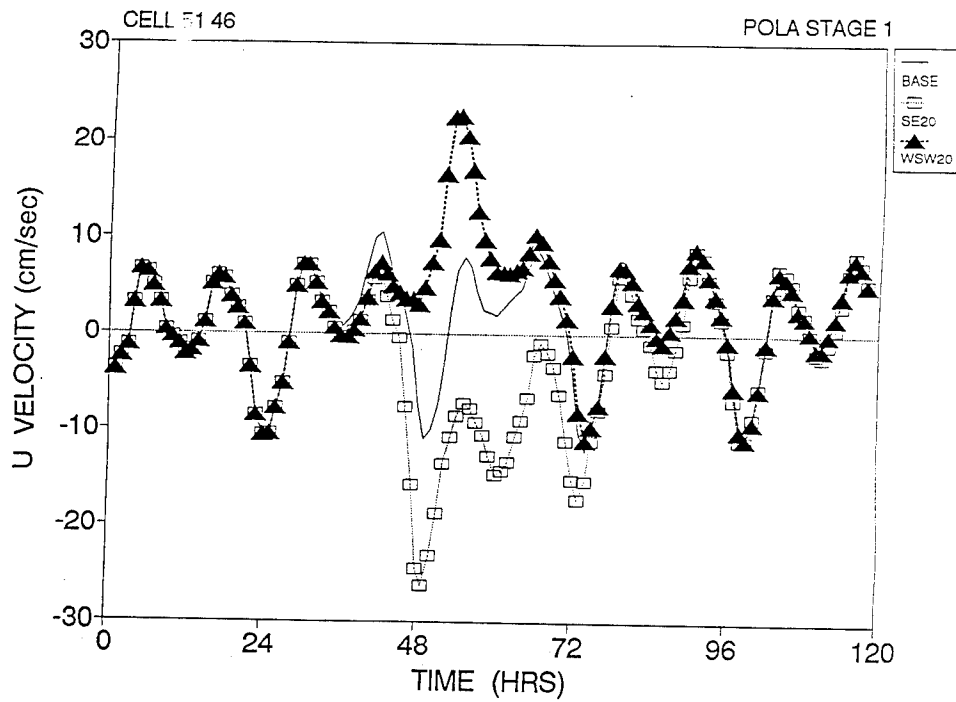
a. u responses to BW, SE20, and WSW20 at station 1
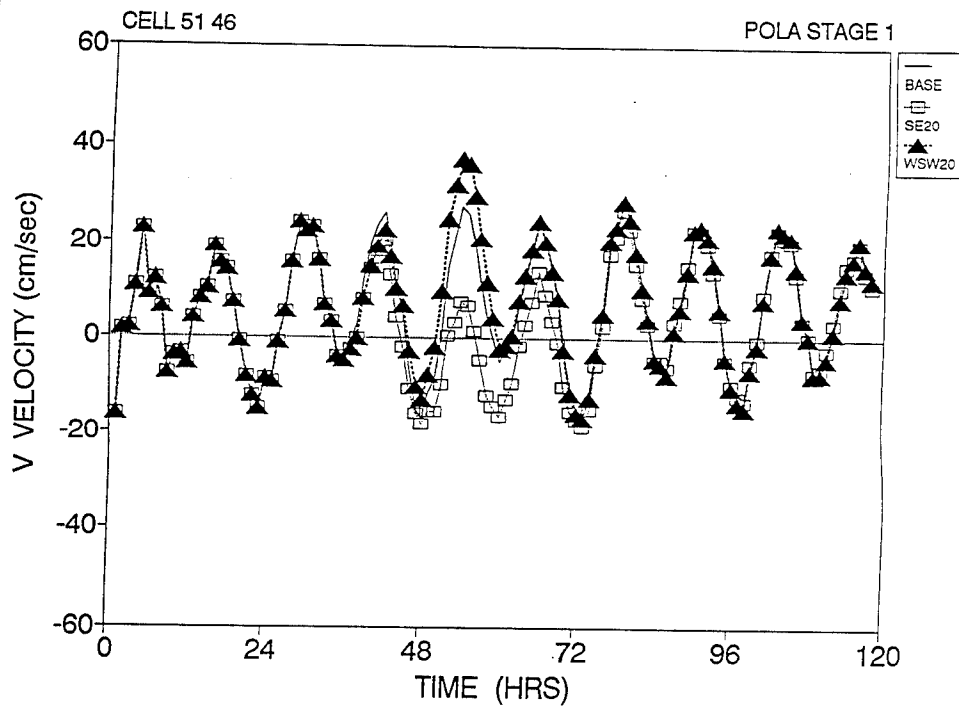
b. v responses to BW, SE20, and WSW20 at station 1

Figure D5. Time series of POLA 1 current velocity
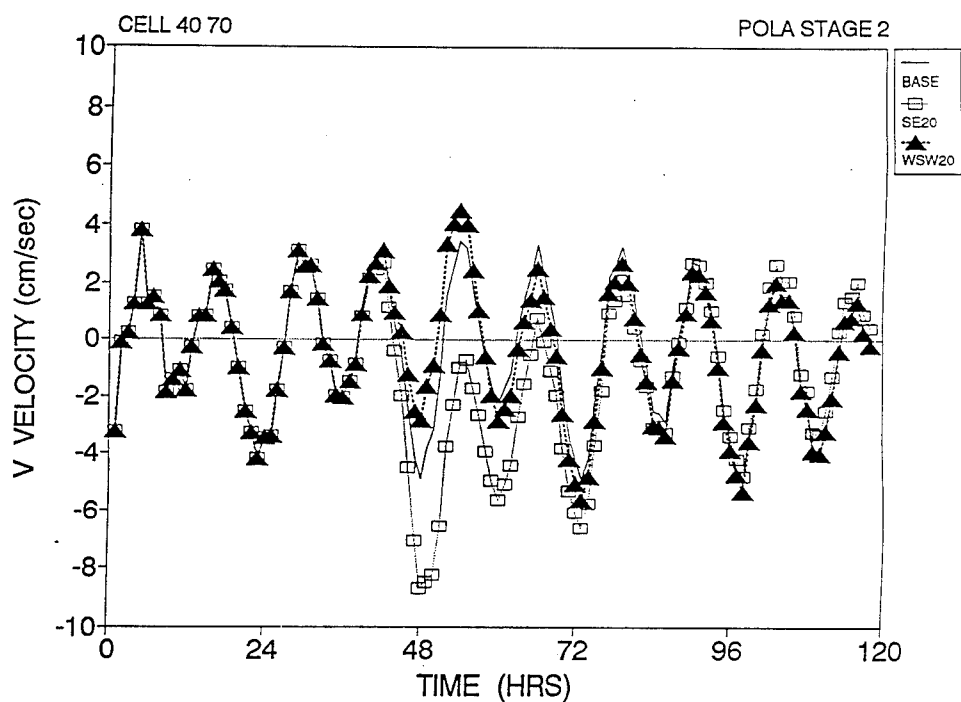
a. u response to BW, SE20, and WSW20 at station 2

b. v response to BW, SE20, and WSW20 at station 2
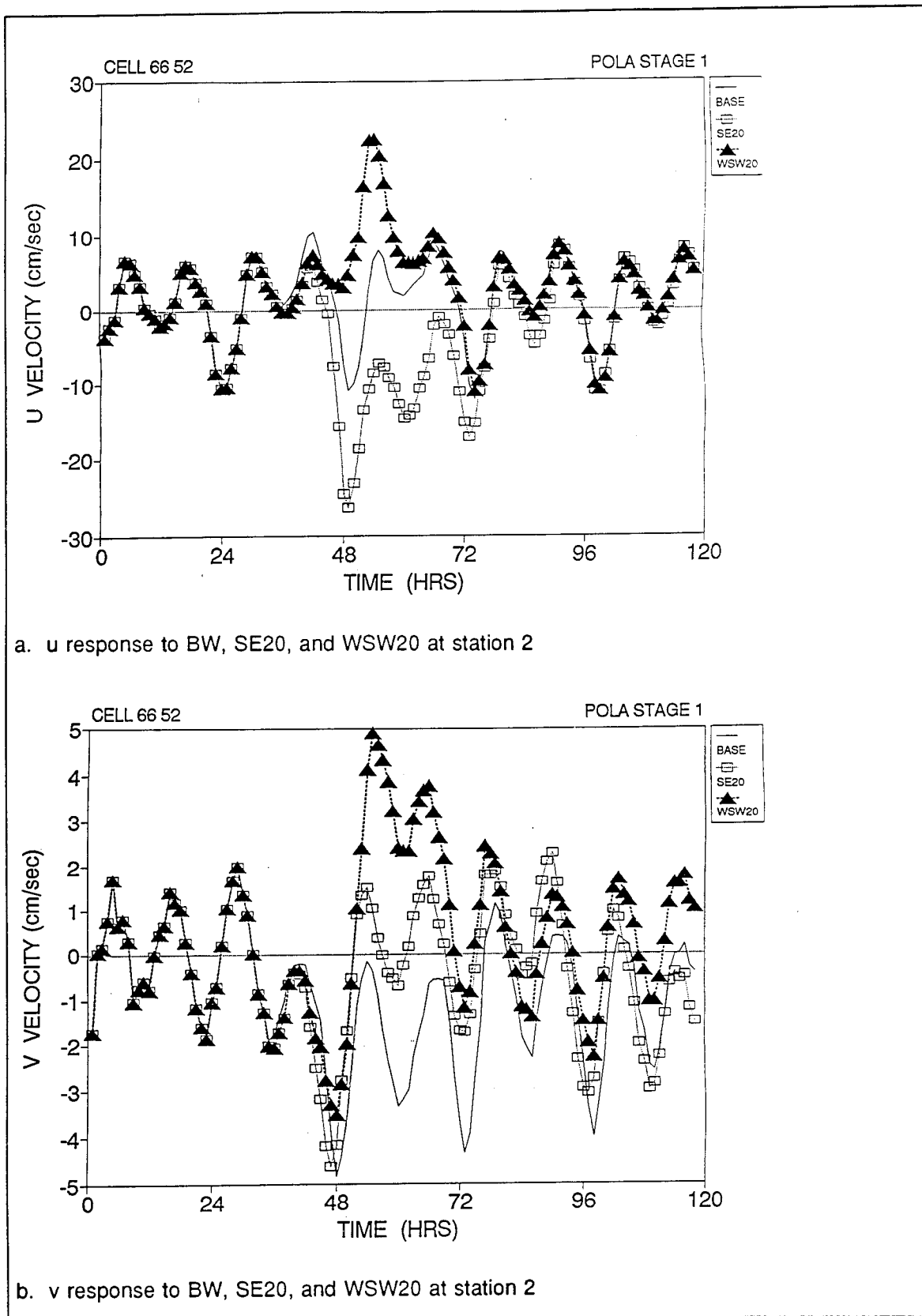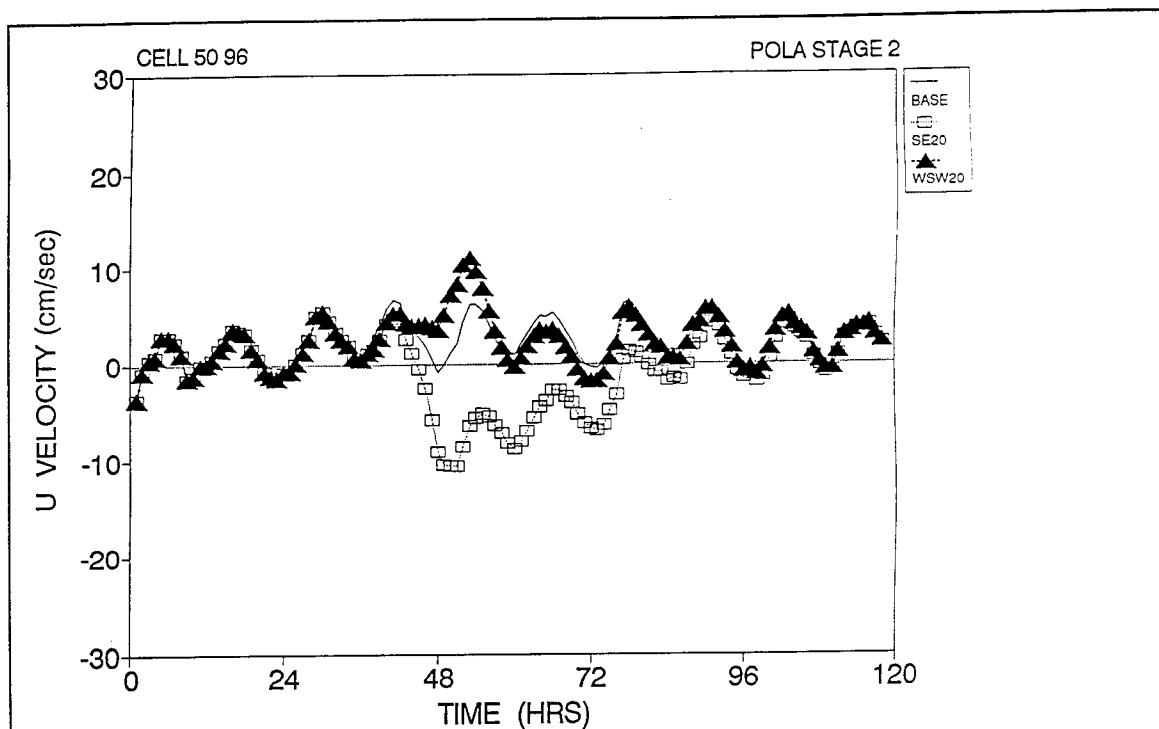
Figure D6. Time series of POLA 1 current velocity
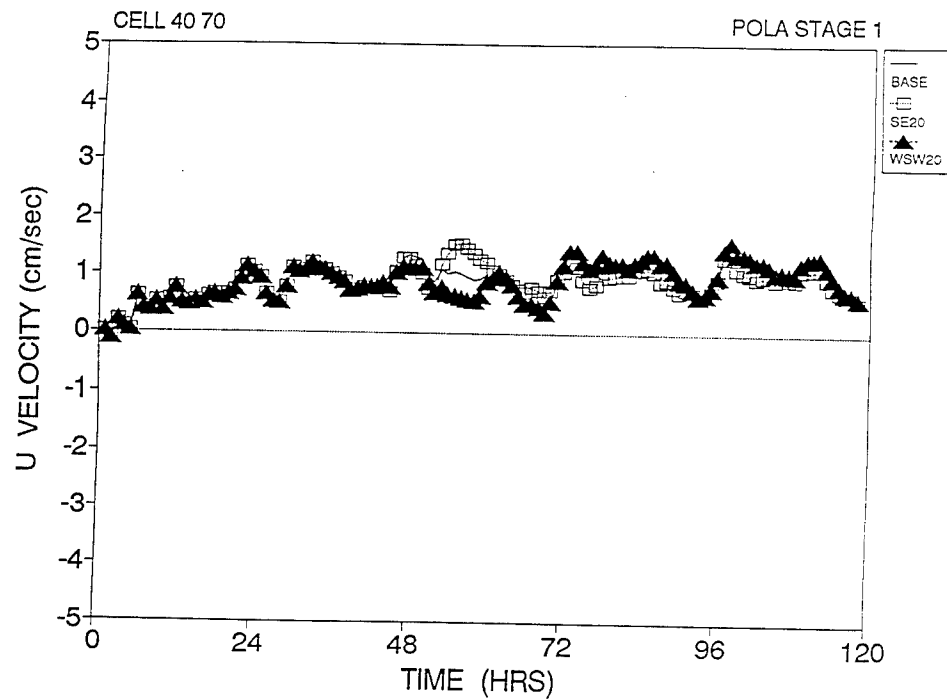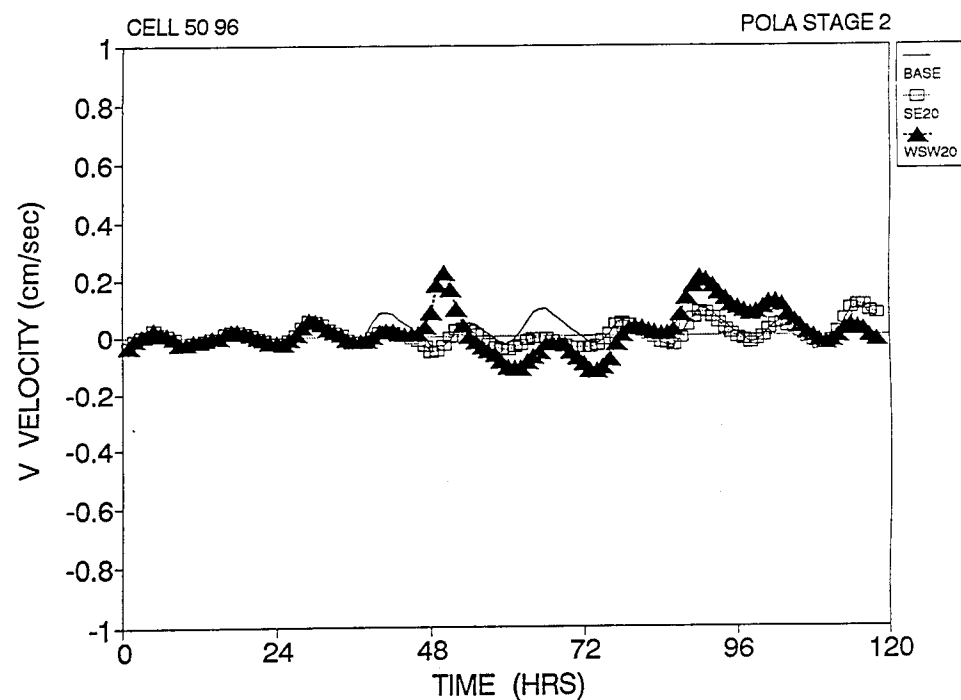
a. u response to BW, SE20, and WSW20 at station 3
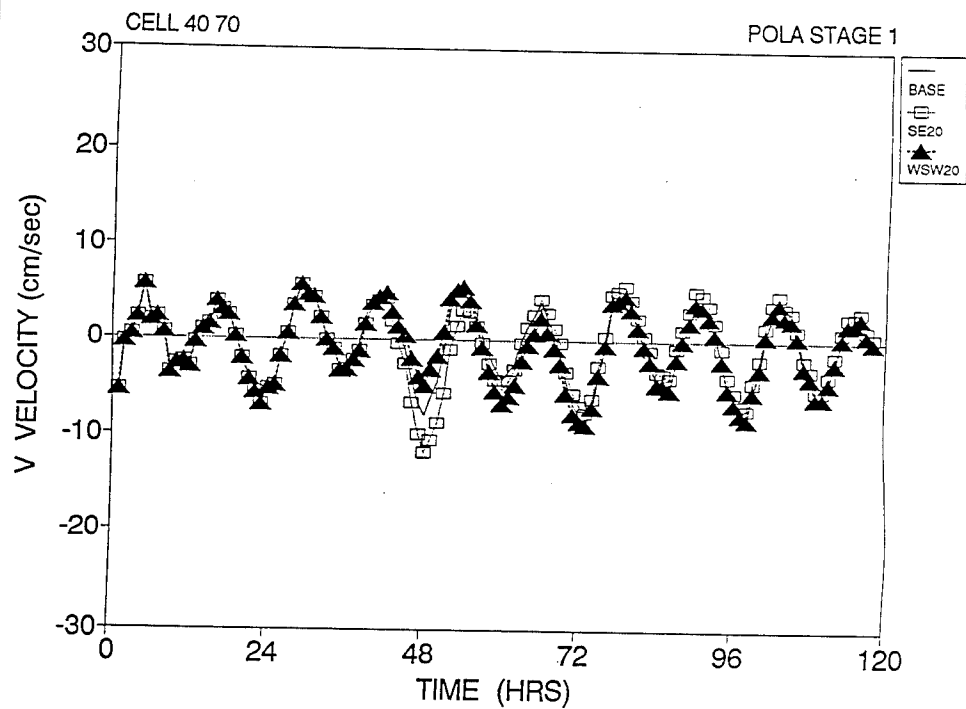
b. v response to BW, SE20, and WSW20 at station 3
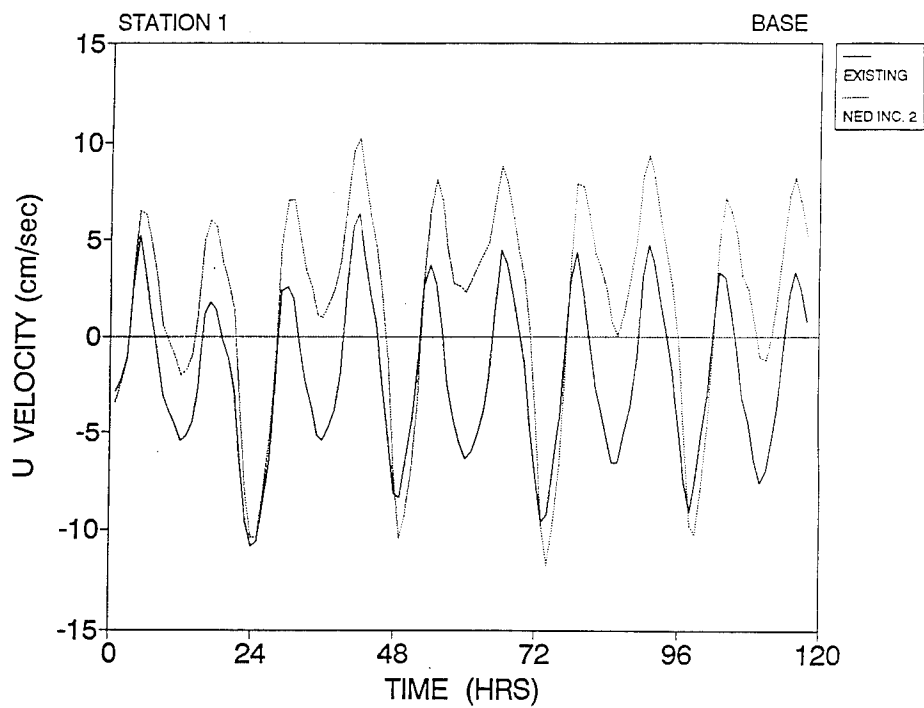
Figure D7. Time series of POLA 1 current velocity
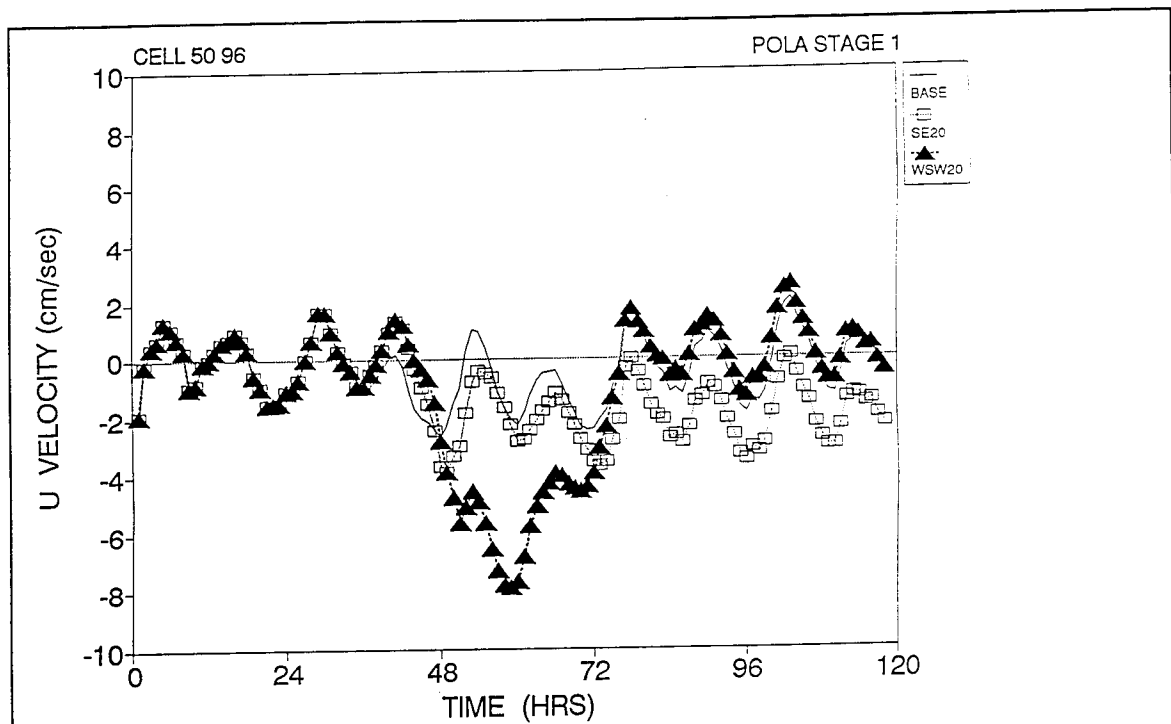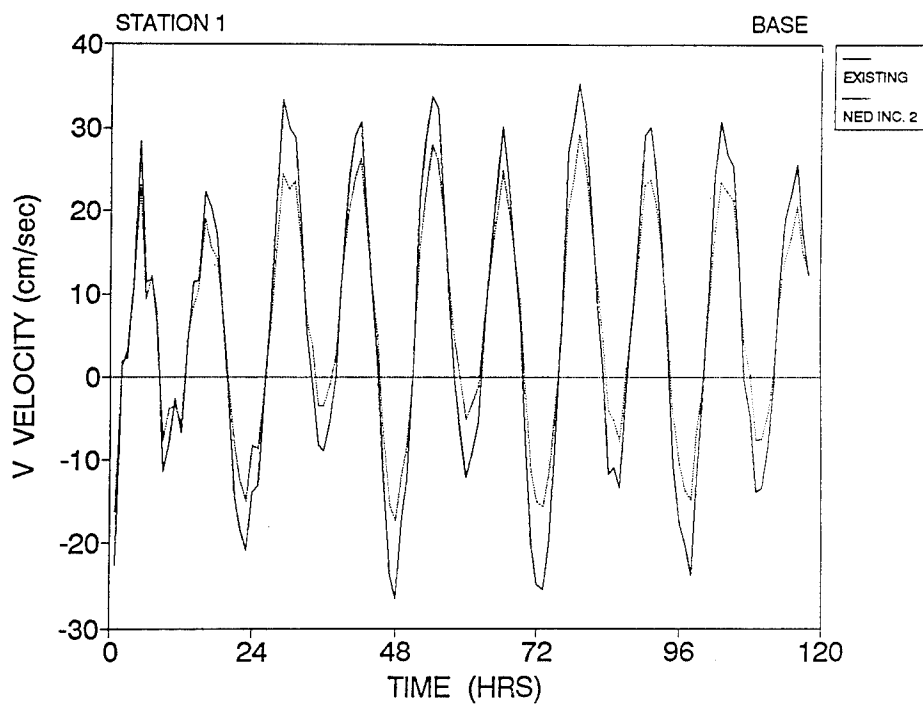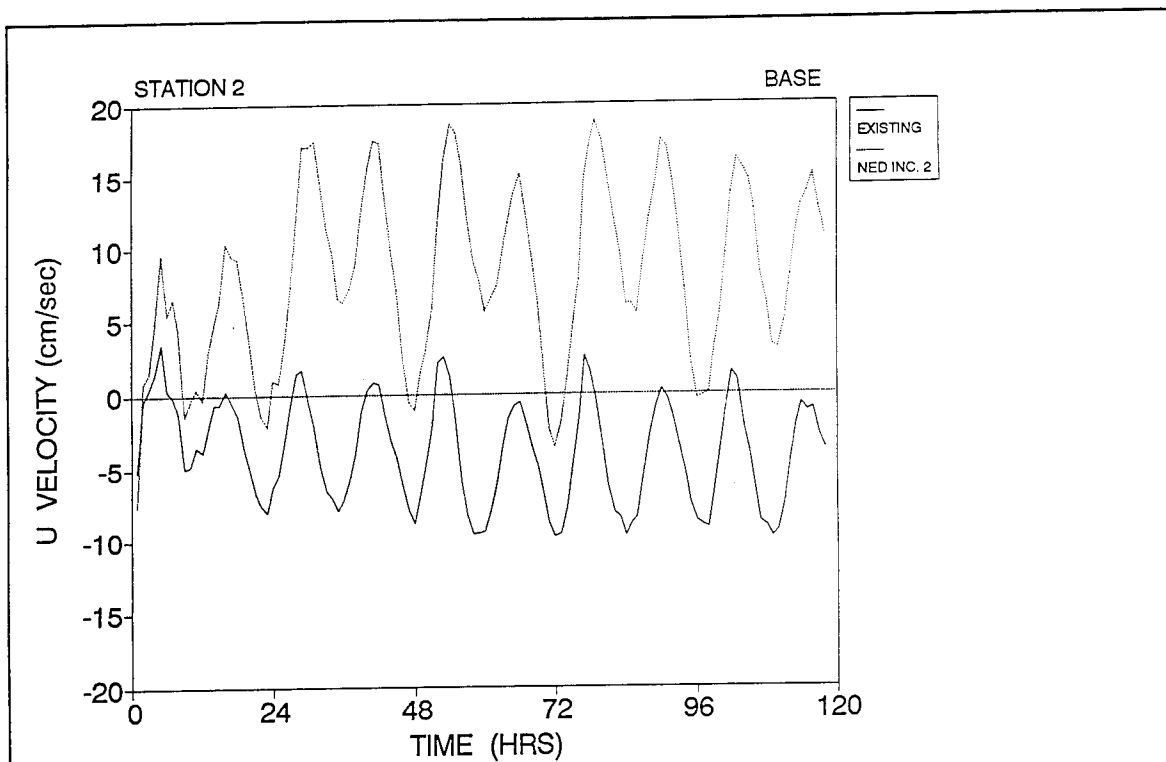
a. u response to BW, SE20, and WSW20 at station **4**
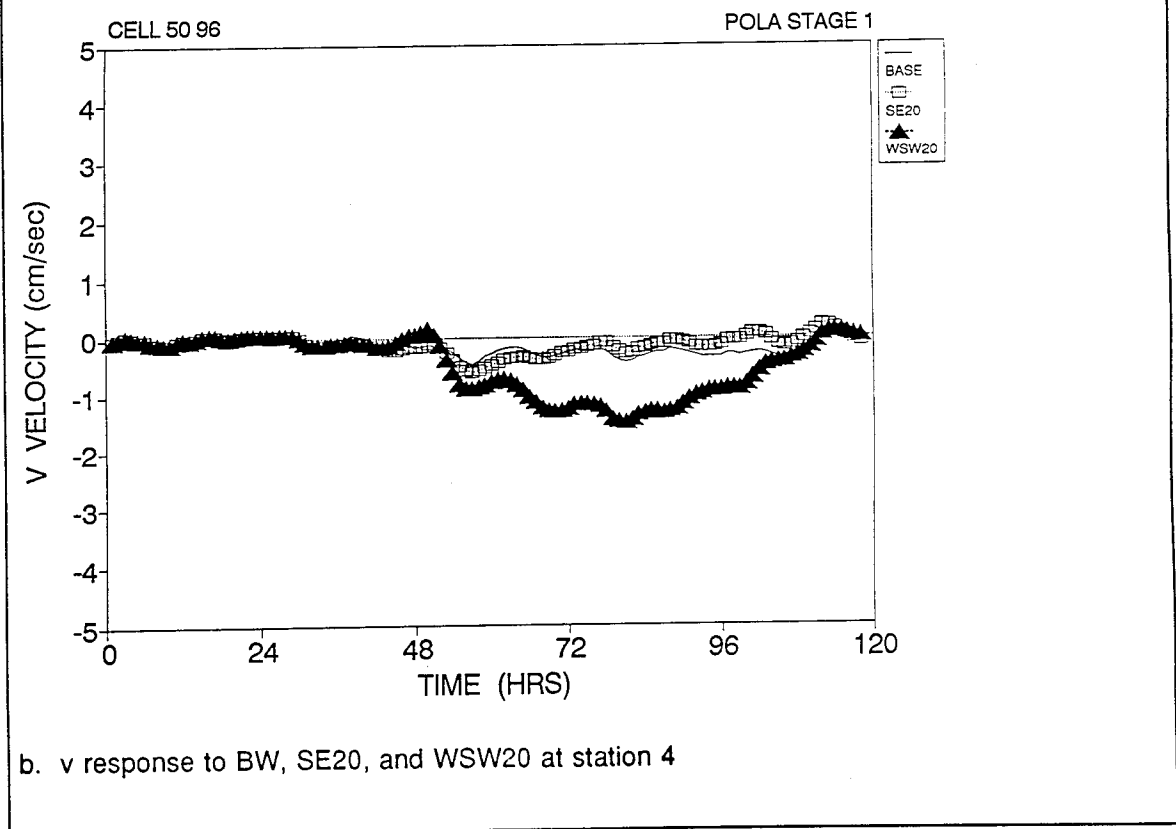
b. v response to BW, SE20, and WSW20 at station **4**

Figure D8. Time series of POLA 1 current velocity

Appendix D   Time Series Plots in Support of the Ship Simulation Model
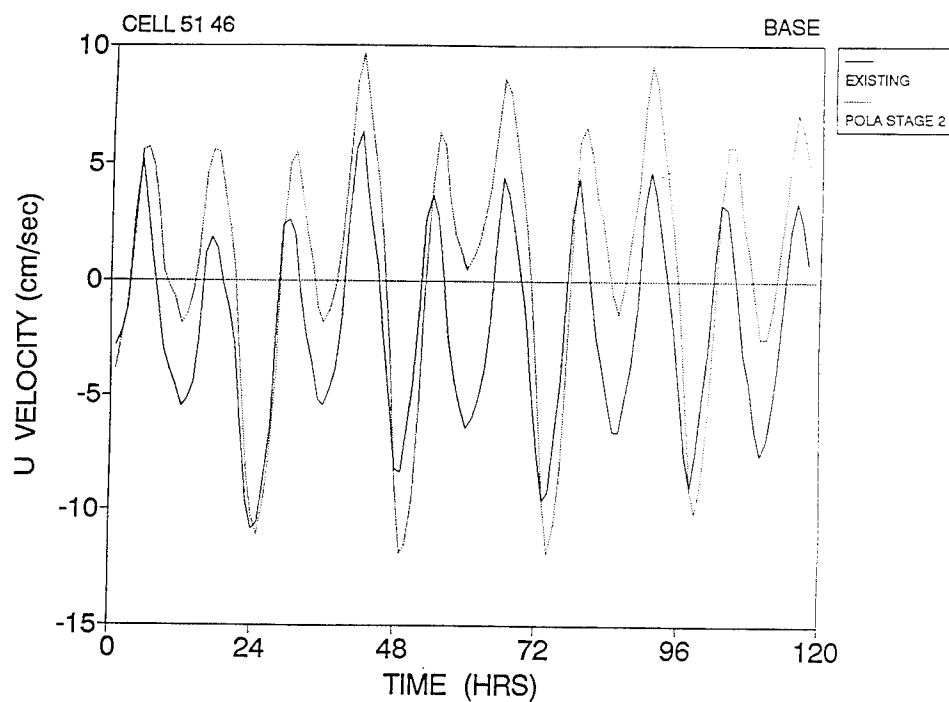
a. u under BW at station 1
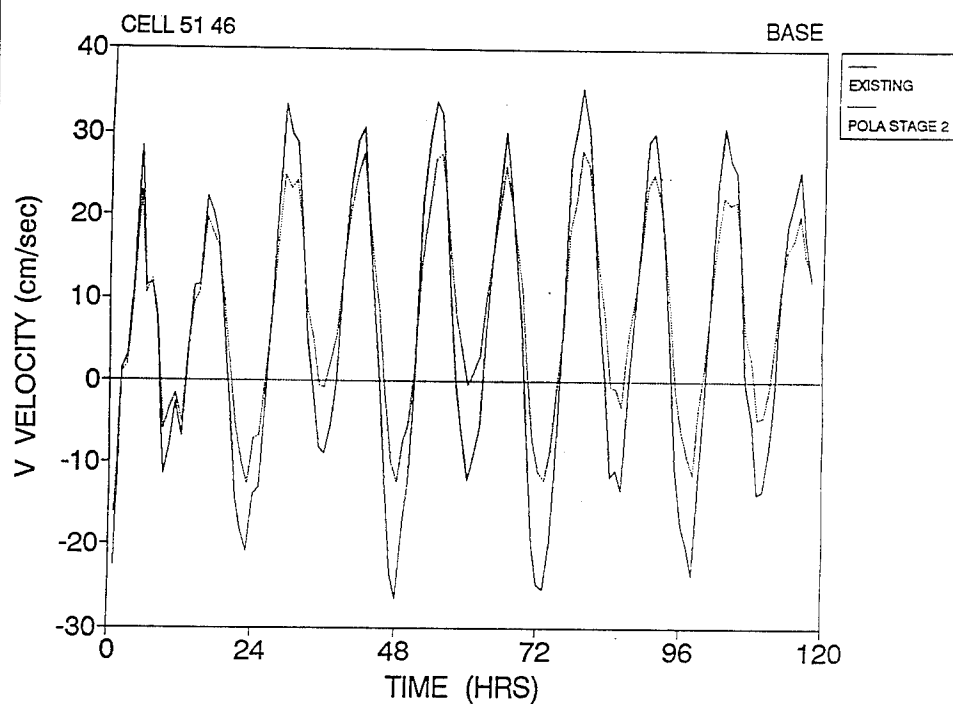
b. v under BW at station 1

Figure D9. Time series of POLA 2 current velocity

D10

a. u under BW at station 2

b. v under BW at station 2
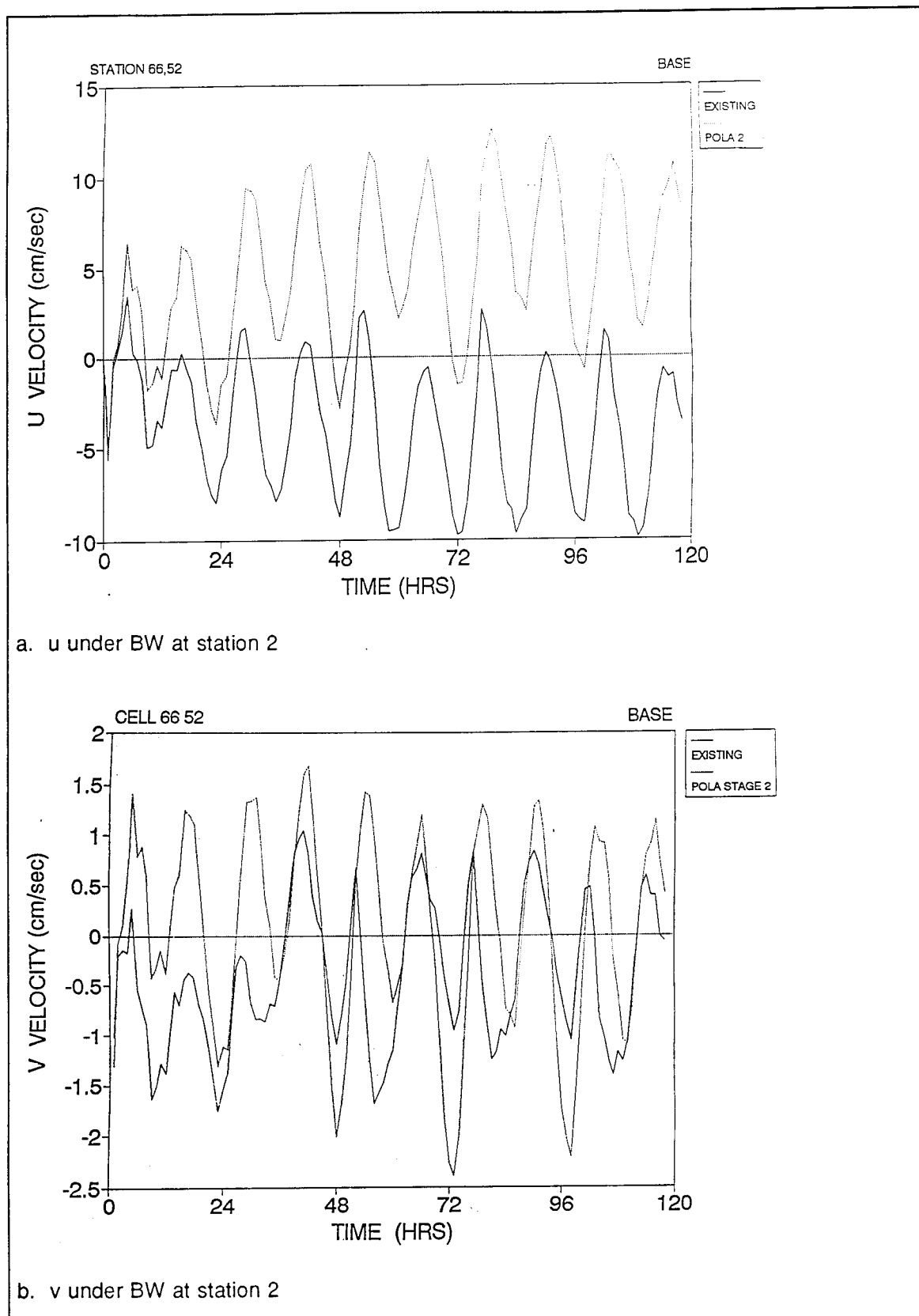
Figure D10. Time series of POLA 2 current velocity

Appendix D   Time Series Plots in Support of the Ship Simulation Model
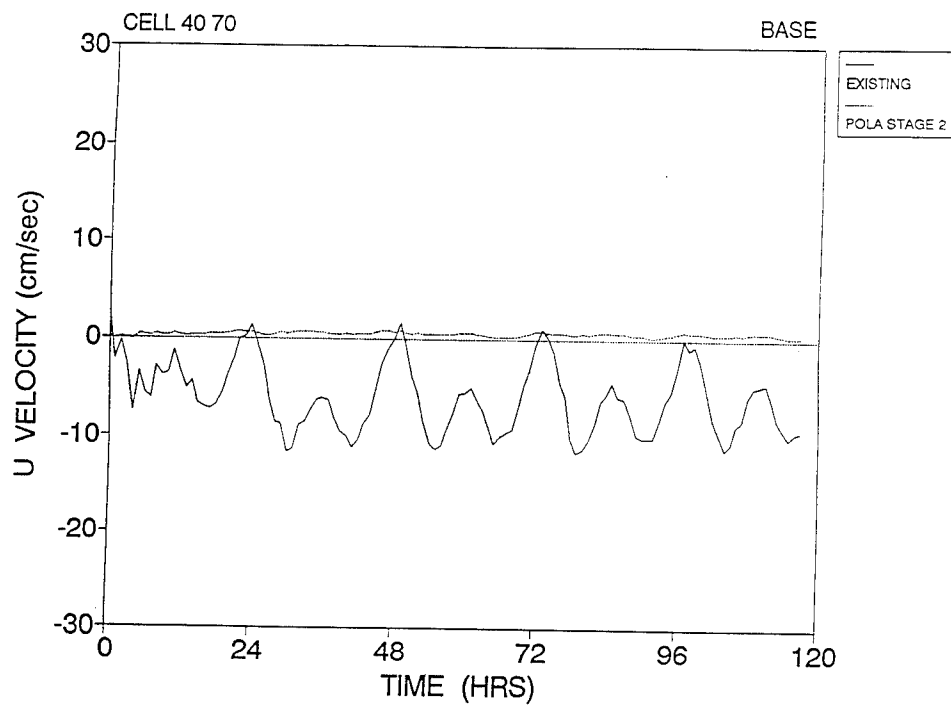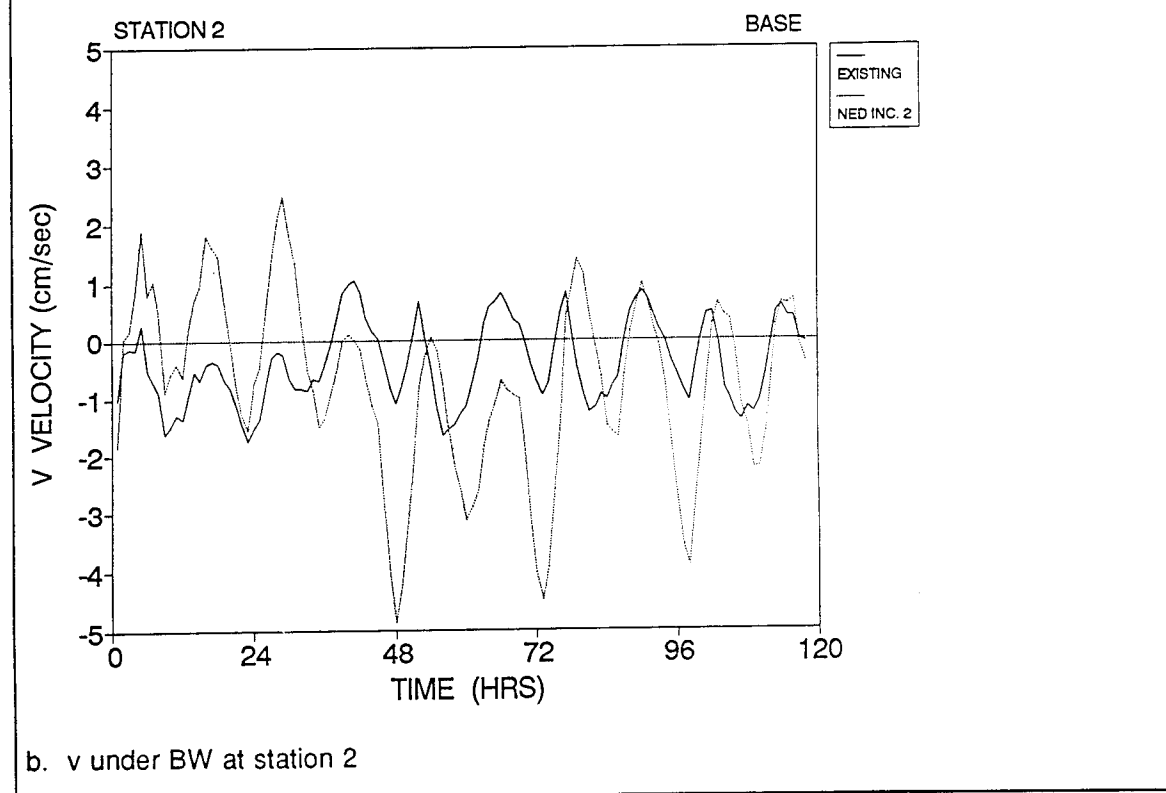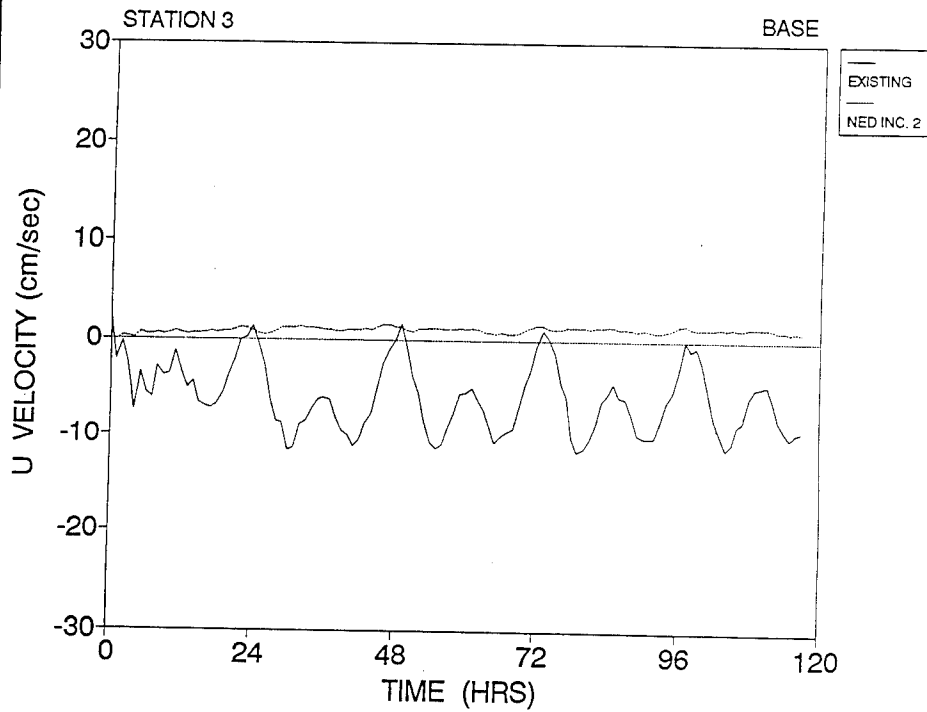
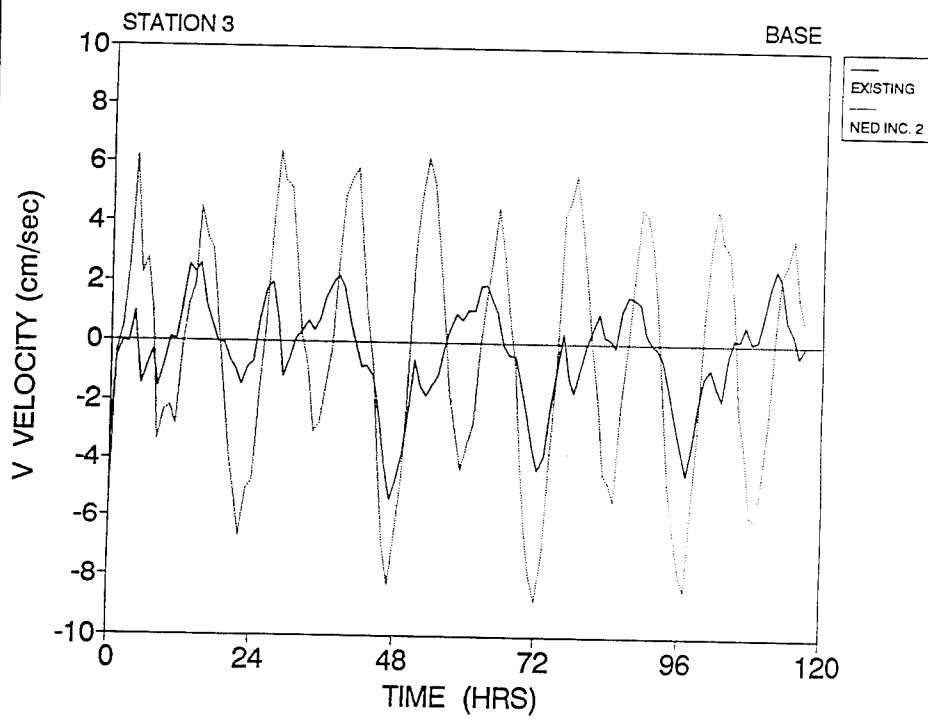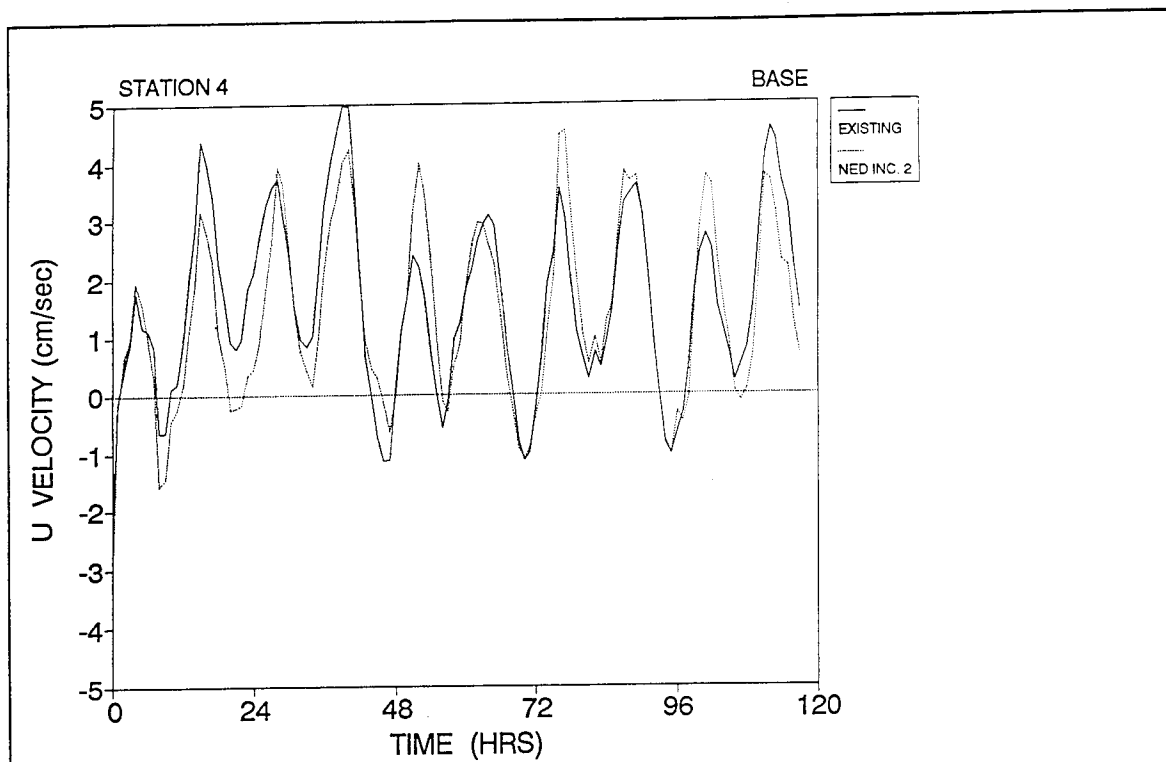a. u under BW at station 3
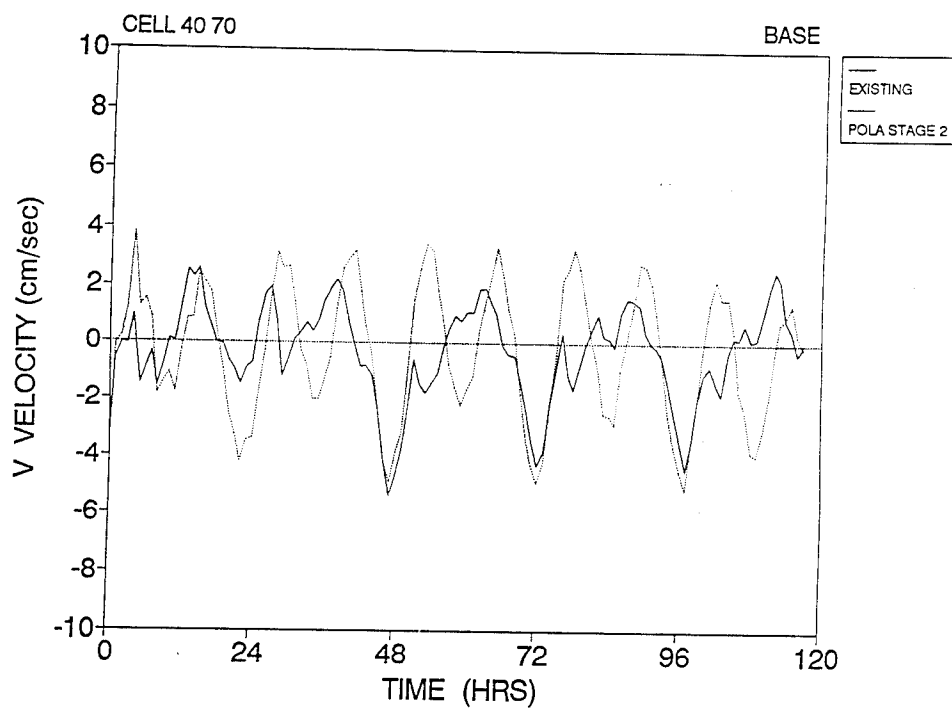
b. v under BW at station 3

Figure D11. Time series of POLA 2 current velocity
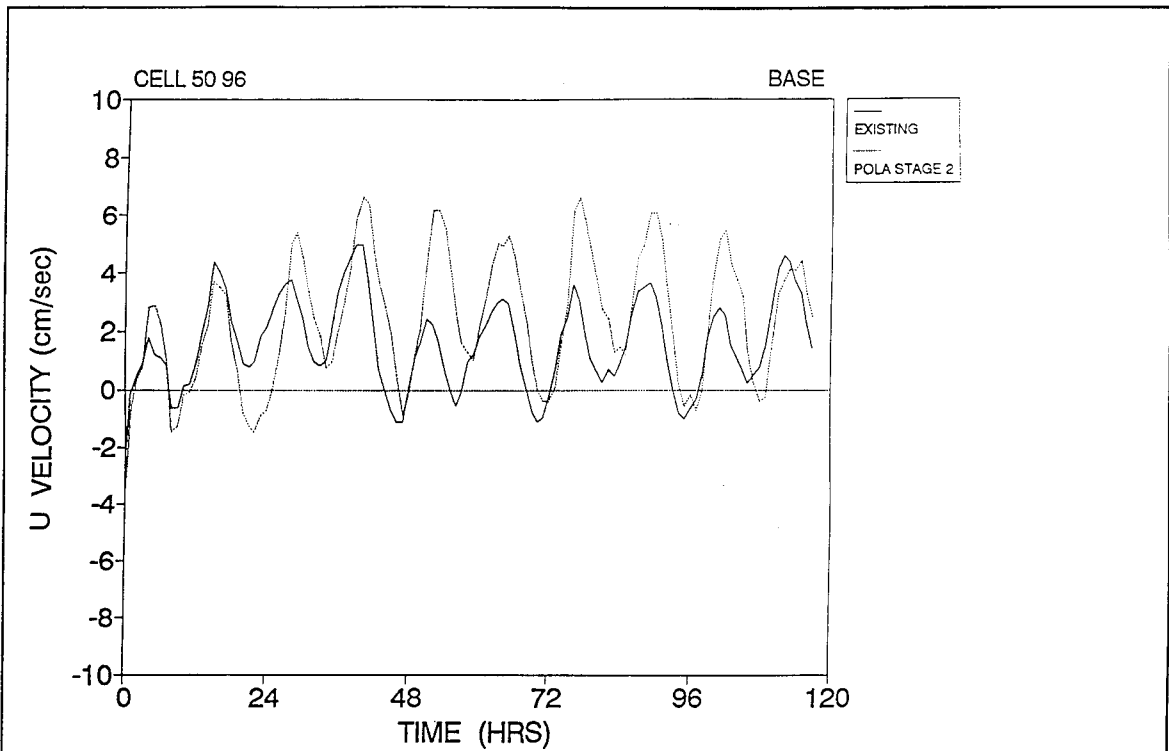
a. u under BW at station 4
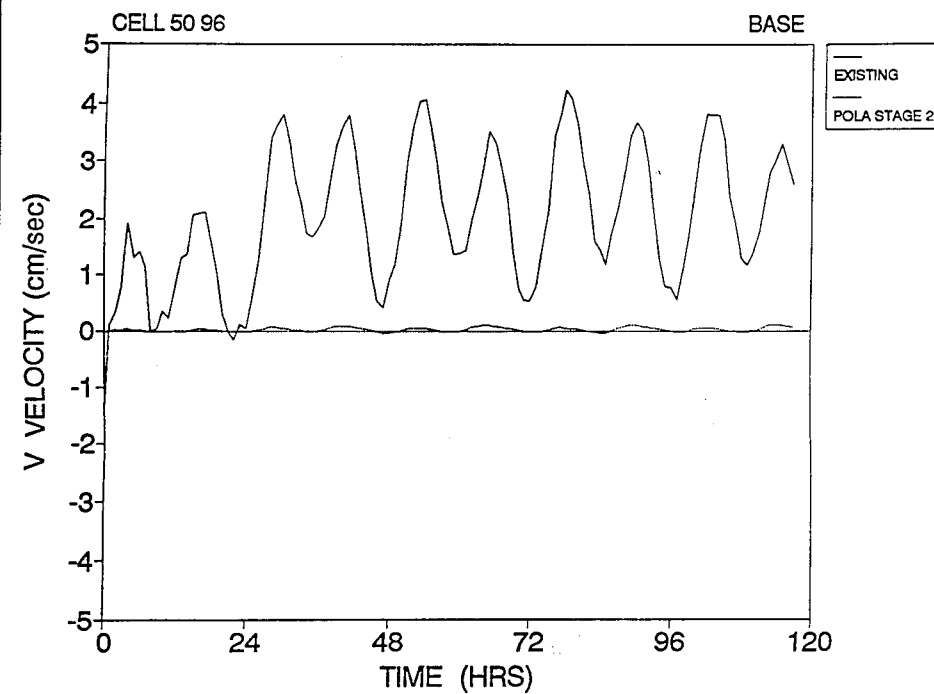
b. v under BW at station 4

Figure D12. Time series of POLA 2 current velocity
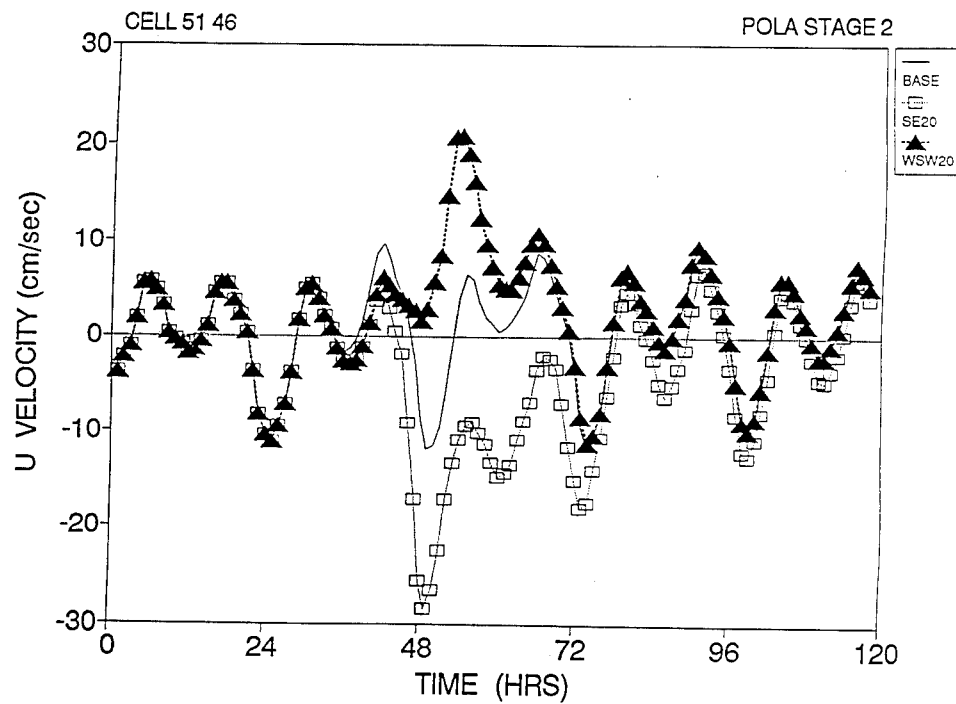
a. u response to BW, SE20, and WSW20 at station 1
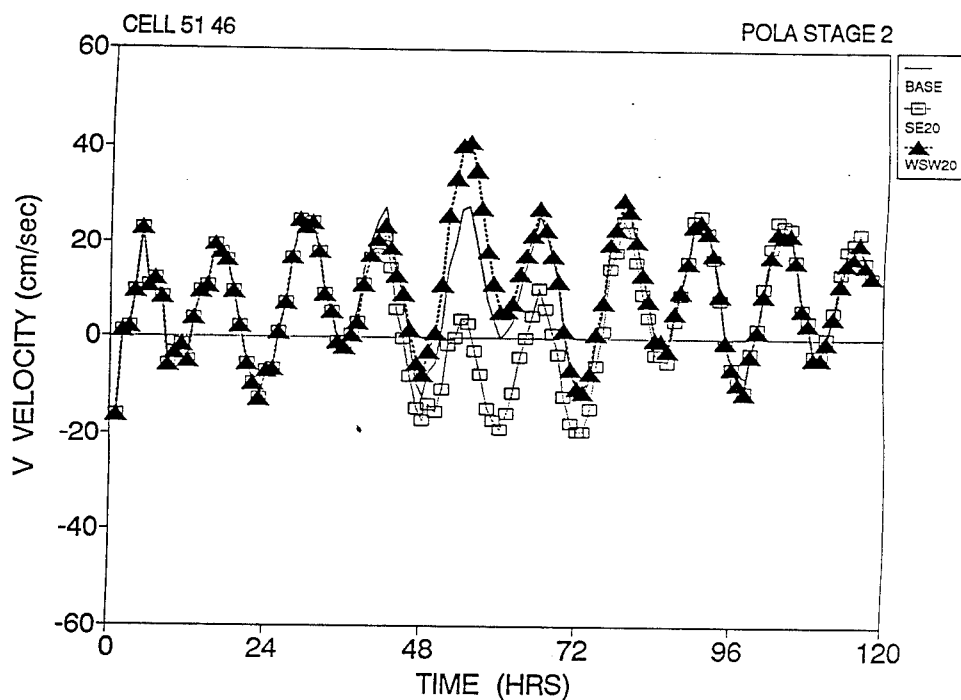
b. v response to BW, SE20, and WSW20 at station 1

Figure D13. Time series of POLA 2 current velocity

a. u response to BW, SE20, and WSW20 at station 2

b. v response to BW, SE20, and WSW20 at station 2

Figure D14. Time series of POLA 2 current velocity
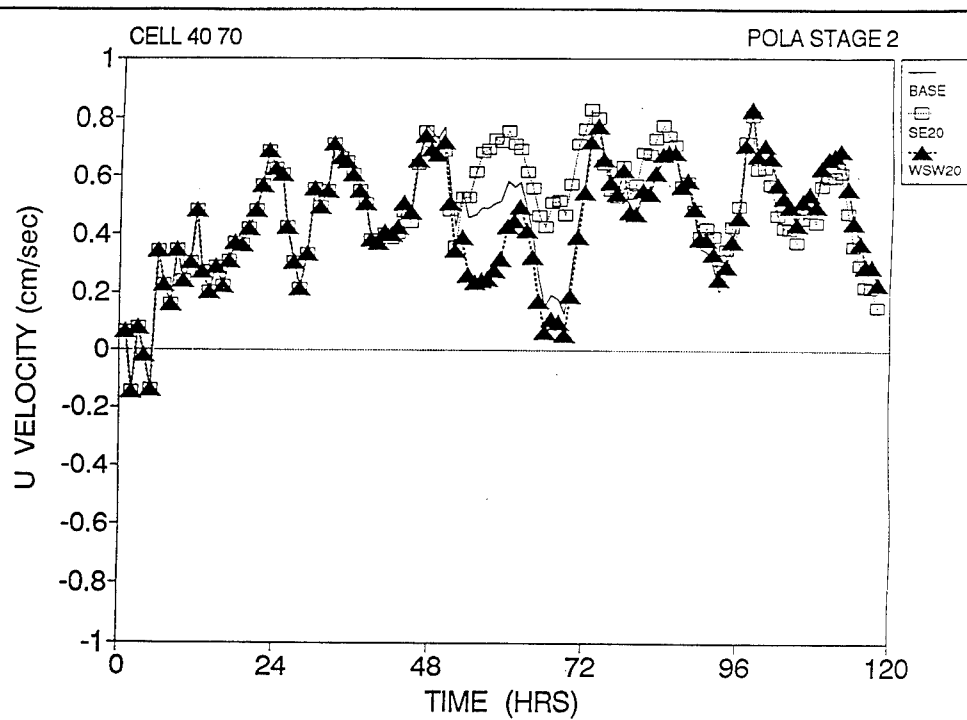
a. u response to BW, SE20, and WSW20 at station 3

b. v response to BW, SE20, and WSW20 at station 3

Figure D15. Time series of POLA 2 current velocity

a. u response to BW, SE20, and WSW20 at station 4

b. v response to BW, SE20, and WSW20 at station 4

Figure D16. Time series of POLA 2 current velocity

D17

a. u under BW at station 1
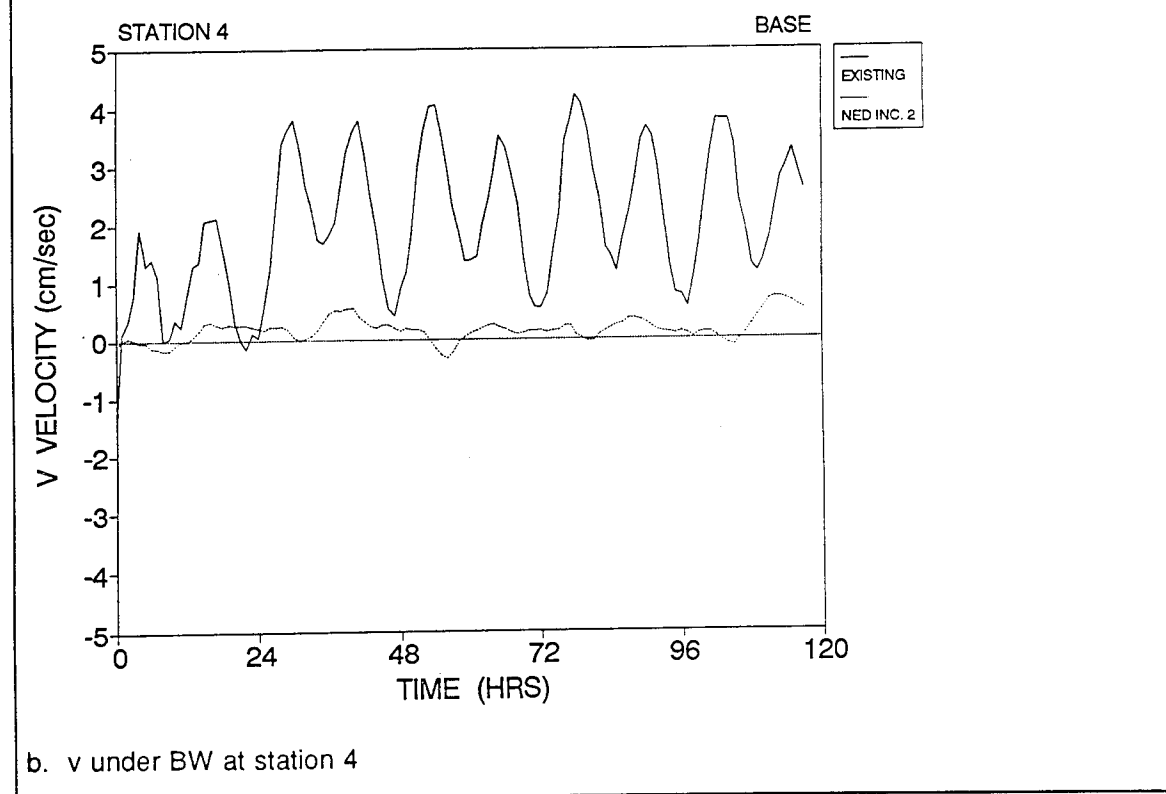

b. v under BW at station 1

Figure D17. Time series of NED2 current velocity

a. u under BW at station 2

b. v under BW at station 2

Figure D18. Time series of NED2 current velocity

a. u under BW at station 3

b. v under BW at station 3

Figure D19. Time series of NED2 current velocity
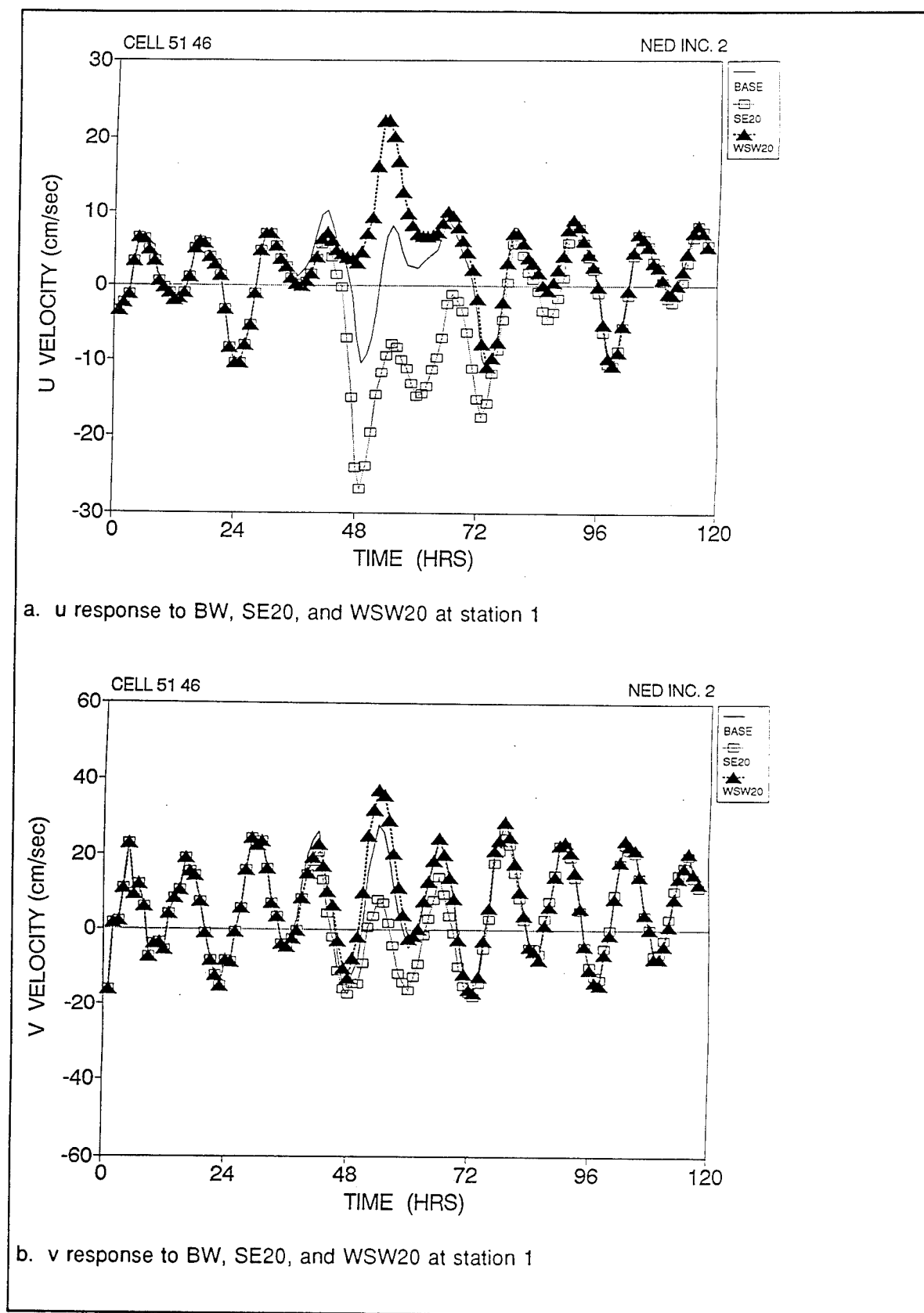
Appendix D   Time Series Plots in Support of the Ship Simulation Model

a. u under BW at station 4

b. v under BW at station 4

Figure D20. Time series of NED2 current velocity

Appendix D   Time Series Plots in Support of the Ship Simulation Model

a. u response to BW, SE20, and WSW20 at station 1
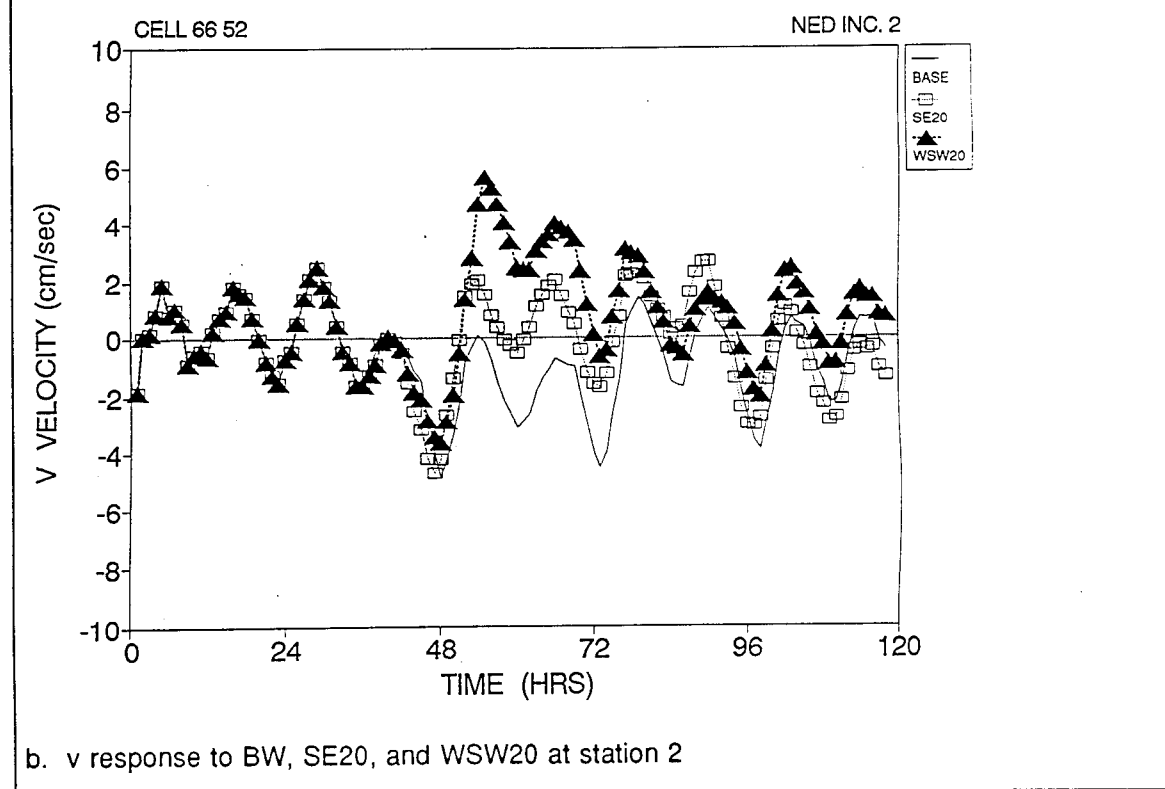

b. v response to BW, SE20, and WSW20 at station 1

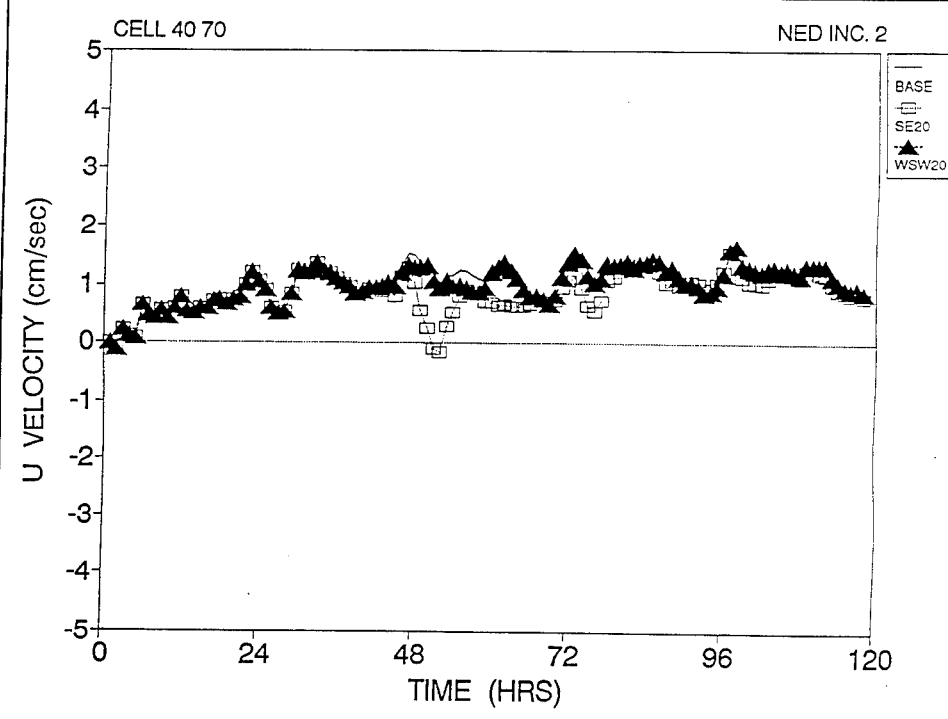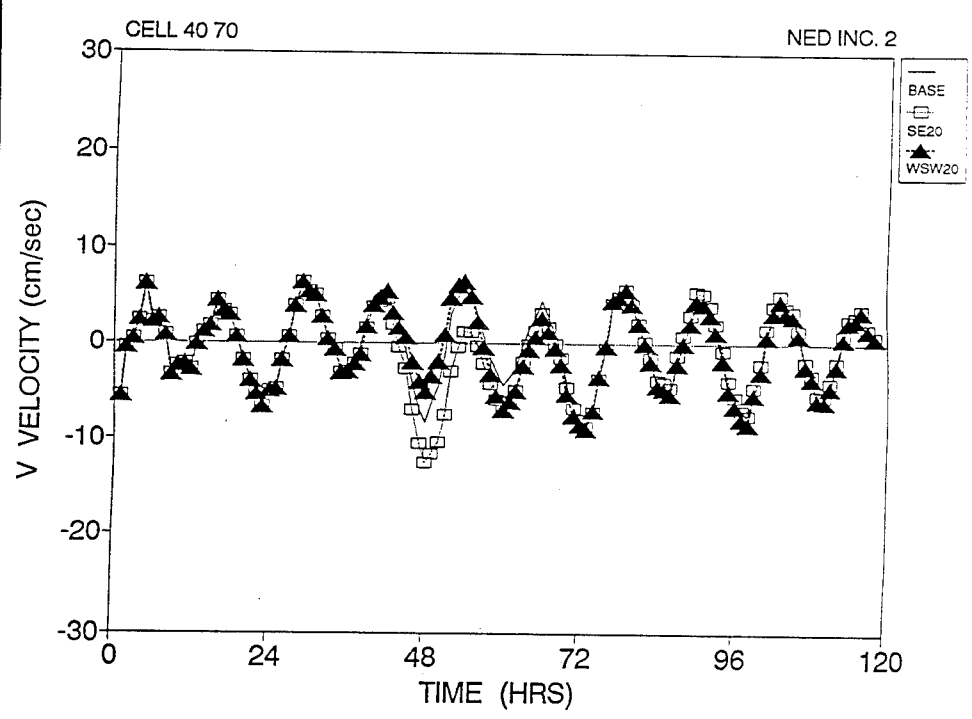Figure D21. Time series of NED2 current velocity
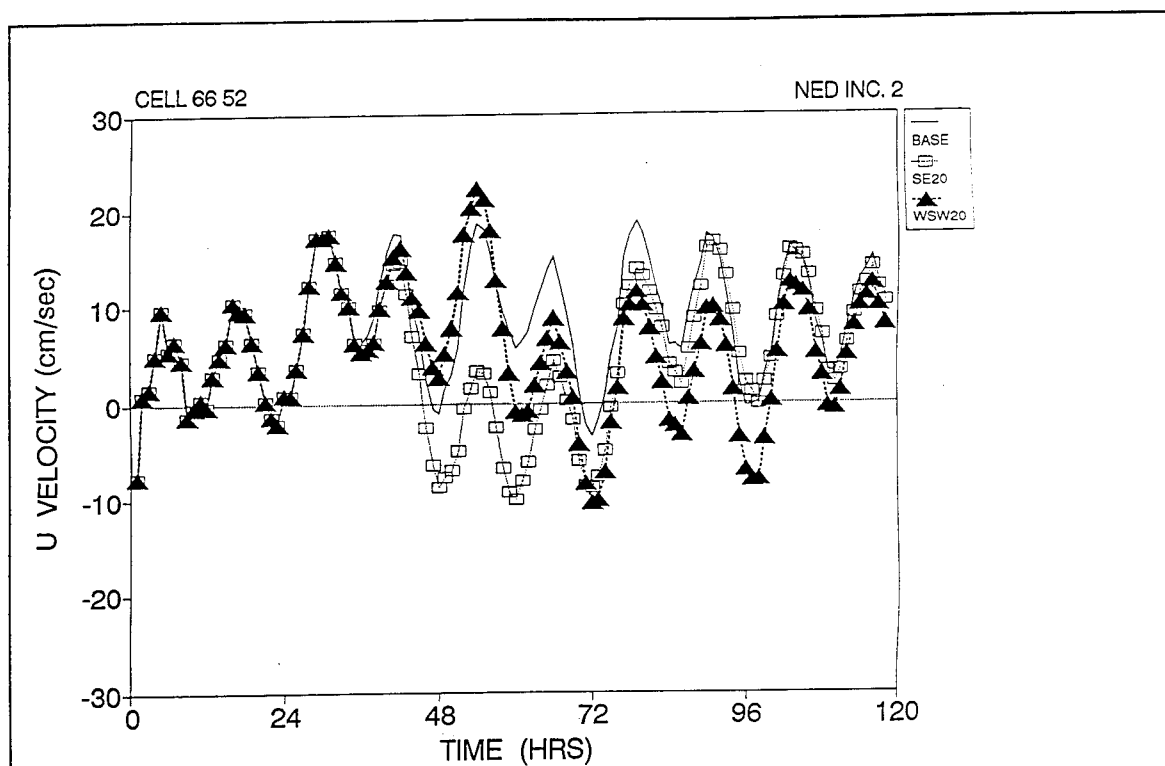
a. u response to BW, SE20, and WSW20 at station 2

b. v response to BW, SE20, and WSW20 at station 2

Figure D22. Time series of NED2 current velocity

Appendix D   Time Series Plots in Support of the Ship Simulation Model
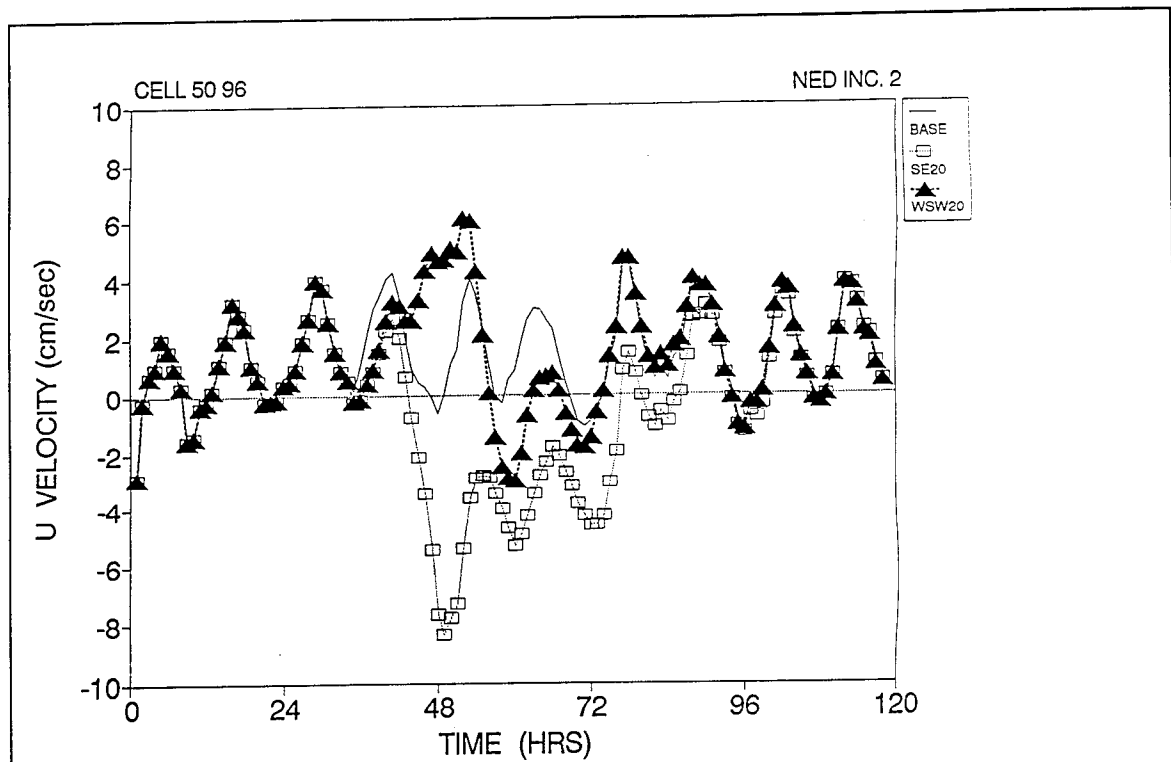
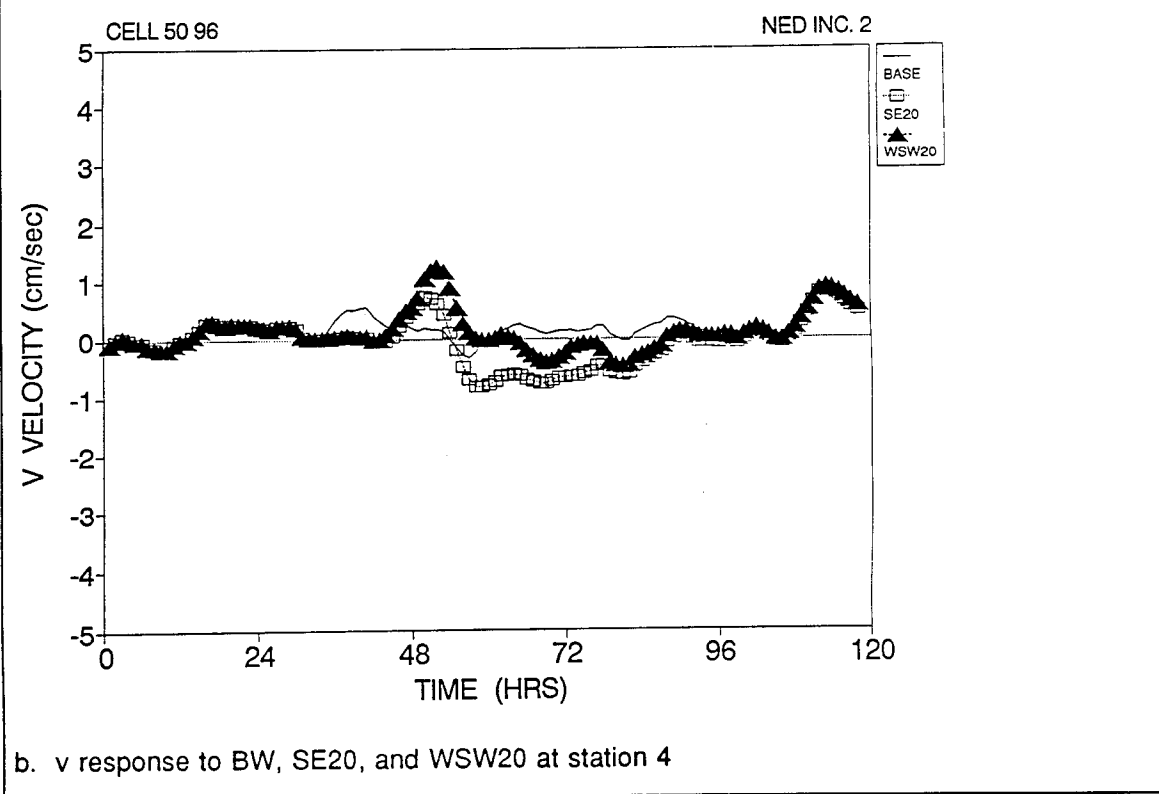a. u response to BW, SE20, and WSW20 at station 3

b. v response to BW, SE20, and WSW20 at station 3

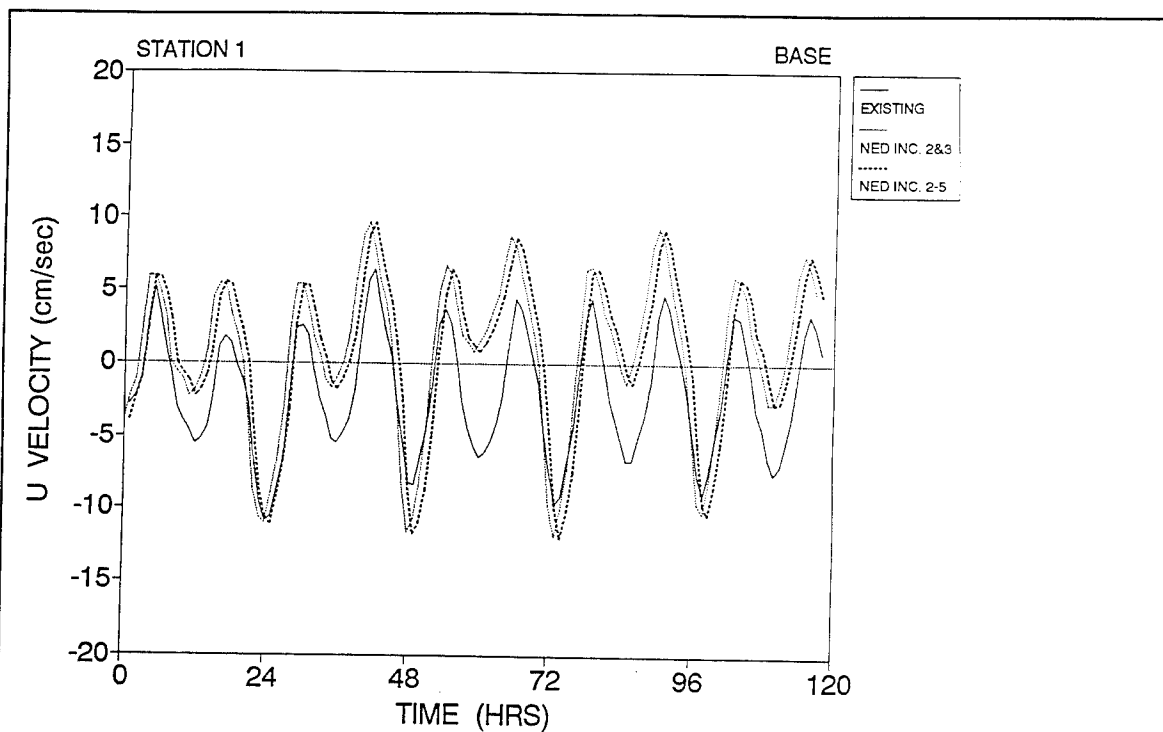Figure D23. Time series of NED2 current velocity

D24

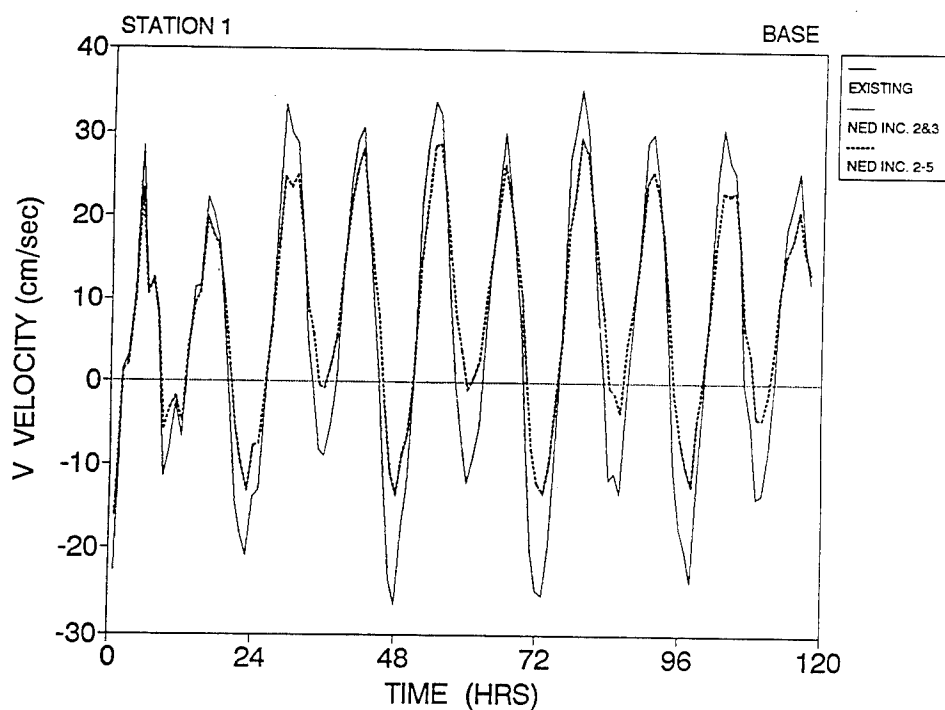a. u response to BW, SE20, and WSW20 at station 4

b. v response to BW, SE20, and WSW20 at station 4

Figure D24. Time series of NED2 current velocity

Appendix D   Time Series Plots in Support of the Ship Simulation Model

a. u under BW at station 1

b. v under BW at station 1

Figure D25. Time series of NED2&3 and NED2-5 current velocity

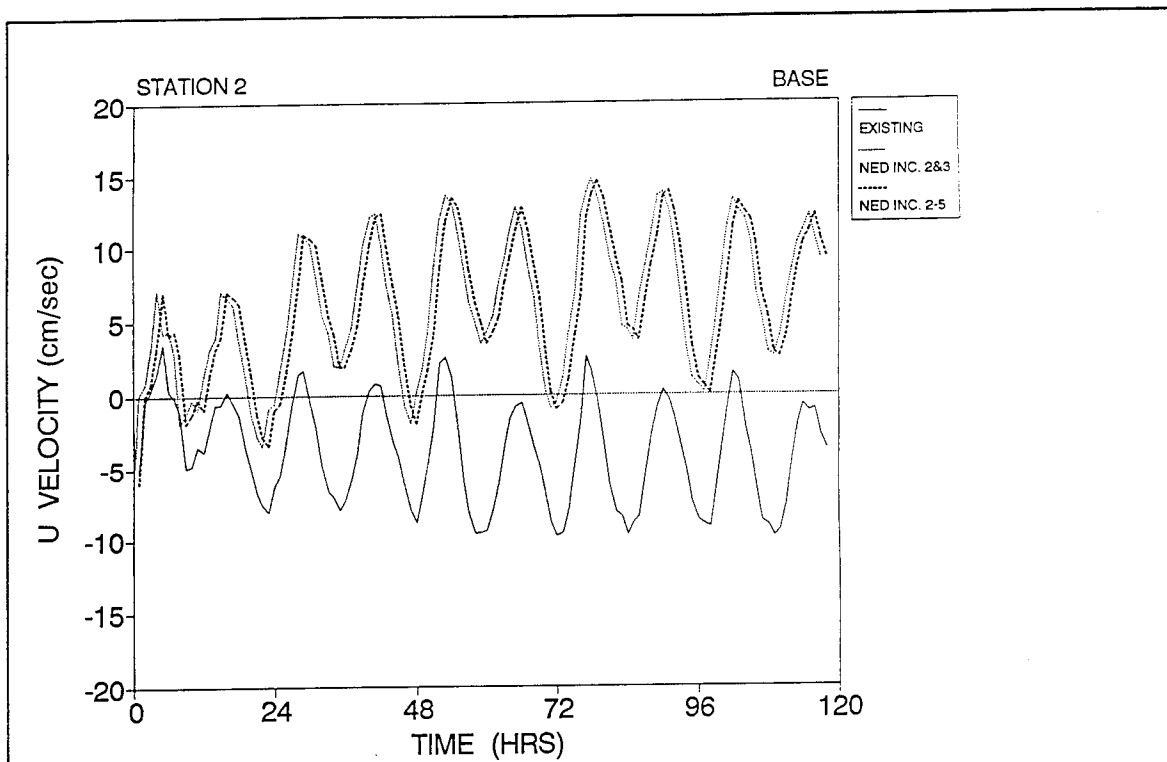Appendix D   Time Series Plots in Support of the Ship Simulation Model
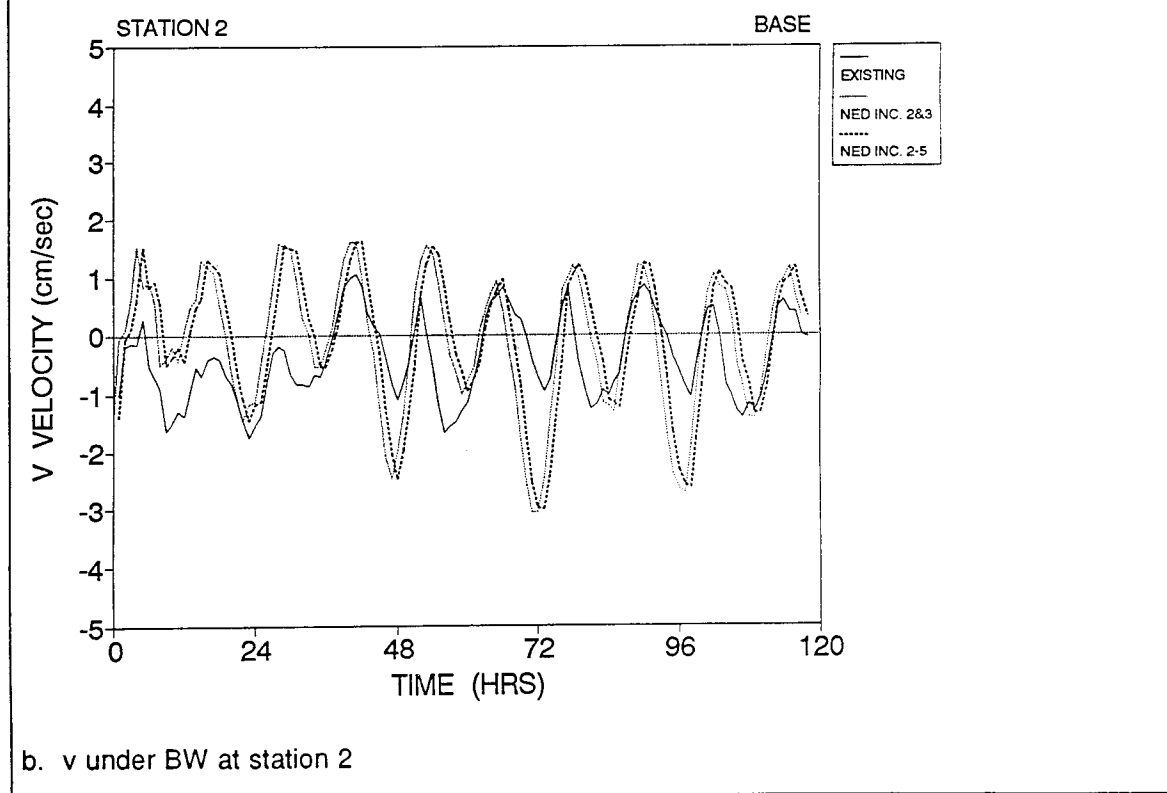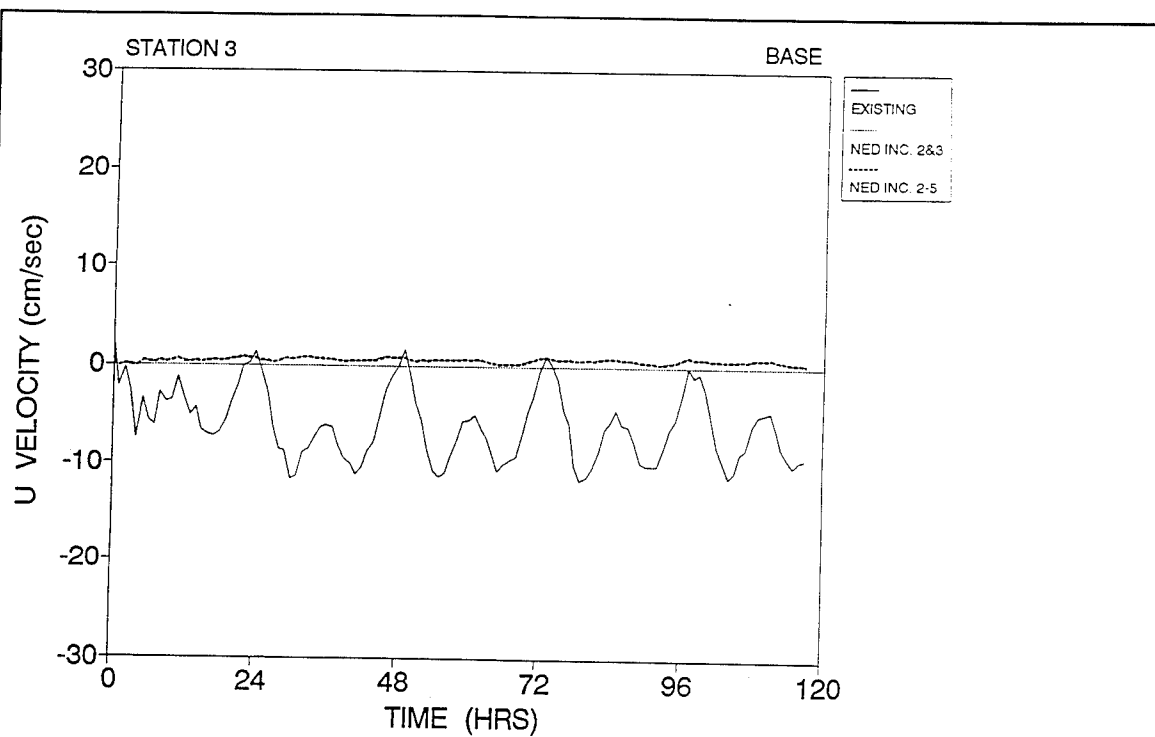
a. u under BW at station 2

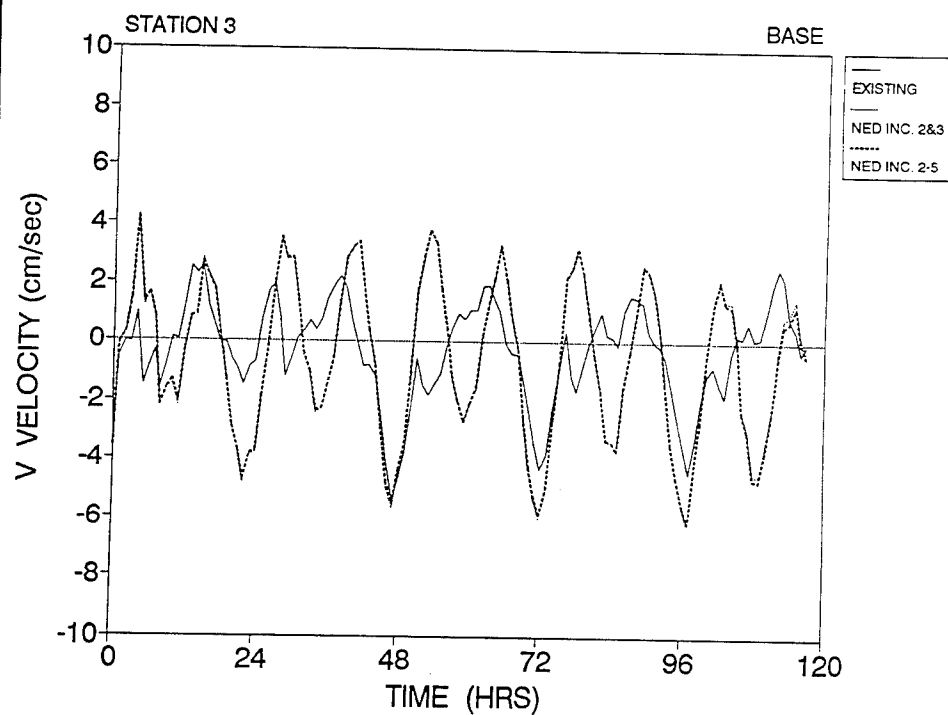b. v under BW at station 2

Figure D26. Time series of NED2&3 and NED2-5 current velocity

a. u under BW at station 3

b. v under BW at station 3

Figure D27. Time series of NED2&3 and NED2-5 current velocity

D28
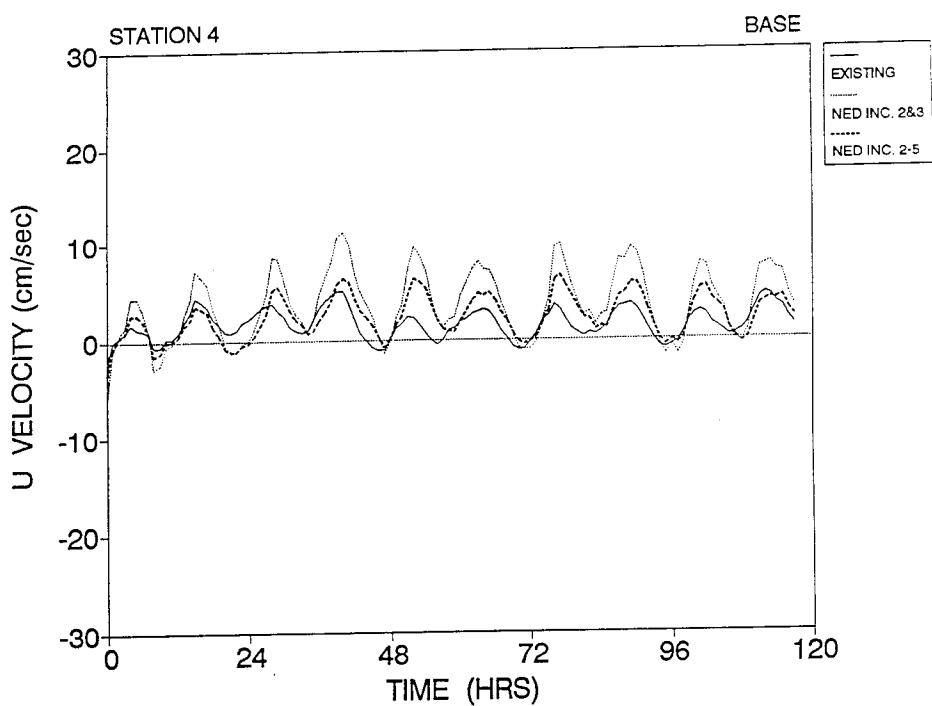
a. u under BW at station 4
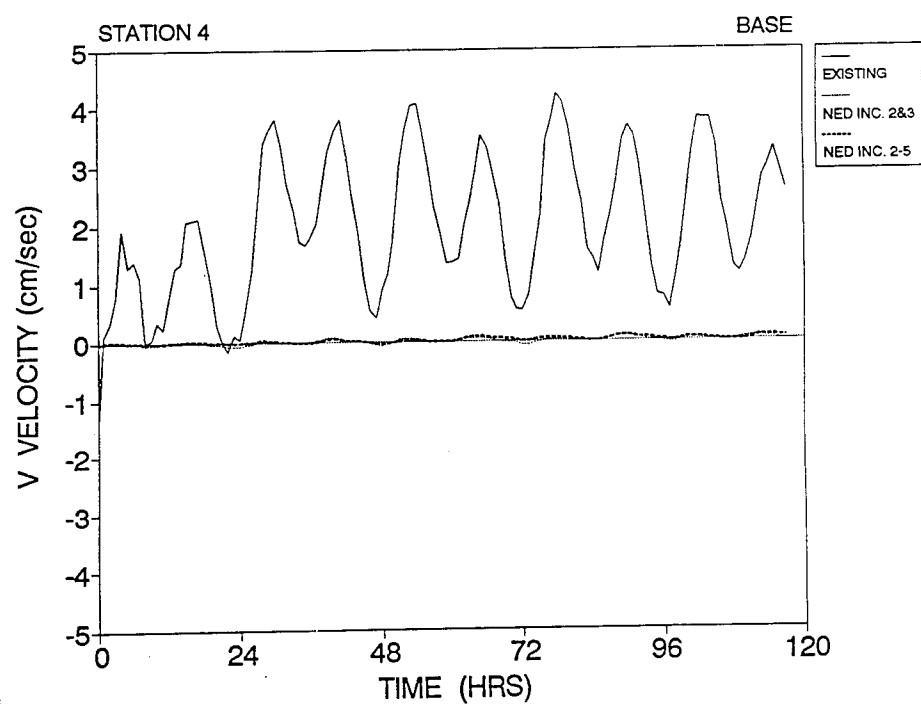
b. v under BW at station 4

Figure D28. Time series of NED2&3 and NED2-5 current velocity
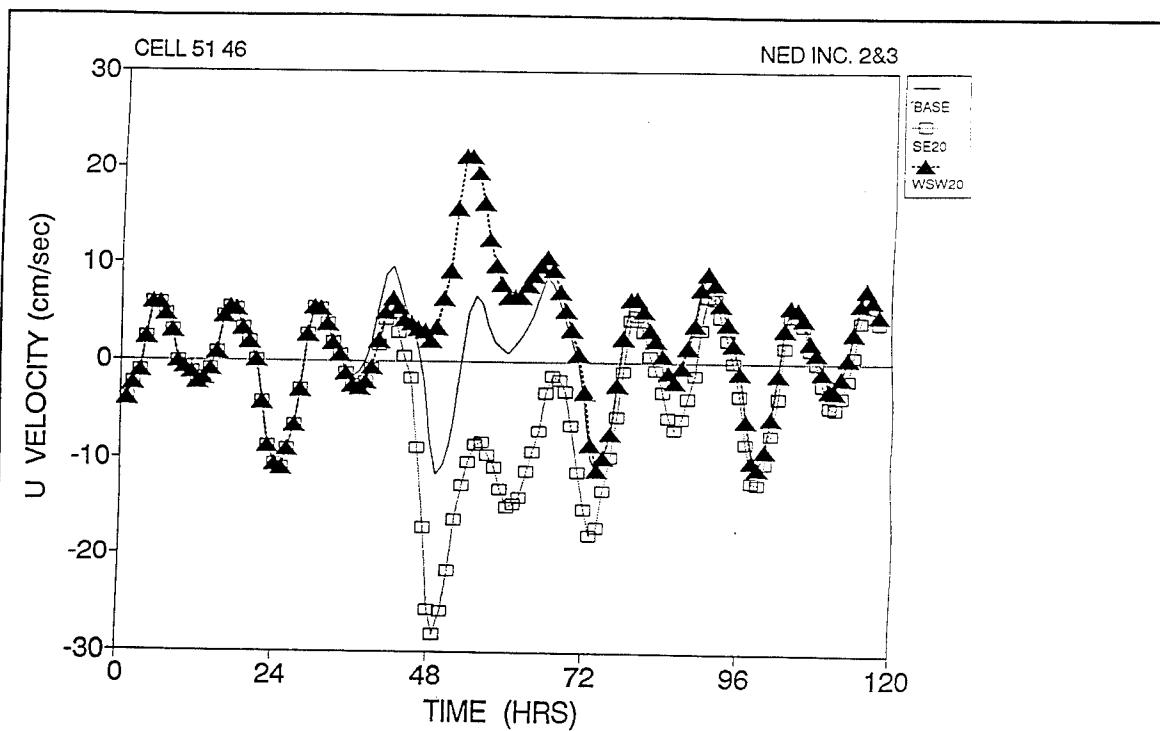
Appendix D   Time Series Plots in Support of the Ship Simulation Model

a. u response to BW, SE20, and WSW20 at station 1

b. v response to BW, SE20, and WSW20 at station 1

Figure D29. Time series of NED2&3 current velocity

Appendix D Time Series Plots in Support of the Ship Simulation Model

a. u response to BW, SE20, and WSW20 at station 2

b. v response to BW, SE20, and WSW20 at station 2

Figure D30. Time series of NED2&3 current velocity

a. u response to BW, SE20, and WSW20 at station 3

b. v response to BW, SE20, and WSW20 at station 3

Figure D31. Time series of NED2&3 current velocity

D32

a. u response to BW, SE20, and WSW20 at station 4

b. v response to BW, SE20, and WSW20 at station 4

Figure D32. Time series of NED2&3 current velocity
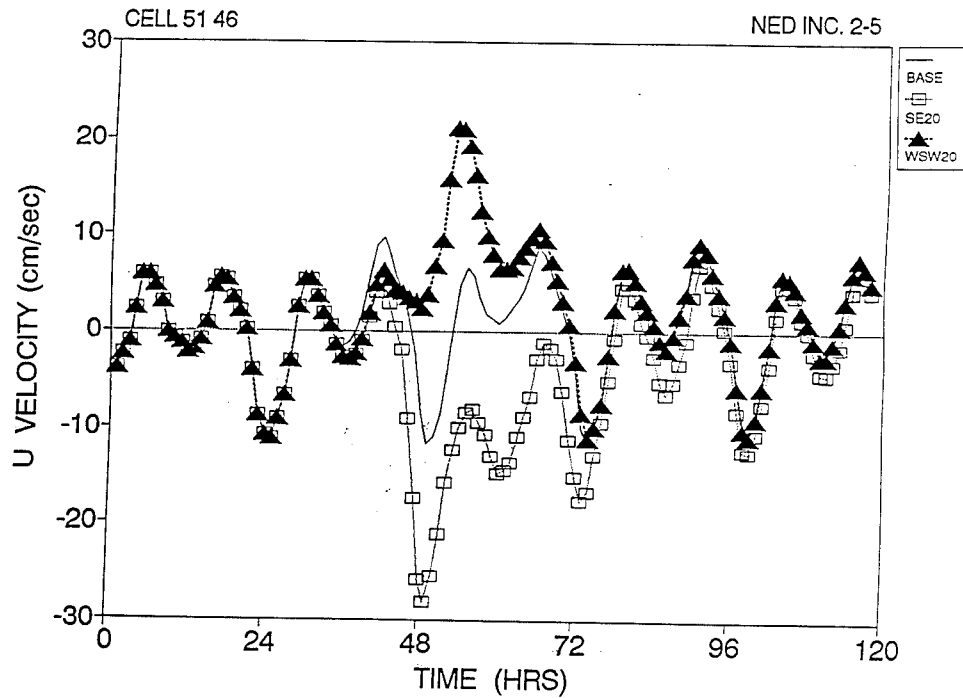
Appendix D   Time Series Plots in Support of the Ship Simulation Model

a. u response to BW, SE20, and WSW20 at station 1
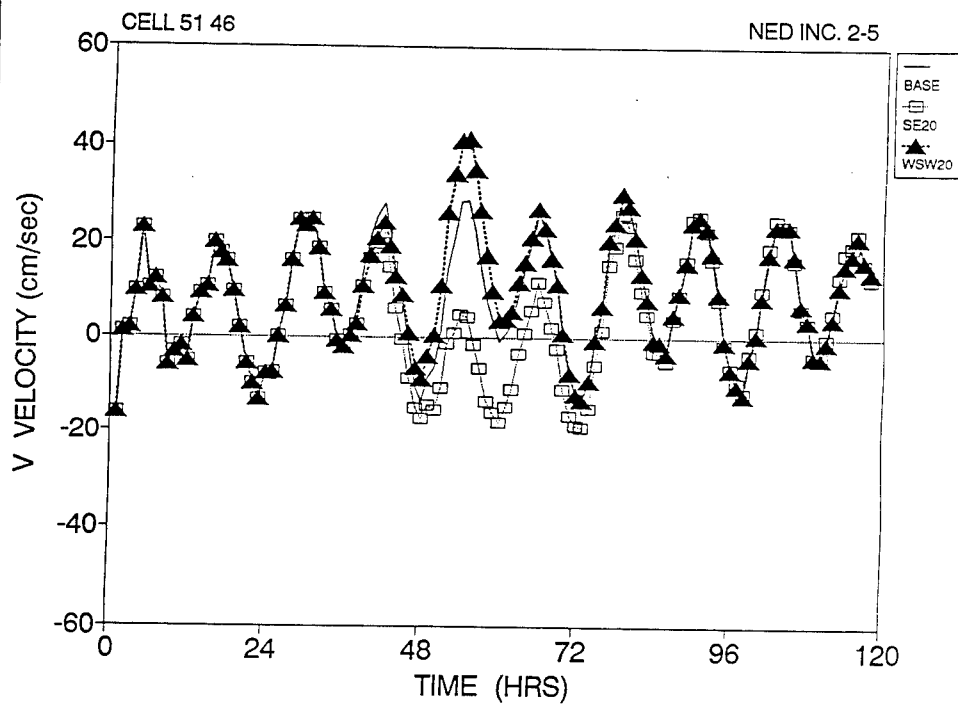
b. v response to BW, SE20, and WSW20 at station 1
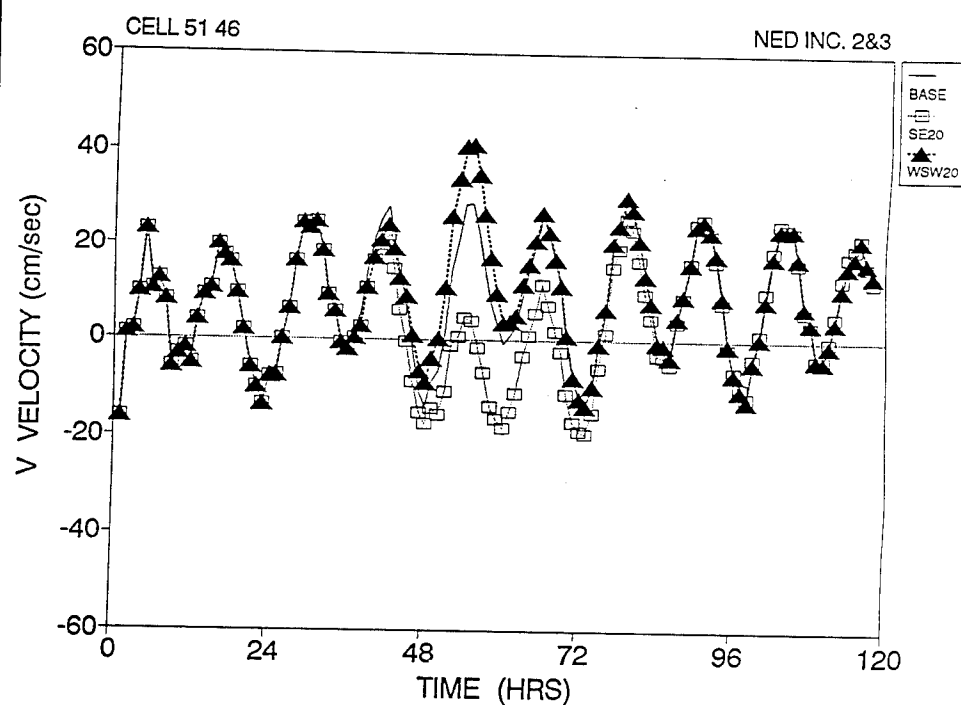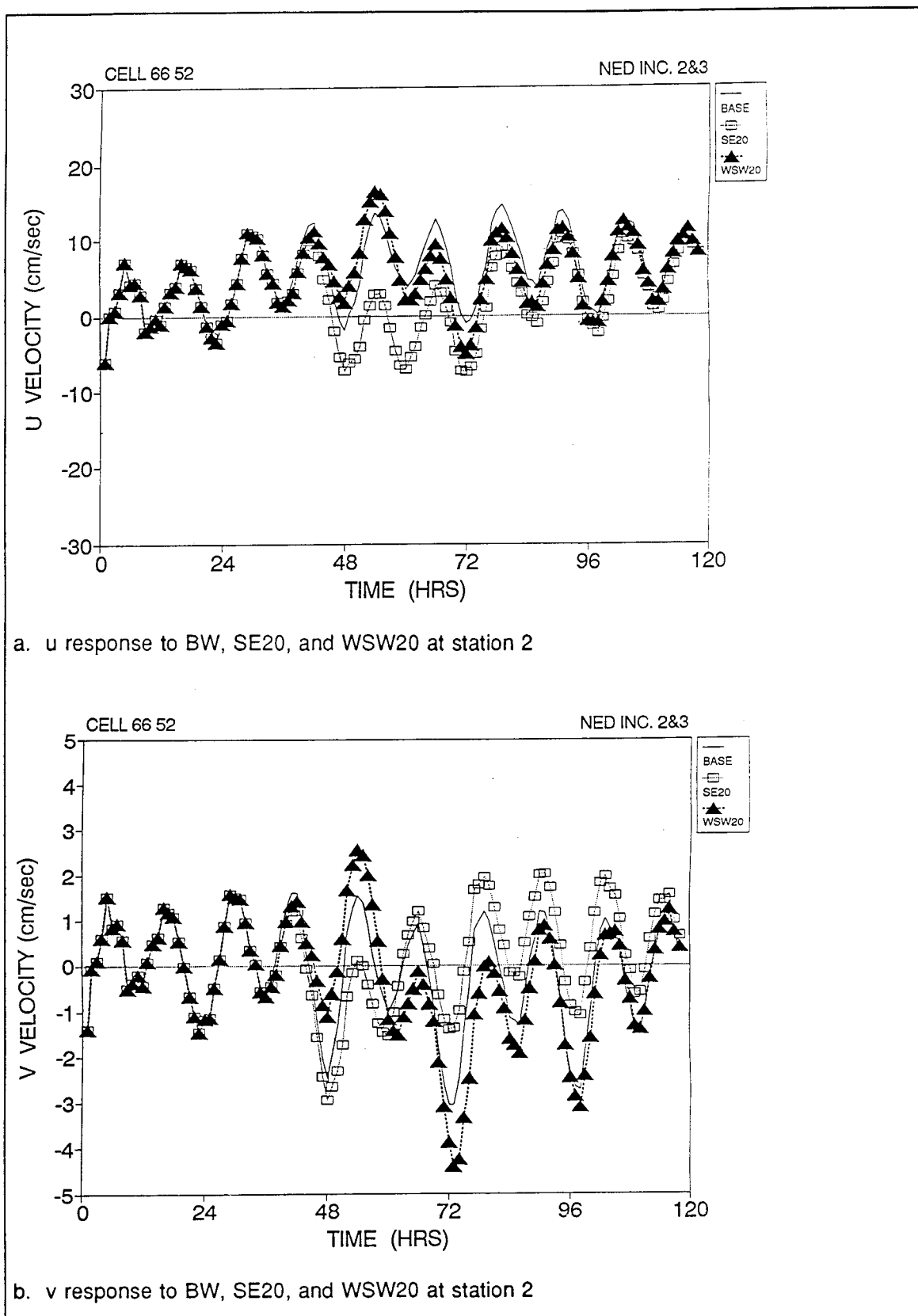
Figure D33. Time series of NED2-5 current velocity
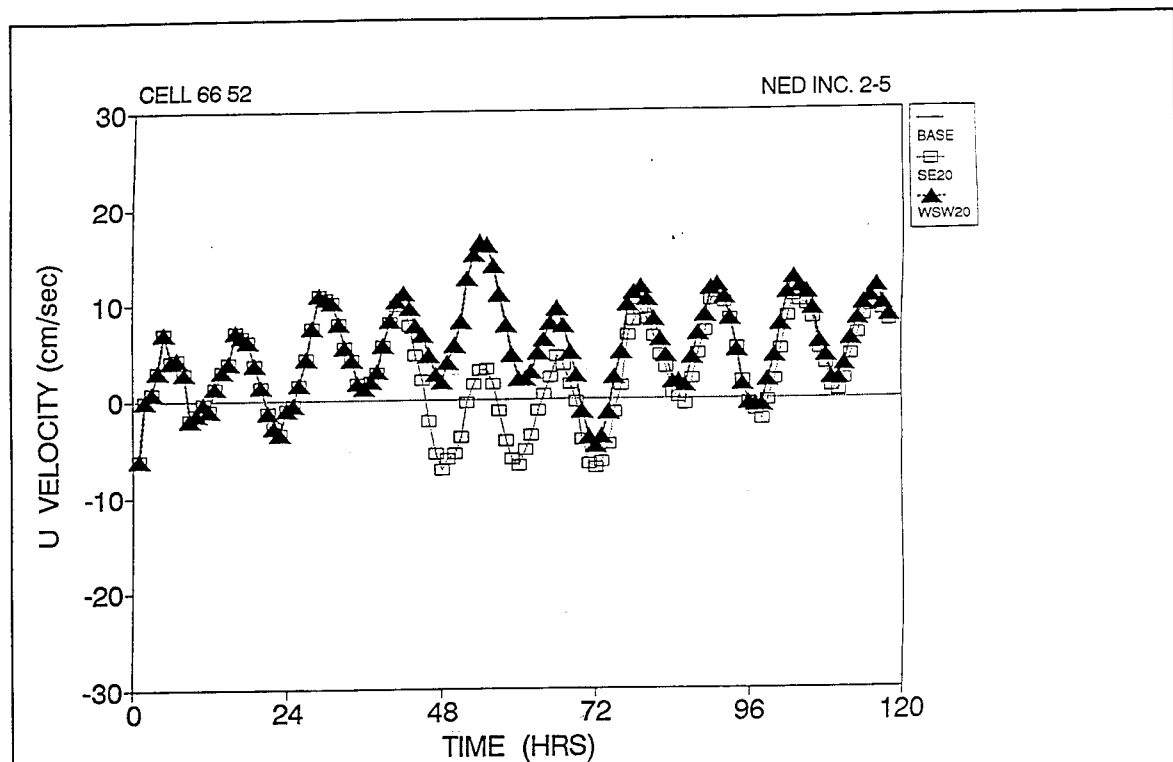
a. u response to BW, SE20, and WSW20 at station 2
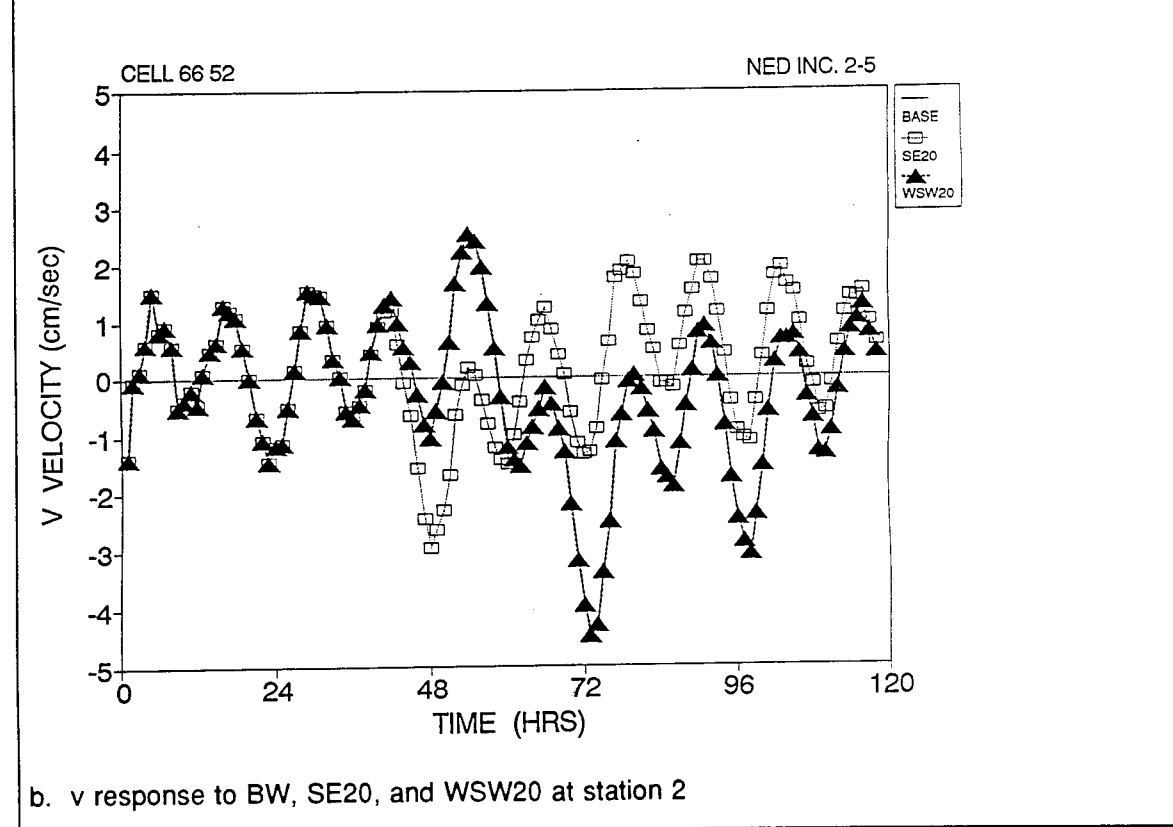
b. v response to BW, SE20, and WSW20 at station 2

Figure D34. Time series of NED2-5 current velocity
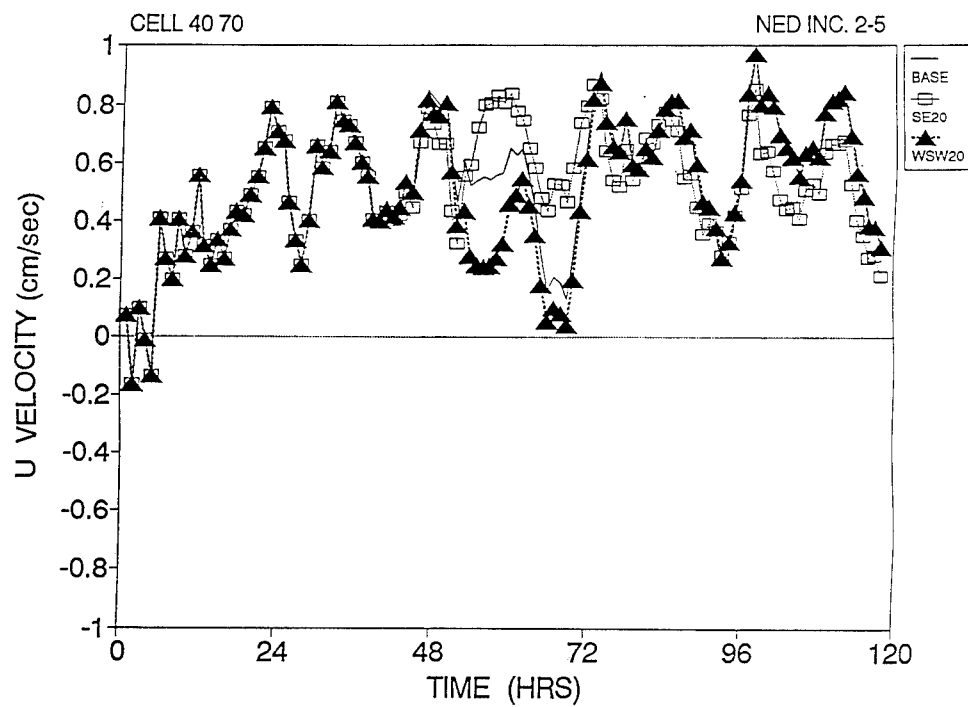
a. u response to BW, SE20, and WSW20 at station 3
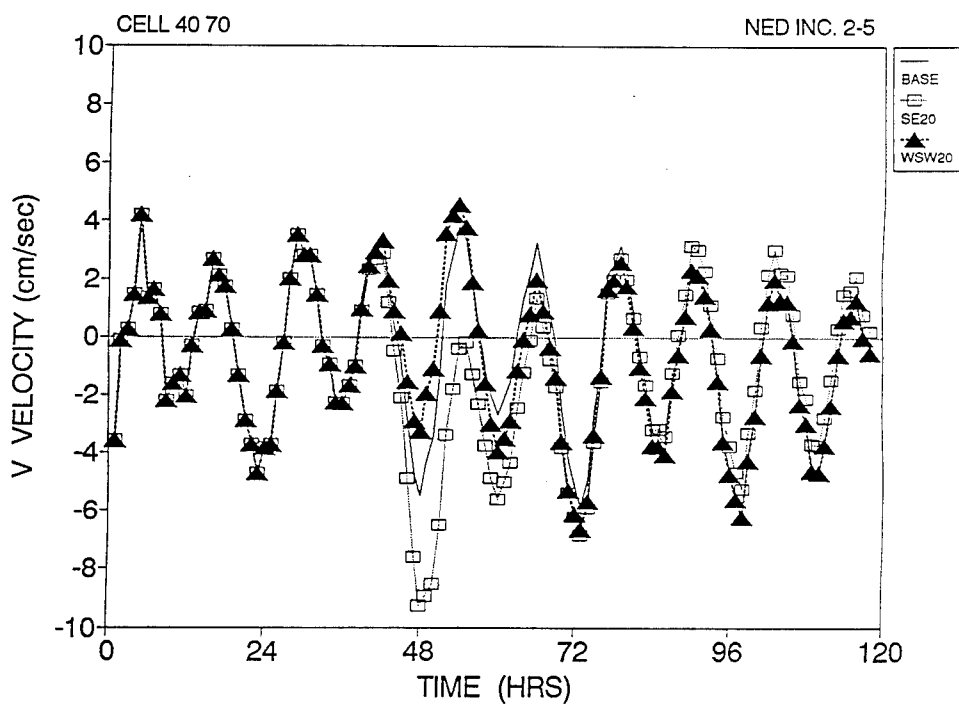
b. v response to BW, SE20, and WSW20 at station 3
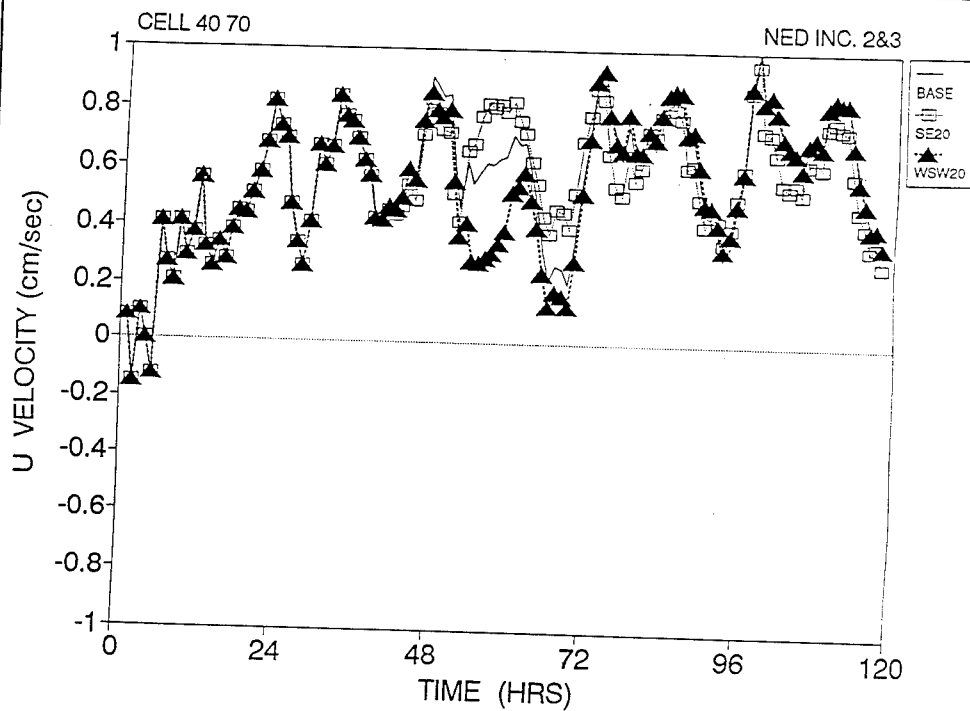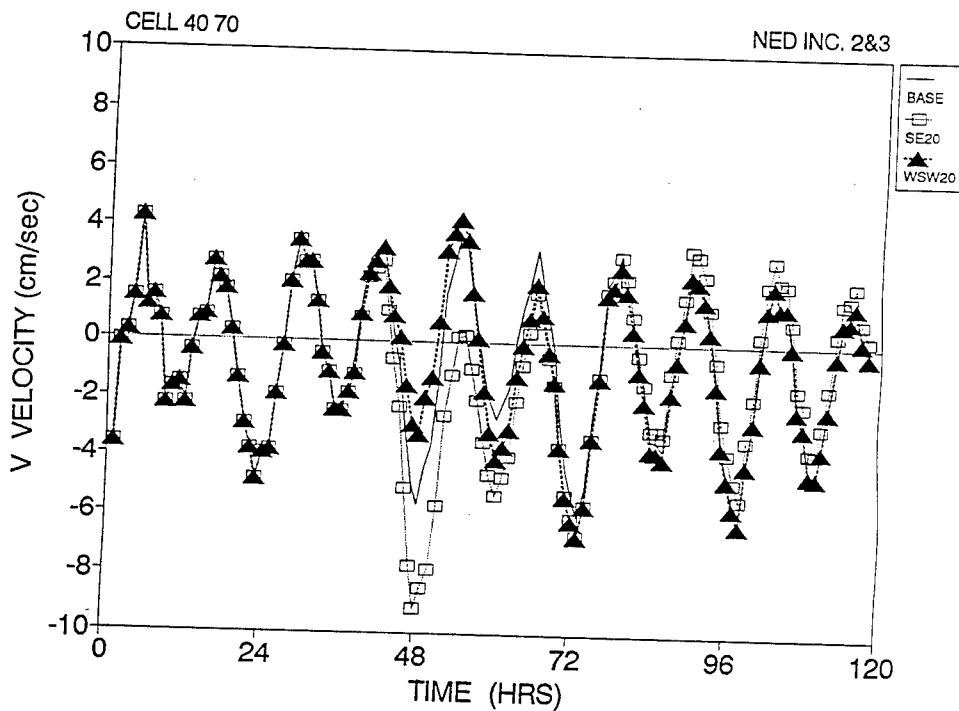
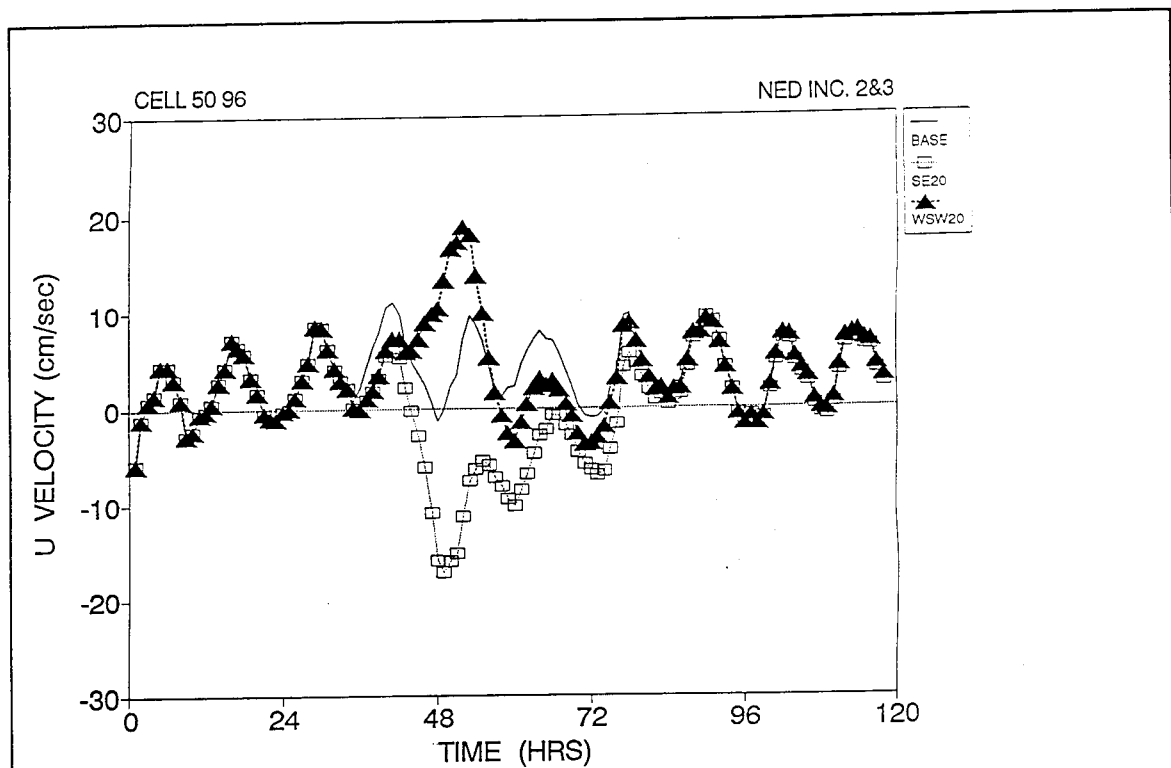Figure D35. Time series of NED2-5 current velocity

D36
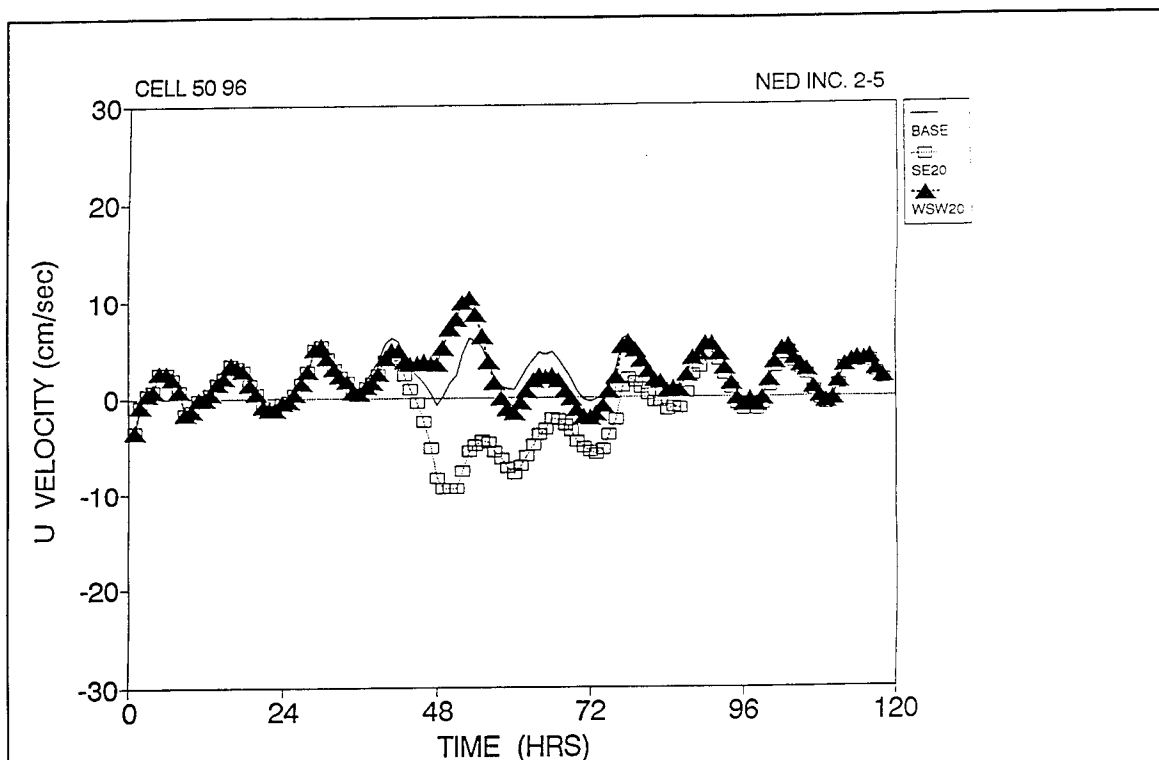
a. u response to BW, SE20, and WSW20 at station 4

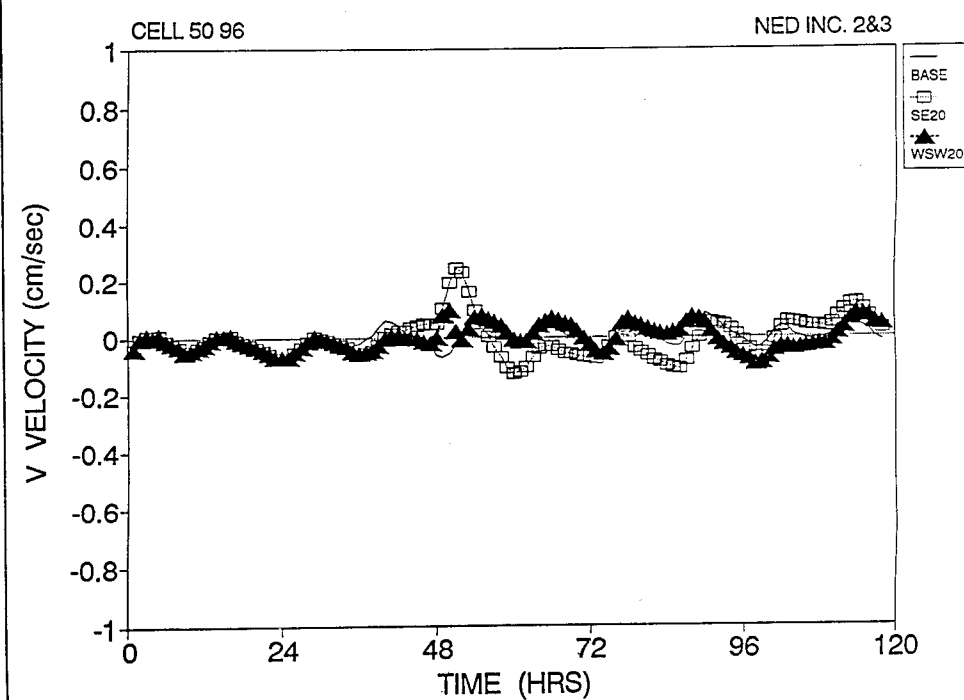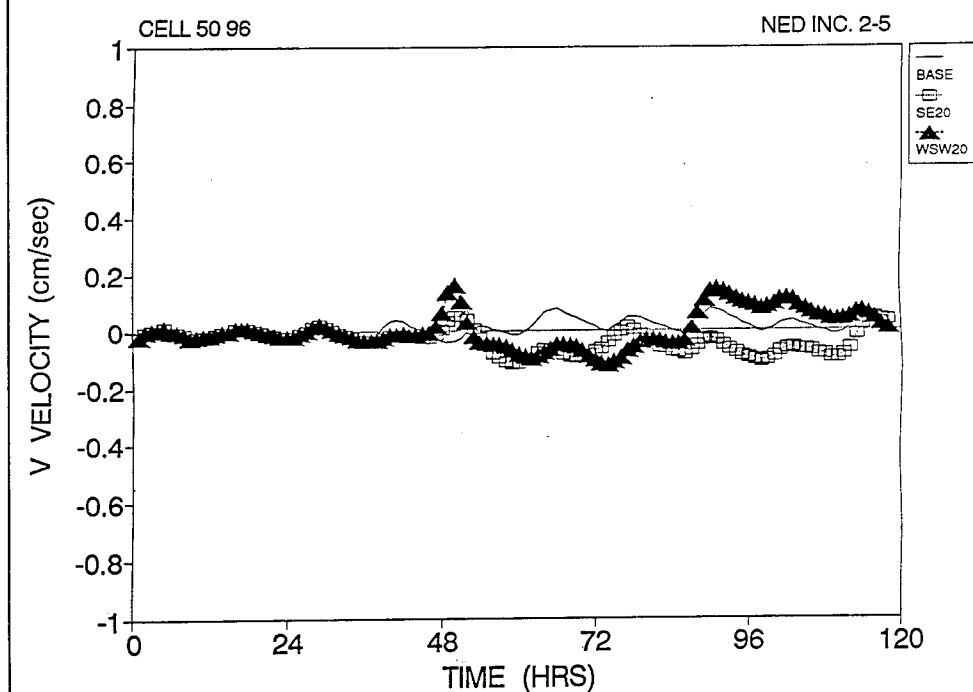b. v response to BW, SE20, and WSW20 at station 4

Figure D36. Time series of NED2-5 current velocity

Appendix D   Time Series Plots in Support of the Ship Simulation Model
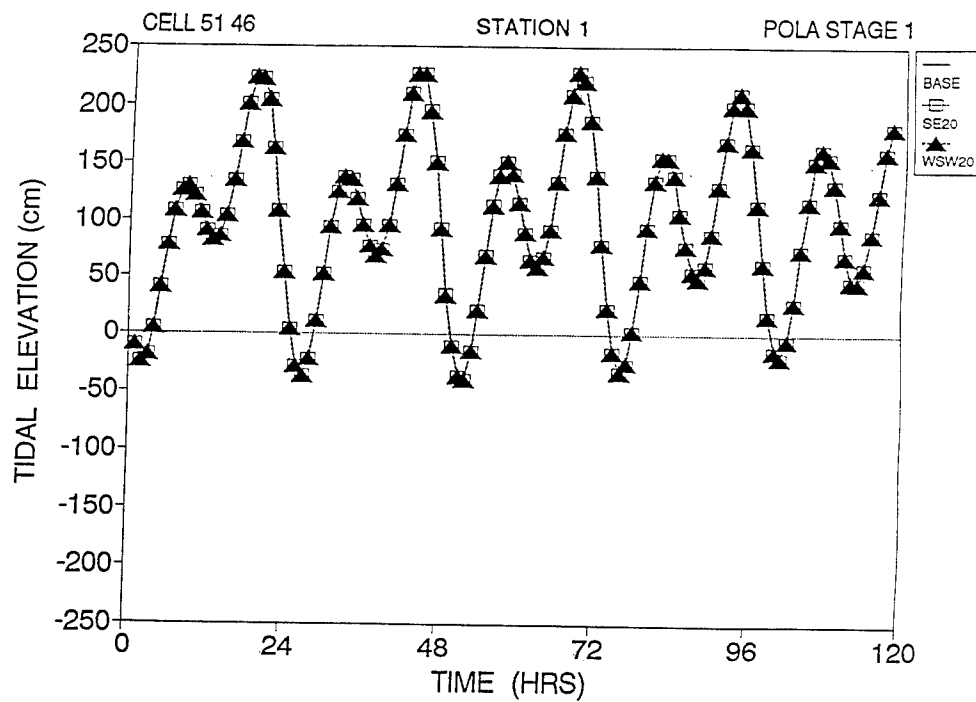
a. at station 1 under POLA 1
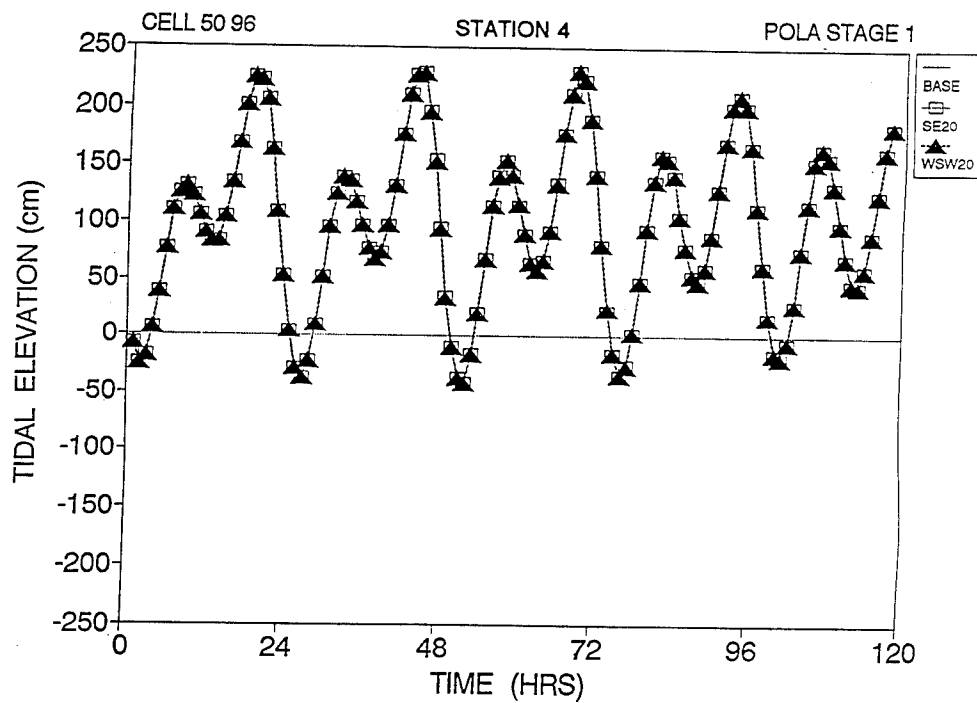
b. at station 4 under POLA 1

Figure D37. Water surface elevation response to wind

D38

a. at station 1 under POLA 2

b. at station 4 under POLA 2
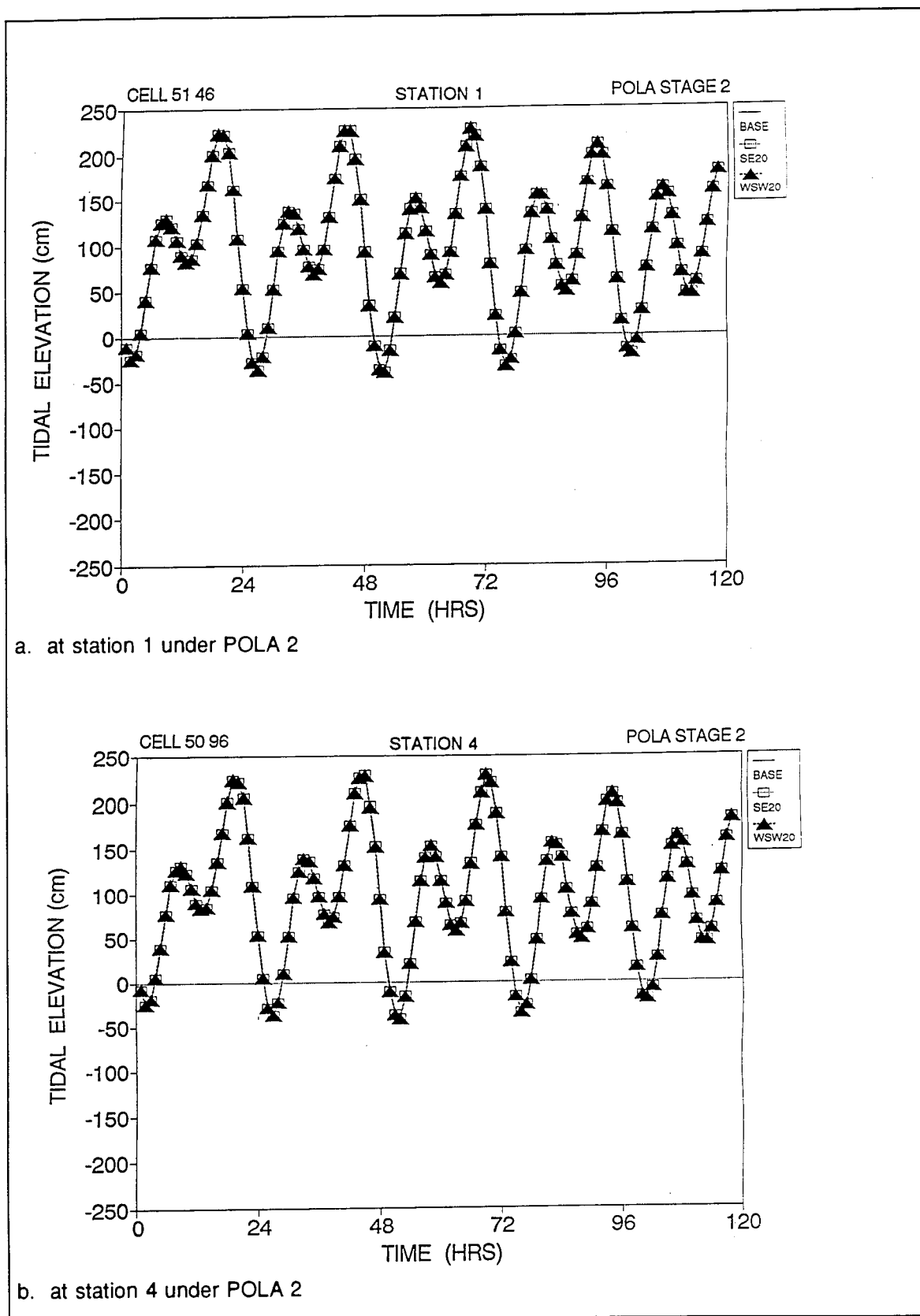
Figure D38. Water surface elevation response to wind

Appendix D   Time Series Plots in Support of the Ship Simulation Model

a. at station 1 under NED 2

b. at station 4 under NED 2

Figure D39. Water surface elevation response to wind

D40

a. at station 1 under NED 2&3

b. at station 4 under NED 2&3
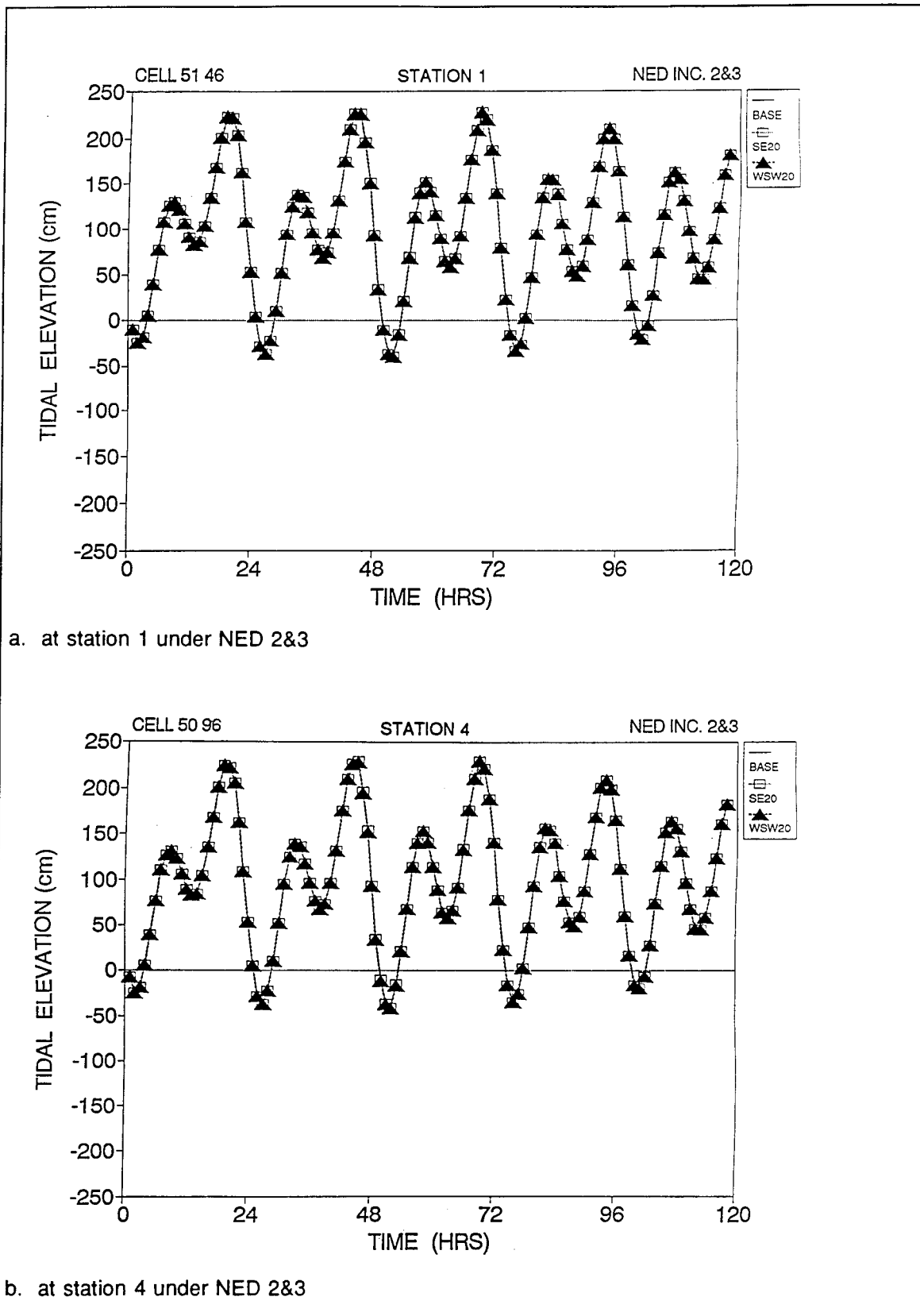
Figure D40. Water surface elevation response to wind
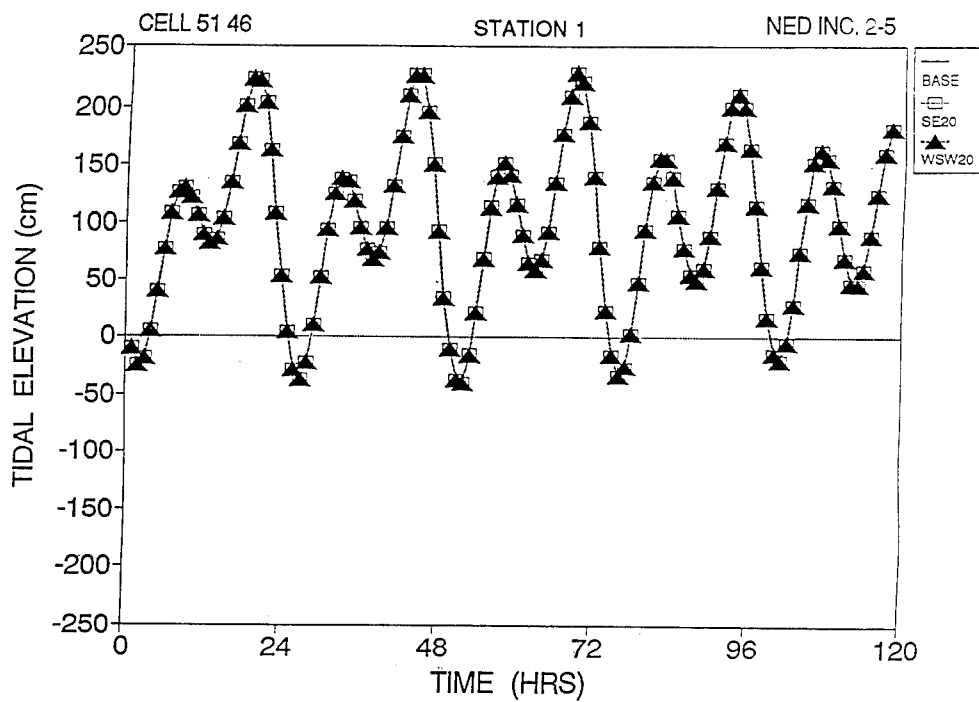
a. at station 1 under NED 2-5
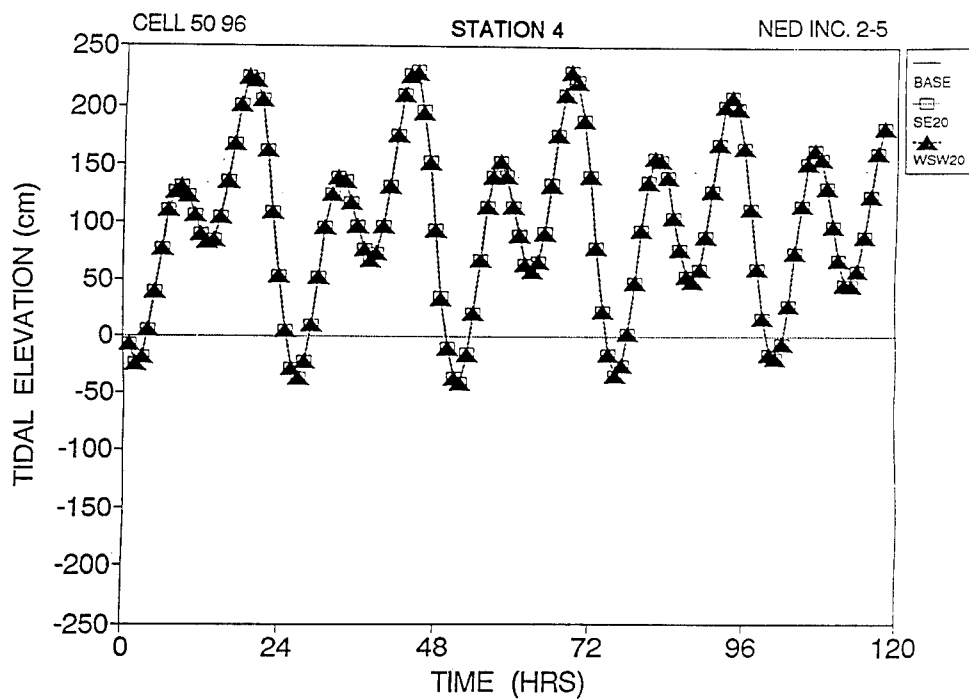
b. at station 4 under NED 2-5

Figure D41. Water surface elevation response to wind

Appendix E
Analysis of Hydrodynamic Impacts from Proposed Plans Under Wind Effects

In order to address issues important to ship simulation such as crosscurrents and adequately detail velocity changes, the authors choose to use the vector components u and v instead of the resultant variations to discuss velocity changes. For those who are interested in the resultant variations, total changes can be obtained by taking the square root of u^2 and v^2, and the direction by taking the inverse tangent of v/u.

A wind event with the wind stress having Gaussian distribution was embedded in the otherwise BW for 48 hr (from hr 24 to hr 72). Wind stress had the strongest effect on the water surface (equivalent to 20 knots steady wind) from hr 36 to hr 60. Figures E1-E4 show the u and v velocity under BW, WSW20, and SE20 for stations 1, 2, 3, and 4. Figure E1 shows the velocity variation at station 1, where u increases by 10 cm/s (a 62-percent increase) during flood; v increases by 10 cm/s (a 19-percent increase) during flood under WSW 20. The u velocity decreases by 7 cm/s (a 44-percent decrease) during ebb; v decreases by 15 cm/s during flood (a 29-percent decrease) under SE 20. Figure E2 shows the variation at station 2, where u increases by 3 cm/s (a 38-percent increase) during flood; v increases by 1 cm/s (a 55-percent increase) during flood under WSW 20 and u decreases by 7 cm/s (a 62-percent decrease) during ebb; v decreases by 0.5 cm/s (a 27-percent decrease) during ebb under SE 20. Figure E3 shows the variation at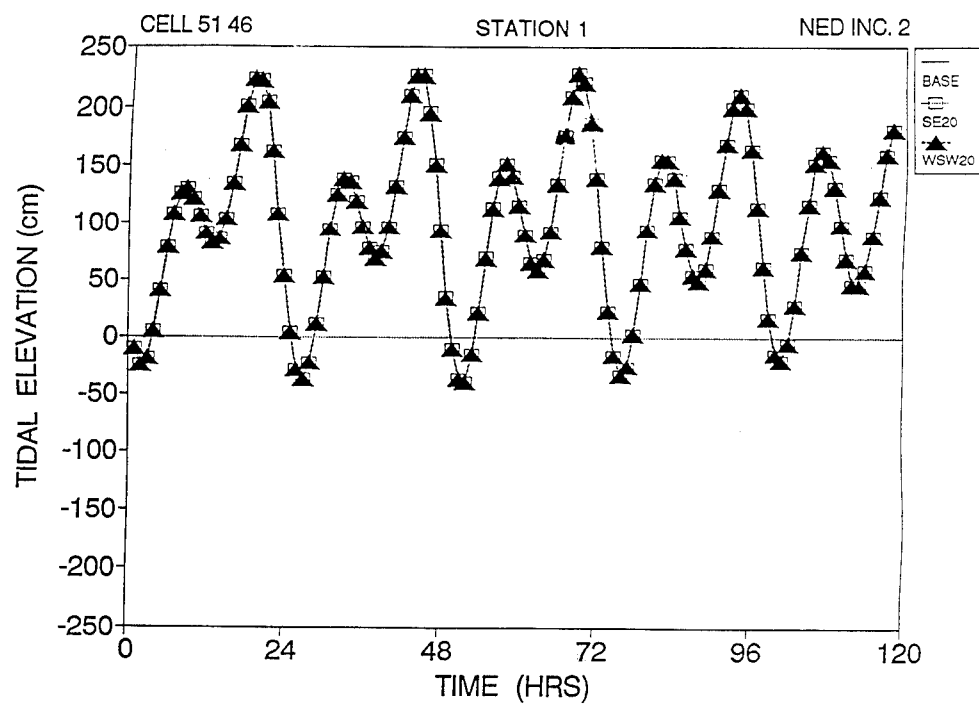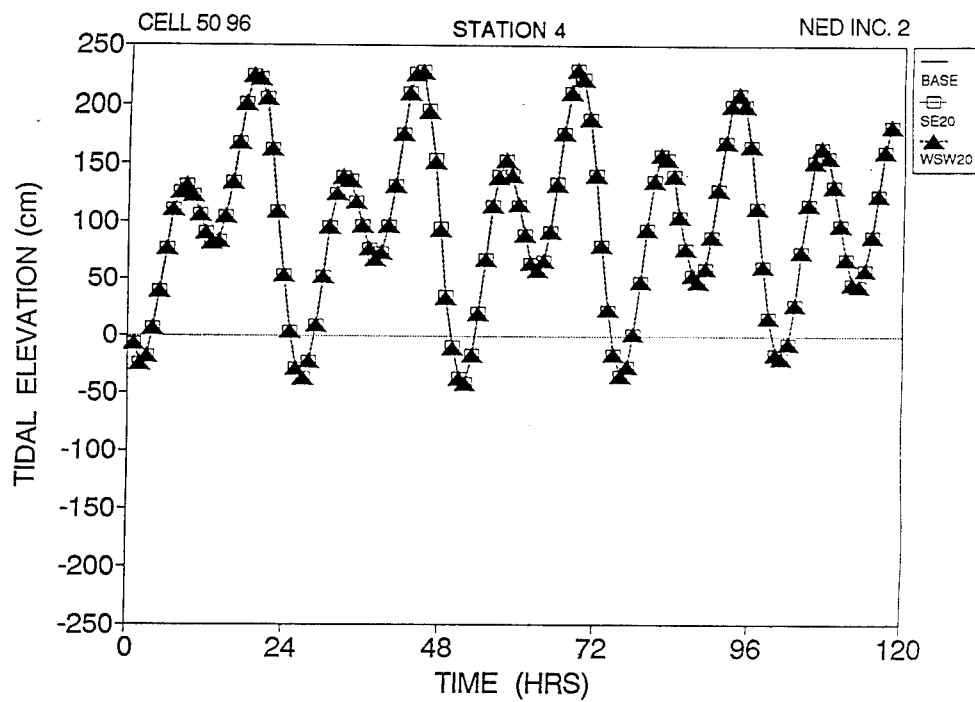 station 3, where u decreases by 5 cm/s (a 45-percent decrease) during ebb; v has a 160-deg phase difference to BW during ebb under WSW 20 and u decreases by 3 cm/s (a 27-percent decrease) during flood under SE 20. Figure E4 shows the variation at station 4, where u increases by 5 cm/s (a 125-percent increase) during flood; v decreases by 2.5 cm/s (a 100-percent decrease) during ebb under WSW 20 and u increases by 3 cm/s (an 85-percent increase) during flood; v decreases by 2 cm/s during flood (a 57-percent decrease) under SE 20.

In order to differentiate the velocity variation under the dual impacts of the proposed harbor plans and critical wind conditions, the analysis proceeds one

harbor plan at a time. Under each plan, the base wind condition and the critical wind condition are discussed separately.

Results for the POLA Stage 1 Condition

Figures C1 and C2 display circulation vector plots for POLA 1 under BW, WSW20, and SE20. In terms of overall pattern, the circulation follows the same basic pattern found before; that is, adjusting to the harbor configuration. The wind's effect is to induce a velocity component toward its traveling direction as long as the fetch distance is sufficient. Specifically, the effect of WSW20 reinforces the flood tide and weakens the ebb tide, while SE20 reinforces the ebb tide and weakens the flood tide.

Impact of harbor configuration under base wind condition

Figures D1-D4 compare time series of u and v velocity under BW for POLA 1 and the existing condition. Noticeable differences between POLA 1 and the existing condition were observed. Figure D1 shows velocity variation at station 1, where u velocity increases while v velocity decreases, an indication of the effect of the blocking effect by Pier 400 near the breakwater entrance. Figure D2 shows the velocity variation at station 2, where while v increases at both flood and ebb tide, the westward velocity corresponds to jet-induced recirculation in the existing condition which disappeared after the introduction of Pier 400. Figure D3 shows velocities at station 3, where the u velocity is virtually diminished to zero while the v velocity increases in magnitude. The reason for the diminishing u velocity is obvious; Pier 400 was located next to the station that inhibits the motion. Figure D4 shows velocities at station 4, where previously strong eastward u velocity was replaced by oscillatory flow, while v velocity is reduced significantly in magnitude.

Impact under critical wind conditions

After learning about the impact of harbor configuration under the base wind condition, the effect of critical wind conditions on current variation is examined.

Figure D5 shows velocity variations at station 1, where u increases by 12 cm/s (a 60-percent increase) during flood; v increases by 9 cm/s (a 21-percent increase) during flood under WSW 20. The u velocity decreases by 15 cm/s (a 75-percent decrease) during ebb; v decreases by 19 cm/s during flood (a 45-percent decrease) under SE 20. Figure D6 shows the variation at station 2, where u increases by 15 cm/s (a 75-percent increase) during flood; v increases by 0.8 cm/s (a 17-percent increase) during flood under WSW 20. The u decreases by 15 cm/s (a 75-percent decrease) during ebb; v decreases by 2.0 cm/s (a 44-percent decrease) during ebb under SE 20. Figure D7 shows

the variation at station 3, where under WSW20, both u and v are out of phase with BW. Under SE20, u decreases by 0.3 cm/s (a 100-percent decrease) during flood. Figure D8 shows the variation at station 4, where under WSW20, u is out of phase; v decreases by 0.5 cm/s (a 71-percent decrease) during ebb. Under SE20, u decreases by 1.5 cm/s (a 35-percent decrease) during ebb.

Results for POLA Stage 2 Condition

Figures C3 and C4 display circulation vector plots for POLA 2 under BW, WSW20, and SE20. The overall circulation pattern and the role of wind effects on tidal motion at the breakwater entrance are similar to those of POLA 1. The detail changes of velocity will be further discussed using the time series analysis.

Impacts of harbor configuration under base wind conditions

Figures D9-D12 compare time series of u and v velocity under the base wind condition for POLA 2 and the existing condition.

Figure D9 shows that u velocity increases while v velocity decreases from the existing, the same manner in which POLA 1 changes, except the magnitude of the changes in u and v are smaller in POLA 2 than in POLA 1 (by 20 percent). Figure D10 shows the u and v velocity changes at station 2, which has the same pattern of changes as POLA 1, except the magnitude is 50 percent less. Figure D11 shows that the u velocity is nearly zero, while v velocity increases versus the existing. The magnitude of change is smaller in POLA 2 than in POLA 1 (by 30 percent). Figure D12 shows that at station 4, v velocity is nearly zero while u velocity for POLA 2 is comparable to POLA 1. This is the only station where the velocity was not reduced, a finding which is consistent with that of the section titled "Current velocity - time series plot" in Chapter 4 (page 42). The cause of the increase of u velocity in POLA 2 at this location is due to the fact that the north channel width was reduced by 70 percent, which offsets other effects such as channel depth, to acquire large velocity increases. However, the velocity remains below 6 cm/s (0.2 ft/s).

Impacts under critical wind conditions

Velocity changes were smaller in POLA 2 than in POLA 1 for most of the stations under BW, primarily due to the deeper channel of POLA 2. The relation still holds under WSW20 and SE20, but results are more versatile and unpredictable because of the inherently transient and nonlinear nature of the velocity response to the turbulent wind forcing.

Figure D13 shows the variations at station 1, where under WSW20, u increases by 13 cm/s (a 62-percent increase) during flood; v increases by

12 cm/s (a 29-percent increase) during flood. Under SE20, u decreases by 16 cm/s (a 76-percent decrease) during ebb; v decreases by 21 cm/s during flood (a 51-percent decrease). Figure D14 shows the variation at station 2, where under WSW20, u increases by 2.5 cm/s (a 20-percent increase) during flood; v increases by 1.2 cm/s (a 34-percent increase) during flood. Under SE20, u decreases by 8 cm/s (a 64-percent decrease) during flood; v decreases by 1.7 cm/s (a 49-percent decrease) during flood. Figure D15 shows the variation at station 3, where under WSW20, u decreases by 0.2 cm/s (a 22-percent decrease) during flood; v increases by 1 cm/s (a 13-percent increase). Under SE20, u increases by 0.2 cm/s (a 22-percent increase) during flood; v decreases by 4 cm/s during ebb (a 50-percent decrease). Figure D16 shows the variation at station 4, where under WSW20, u increases by 3 cm/s (a 59-percent increase) during flood; v is out of phase. Under SE20, u decreases by 9 cm/s (a 176-percent decrease) during ebb.

Results for the NED 2 Condition

Figures C5 and C6 display circulation vector plots for NED 2 under BW, WSW20, and SE20. The overall circulation pattern is similar to POLA 1, except at the station near the north channel, where NED 2 has slightly higher velocity.

Impacts of harbor configuration under base wind condition

Figures D17-D20 compare the velocity variation between NED 2 and the existing condition under BW.

Figure D17 shows velocity variation at station 1, where u velocity increases while v velocity decreases. Figure D18 shows the velocity variation at station 2, where the amplitude of the v velocity increases both at flood and ebb tide. The mean westward velocity was replaced by small eastward velocity after the introduction of Pier 400. Figure D19 shows velocities at station 3, where the u velocity is virtually diminished to zero while v velocity increases in magnitude. The u velocity diminishes because this station is located next to the west side of Pier 400, where the cross-structure motion is inhibited. Figure D20 shows velocities at station 4, where previously strong eastward u velocity was replaced by smaller oscillatory flow, while v velocity is reduced significantly in magnitude.

Impacts under critical wind conditions

After examining the impact of the harbor configuration under the base wind condition, we continue to investigate the critical wind effect.

E4

Figure D21 shows the variation at station 1, where under WSW20, u increases by 15 cm/s (a 75-percent increase) during flood; v increases by 8 cm/s (a 19-percent increase) during flood. Under SE20, u decreases by 16 cm/s (an 80-percent decrease) during ebb; v decreases by 19 cm/s (a 45-percent decrease) during ebb. Figure D22 shows the variation at station 2, where under WSW20, u increases by 3 cm/s (a 16-percent increase) during flood; v increases by 5.5 cm/s (a 106-percent increase) during flood. Under SE20, u decreases by 15 cm/s (a 79-percent decrease) during ebb; v increases by 2 cm/s (a 38-percent increase) during flood. Figure D23 shows the variation at station 3, where under WSW20, u decreases by 0.5 cm/s (a 33-percent decrease) during flood; v nearly matches the velocity at BW. Under SE20, u decreases by 1 cm/s (a 66-percent decrease) during ebb; v decreases by 3 cm/s (a 25-percent decrease) during ebb. Figure D24 shows the variations at station 4, where under WSW20, u is out of phase; v increases by 0.5 cm/s (a 62.5-percent increase) during flood. Under SE20, u decreases by 7.5 cm/s (a 156-percent decrease) during ebb; v decreases by 1 cm/s during ebb (a 125-percent decrease).

Results for the NED 2&3 Condition

Figures C7 and C8 display circulation vector plots for NED 2&3 under BW, WSW20, and SE20. NED 2&3 is compared to the existing condition. The overall circulation pattern shows resemblance to POLA 2 because of the similarity of the harbor configuration.

Impacts of harbor configuration under base wind condition

Time series data were presented in Figures D25-D28 for comparison between NED 2&3 and the existing condition. From time to time, NED 2 was also used for comparison.

Figure D25 shows that u velocity increases while v velocity decreases from the existing condition. These are the same results as NED 2, except the magnitude of the changes in u and v are smaller in NED 2&3 than in NED 2 (by 20 percent). Figure D26 shows the u and v velocity change at station 2, which has the same pattern as NED 2, except the magnitude is 50 percent less. Figure D27 shows the u velocity is nearly zero, while the v velocity increases compared with the existing condition. The change is again smaller in NED 2&3 than in NED 2 (by 30 percent). Figure D28 shows that at station 4, v velocity is nearly zero, while u velocity for NED 2&3 is comparable to NED 2.

Impacts under critical wind conditions

Figure D29 shows the variation at station 1, where under WSW20, u increases by 15 cm/s (a 71-percent increase) during flood; v increases by 10 cm/s (a 24-percent increase) during flood. Under SE20, u decreases by

18 cm/s (an 86-percent decrease) during ebb; v decreases by 22 cm/s during flood (a 54-percent decrease). Figure D30 shows the variation at station 2, where under WSW20, u increases by 2 cm/s (a 14-percent increase) during flood; v increases by 2 cm/s (a 50-percent increase) during flood. Under SE20, u decreases by 6 cm/s (a 43-percent decrease) during ebb; v decreases by 1.5 cm/s (a 38-percent decrease) during flood. Figure D31 shows the variation at station 3, where under WSW20, u is out of phase; v decreases by 2 cm/s (a 22-percent decrease) during ebb. Under SE20, u increases by 0.1 cm/s (a 10-percent increase) during flood; v decreases by 3.5 cm/s (a 39-percent decrease) during ebb. Figure D32 shows the variation at station 4, where under WSW20, u increases by 9 cm/s (an 82-percent increase) during flood; v increases by 0.1 cm/s (a 50-percent increase) during flood. Under SE20, u decreases by 16 cm/s (a 145-percent decrease) during ebb; v decreases by 0.1 cm/s during flood (a 50-percent decrease).

Results for the NED 2-5 Condition

Figures C9 and C10 display circulation vector plots for NED 2-5 under BW, WSW20, and SE20. The overall circulation pattern is similar to NED 2&3. However, as one will see from later analysis, NED 2-5 has slight phase differences from NED 2&3 at the stations near the harbor entrance.

Impacts of harbor configuration under base wind condition

Time series data are presented in Figures D25-D28 for comparison of velocity variation between NED 2-5 and the existing condition. From time to time, NED2&3 is also used for comparison.

Figure D25 shows that at station 1, while NED 2-5 has u and v velocities comparable to NED2&3, a consistent phase lag behind NED2&3 (by 5 min) was observed. Figure D26 shows that at station 2, NED 2-5 has velocity amplitudes similar to NED 2&3. However, NED 2-5 has a phase lag behind NED 2&3 (by approximately 5 min). Figure D27 shows that at station 3, u velocity is very small (less than 1 cm/s). No phase difference was observed at this station. Figure D28 shows that NED 2-5 has a smaller u velocity than NED 2&3 at station 4.

Impacts under the critical wind condition

Figure D33 shows the variation at station 1, where under WSW20, u increases by 15 cm/s (a 71-percent increase) during flood; v increases by 10 cm/s (a 24-percent increase) during flood. Under SE20, u decreases by 19 cm/s (a 91-percent decrease) during ebb; v decreases by 12 cm/s during flood (a 24-percent decrease). Figure D34 shows the variation at station 2, where under WSW20, u and v both closely matched BW. Under SE20, u decreases by 7 cm/s (a 50-percent decrease) during ebb; v decreases by 2 cm/s

E6

(a 50-percent decrease) during flood. Figure D35 shows the variation at station 3, where under WSW20, u is out of phase; v closely matches the BW results. Under SE20, u increases by 0.2 cm/s (a 20-percent increase) during flood; v decreases by 3.5 cm/s (a 39-percent decrease) during ebb. Figure D36 shows the variation at station 4, where under WSW20, u increases by 3 cm/s (a 50-percent increase) during flood; v increases by 0.1 cm/s (a 50-percent increase) during flood. Under SE20, u decreases by 8 cm/s (a 133-percent decrease) during ebb; v decreases by 0.1 cm/s during ebb (a 50-percent decrease).
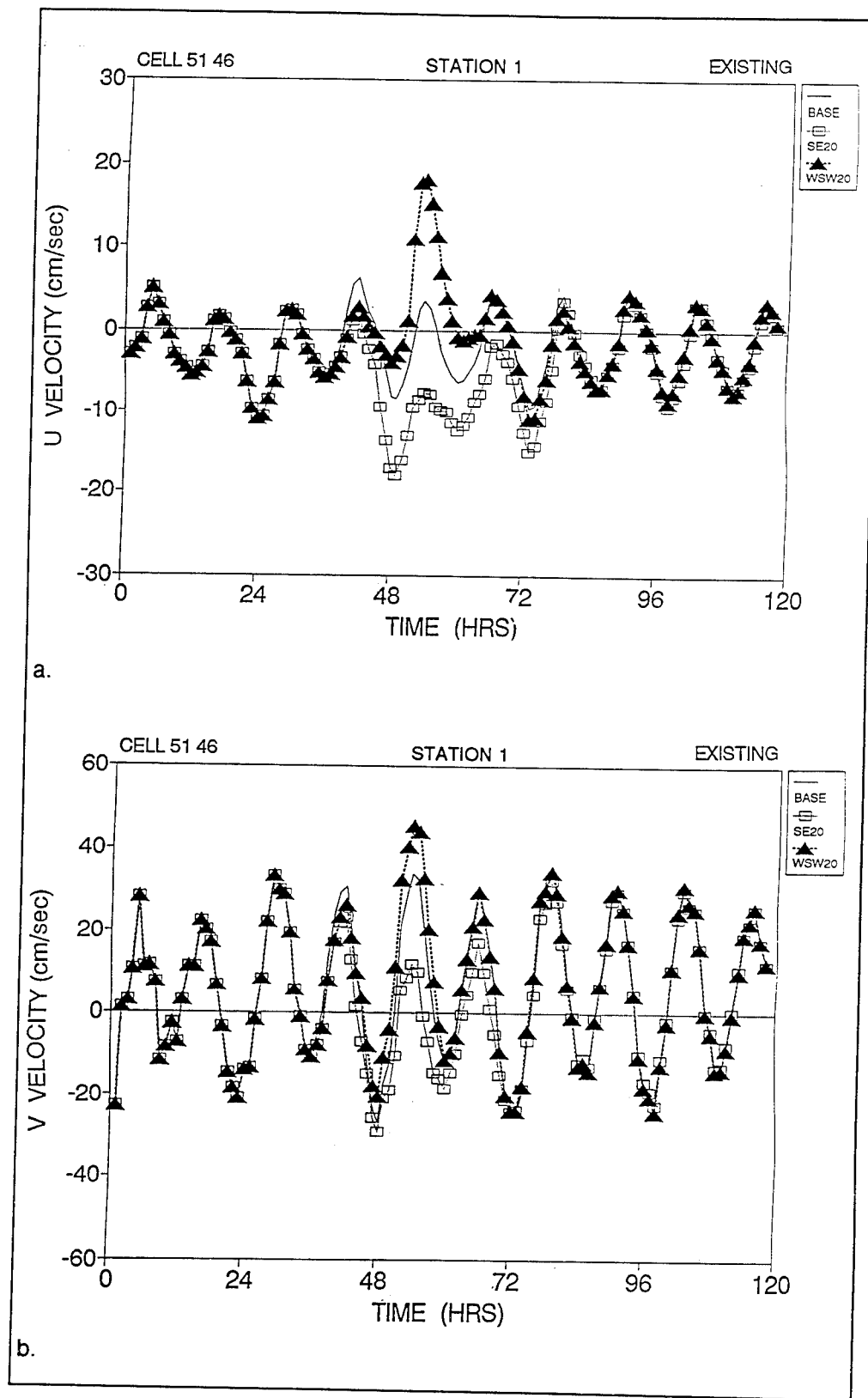
Figure E1. Time series of response of u and v current velocity components (a and b, respectively) to BW, SE20, and WSW20 at station 1 for the existing condition
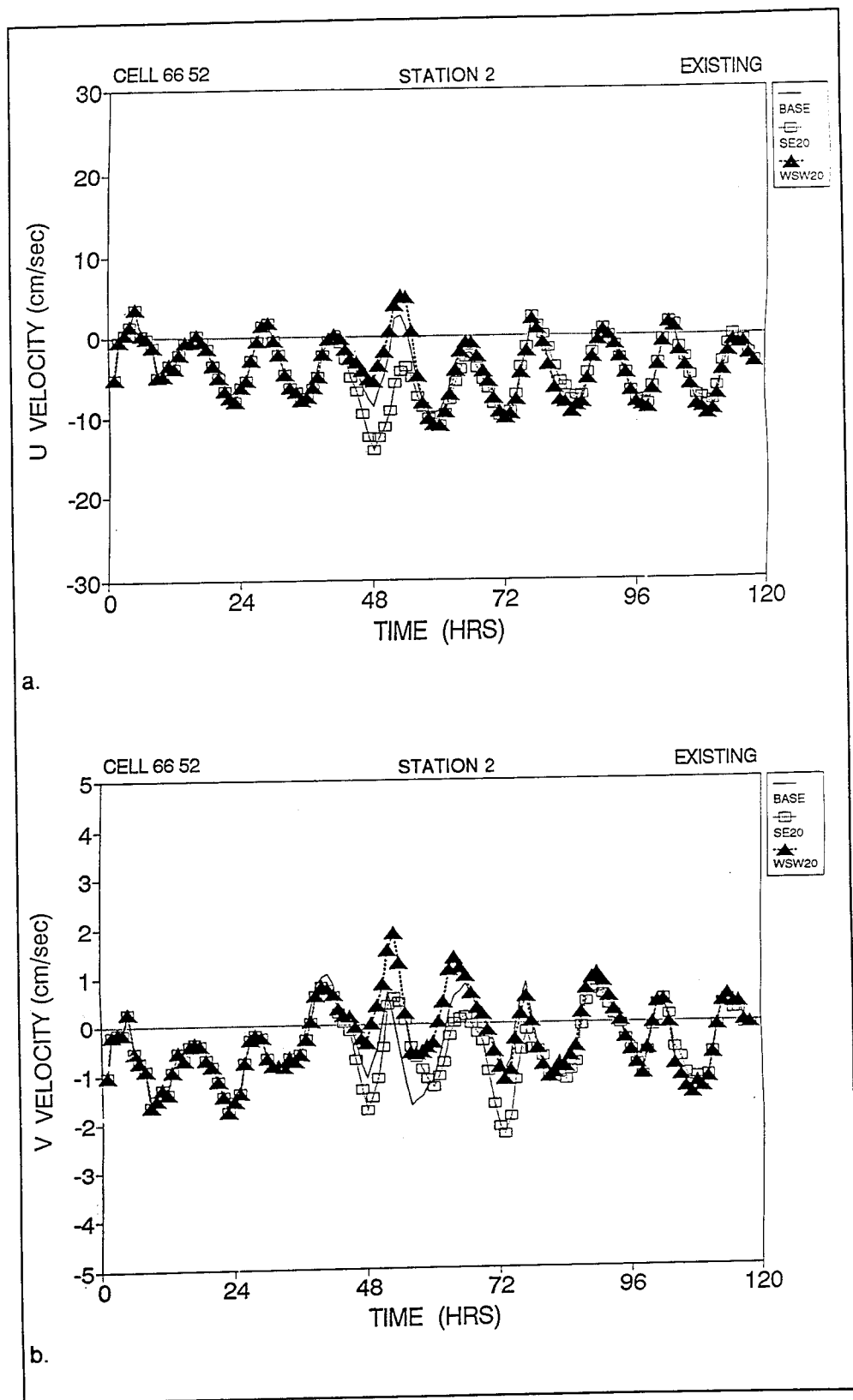
Figure E2. Time series of response of u and v current velocity components (a and b, respectively) to BW, SE20, and WSW20 at station 2 for the existing condition
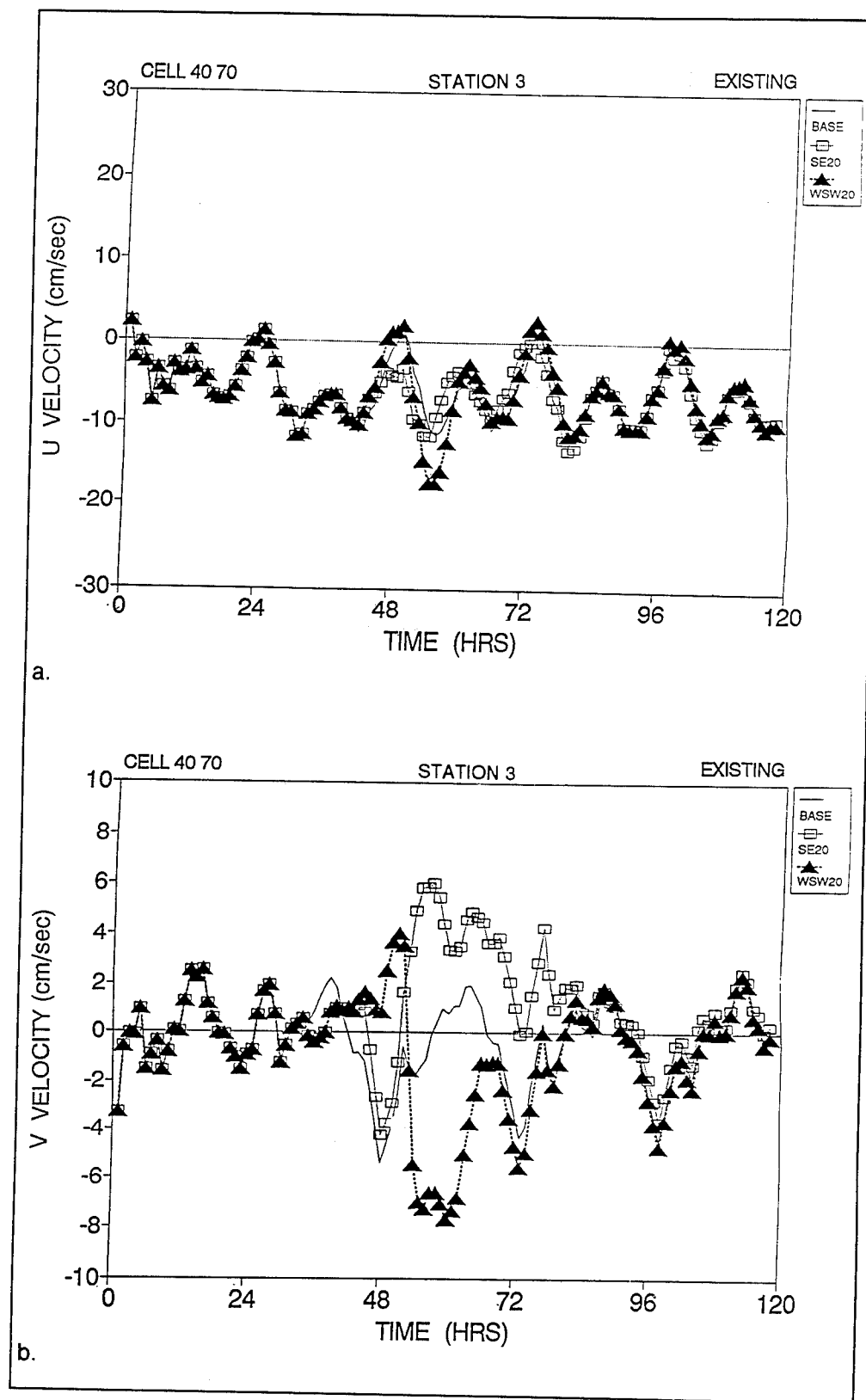
Figure E3. Time series of response of u and v current velocity components (a and b, respectively) to BW, SE20, and WSW20 at station 3 for the existing condition
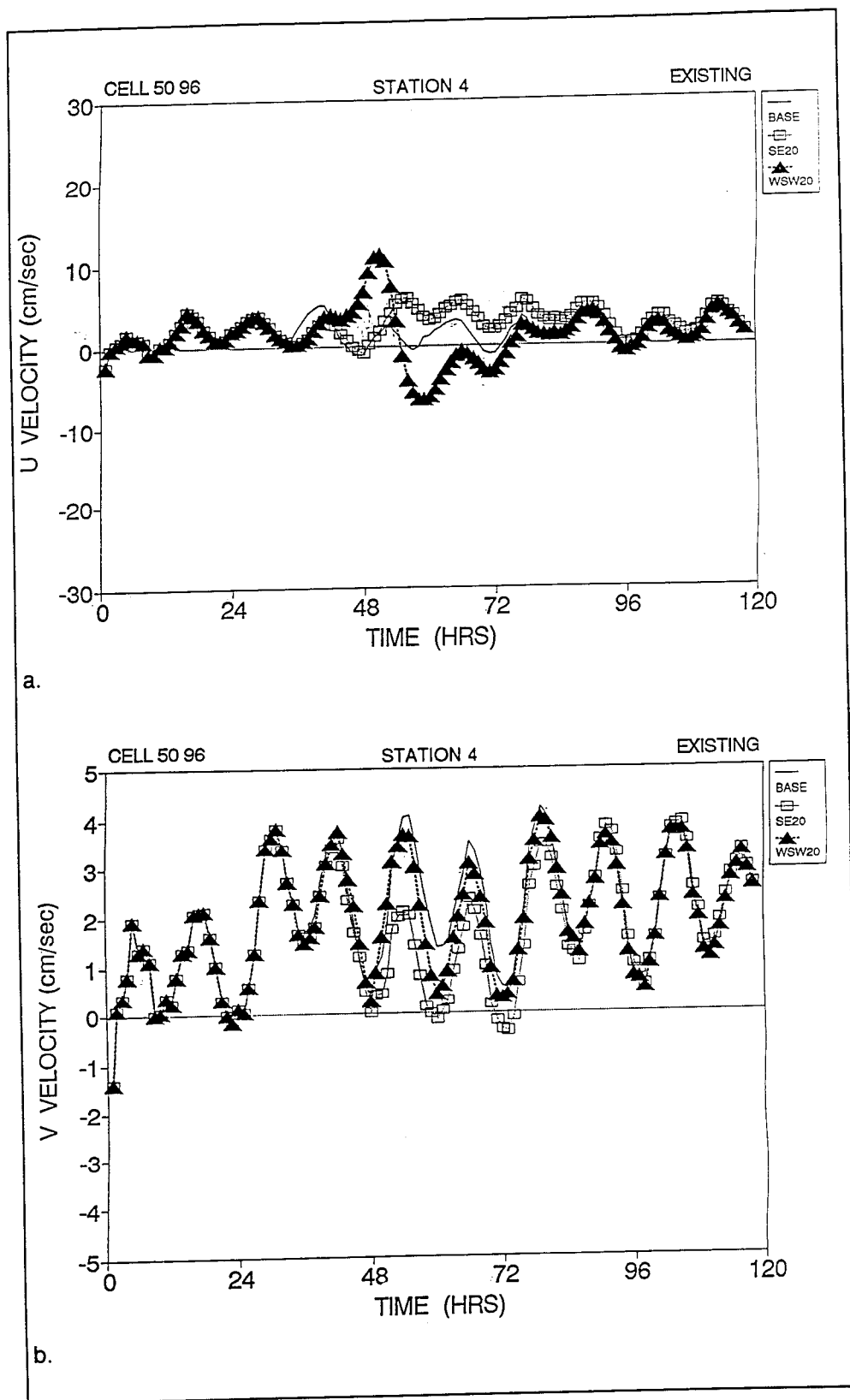
Figure E4. Time series of response of u and v current velocity components (a and b, respectively) to BW, SE20, and WSW20 at station 4 for the existing condition

Appendix E   Analysis of Hydrodynamic Impacts

REPORT DOCUMENTATION PAGE

1. AGENCY USE ONLY (Leave blank)	2. REPORT DATE January 1995	3. REPORT TYPE AND DATES COVERED Final report

4. TITLE AND SUBTITLE

Numerical Hydrodynamic Modeling in Support of Water Quality and Ship Simulation Models in Los Angeles Harbor

5. FUNDING NUMBERS

6. AUTHOR(S)

Harry V. Wang
Alan Cialone
Panola Rivers

7. PERFORMING ORGANIZATION NAME(S) AND ADDRESS(ES)

U.S. Army Engineer Waterways Experiment Station
3909 Halls Ferry Road
Vicksburg, MS 39180-6199

8. PERFORMING ORGANIZATION REPORT NUMBER

Miscellaneous Paper
CERC-95-1

9. SPONSORING/MONITORING AGENCY NAME(S) AND ADDRESS(ES)

U.S. Army Engineer District, Los Angeles
Los Angeles, CA 90053-2325

10. SPONSORING/MONITORING AGENCY REPORT NUMBER

11. SUPPLEMENTARY NOTES

Available from National Technical Information Service, 5285 Port Royal Road, Springfield, VA 22161.

12a. DISTRIBUTION/AVAILABILITY STATEMENT

Approved for public release; distribution is unlimited.

12b. DISTRIBUTION CODE

13. ABSTRACT (Maximum 200 words)

A previously calibrated three-dimensional, numerical circulation model for Los Angeles Harbor has been used to assess the hydrodynamic impact of proposed ship channel dredging and landfill at Pier 400 in the Los Angeles Harbor. Supplemental calibration and verification were conducted for both coarse and fine model grids used in support of water quality and ship simulation models, respectively. Results of numerical modeling show that the water surface elevation in the harbor was very little affected by either the deepening of the channel or by the construction of Pier 400. Flow velocities, on the other hand, changed. Flow velocities were mainly forced to conform to the shape of Pier 400, which is proposed to be placed in the middle of outer Los Angeles Harbor. Overall velocity magnitudes are slightly lower for the proposed deeper channel depth versus the existing shallower depth. Critical wind forcings (20-knot speed from the west southwest and southeast directions) were simulated in order to predict the highly transient current velocity in the navigation channel. Results indicate that the wind's effect can be significant. Nevertheless, current velocities are generally under 1 knot in the harbor channel, except for extremely high wind conditions.

14. SUBJECT TERMS

Circulation
Hydrodynamics
Los Angeles harbor
Numerical model
Wind effects

15. NUMBER OF PAGES
223

16. PRICE CODE

17. SECURITY CLASSIFICATION OF REPORT UNCLASSIFIED	18. SECURITY CLASSIFICATION OF THIS PAGE UNCLASSIFIED	19. SECURITY CLASSIFICATION OF ABSTRACT	20. LIMITATION OF ABSTRACT